UNIVERSIDAD COMPLUTENSE DE MADRID

FACULTAD DE CIENCIAS MATEMÁTICAS

Sección Departamental de Física de la Tierra, Astronomía y Astrofísica I
(Geofísica y Meteorología) (Astronomía y Geodesia),

DEVELOPMENT OF ALGORITHMS FOR THE GNSS DATA PROCESSING: THEIR APPLICATION TO THE MODERNIZED GPS AND GALILEO SCENARIOS. DESARROLLO DE ALGORITMOS PARA EL TRATAMIENTO DE DATOS GNSS: SU APLICACIÓN A LOS ESCENARIOS GPS MODERNIZADO Y GALILEO

MEMORIA PARA OPTAR AL GRADO DE DOCTOR
PRESENTADA POR

Beatriz Moreno Monge

Bajo la dirección de los doctores

Gracia Rodríguez Caderot
M. Clara de Lacy Pérez de los Cobos

Madrid, 2012

Development of Algorithms for the GNSS data processing: their application to the Modernized GPS and Galileo Scenarios

Desarrollo de algoritmos para el tratamiento de datos GNSS: su aplicación a los escenarios GPS modernizado y Galileo

DOCTORAL THESIS

Beatriz Moreno Monge
Department of Geophysics, Astronomy and Astrophysics I
Faculty of Mathematics
Universidad Complutense de Madrid

Interuniversitary doctoral program
"Science and Technology of the Geodetic and Cartographic Engineering"

Universidad Complutense de Madrid

Development of Algorithms for the GNSS data processing: their application to the Modernized GPS and Galileo Scenarios

Desarrollo de algoritmos para el tratamiento de datos GNSS: su aplicación a los escenarios GPS modernizado y Galileo

Dissertation submitted by **Beatriz Moreno Monge** in support of her candidature for the doctoral degree by the University Complutense of Madrid
*Memoria presentada por **Beatriz Moreno Monge** para optar al grado de Doctor por la Universidad Complutense de Madrid*

Directors

Dr. Gracia Rodríguez Caderot

Dr. M. Clara de Lacy Pérez de los Cobos

Madrid, 13th May, 2012

Acknowledgments

First of all, I would like to thank Gracia and Clara for their priceless guidance all through these five years, for their constant support and understanding, for the innumerable discussions and advises. Thank you for proposing me such a beautiful theme for my thesis and for encouranging me day by day and, especially thank you for making work a pleasant experience.

Then I want to thank Michel for his kindness and his help during these years. Thank you Michel for counting on me, it has been a pleasure to collaborate with you, with Lidia, Sergio, Izarra and Marta.

I would like also to thank the ESA TEC-ETN section for their warm welcome during my stage at ESTEC between September of 2008 and February of 2009. I am especially grateful to Fran, who managed that stage to be possible and scratched his head trying to solve all the problems I always came up with. Thank you Fran, for your willingness to help me always without expecting anything in change. I also want to say thank you so much to Michelangelo, for his kind tuition in the use the GNSS signal simulators and receivers at the ESA Radio Navigation Laboratory and for providing me several datasets of simulated observations, which would have been imposible to find otherwise.

I am very thankful to Prof. Sandro Radicella, for his kind reception at ICTP and his invaluable help and advises during the last years, which have been essential for the development of this thesis.

I thank my family for their patience and understanding and I ask them to continue supporting me in the years to come, since a researching career may keep one far from home for a very long time.

Finally, I would like to dedicate this thesis to my grandmothers, who have recently left us.

To the memmory of Eloisa Ruíz Hervás (1921-2011)
and Isabel Mata Monasterio (1924-2012)

Contents

Contents

List of Figures

List of Tables

Acronyms

AC Analysis Center.

AltBOC Alternative Binary Offset Carrier.

APPS Automatic Point Positioning Service.

ARP Antenna Reference Point.

BDT COMPASS/BeiDou Time.

BGD Broadcast Group Delay.

BIH Bureau International de l'Heure.

BKG German Federal Agency for Cartography and Geodesy.

BOC Binary Offset Carrier.

BSW Bernese GPS software.

C/NAV Galileo Commercial NAVigation message.

CBOC Composite Binary Offset Carrier.

CDMA Code Division Multiple Access.

CGS2000 China Geodetic System 2000.

CNAV GPS Civil NAVigation message.

CODE Center for Orbit Determination in Europe.

CONGO COperative Network for Giove Observation.

CS Commercial Service.

CWAAS Canadian Wide Area Augmentation System.

DCB Differential Code Bias.

DLR German Aerospace Center.

DOP Dilution of Precision.

DOY Day of Year.

DSF Galileo Data Server Facility.

Dst Disturbance storm-time.

E-OSPF Experimental Orbit Synchronisation Processing Facility.

EA Equatorial Anomaly.

EC European Commission.

ECEF Earth-Centered Earth-Fixed.

EDAS EGNOS Data Access Service.

EGGTO Experimental GPS to Galileo Time Offset.

EGNOS European Geostationary Navigation Overlay Service.

EGST Experimental Galileo System Time.

EOP Earth Orientation Parameters.

EPB Equatorial Plasma Bubble.

ESA European Space Agency.

EU European Union.

F/NAV Galileo Freely accessible NAVigation message.

FAA U.S. Federal Aviation Administration.

FDMA Frequency Division Multiple Access.

FOC Full Operational Capability.

G/NAV Galileo Governmental NAVigation message.

GAGAN GPS/GLONASS And Geo-stationary Augmented Navigation.

GBAS Ground-Based Augmentation Systems.

GCC Galileo Control Center.

GDOP Geometric Dilution of Precision.

GEO GEOstationary.

GESS Galileo Experimental Sensor Station.

GETR Galileo Experimental Test Receiver.

GGSP Galileo Geodetic Service Provider.

GGTO GPS to Galileo Time Offset.

GIM Global Ionospheric Map.

GIOVE Galileo In-Orbit Validation Element.

GLONASS GLObal NAvigation Satellite System.

GLoTS GLONASS Time System.

GNSS Global Navigation Satellite System.

GPC Galileo Processing Center.

GPS Global Positioning System.

GPST GPS Time system.

GSS Galileo Sensor Stations.

GST Galileo System Time.

GTRF Galileo Terrestrial Reference Frame.

I/NAV Galileo Integrity NAVigation message.

IAU International Astronomical Union.

IERS International Earth Rotation Service.

IFB Inter Frequency Bias.

IGS International GNSS Service.

IGSO Inclined GeoSynchronous Orbit.

INLUS INdian Land Uplink Station.

INMCC INdian Master Control Centre.

INRES INdian REference Stations.

IOC Initial Operational Capability.

IOV In-Orbit Validation.

IP Ionospheric Piercing point.

ISB InterSystem Bias.

ISRO Indian Space Research Organization.

ITRF International Terrestrial Reference Frame.

ITRS International Terrestrial Reference System.

ITU International Telecommunications Union.

IUGG International Union of Geodesy and Geophysics.

JPL Jet Propulsion Laboratory.

LAAS Local-Area Augmentation System.

LEO Low Earth Orbit.

LSA Least Squares Adjustment.

MAP3 Multi-frequency Algorithms for PPP.

MBOC Multiplexed Binary Offset Carrier.

MCS Master Control Station.

MEO Medium Earth Orbit.

MOPS Minimal Operation Performance System.

MSAS Multifunctional transport Satellite Augmentation System.

MTSAT Multifunctional Transport Satellites.

MW Melbourne-Wübbena.

NDS Nuclear Detonation detection System.

NLES Navigation Land Earth Stations.

NMF Niell Mapping Function.

NOAA National Oceanic and Atmospheric Administration.

NRCan Natural Resources of Canada.

ODTS Orbit Determination and Time Synchronisation.

OS Open Service.

PCO Phase Center Offset.

PCV Phase Center Variation.

PHM Passive Hydrogen Maser.

PPP Precise Point Positioning.

PPS Precise Positioning Service.

PRN Pseudo-Random Noise.

PRS Public Regulated Service.

PVT Position, Velocity and Timing.

PZ-90 Parametri Zemli 1990.

QPSK Quadrature Phase Shift Keying.

RAFS Rubidium Atomic Frequency Standard.

RIMS Ranging and Integrity Monitoring Stations.

ROT Rate of TEC.

SAR Search And Rescue.

SBAS Satellite-Based Augmentation System.

SDCM System for Differential Correction and Monitoring.

SNAS Satellite Navigation Augmentation System.

SNR Signal to Noise Ratio.

SoL Safety-of-Life.

SPS Standard Positioning Service.

sTEC slant Total Electron Content.

TAI International Atomic Time.

TEC Total Electron Content.

TECU Total Electron Content Unit.

TUR Test User Receiver.

USNO United States Naval Observatory.

UT Universal Time.

UTC Coordinated Universal Time.

VHF Very High Frequency.

vTEC vertical Total Electron Content.

WAAS Wide Area Augmentation System.

WGS-84 World Geodetic System 1984.

ZWD Zenith Wet Delay.

Resumen en español

El término GNSS (Global Navigation Satellite System) comprende, tanto los sistemas individuales de posicionamiento global por satélite (GPS, Galileo, GLONASS, etc), como su combinación y aumentación mediante otros sistemas.

Actualmente, los únicos sistemas globales de navegación por satélites operativos son GPS y GLONASS, sin embargo, en un futuro cercano el proyecto europeo Galileo y el sistema chino COMPASS entrarán a formar parte del actual escenario GNSS.

Desde su comienzo en los años 90, el sistema GPS ha proporcionado múltiples servicios a diferentes comunidades de usuarios, convirtiéndose en el principal sistema de navegación. Sin embargo, el continuo desarrollo tecnológico, el creciente número en las necesidades de los usuarios y la competitividad con el sistema de navegación europeo, han propiciado la modernización del programa GPS (Hofmann-Wellenhof et al., 2008). Los primeros satélites del sistema GPS modernizado han sido lanzados recientemente, esperando alcanzar la operatividad total de este sistema a partir del año 2018. Al GPS modernizado le seguirá el GPS III, que contará con una nueva infraestructura, nuevos satélites y señales optimizadas.

Por otra parte, el sistema soviético GLONASS fue declarado disponible para uso civil en 1999 y en 2001 se adoptó un programa federal para su revitalización y modernización. Actualmente, GLONASS ha alcanzado la operabilidad total y cuenta con 24 satélites operativos.

El proyecto Galileo surge en los años 80 como una iniciativa conjunta entre la Unión Europea (UE) y la Agencia Espacial Europea (ESA), tras reconocer la importancia estratégica, económica, social y tecnológica de la navegación por satélite (Hofmann-Wellenhof et al., 2008). Galileo es el primer sistema de posicionamiento global diseñado fundamentalmente para uso civil, capaz de trabajar de forma completamente independiente del sistema GPS, siendo compatible e interoperable con éste y otros sistemas de navegación por satélites (Prasad and

Ruggieri, 2005). Actualmente, Galileo se encuentra en periodo de validación en órbita mediante dos satélites experimentales, GIOVE-A y B, y una red global de estaciones permanentes, GESS (Galileo Experimental Sensor Stations) y se prevé que alcanzará la operabilidad total a partir del año 2014. Los dos primeros satélites Galileo se han lanzado recientemente y ya han comenzado a transmitir las nuevas señales.

Una característica común de estos nuevos sistemas de posicionamiento es la adquisición de nuevas frecuencias, códigos y mensajes de navegación optimizados (Hofmann-Wellenhof et al., 2008). Las señales a que darán lugar presentarán mejores propiedades de correlación y una mayor potencia y protección frente a interferencias, lo que facilitará la rápida adquisición de la señal y permitirá alcanzar una mayor precisión en el posicionamiento. Adicionalmente, se emplearán por primera vez, al menos, tres frecuencias distintas por parte de cada uno de los sistemas, dando lugar a un escenario multi-frecuencia que revolucionará las técnicas de posicionamiento.

La presencia de nuevas frecuencias, así como la existencia de una constelación múltiple de satélites, contribuirá a aumentar considerablemente la redundancia de observaciones y mejorará la geometría de los satélites visibles. Por otra parte, las observaciones triple frecuencia darán lugar a un mayor número de combinaciones lineales, con las que será posible reducir los efectos atmosféricos en un mayor orden y optimizar los métodos de resolución de ambigüedades y detección y corrección de saltos de ciclo (de Lacy et al., 2008a).

Entre las técnicas actuales de posicionamiento con GNSS destaca el Posicionamiento Preciso Puntual (PPP), dada su gran flexibilidad, bajo coste y las altas precisiones alcanzables en la determinación de la posición, tanto en modo estático como cinemático. El PPP consiste en determinar la posición de un receptor a partir de observaciones de código y fase no differenciadas y productos precisos. Si bien las técnicas diferenciales proporcionan mejores precisiones y repetibilidad de las soluciones, el PPP no requiere la existencia de redes permanentes ni la utilización de varios receptores simultáneamente, lo que reduce significativamente su coste y permite determinar la posición incluso en los lugares más remotos. Además, el PPP proporciona exactitudes del orden de dm en modo cinemático y de cm en modo estático (Bisnath and Gao, 2007) llegando a alcanzar una exactitud del orden de mm tras 24 horas de observación (Geng et al., 2009). La técnica clásica de PPP está basada en la aplicación de un ajuste mínimos cuadrados o un filtro secuencial a la combinación ionofree de observaciones de código y fase doble frecuencia.

Por el momento, los únicos software existentes para PPP sólo están preparados para trabajar con observaciones doble frecuencia procedentes de los sistemas GPS y GLONASS y, por tanto, es necesario desarrollar nuevos algoritmos que permitan procesar observaciones multi-frecuencia de los futuros sistemas y saquen el máximo partido a las múltiples ventajas del futuro escenario GNSS. Entre los software actuales para PPP destacan Bernese 5.0 (Dach et al., 2007) y los servicios online CSRS-PPP de NRCan (`www.geod.nrcan.gc.ca`), APPS de JPL (`apps.gdgps.net/apps/index.php`) y MagicGNSS de GMV (`magicgnss.gmv.es`).

En este trabajo de tesis se ha desarrollado unos nuevos y originales algoritmos para PPP, capaces de procesar observaciones GNSS multi-frecuencia y multisistema y determinar la posición de un receptor de forma precisa y exacta. En particular, estos algoritmos permiten trabajar con los sistemas GPS modernizado y Galileo del futuro escenario GNSS.

Estos nuevos algoritmos se han denominado MAP3, del inglés, Multifrequency Algorithms for PPP, y se han integrado dentro de un software de PPP, que hemos desarrollado en colaboración con personal científico de la ESA.

En el diseño de los algoritmos se ha partido de las expresiones de las observaciones GPS dadas en Euler and Goad (1991), las cuales se han aplicado al caso multi-frecuencia. Empleando la teoría mínimos cuadrados se han obtenido expresiones explícitas para estimar el retraso ionosférico, ambigüedades de fase inicial y pseudodistancias suavizadas, las cuales a su vez se emplean para determinar la posición del receptor y el offset de su reloj.

A continuación se presentan las expresiones finales de estos algoritmos MAP3, los desarrollos teóricos completos están recogidos en el capítulo 4. Las expresiones para la estimación de las ambigüedades de fase inicial como valores reales y del retraso ionosférico y la pseudodistancia suavizada en cada época son:

$$\begin{aligned}\hat{\boldsymbol{\beta}} = \begin{pmatrix} \hat{\beta}_1 \\ \hat{\beta}_2 \\ \hat{\beta}_3 \end{pmatrix} &= \left(D^{-1} - Q_L D^{-1} Q_L^{-1} A_2 N^{-1} A_2^T Q_L^{-1}\right) \bar{\boldsymbol{L}} \\ &- Q_L D^{-1} Q_L^{-1} A_2 N^{-1} A_1^T Q_P^{-1} \bar{\boldsymbol{P}}\end{aligned} \tag{1}$$

$$\begin{aligned}\hat{\boldsymbol{\xi}}(t) = \begin{pmatrix} \hat{\tilde{\rho}}(t) \\ \hat{J}_1(t) \end{pmatrix} &= N^{-1} A_2^T D^{-1} Q_L^{-1} A_2 N^{-1} \left(A_1^T Q_P^{-1} \bar{\boldsymbol{P}} + A_2^T Q_L^{-1} \bar{\boldsymbol{L}}\right) \\ &+ N^{-1} \left(A_1^T Q_P^{-1} \boldsymbol{P}(t) + A_2^T Q_L^{-1} \boldsymbol{L}(t)\right) - N^{-1} A_2^T Q_L^{-1} D^{-1} \bar{\boldsymbol{L}}\end{aligned} \tag{2}$$

donde $\tilde{\rho}(t)$ contiene la distancia geométrica entre el receptor y el satélite, los offset de los relojes y el retraso troposférico y J_1 es el retraso ionosférico en la frecuencia f_1. Además,

$$\begin{aligned} N^{-1} &= M^{-1} - M^{-1}A_2^T Q_L^{-1}\left(I_3 + A_2 M^{-1} A_2^T Q_L^{-1}\right)^{-1} A_2 M^{-1}, \\ D^{-1} &= I_3 + A_2 M^{-1} A_2^T Q_L^{-1}, \end{aligned} \tag{3}$$

con $M = A_1^T Q_P^{-1} A_1$, I_3 es la matriz identidad de dimensión 3, las matrices

$$A_1 = \begin{pmatrix} 1 & 1 \\ 1 & k_{12} \\ 1 & k_{13} \end{pmatrix}, \quad A_2 = \begin{pmatrix} 1 & -1 \\ 1 & -k_{12} \\ 1 & -k_{13} \end{pmatrix},$$

$k_{1i} = f_i^2/f_1^2$ y $\bar{\boldsymbol{P}}$, $\bar{\boldsymbol{L}}$ representan la media aritmética de las medidas de código y fase, resp., a lo largo de todo el periodo de observación.

En este modelo, las ambigüedades de fase inicial se consideran constantes durante todo el periodo de observación y, por tanto, las observaciones de fase deben estar libres de saltos de ciclo, lo que se debe asegurar mediante un buen preprocesado. El modelo estocástico está formado por las matrices

$$Q_P = \begin{pmatrix} \nu_{P_1} & 0 & 0 \\ 0 & \nu_{P_2} & 0 \\ 0 & 0 & \nu_{P_3} \end{pmatrix} y \quad Q_L = \begin{pmatrix} \nu_{L_1} & 0 & 0 \\ 0 & \nu_{L_2} & 0 \\ 0 & 0 & \nu_{L_3} \end{pmatrix},$$

donde ν_{P_i} son del orden de dm y ν_{L_i} del orden de mm. En la práctica, este modelo estocástico se ha mejorado teniendo en cuenta la elevación del satélite en cada época de observación.

La teoría mínimo-cuadrática también proporciona matrices de covarianza para los parámetros estimados:

$$C_{\hat{\boldsymbol{\beta}}\hat{\boldsymbol{\beta}}} = \hat{\sigma}_0^2 \frac{1}{n_t} D^{-1} Q_L, \tag{4}$$

$$C_{\hat{\boldsymbol{\xi}}(t)\hat{\boldsymbol{\xi}}(t)} = \hat{\sigma}_0^2 \left(N^{-1} + \frac{1}{n_t} N^{-1} A_2^T D^{-1} Q_L^{-1} A_2 N^{-1} \right) \tag{5}$$

donde n_t representa el número total de observaciones y $\hat{\sigma}_0^2$ es la varianza a posteriori del ajuste.

Las pseudodistancias suavizadas obtenidas en la primera parte se pueden emplear en la estimación de la posición del receptor y el offset de su reloj, dado que, para un satélite s y una época de observación t, se tiene:

$$\tilde{\rho}^s(t) = \rho^s(t) + c\,(dt_r(t) - dt^s(t)) + Trop^s(t) + \nu \tag{6}$$

donde $\tilde{\rho}^s(t)$ es la pseudodistancia suavizada obtenida con (2),

$$\rho^s(t) = \sqrt{(X^s(t) - X_r)^2 + (Y^s(t) - Y_r)^2 + (Z^s(t) - Z_r)^2},$$

con (X^s, Y^s, Z^s) las coordenadas del satélite s y (X_r, Y_r, Z_r) las del receptor. Por otro lado, $dt_r(t)$ y $dt^s(t)$ son los términos del reloj del receptor y el satélite, multiplicados por la velocidad de la luz, c; $Trop^s(t)$ es el retraso troposférico y ν representa el ruido de las pseudodistancias suavizadas obtenidas anteriormente (del orden de mm). El offset del reloj del satélite, dt^s, se obtiene a partir de productos precisos proporcionados por diferentes centros de análisis y el retraso troposferico se corrige mediante un modelo (p. ej. Hopfield (1969), Saastamoinen (1973), etc). Sin embargo, es preciso estimar una corrección al retraso troposférico zenital húmedo, ZWD, por lo menos, cada dos horas.

Empleando de nuevo la teoría mínimos cuadrados se obtienen expresiones para la estimación de la corrección a la posición a priori del receptor, $(\delta X, \delta Y, \delta Z)$, el offset del reloj del receptor en cada época, $dt_r(t)$, y una corrección al retraso troposférico zenital cada dos horas, ZWD:

$$\boldsymbol{\delta\hat{X}} = \begin{pmatrix} \delta\hat{X} \\ \delta\hat{Y} \\ \delta\hat{Z} \\ \boldsymbol{Z\hat{W}D} \end{pmatrix} = \Delta^T d_1 + \gamma d_2 \tag{7}$$

$$c \cdot \hat{\boldsymbol{dt_r}} \quad = \Gamma d_1 + \Delta d_2. \tag{8}$$

También se obtienen matrices de covarianza de los parámetros estimados:

$$C_{\boldsymbol{\delta\hat{X}\delta\hat{X}}} = \hat{\sigma}^2\gamma \qquad C_{c\hat{\boldsymbol{dt}}_{\boldsymbol{r}}c\hat{\boldsymbol{dt}}_{\boldsymbol{r}}} = \hat{\sigma}^2\Gamma. \tag{9}$$

En estas expresiones

$$\begin{pmatrix} d_1 \\ d_2 \end{pmatrix} = \begin{pmatrix} \sum_{s=1}^{n_s} C^{-1}_{\boldsymbol{y^s y^s}} \boldsymbol{y}^s \\ \sum_{s=1}^{n_s} G^{sT} C^{-1}_{\boldsymbol{y^s y^s}} \boldsymbol{y}^s \end{pmatrix},$$

y

$$\begin{aligned} \gamma &= \left(F - E^T \tilde{N}^{-1} E\right)^{-1}, \\ \Delta &= -\tilde{N}^{-1} E\gamma, \\ \Gamma &= \tilde{N}^{-1}\left(I_{n_t} - E\Delta^T\right), \end{aligned}$$

con

$$\tilde{N} = \sum_{s=1}^{n_s} C^{-1}_{\boldsymbol{y^s y^s}}, \quad E = \sum_{s=1}^{n_s} C^{-1}_{\boldsymbol{y^s y^s}} G^s, \quad F = \sum_{s=1}^{n_s} G^{sT} C^{-1}_{\boldsymbol{y^s y^s}} G^s,$$

donde el vector de observación $\boldsymbol{y^s}$ está formado por las observaciones corregidas con la distancia receptor-satélite calculada con unas coordenadas a priori de la estación, los offset de los relojes de los satélites y el retraso troposférico obtenido con un modelo. Las matrices G^s forman parte de la matriz de diseño y contienen los coeficientes de las incógnitas.

El modelo estocástico empleado en esta segunda parte es:

$$C_{\boldsymbol{yy}} = \begin{pmatrix} C_{\boldsymbol{y}^1\boldsymbol{y}^1} & 0 & \dots & 0 \\ 0 & C_{\boldsymbol{y}^2\boldsymbol{y}^2} & \dots & 0 \\ \vdots & \vdots & \ddots & \vdots \\ 0 & 0 & \dots & C_{\boldsymbol{y}^{n_s}\boldsymbol{y}^{n_s}} \end{pmatrix},$$

donde, para cada satélite s y para cada arco continuo de observación, se ha formado la matriz completa

$$Q_{\boldsymbol{yy}} = \begin{pmatrix} d+a & a & \dots & a \\ a & d+a & & \vdots \\ \vdots & & \ddots & a \\ a & \dots & a & d+a \end{pmatrix} = dI_n + a\boldsymbol{e}\boldsymbol{e}^T.$$

En esta expresión, d es el primer elemento de la matriz N^{-1} dada en (3), y a el primer elemento de $N^{-1}A_2^T D^{-1} Q_L^{-1} A_2 N^{-1}$ dividido por n. Aunque esta matriz es una simplificación de la matriz de covarianzas completa (5), su utilización mejora las estimaciones con respecto a las obtenidas con una matriz diagonal. Además, esta matriz posee una inversa conocida:

$$Q_{\boldsymbol{yy}}^{-1} = \frac{1}{d}\left(I_n - \frac{a}{d+na}\boldsymbol{e}\boldsymbol{e}^T\right)$$

cuya utilización reduce el tiempo de computación requerido por el proceso.

Estos algoritmos permiten combinar observaciones procedentes de diferentes sistemas de satélites, siempre que se tenga en cuenta el InterSystem Bias (ISB), que es debido a que la señal de diferentes sistemas se procesa en partes distintas del receptor.

Los algoritmos MAP3 se han implementado en Matlab y se han integrado dentro de un software para PPP denominado PCube, que hemos desarrollado junto con personal científico de la ESA. PCube permite procesar observaciones de los sistemas GPS modernizado y Galileo/GIOVE, junto con productos precisos de IGS (International GNSS Service) o GPC (Galileo Processing Center), siendo posible combinarlos entre sí. PCube efectua un preprocesado completo de las observaciones, eliminando los outliers y saltos de ciclo, interpolando los productos

precisos de los satélites a las épocas de observación y corrigiendo todos los distintos efectos en las observaciones. Para la estimación de la posición del receptor, PCube permite elegir entre un filtro secuencial y los algoritmos MAP3, después se efectúa un análisis estadístico de los residuos, eliminando los últimos outliers y se corrige la posición estimada de los efectos de mareas y carga oceánica.

Para estudiar la bondad de los algoritmos MAP3 se han llevado a cabo una serie de test numéricos en diferentes escenarios. En primer lugar, se han procesado datos GPS reales tomados en la estación permanente USN3, de la red IGS, y los resultados obtenidos se han contrastado con los proporcionados por otros software de PPP ya conocidos (CSRS-PPP, magicGNSS, APPS, Bernese 5.0). En segundo lugar, se han procesado conjuntamente observaciones GPS y GIOVE de las estaciones de la red GESS, entre las que se incluyen observaciones GIOVE triple frecuencia. Además, se ha realizado un test con algunos de los primeros datos GPS triple frecuencia que ya transmite el satélite PRN25 y se han procesado observaciones simuladas de los futuros sistemas GPS modernizado y Galileo, proporcionadas por ESA. En la simulación de estos datos se empleó un generador de señal Spirent y un receptor triple frecuencia de la casa Septentrio.

Por otra parte, los algoritmos MAP3 proporcionan estimaciones del retraso ionosférico en las observaciones GNSS junto con la estimación de la posición del receptor y, como consecuencia, una aplicación interesante de MAP3 es su utilización en la detección de perturbaciones ionosféricas a partir de la señal GNSS y el análisis de sus efectos en el posicionamiento.

En este trabajo, los algoritmos MAP3 se han aplicado en el análisis de los efectos de las perturbaciones ionosféricas ecuatoriales en el posicionamiento puntual. En particular, se han procesado observaciones GPS doble frecuencia de la estación permanente IGS, MALI, situada en la región ecuatorial africana. Dichas observaciones corresponden a los días 108, 109 y 112 del año 2004, en los que Portillo et al. (2008) detectaron burbujas ionosféricas en esta región. También se han procesado observaciones de estos mismos días en las estaciones PRE1 y MAS1, que están situadas en latitudes medias y, por tanto, alejadas de la región ecuatorial, con el fin de contrastar los resultados obtenidos en diferentes latitudes.

La metodología seguida en este estudio consiste en estimar, en primer lugar, el Contenido Total de Electrones (TEC) mediante los algoritmos MAP3, multiplicando por el seno de la elevación del satélite se elimina la dependencia de la elevación y se obtiene el TEC vertical (vTEC). Entonces, el Rate of TEC (ROT) es calculado como la diferencia entre dos valores consecutivos de vTEC. Por otro lado, la posición de estas estaciones se estima a partir mediante la técnica del

posicionamiento puntual época por época y el error en la posición estimada se obtiene al comparar con las coordenadas precisas que proporciona el IGS para estas estaciones. Con el fin de eliminar los errores en la posición estimada debidos a variaciones en la geometría de los satélites visibles, el error en la posición es pesado mediante una función dependiente del GDOP.

En este estudio se ha mostrado que, aunque el retraso ionosférico se elimina en un primer orden mediante la combinación de observaciones doble frecuencia, la estimación de la posición en bajas latitudes presenta errores de varios metros en la altitud y muchos dm en las componentes horizontales en periodos en que se ha registrado un elevado ROT. Por el contrario, durante periodos de bajo ROT, en bajas y medias latitudes, no se han observado errores significativos en la estimación de la posición. Las influencia de la geometría de los satélites se ha descartado como posible fuente de error mediante el pesado de las estimaciones por GDOP.

Las principales conclusiones que se desprenden de este trabajo de tesis son los siguientes. Los nuevos algoritmos MAP3 constituyen una nueva y original estrategia para efectuar el PPP estático a partir de observaciones multi-sistema y multi-frecuencia del futuro escenario GNSS. En particular, MAP3 permite combinar observaciones y productos de varios sistemas de satélites en un mismo procesado. Aunque han sido diseñados para trabajar con los futuros sistemas GPS modernizado y Galileo, también se pueden aplicar a los sistemas GLONASS, COMPASS y sus sistemas de aumentación.

Además, MAP3, junto con el programa PCube, son unas de las primeras herramientas que procesan observaciones de los sistemas GPS modernizado y Galileo y que ya han proporcionado los primeros resultados en el posicionamiento con observaciones GIOVE y productos del GPC. Esta es una característica destacable de MAP3, dado que los programas actuales de PPP únicamente procesan observaciones doble frecuencia de los sistemas GPS y GLONASS.

En los test numéricos realizados en este trabajo de tesis se ha mostrado que MAP3 presenta las mismas prestaciones que los programas online CSRS-PPP y magicGNSS a partir de observaciones doble frecuencia y productos IGS, e incluso se obtienen mejores resultados con MAP3 en periodos cortos de observación. En particular, MAP3 proporciona una estimación de la posición con una exactitud de 2.5 cm aprox. tras 2 horas de observación y de 7 mm tras 24 h.

Un resultado interesante obtenido con MAP3 es que, al combinar observaciones GPS y GIOVE, la exactitud en la posición estimada mejora en aproximadamente 2 cm con respecto a la solución únicamente GPS. En vista de este resultado,

se tiene previsto realizar un análisis más exhaustivo acerca de los beneficios de la introducción de lo nuevos satélites en el posicionamiento, especialmente con la llegada de los cuatro primeros satélites Galileo en los próximos meses.

El principal problema encontrado al testear los algoritmos MAP3 es la falta de datos reales multi-frecuencia, por lo que ha sido necesario recurrir al uso de simuladores. Sin embargo, las observaciones simuladas empleadas en estos test numéricos se encuentran todavía bastante lejos de ser realistas, dado que carecen de los errores reales que están presentes en las observaciones y, por tanto, no se pueden extraer conclusiones definitivas de los resultados obtenidos a partir de estos datos. Esto pone de manifiesto la necesidad de desarrollar un simulador de señal GNSS, capaz de proporcionar observaciones realistas del futuro escenario, en el cual estamos trabajando actualmente.

Además, una aplicación importante de MAP3 es su utilización en la detección de perturbaciones ionosféricas y el análisis de sus efectos en el posicionamiento. En esta tesis se ha mostrado como la presencia de un ROT elevado, observado en latitudes ecuatoriales, refleja una degradación significativa del posicionamiento puntual con observaciones doble frecuencia. Dado que las perturbaciones en la distribución del plasma ionosférico pueden degradar el posicionamiento con errores de varios metros, los algoritmos MAP3 resultan de mucho interés para los sistemas de navegación y aumentación por satélites. En la actualidad se está llevando a cabo un estudio más general, empleando un mayor número de estaciones y periodos de observación, con la finalidad de detectar cierta periodicidad en la aparición de ROT elevado y fijar un umbral mínimo de ROT a partir del cual se van a obtener errores significativos en el posicionamiento.

Introduction

The term Global Navigation Satellite System (GNSS) comprises all the navigation systems based on the use of artificial satellites, their combination and augmentations. The first global positioning systems were conceived to precisely locate military vessels and submarines offshore during the cold war. However, all through the last 50 years, that initial technology has hugely evolved to develop into a very powerful tool, able to determine precise user position, velocity and time anywhere in the globe and at any time, providing a large variety of services to the military, scientific and civil communities.

Many fields of geosciences and engineering have incorporated the GNSS technology into their routine work in order to complement their techniques and to create many other new applications. In this respect, geodesy and surveying have been some of the most benefited disciplines, given that the position can be easily determined with high accuracy by means of GNSS techniques, avoiding the intervisibility between points and reducing considerably work time and effort. Thus, GNSS is currently used in the setting up and densification of geodetic networks (Dow et al., 2009), in the precise definition and maintenance of reference systems (`itrf.ensg.ign.fr/net_desc.php`), in the study of the Earth rotation (Charlot, 1995), nutation and precession movements (Rothacher and Beutler, 1998), Earth and ocean tides (Weber et al., 2003), crustal motion (Buble et al., 2010), etc. A few more scientific applications of GNSS are remote sensing and altimetry (Martín-Neira et al., 2001), time transfer (Miranian and Klepczynski, 1991), ionosphere tomography (Jakowski et al., 2004) and meteorology (Bevis et al., 1992; Elgered, 1998).

On the other hand, terrestrial, maritime and air navigation have been enormously improved thanks to the introduction of the GNSS systems and the authorities and administrations can apply the GNSS technology in traffic control, search and rescue services and in the control of natural hazards. The industry and the civil community can also obtain large benefits and revenues, from precise timing provided by a GNSS receiver, touristic or blind people guidance, infor-

mation about traffic, etc (ec.europa.eu/enterprise/policies/satnav/galileo/applications/index_en.htm).

In view of this trend, it is reasonable to expect that more satellite navigation based applications, in parallel with new satellite navigation systems, will be arriving in the future.

Nowadays, the major GNSS systems are the American Global Positioning System (GPS) and the Russian GLObal NAvigation Satellite System (GLONASS) although, in a near future, other projects such as the European Galileo and the Chinese COMPASS will join the current GNSS scenario. On the other hand, the increasing number of services and capabilities demanded by the society have triggered the modernization of the existing GPS and GLONASS systems and, additionally, some countries are developing regional Satellite-Based Augmentation Systems (SBASs) in order to enhance the current GPS capabilities for air navigation and high precision applications. Among the SBAS systems, the American Wide Area Augmentation System (WAAS), the European Geostationary Navigation Overlay Service (EGNOS) and the Japanese Quasi-Zenithal Satellite System (QZSS) have already shown promising results (Zaidman, 2008; Ventura-Traveset and Flament, 2006). In consequence, by the 2020s, more than 100 modernized GNSS satellites, corresponding to several systems and augmentations, will be providing different services to worldwide users.

The future systems will add new frequencies, improved codes and optimised navigation messages and thereby, the GNSS signals will present better code correlation properties, higher signal power and protection against interferences and multipath (Hofmann-Wellenhof et al., 2008). Moreover, the new signals have been designed to enhance the interoperability between different satellite systems, thus favoring their possible combinations. In addition, for the first time, the GNSS systems will broadcast, at least, three different civil frequencies, what will give place to a multi-system, multi-frequency scenario which will dramatically push the boundaries of the positioning techniques.

Nowadays, one of the most studied positioning techniques is known as Precise Point Positioning (PPP), which is aimed at estimating precise receiver position from undifferenced GNSS code and carrier phase observations and precise satellite products. Typically, the PPP technique employs the ionofree linear combination of dual-frequency observations to get rid of the ionospheric delay, what limits its application to the current dual-frequency scenario. Moreover, the existing PPP programs only support GPS and GLONASS data and, as a consecuence, further research is needed in order to adapt the current PPP programs to the fea-

tures of the arriving navigation systems and design new algorithms which exploit the multiple advantages of the future GNSS scenario.

On the grounds of this, a new and original PPP strategy, capable to deal with the future multi-system and multi-frequency GNSS observations, has been developed and is presented in this work. In the new approach, the least squares theory is applied to estimate the ionospheric delay, initial ambiguities and smoothed pseudodistances from undifferenced observations, which in turn are used to recover the receiver position and its clock offset. The first part of the new PPP algorithms was already applied in de Lacy et al. (2008a) and some results obtained with the complete approach were presented in Moreno et al. (2009).

These new algorithms have been called Multi-frequency Algorithms for PPP (MAP3) and have been integrated within a PPP software, named PCube and developed in collaboration with scientists of the European Space Agency (ESA). The formal expressions of the new algorithms and the results obtained in the numerical tests are presented in this thesis.

In addition, MAP3 has been applied in the analysis of the influence of ionospheric disturbances on the point positioning, since they may constitute a serious threat for the GNSS services in the equatorial regions. This analysis has provided very interesting results, which have been already published in Moreno et al. (2011) and are presented in this work.

Thus, this thesis has been organised in the following chapters:

Chapter 1 The main features of the current and future GNSS systems are summarised, emphasizing the GPS modernization process and the advent of the European project Galileo.

Chapter 2 The GNSS observables and the different error sources affecting the GNSS observations are presented, as well as the required models and indications that may be followed in the correction of the measured ranges.

Chapter 3 The main features of the PPP technique are detailed, along with the strategies that may be used in the processing of the observations in PPP. The physical models accounting for the site displacement effects and required to reach the few mm-level accuracy in the positioning are also presented.

Chapter 4 The formal expressions of the new MAP3 algorithms are obtained, a strategy to correct the satellite and receiver electronic delays is proposed and a brief description of the PCube software is presented.

Chapter 5 The results obtained in the numerical tests of MAP3 are shown. Different scenarios have been considered, including real dual and triple-frequency GPS and Galileo In-Orbit Validation Element (GIOVE) observations and simulated modernized GPS and Galileo data.

Chapter 6 The MAP3 algorithms are applied in the analysis of the influence of equatorial ionospheric disturbances on point positioning. The methodology followed in this study and the results obtained are presented.

Chapter 7 The most relevant conclusions drawn in this work are summarised and the possible future work lines are pointed out.

This thesis has been developed thanks to a UCM predoctoral fellowship and it is framed within the research projects *New algorithms for the future multi-frequency GNSS system* (AYA2008-02948) and *Application of the satellite radar interferometry and the global navigation satellite systems to the control of distortions in the Baetic Cordillera* (AYA2010-15501), funded by the Spanish Ministry of Science and Innovation.

Chapter 1

The Future Scenario GNSS

In recent years, many countries in the world have embarked on the development of their own satellite navigation systems, due to the large benefits that such systems can bring to the economy, the industrial and technological development and defence of a nation. The U.S. and Russia currently own the only operational global positioning systems, GPS and GLONASS, however, China's and Europe's plans for the development of their respective satellite constellations, COMPASS and Galileo, foresee the Full Operational Capability (FOC) in a near future. The Chinese COMPASS will be the global extension of the current Beidou-1, which is conformed by three geostationary satellites covering the Asian continent, and the European project Galileo is completing the In-Orbit Validation (IOV) phase through two experimental satellites. In turn, GPS and GLONASS have started their modernization processes with the objective of bringing numerous improvements to the current services and become more competitive.

Any of these satellite systems has been designed to fulfill the strong requirements imposed by the administration, the industry and the military, scientific and civil communities, being able to work independently from the rest and, at the same time, to interoperate with each other, therefore enhancing considerably the capabilities of a single satellite system. Additionally, for the first time, at least three different frequencies will be broadcast by any of the satellite systems, what will give place to a multi-frequency scenario that will largely optimise the current navigation techniques.

It is foreseen that the triple-frequency GPS system will be fully operational after the year 2018 (Kim, 2009) and the Galileo project by the year 2014 (Oehler et al., 2009). Moreover, COMPASS is expected to reach FOC before 2020 and the modernized GLONASS in 2011 (Tab. 1.1).

As of September 2011, the only global navigation systems that can be used are GPS (with 31 operational satellites, 8 IIR-M satellites and a single IIF satellite

in space, SVN62/PRN25) and GLONASS (with 21 operational satellites), both in modernization process. Galileo is currently in IOV phase through the two first satellites GIOVE-A and B and COMPASS is already formed by 12 satellites.

Moreover, the SBAS have proven to be a key element in the regional enhancement of the global positioning systems and are essential to ensure the reliability of the services required nowadays by the aviation. The American WAAS, the European EGNOS and the Indian GPS/GLONASS And Geo-stationary Augmented Navigation (GAGAN) are some of these augmentation systems. Moreover, India and Japan are building their own regional navigation systems based on their previous GPS augmentations.

In conclusion, in the near future the number of satellite systems and augmentations will increase considerably. In particular, the modernized GPS and GLONASS, Galileo and COMPASS will become the major global positioning systems, fully operational by the year 2020.

	2011	2012	2013	2014	2015	2016	2017	2018	2019	2020	2021
Mod. GPS								⊙			
GPS III											⊙
GLONASS	⊙										
Galileo				⊙							
COMPASS										⊙	

Table 1.1: *Global positioning systems FOC dates.*

1.1. GPS Modernization

GPS is a radio navigation satellite system under development by the U.S. Department of Defence, which was initially designed for military applications in the early 1970s to overcome the limitations of previous positioning systems. It was declared fully operational in the year 1995, replacing the TRANSIT system, which was based on the Doppler technology. Soon after the system became operational its full potential for military and civil applications became clear and then, in 1998, the plans for GPS modernization were announced by Vice President Gore. Such plans included the introduction of a second civil signal on L2, named L2C, and a third civil signal in L5, L5C, to be broadcast in 2005 (Shaw et al., 2000).

Currently, GPS counts on a constellation of 32 operational satellites, deployed in six orbital planes at 55° inclination, at an altitude of about 20.200 Km

and with a 12-hour period. With the full constellation, the space segment provides global coverage with 4 to 8 observable satellites at any time. The control segment consists of 12 monitor stations (Hawaii, Kwajalein, Ascension Island, Diego Garcia, Colorado Springs, Washington DC, Ecuador, Argentina, England, Bahrain, Australia), 4 ground antennas (Ascension Island, Diego Garcia, Kwajalein, Cape Canaveral) and a Master Control Station (MCS) located at Schriever (formerly Falcon) in Colorado, Fig. 1.1. The monitor stations passively track all satellites in view, collecting ranging data. These data is processed at the MCS to determine satellite orbits and to update satellite navigation message. Finally, the updated information is transmitted to each satellite via the ground antennas.

Figure 1.1: *GPS control segment.*

From the beginning, GPS has employed three different pseudorandom codes (Pseudo-Random Noise (PRN)) modulated on the two carrier frequencies L1 and L2. The C/A code or coarse acquisition code is modulated on the L1 and defines the Standard Positioning Service (SPS), conceived for non-military applications and open to civilian users. The P code or precise code is modulated on the L1 and L2 and defines Precise Positioning Service (PPS). The encrypted P-code, denoted by Y, is only available to authorised users. These PRN codes vary slightly from one satellite to the other, what enables to differentiate them by means of the Code Division Multiple Access (CDMA) technique. The navigation message is common to all satellites, with a fixed structure and length, containing information about the satellite orbit and health, corrective terms and other data. Further information about GPS L1 and L2 signals can be found in IS-GPS-200E, updated in June 2010 and available at `www.gps.gov/technical/icwg`.

Nevertheless, the continuous technological development, the increasing number of user needs and the competitiveness with the European system have led to the modernization of the GPS program. The first IIR-M Block satellite was launched in 2005, from when users dispose of a second civil signal modulated on L2, L2C, designed to meet commercial needs. Moreover, the first IIF satellite carrying a L5 payload was launched in May 2010 and the second one in July 2011 (Schaer, 2011).

A full constellation of satellites broadcasting the C/A, L2C and L5 signals for the civil users, and P(Y) and M-codes on both L1 and L2, seems unlikely before 2015. The GPS satellites launch history and the consequent steps in the GPS signal transmission are summarised in Tab. 1.2.

Block	Launch Period	Number of satellites	Still in service	Signal Acquisition
I	1978 - 1985	10	0	L1C/A, L1P, L2P
II	1989 - 1990	9	0	
IIA	1990 - 1997	19	11	
IIR	1997 - 2004	13	12	
IIR-M	2005 - 2009	8	7 + 1 unusable	L2C, M-code
IIF	2010 - 2011	2	2	L5C

Table 1.2: *GPS satellite launch history. Source:* `www.usno.navy.mil`.

Further information related to the GPS system and modernization can be widely found in the literature as, for example, in El-Rabbany (2002); Seeber (2003); Leick (2004); Misra and Enge (2006); Hofmann-Wellenhof et al. (2008), as well as in several websites (`www.gps.gov`, `gpshome.ssc.nasa.gov`). Information about GPS current state is provided by the United States Naval Observatory (USNO) in `ftp://tycho.usno.navy.mil/pub/gps`.

1.1.1. GPS Signal

The future GPS civil signals will count on the L5 frequency, the L1C, L2C and L5C codes and the GPS Civil NAVigation message (CNAV), which will present a higher power, better correlation properties and a higher precision and protection against interferences. A representation of the current and future GPS signals is shown in Fig. 1.2.

For block IIR-M, IIF, and subsequent blocks, the second civil signal modulated on L2 is introduced to meet commercial needs. It started to be broadcast in 2005 and is composed of the modulated L2 civil-moderate (L2CM) and the pilot L2 civil-long (L2CL) (IS-GPS-200E). Since the L2C civil code has better cross cor-

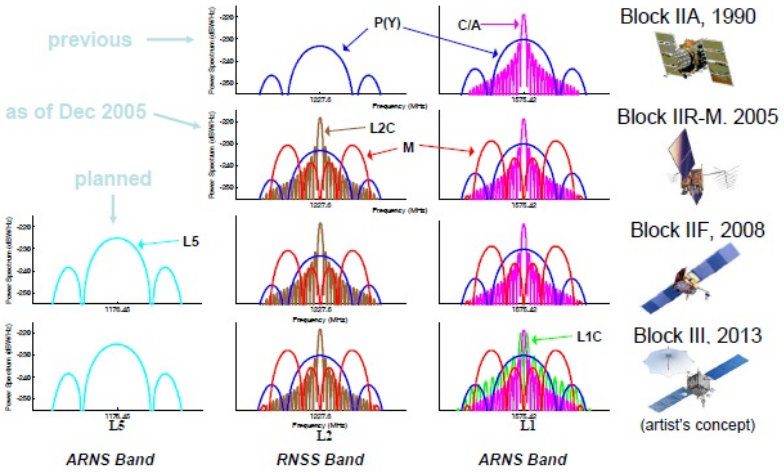

Figure 1.2: *GPS signal.*

relation properties, it will be much more effective in weak signal environments. Moreover, the new military M-code was introduced in the IIR-M block modulated on frequencies L1 and L2 to reduce the interferences in the military services.

The L5 signal has been specifically designed to improve performance in safety-of-life applications over the current L1 C/A signal. The L5 power will be increased 6 dB compared to L1 signal (-154 dBW vs. -160 dBW) and a minimum 20-MHz broadcast bandwidth and a higher chipping rate will provide greater accuracy in the presence of noise and multipath (Shaw et al., 2000). The L5 signal is equally split between an in-phase (I) data channel and a quadrature (Q) data-free channel, which will improve resistance to interference, especially from other systems in the same band (IS-GPS-705A). The data-free component of the L5C, L5Q, also provides for more robust carrier-phase tracking. Moreover, L5I and L5Q are modulated with synchronization sequences to reduce the narrowband interference effect (Shaw et al., 2000). Finally, a longer code than the C/A will reduce system self-interference caused by CDMA cross-correlation.

The first transmission of the L5 signal was planned to be carried out by a IIF block satellite during year 2005, however, due to a variety of technical problems, the launch of the first IIF-block satellite was delayed and the new civil L5 began transmitting a demonstration signal on April 2009 by using a modified navigation payload on a IIR-M satellite (SVN49/PRN01), placed in orbit on March 24, 2009 (Gao et al., 2009). The first transmission of the L5 signal by satellite SVN49 was successful, however the L1 code ranges were affected by an elevation-dependent bias of about 150 metres, what made SVN49 not suitable for positioning (Springer and Dilssner, 2009). The cause of such anomaly must be in the way that L5 pay-

load was integrated in the satellite, producing the reflexion of the L1 and L2 signals back into the broadcast antenna and causing a shift between L1 and L2 (Langley, 2009). In May 2011 the satellite SVN49 was decommissioned. The first IIF satellites carrying a L5 payload were launched in May 2010 and July 2011 and some of the first analysis of the L5C signal were presented by Thoelert et al. (2010).

On the other hand, the L1C signal will be added in the next generation of GPS III satellites, to increase the interoperability between different satellite systems. The new L1C will be formed by the L1CD data channel and the L1CP pilot channel and will not replace the L1C/A (IS-GPS-800A).

The introduction of these GPS signals will improve considerably the positioning techniques, since they present better correlation properties, higher protection against interferences and the data redundancy will increase considerably. Moreover, the combined used of the observations in L1 and L5 will be especially useful in the ionospheric delay correction, due to the wide difference between both frequencies (de Lacy et al., 2008a). In addition, the existing offset between L2 and L5 will result in a combined phase of 5.9 m wavelength, what will be particularly interesting in ambiguities resolution and cycle slips correction.

1.1.2. GPS III

In order to meet the ever growing military and civil requirements, the development of the next generation of satellites (GPS Block III) and the associated ground control network was approved by the U.S. government in 2000. The GPS III program objective is to preserve and build on the successes of the current GPS system, by creating a new architecture for the assured delivery of enhanced Position, Velocity and Timing (PVT) signals and related services to meet the needs of the next generation of GPS users (`www.navcen.uscg.gov/?pageName=gpsModernization`).

The future GPS III architecture will optimize cost (to include economic benefits), schedule, performance, risk and technology insertion, improving system security, accuracy and reliability. Moreover, GPS III will be fully interoperable with all current global radionavigation systems, will incorporate the Nuclear Detonation detection System (NDS), will provide a potential platform for supporting additional synergistic payloads and services and the integrity will be a remarkable new property. The GPS III system is expected to have about 500 times the transmitter power of the current system, multiplying its resistance to jamming. Furthermore, the fourth civil L1C signal will be introduced, which has been de-

signed with international collaboration in order to increase the interoperability between GPS and Galileo (Hofmann-Wellenhof et al., 2008).

At the 2010 Annual GPS Enterprise Review, GPS IIIA received formal approval to enter production and a total of 8 GPS IIIA satellites will be built with first delivery scheduled for mid-2014 (www.afspc.af.mil).

1.2. Galileo

Galileo will be the Europe's own global navigation satellite system, emerged as a joint initiative of the European Commission (EC) and ESA after recognising the strategic, economic, social and technological relevance of the satellite navigation. Galileo is characterised for being the first global positioning system for civilian use and for guarantying availability of the service under all but the most extreme circumstances, informing users within seconds of a failure of any satellite (Hofmann-Wellenhof et al., 2008; Prasad and Ruggieri, 2005).

The Galileo programme has been structured according to three main phases (ec.europa.eu/enterprise/policies/satnav/galileo/index_en.htm):

1. The Galileo definition phase: completed in 2003.
2. The IOV phase: consisting of qualifying the system through tests and the operation of two experimental satellites (GIOVE-A and B), a reduced constellation of four operational Galileo satellites and their related ground infrastructure.
3. The FOC phase: consisting of the deployment of the remaining ground and space infrastructure. It includes an intermediate initial operational capability phase with 18 satellites in operation (the four IOV satellites plus 14 others). The full system will consist of 30 satellites (Fig. 1.3), control centers located in Europe and a network of sensor and uplink stations installed around the globe (Fig. 1.4).

The two experimental satellites, GIOVE-A and B, were launched in December 2005 and April 2008, respectively. The launch of the first two operational Galileo satellites was carried out in October 2011 (www.esa.int/export/esaNA/galileo.html) and it will be followed by the third and fourth operational satellites in the first half of 2012 (ec.europa.eu/enterprise/policies/satnav/galileo/index_en.htm).

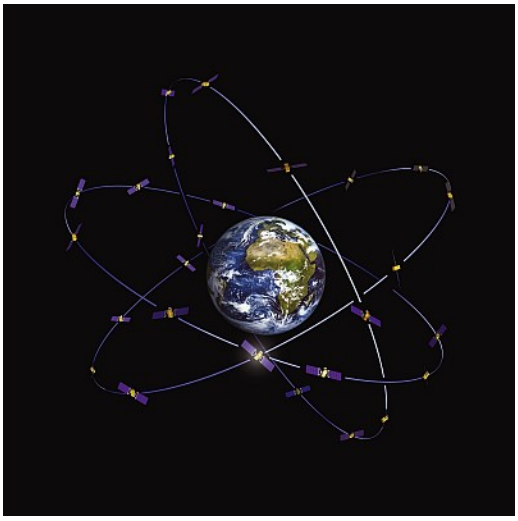

Figure 1.3: *Galileo constellation.*

The fully deployed Galileo system will consist of 30 satellites (27 operational + 3 active spares), positioned in three circular Medium Earth Orbit (MEO) planes at 23.222 Km altitude in order to avoid the gravitational resonance associated with a 12-hour orbital period (`www.esa.int/export/esaNA/galileo.html`, Fig. 1.3). The inclination of the orbital planes will be 56° with reference to the equatorial plane. From most locations, 6 to 8 satellites will always be visible, allowing positions to be determined very accurately to within a few cm. The inclination of the orbits was chosen to ensure good coverage of polar latitudes, even at latitudes up to 75° north, which are poorly served by the U.S. GPS system. The large number of satellites together with the optimisation of the constellation and the availability of the three active spare satellites will ensure that the loss of one satellite has no discernible effect on the user (`www.esa.int/export/esaNA/galileo.html`).

The ground infrastructure is composed by two Galileo Control Centers (GCCs), five stations of telemetry, tracking and control, 9 C-band up-link stations around the globe and a network of about 40 Galileo Sensor Stations (GSS) (`www.esa.int/export/esaNA/galileo.html`). The data provided by the GSS will be sent to the GCC through a redundant communications network. The GCC will use the data from the sensor stations to compute the integrity information and to synchronise the time signal of all satellites with the ground station clocks. The exchange of the data between the control centres and the satellites will be performed through the up-link stations. Currently, the GIOVE mission counts on a network of 13 Galileo Experimental Sensor Stations (GESSs), two GCC and one Galileo Processing Center (GPC).

The Galileo system will provide five different services (Benedicto and Ludwig, 2001):

- the Open Service (OS),
- the Commercial Service (CS),
- the Safety-of-Life (SoL),
- the Public Regulated Service (PRS) and

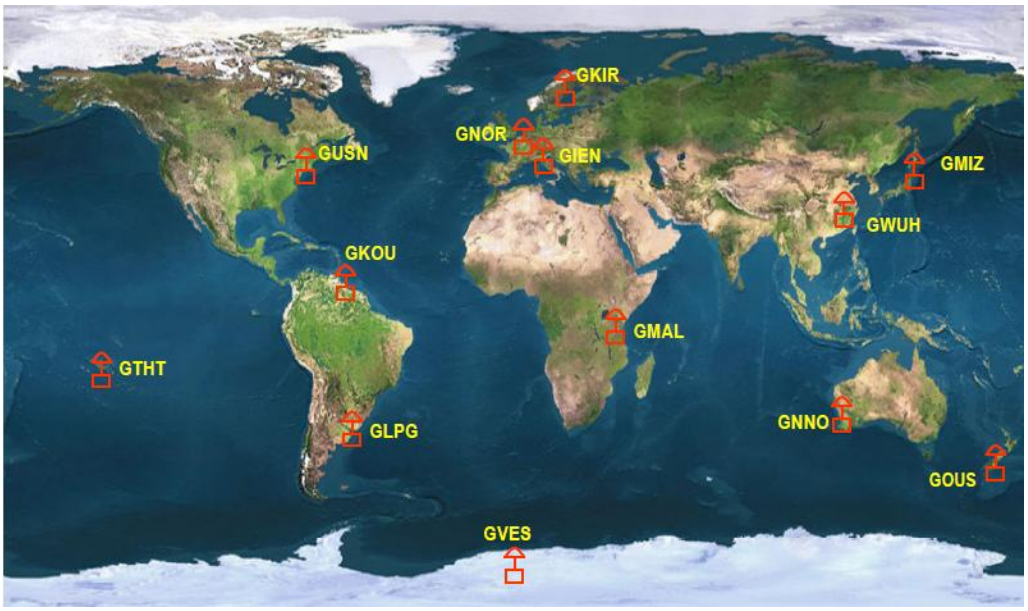

Figure 1.4: *Galileo Experimental Sensor Stations (GESS). Source:* `www.giove.esa.int`.

- the Search And Rescue (SAR) service.

The OS is intended for the mass market, accessible to all users free of charge and providing simple positioning and timing. It will be interoperable with GPS and GLONASS and a user will be able to take a position with the same receiver from any of the satellites in any combination. By offering dual frequencies as standard, however, Galileo will deliver real-time positioning accuracy down to the metre range. The SoL improves OS performance through the provision of timely warning to users when it fails, to meet certain margins of accuracy (integrity). The CS provides access to two additional signals to allow for higher data-rate throughput and enable users to improve accuracy. This pair of signals is protected through commercial encryption and, on payment, will provide added-value services such as data broadcasting, precise timing, etc. The PRS provides positioning and timing for specific users requiring high continuity of service (governmental applications). SAR broadcasts globally the alert messages received from distress-emitting beacons. It will improve the existing Search and Rescue system, including near real-time reception of messages from anywhere on Earth and will also provide a return link from SAR operator to the beacon, helping to coordinate rescue operations. As it can be seen in Tab. 1.3, all services will be global and available the 99.8 % of the time, providing metre-level accuracy when dual-frequency observations are used, and the CS and PRS will also count on local augmentations reaching centimetric accuracies.

	Open Service (OS)	Safety of Live Service (SoL)	Commercial Service (CS)		Public Regulated Service (PRS)	
Coverage	Global	Global	Global	Local	Global	Local
Accuracy	h = 4 m v = 8 m (dual freq)	4 - 6 m (dual freq)	< 1 m (dual freq)	< 10 cm (locally augmented	h = 6.5 m v = 12 m	1m (locally augmented)
Availability	99.8 %	99.8 %	99.8 %		99-99.9 %	
Integrity	No	Yes	Value-added service		Yes	

Table 1.3: *Performance of the four Galileo navigation services. Source: Butsch (2007).*

All Galileo products will rest upon a highly precise and stable Galileo Terrestrial Reference Frame (GTRF) (Gendt et al., 2011). The GTRF is designed to be compatible with the International Terrestrial Reference Frame (ITRF) and will therefore be a realisation of the International Terrestrial Reference System (ITRS). The GTRF station coordinates shall be identical to the ITRF station coordinates within a tolerance of 3 cm (at 95 % confidence level) for all station markers that appear in both frame realisations.

The realisation of the GTRF is the main function of the Galileo Geodetic Service Provider (GGSP) (`www.ggsp.eu/ggsp_home.html`) serving both, the Galileo Core System and the Galileo users. The GGSP is a project fully funded by the Sixth Framework Programme of the EC, whose goal is to build up a prototype for the development of the GTRF and the establishment of a service with products and information for the potential users. For the determination of the GSS positions a global free network adjustment is applied, providing in this way the highest internal network quality. The precise network solution is then aligned to the ITRF using the well-defined geodetic approach of minimum constraints, preserving thus full internal consistency of the GTRF. For this purpose, a significant number of ITRF stations have to be part of the GTRF network (Fig. 1.5). To achieve the highest possible quality, additional International GNSS Service (IGS) sites will be included to fill sparse regions for an optimal ambiguity fixing and for a more efficient alignment to the ITRF. Currently, the total number of stations is 131 IGS sites and 13 GESSs (Fig. 1.4).

Moreover, Galileo will use its own time system (Galileo System Time (GST)) steered to the International Atomic Time (TAI). The offset between the GST and TAI shall be kept within 50 ns (Prasad and Ruggieri, 2005). In the GIOVE mission, the reference time scale can be selected from any of the three GESS connected to an Active Hydrogen Maser (GIEN, GNOR connected to a free-running Maser or GUSN connected to a steered maser). Currently, GUSN constitutes the reference station for the GIOVE time scale. Passive Hydrogen Masers (PHMs) and Rubid-

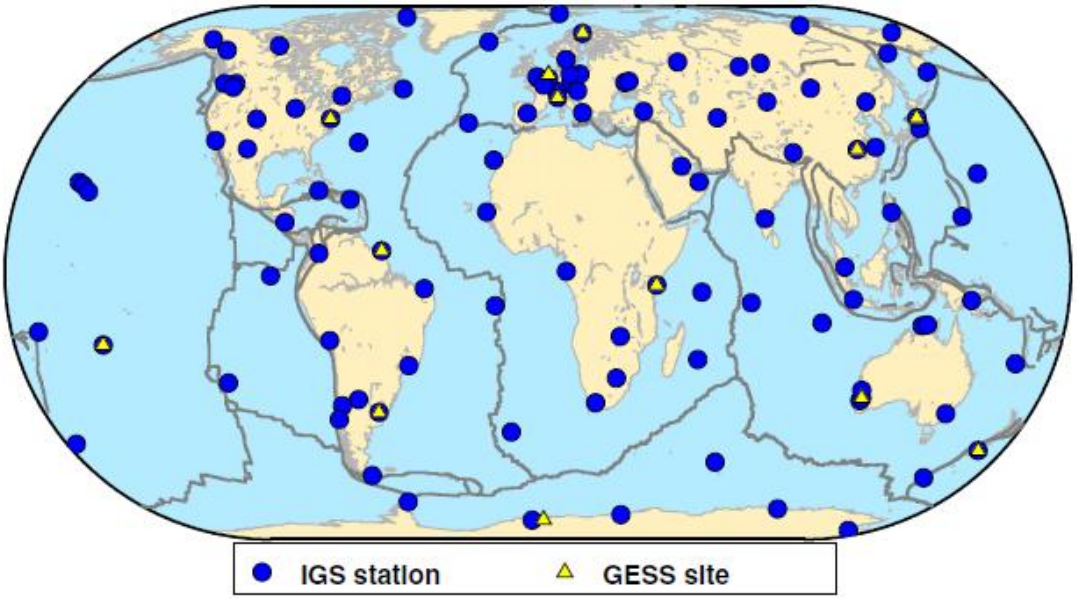

Figure 1.5: *GTRF station network (February 2009). Source: Gendt et al. (2011).*

ium Atomic Frequency Standards (RAFSs) are the two baseline clock technologies for Galileo, which are currently being validated on-board through the two experimental spacecrafts, GIOVE-A and B. They will keep time to within a few hundred-millionths of a second per day. Each of the 30 satellites in the Galileo system will have two of each type of clock on board.

Further information about the Galileo program can be found in the sites `ec.europa.eu/enterprise/policies/satnav/galileo/index_en.htm`, `www.esa.int/export/esaNA/galileo.html` and in the literature like, for example in Hofmann-Wellenhof et al. (2008); Prasad and Ruggieri (2005), among others.

1.2.1. Galileo Signal

In the Galileo signal design, the acquisition, tracking characteristics, interoperability with other GNSS systems, resistance against interference and multipath mitigation were taken into account. Galileo will broadcast three different frequencies in the L-band, denoted by E1, E5 and E6, modulated with an open-access code and commercial and governmental encrypted codes (OS SIS ICD). The C-band was under investigation before choosing the L-band for Galileo frequencies allocation, although it is still a possible option for next Galileo generations. Galileo signals will be differentiated by means of the CDMA technique. A total of ten signals, E1A, E1B, E1C, E6A, E6B, E6C, E5a-I, E5a-Q, E5b-I and E5b-

Q will be transmitted to provide different services, Tab. 1.4. All Galileo signals come in pairs, except the E1A and E6A. The channels B and I correspond to data signals and C and Q to pilot ones. The combination of the signals E5a and E5b gives place to the E5a+b or E5, whose central frequency is 1191.796 MHz.

Signal			Central Frequency	Chip rate	Ranging Code	Data Rate symbols	Data	Reference
Id	Name		[MHz]	[Mchips/s]	encryption	[bit/s]	encryption	Service
1	E5a-I	data	1176.45	10	None	50 (25)	None	OS/SoL
2	E5a-Q	pilot	1176.45	10	None	No data	No data	OS/SoL
3	E5b-I	data	1207.14	10	None	250 (125)	some	OS/SoL/CS
4	E5b-Q	pilot	1207.14	10	None	No data	No data	OS/SoL/CS
5	E6-A	data	1278.75	5	Government	tbd	Yes	PRS
6	E6-B	data	1278.75	5	Commercial	1000 (500)	Yes	CS
7	E6-C	pilot	1278.75	5	Commercial	No data	No data	CS
8	E2-L1-E1-A	data	1575.42	-	Government	tbd	Yes	PRS
9	E2-L1-E1-B	data	1575.42	2	None	250 (125)	some	OS/SoL/CS
10	E2-L1-E1-C	pilot	1575.42	2	None	No data	No data	OS/SoL/CS
11	L6 downlink	data	1544.10	-	-	-	-	SAR

Table 1.4: *Galileo signal features and distribution. Source: European Commission, 2003.*

Galileo OS is defined by the three signals E1BC, E5a and E5b, with both data and pilot channels. The ranging sequences E1B and E1C will be modulated by the Multiplexed Binary Offset Carrier (MBOC)(6,1,1/11) and the E5a and E5b components will be modulated with the Alternative Binary Offset Carrier (AltBOC)(15,10) (Hofmann-Wellenhof et al., 2008). E5a and E5b signals can be processed independently by the user receiver as though they were two separate Quadrature Phase Shift Keying (QPSK) signals (OS SIS ICD). In Figs. 1.6 and 1.7 a representation of the modulation in E1 and E5 is shown.

For interoperability reasons, the carrier frequency E5a coincides with the GPS L5, which are used as synonym, and E1 includes de GPS L1 and two adjacent bands, ending up in the terminology E2-L1-E1 or E1. Moreover, the civil code C modulated on E1 will be similar to the future GPS L1C.

As it is shown in Tab. 1.4, the Galileo CS will use the signals E1BC, E6BC and E5b; the SoL is defined by signals E1BC, E5b and E5a; the PRS will use E1A and E6A and SAR the L6 downlink.

Due to the use of advanced code modulations, the ranging signals of Galileo will provide significant improvement of the multipath performance as compared to current GPS (Simsky et al., 2008a). Multipath error envelopes for GPS L1CA and Galileo code modulations are presented in Fig. 1.8. It can be observed that the

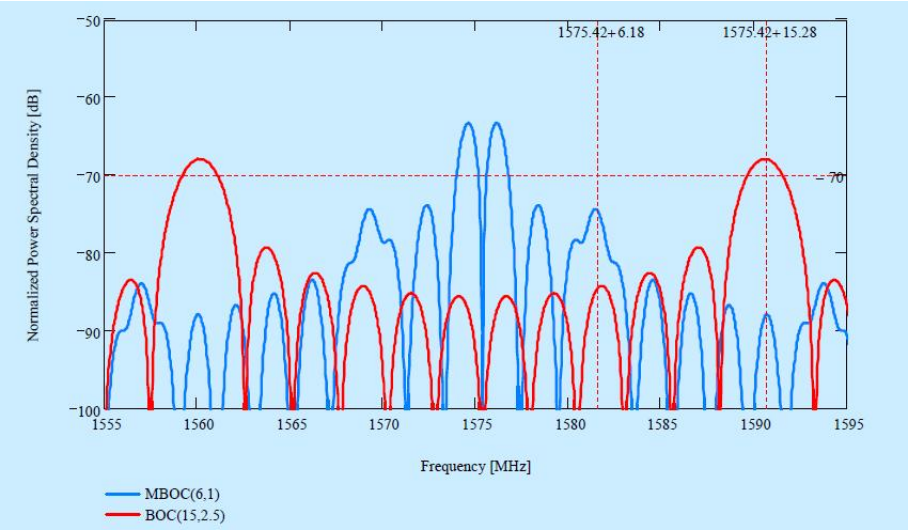

Figure 1.6: *Galileo E1 signal modulation. Source: Butsch (2007).*

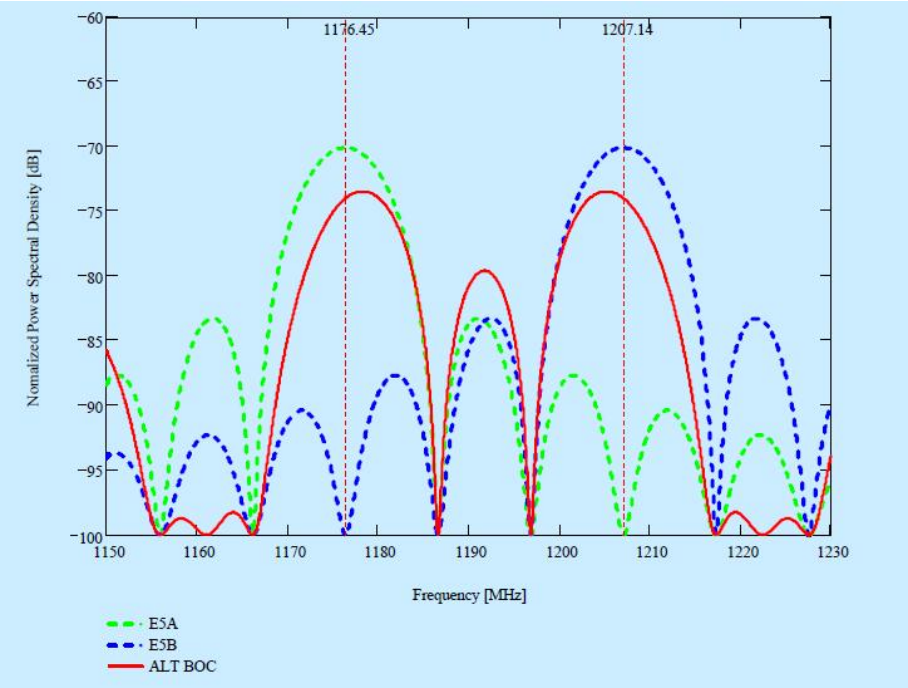

Figure 1.7: *Galileo E5 signal modulation. Source: Butsch (2007).*

error envelopes for all the Galileo modulations are well within the error envelope of the GPS L1CA code. The exceptional qualities of E5 AltBOC are due to its very high bandwidth.

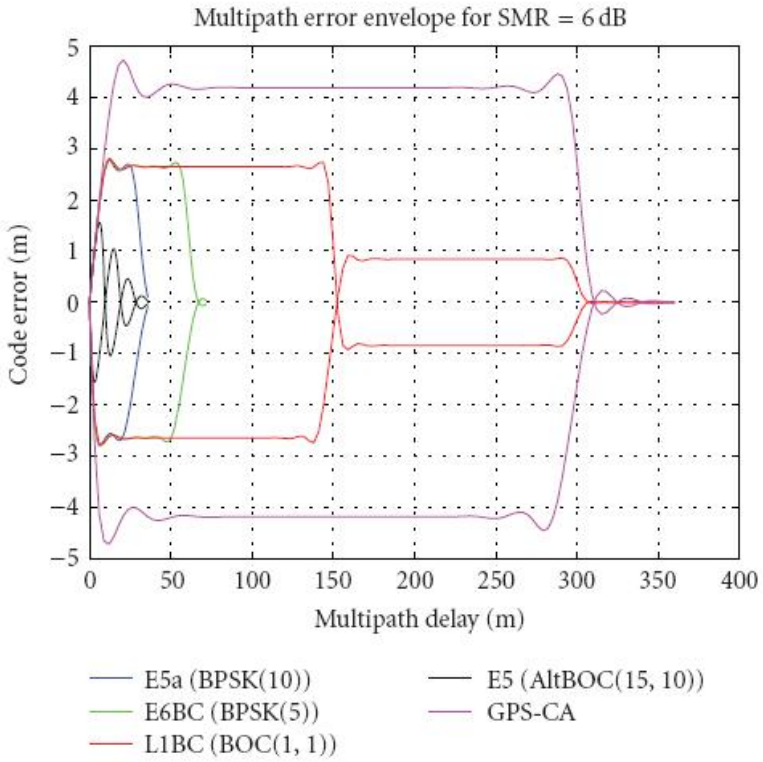

Figure 1.8: *Multipath error envelopes of GNSS code modulation at signal/-multipath ratio of 6 dB: GPS-C/A (magenta), Galileo L1BC (red), E6BC (green), E5a (blue), E5AltBOC (black). Source: Simsky et al. (2008a).*

In addition, the Galileo signal will transmit four different navigation messages, attending to their primary end users (OS SIS ICD). The Galileo Freely accessible NAVigation message (F/NAV) is destined to the OS and the Galileo Integrity NAVigation message (I/NAV) will be transmitted by the OS, CS and SoL services. The other two types are the Galileo Commercial NAVigation message (C/NAV) and the Galileo Governmental NAVigation message (G/NAV), for commercial and governmental uses respectively.

The first Galileo signals are being transmitted by the GIOVE satellites since 2006 and received by the worldwide network of GESS stations.

1.2.2. Galileo In-Orbit Validation Elements (GIOVE)

The first Galileo experimental satellite (GIOVE-A, Fig. 1.9) was launched the 28 December 2005 with the objective of characterising the critical technologies developed under ESA contracts (`www.giove.esa.int`). GIOVE-A was placed in the first orbital plane from where it is being used to test the instrumentation on board and the functioning of ground station equipment. It has also permitted the securing of the Galileo frequencies within the International Telecommunications Union (ITU). Over the course of the test period, scientific instruments on board are measuring various aspects of the space environment around the orbital plane, in particular the level of radiation, which is greater than in low Earth or geostationary orbits.

Initially the performance of the two atomic clocks on-board was characterised. Then the signal generator was turned on to provide experimental signals with various modulation characteristics. GIOVE-A started emitting the first Galileo signals on January 12, 2006. These signals were received with the Galileo Experimental Test Receiver (GETR) (Simsky et al., 2005) and closely monitored by the radio telescopes in Redu (Belgium) and Chilbolton (UK), on behalf of the Galileo project (Montenbruck et al., 2006). GETR receivers are able to track simultaneously 4 general Galileo signals, one AltBOC signal and 9 GPS satellites (L1+L2).

A second experimental satellite (GIOVE-B, Fig. 1.10) was launched in April 2008. GIOVE-B continued the testing begun by GIOVE-A but with the addition of a PHM (stability 1 ns per day, the most accurate clock ever flown in space), two compact rubidium atomic clocks (stability 10 ns per day) and a mechanical design more representative of the operational satellites `www.giove.esa.int`.

Figure 1.9: *GIOVE-A vehicle.*

Figure 1.10: *GIOVE-B vehicle.*

The future Galileo navigation signals are currently being transmitted by the GIOVE-A and GIOVE-B spacecrafts in the bands E1, E6, and E5. GIOVE satellites are designed to transmit only two of the three different frequencies at a time, changing periodically. These GIOVE signals are representative for the Galileo signals in terms of spreading code chip rates, spreading symbols, spectrum shape and data rates, with exception of the E1-A signal type of GIOVE-B and the data rates signals E1-A and E6-A of both GIOVE (`www.giove.esa.int`). However, Galileo codes are different from GIOVE ones and GIOVE satellites transmit a lower signal power than specified for the final Galileo constellation (Crisci et al., 2007). The signal E1-A is modulated with a BOCcos(15,2.5) and GIOVE-B transmits Composite Binary Offset Carrier (CBOC) on E1-BC, while GIOVE-A provides Binary Offset Carrier (BOC)(1,1) on E1-BC (Giove SIS ICD). Moreover, GIOVE-A and GIOVE-B have different transmission hardware, and hence have different power of transmitted signals. GIOVE-B have higher power than the signals of GIOVE-A by about 3 dB on L1 and by about 5 dB on E5 (Simsky et al., 2008b). In Fig. 1.11, one of the first received GIOVE-A signals is shown (Butsch, 2007). The status of the GIOVE satellites by July, 2011 is presented in Tab. 1.5 and can be consulted in `www.giove.esa.int`.

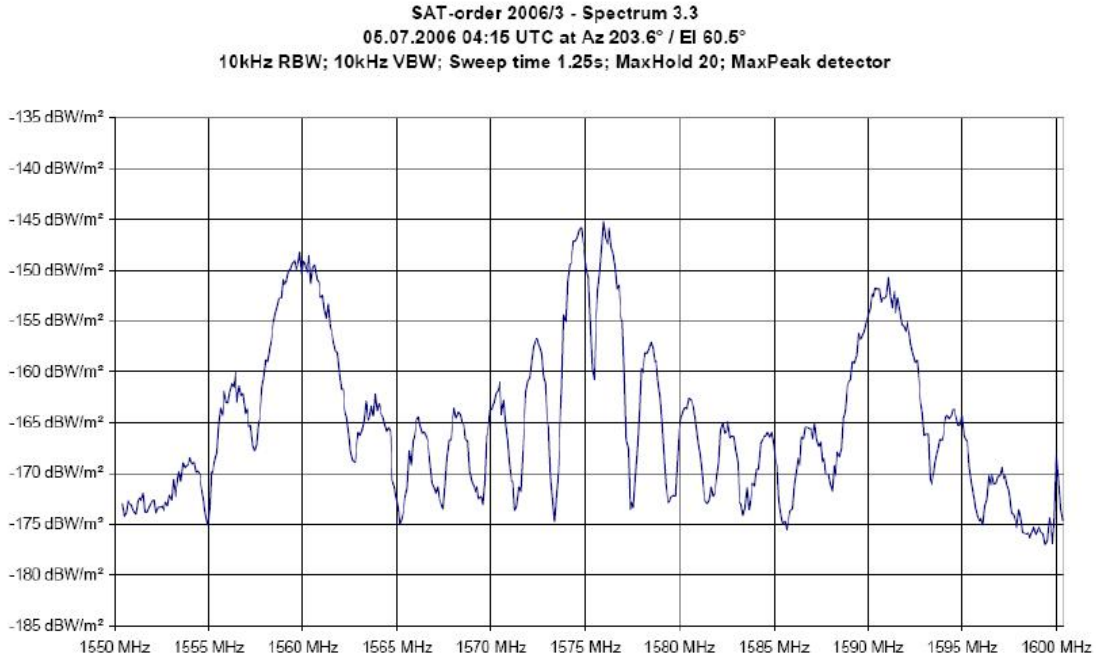

Figure 1.11: *GIOVE-A received signal. Source: Butsch (2007).*

Satellite	Frequencies
GIOVE-A	E1-BOC(1,1) and E6
GIOVE-B	E1-CBOC and E5

Table 1.5: *Status of GIOVE satellites signal broadcast by July, 2011 (last update: 2010-12-22). Source:* `www.giove.esa.int`.

The GIOVE signals are received by the worldwide distributed network of GESS stations (Fig. 1.4). The GPC, located at ESA-ESTEC in Noordwijk, conducts experimentation activities using GIOVE two satellites, collecting data through the GESS data servers and computing the near real-time orbit and clock information by means of the Experimental Orbit Synchronisation Processing Facility (E-OSPF) (Píriz, 2007).

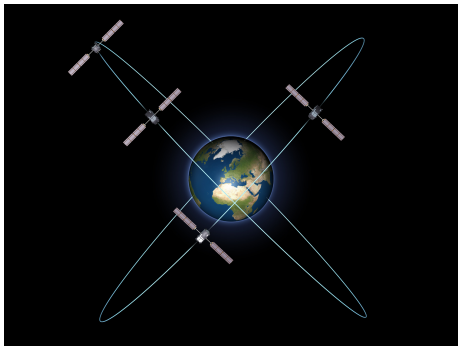

Figure 1.12: *First Galileo operational satellites. Source:* `www.giove.esa.int`.

Each GESS station integrates the GETR, the Galileo antenna, an atomic clock and a core computer to collect GIOVE/GPS data and make them available for archiving in the Galileo Data Server Facility (DSF) in the GPC (`www.giove.esa.int`). Integrated in E-OSPF is the Orbit Determination and Time Synchronisation (ODTS) facility, which determines station position, satellite orbits and clocks, InterSystem Bias (ISB) and generates the experimental navigation message for the two GIOVE satellites in a single batch Least Squares Adjustment (LSA) (Píriz, 2007). There is also another module, called IONO which is in charge of estimating Inter Frequency Bias (IFB), Broadcast Group Delay (BGD) and the parameters used in the NeQuick ionospheric model. The E-OSPF also calculates the Experimental GPS to Galileo Time Offset (EGGTO), whose aim is to facilitate the combined navigation solution with GPS and GIOVE observations (Tobías et al., 2009). The GIOVE navigation messages are calculated by the E-OSPF based on dual-frequency ionofree GIOVE and GPS code and phase combinations received

via the GESS network. The GPC is designed to routinely generate and uplink the GIOVE-A and GIOVE-B navigation messages. Currently a fresh new GIOVE-A navigation message is generated every 2 hours.

The GPS and GIOVE observations taken by the GESS stations are available at `www.giove.esa.int` to authorised users, along with GPS and GIOVE orbits and clocks obtained by GPC, GIOVE and GESS estimated IFB, signal quality statistics, GESS maintenance archives and periodic reports on GPC operations. Moreover, since April 2010, the German Aerospace Center (DLR) and the German Federal Agency for Cartography and Geodesy (BKG) provide GPS+GIOVE real-time orbit and clock products based on data from the COperative Network for Giove Observation (CONGO) (Hauschild, 2010).

Recently the first two operational satellites have joined the GIOVE space segment and the next two satellites will be launched in 2012 (Fig. 1.12, `www.esa.int/export/esaNA/galileo.html`). Once this IOV phase has been completed, additional satellites will be launched to reach the Initial Operational Capability (IOC). At this stage, the OS, SAR and PRS services will be available with initial performances. Then, along the build-up of the constellation, new services will be tested and made available to reach the FOC.

1.3. Galileo and GPS Interoperability

The agreement in 2004 between the U.S. and the European Union (EU) on GPS and Galileo recognized the benefits of interoperable systems. The parties agreed to pursue a common, open, civil signal on both Galileo and future GPS satellites, in addition to ongoing cooperation on the GPS-based EGNOS augmentation system (`europa.eu/rapid/`).

Therefore, the Galileo and modernized GPS have been designed to be able to work independently from the rest of satellite systems and, at the meantime, to be compatible and partially interoperable among them. They will coexist without degrading each other services and will partially share the allocated frequency (Prasad and Ruggieri, 2005). In Fig. 1.13 the allocation of the Galileo and GPS frequencies is shown. The pairs of signals E1C/L1C and E5a/L5 share the same central frequencies and have been designed to increase interoperability. Figures 1.14 and 1.15 show the Galileo and GPS E1C/L1C and E5a/L5 modulations.

However, the military codes will be encrypted and non-interoperable for obvious security reasons. Moreover, Galileo and GPS systems have been intentionally designed to use different reference frames, in order to avoid common

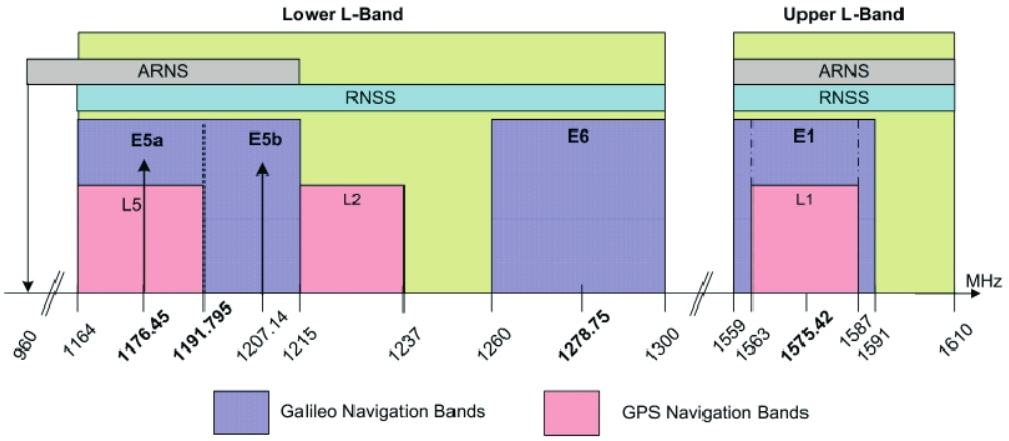

Figure 1.13: *Galileo and GPS frequency plan. Source: OS SIS ICD.*

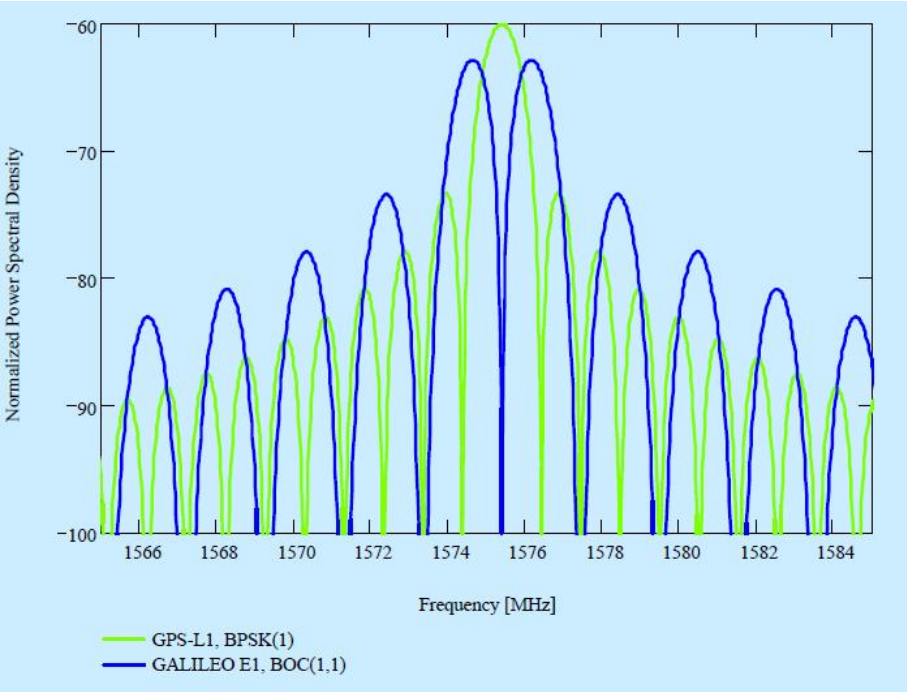

Figure 1.14: *Galileo-BOC(1,1) and GPS L1C/A modulation. Source: Butsch (2007).*

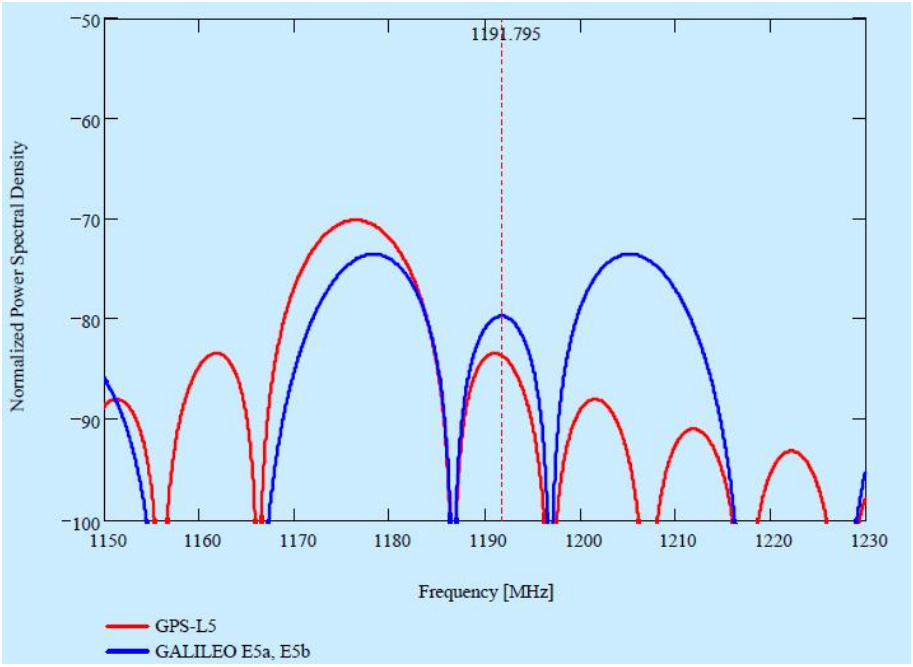

Figure 1.15: *Galileo E5A/B and GPS L5 modulation. Source: Butsch (2007).*

failures and to increase the integrity of the combined solution (Hein et al., 2002). As it was mentioned above, Galileo will use the GTRF as geodetic standard, realised and maintained by the GGSP (`www.ggsp.eu/ggsp_home.html`), while GPS uses the World Geodetic System 1984 (WGS-84). Since satellite coordinates will be given in different reference frames, they should be transformed to a common system by means of a Helmert transformation. However, the GTRF is specified to differ from the ITRF no more than 3 cm (2 sigma), the same difference as between ITRF and WGS-84. Therefore, for navigation purposes and most user requirements, it is not necessary to perform a coordinate transformation between Galileo and GPS satellite orbits. However, for high-accuracy applications, an appropiate transformation will be required (Hofmann-Wellenhof et al., 2008).

On the other hand, Galileo will use its own time system (GST), whereas GPS uses two timescales, the internal GPS Time system (GPST), for position calculation, and the Coordinated Universal Time (UTC), for timing users. The offset between the GST and TAI shall be kept within 50 ns (Prasad and Ruggieri, 2005) and the relation between GPST and UTC is $UTC = GPST$- leap seconds. Galileo will broadcast the difference between TAI and UTC. From the 1^{st} of January of 2009, TAI is ahead UTC by 34 seconds (`ftp://maia.usno.navy.mil/ser7/tai-utc.dat`). The bias with respect to the GPST is denoted as GPS to Galileo Time Offset (GGTO) and will be broadcast in the GPS and Galileo navigation messages, i.e., the predicted difference between GPST and GST system times, to

guarantee their interoperability (Píriz et al., 2008). This time offset must be either used in the observations correction to obtain a combined navigation solution, or modeled as an additional unknown to be estimated.

The experimental version of the GST in the IOV phase is called Experimental Galileo System Time (EGST) and the experimental version of the GGTO is the EGGTO. The EGST was defined as the clock of GIEN station as observed through the GPS part of the station, including the group delays up to the antenna, and it is obtained from the ionofree P1-P2 GPS pseudorange combination (Píriz et al., 2008). However, some time later, the reference station for GST was switched to the GUSN station. The EGGTO is obtained in the GPC through two different techniques: one based on ground stations clock information and another based on satellite clock information. Both GGTO estimations are fitted to a model (a straight line) and then the GGTO is predicted (Píriz et al., 2008). The predicted values can be added to the GIOVE navigation message and the precise GGTO values estimated from observations are provided by GPC, together with precise satellite orbits and clocks. However, the GGTO estimation process in the GIOVE experimentation is different to what will be implemented in the FOC (Tobías et al., 2009).

In addition, it must be taken into account that, when observations from different satellite systems are used, an electronical bias emerges, since GPS and Galileo signals are processed in different parts of the receiver. This bias is known as ISB and for GESS stations it will be obtained by GPC as the difference between the ionofree combinations of the receiver IFB for GPS and Galileo signals (Píriz et al., 2008). The ISB must be taken into account by Galileo (GIOVE)/GPS receivers. It can be either corrected or estimated within the data processing. Currently, the GPC estimates GESS ISB values as the difference between GPS P1-P2 IFB and GIOVE C1C-C7Q IFB. Given that, in positioning techniques used by ODTS it is not possible to separate the offsets observed in GIOVE satellites and the stations ISB, the ISBs are obtained relative to GIEN station. This is done by fixing the GIEN ISB to zero and, then, the GIEN ISB is obtained by estimating station IFB and fixing GPS P1-P2 IFB to the values given by Jet Propulsion Laboratory (JPL) and GIOVE C1C-C7Q IFB to the values provided by the satellite manufacturer (Píriz et al., 2008). The Fig. 1.16 shows the estimated GESS IFB and ISB obtained in the week 40, 2009.

Another error may arise from the fact that GPS and Galileo satellite Differential Code Bias (DCB) and BGD may not be calibrated in an absolute way. Satellite clock offsets are estimated from the P1-P2 ionofree observations combi-

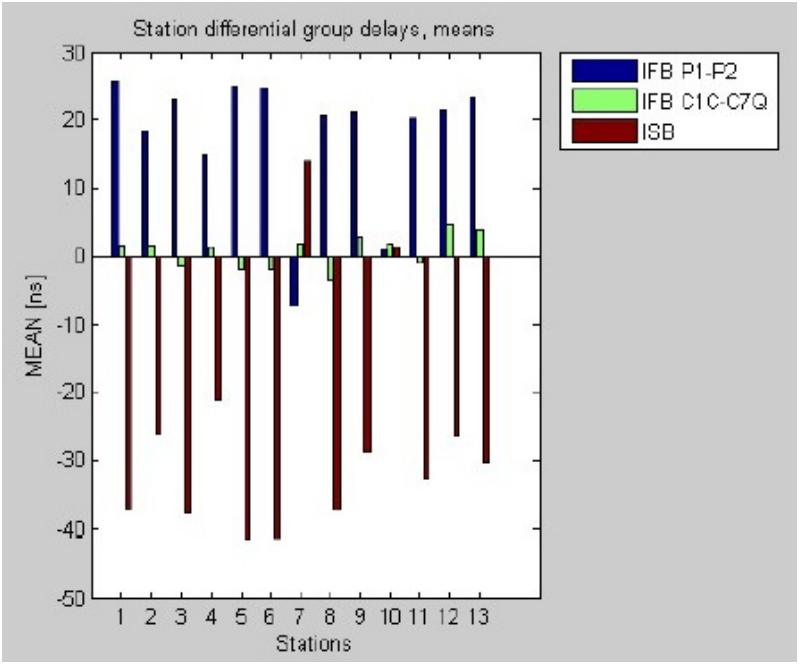

Figure 1.16: *GESS IFB and ISB obtained by GPC in the week 40, 2009. Stations: 1.GNOR, 2.GIEN, 3.GLPG, 4.GMIZ, 5.GNNO, 6.GOUS, 7.GKOU, 8.GWUH, 9.GKIR, 10.GUSN, 11.GMAL, 12.GVES, 13.GTHT. Source:* `www.giove.esa.int`.

nation, containing the ionofree combination of the satellite electronic biases for every code observation (Príiz et al., 2008). When the ionofree linear combination is used along with the satellite clock offsets, no DCB corrections are needed, however, for single-frequency users, the DCB correction must be taken into account.

Nevertheless, the combined use of both modernized satellite systems will enhance tremendously the potential of the navigation techniques, given that the number of visible satellites will double, what will be very advantageous in poor visibility conditions, and the larger redundancy of observations will optimise the estimation techniques.

1.4. GLONASS

GLONASS was originally built as a military system operated by the Russian Ministry of Defense, however, the Presidential Decree of 1999 declared GLONASS to be available for civil use (Hofmann-Wellenhof et al., 2008). Currently, the purpose of GLONASS is to provide an unlimited number of air, marine and any other type of users with all-weather three dimensional positioning, velocity measuring and timing anywhere in the world or near-Earth space (`www.glonass-ianc.rsa.ru`). The GLONASS constellation was fully de-

ployed by 1995 but the russian economical problems following 1996 led to the decline of the navigation system. In order to improve the situation and encourage civil applications, Russia adopted a Federal Program in 2001, aimed at completion of the GLONASS satellite constellation, modernization of its Ground Segment, improved accuracy and facilitation of civil applications. The program was amended in July 2006 with extra funding and increased requirements.

The first modernized satellite (GLONASS-M) became operational in 2003. GLONASS-M satellites include a second civil signal, carry improved onboard clocks (higher performance, longer lifetime) and count on improved onboard platform (better solar panel pointing, etc) in addition to those of standard GLONASS satellites. The next generation of GLONASS is called GLONASS-K. These satellites will have a lifetime of 10 years, will introduce the new civil signals and will show an improved performance (Revnivykh, 2007). After the failed launch of three GLONASS satellites in December 2010, the first GLONASS-K has been put into orbit in February, 2011 (`new.glonass-iac.ru`) and other three GLONASS-M satellites were launched on board a Proton rocket in November 2011, to complete the orbiting grouping.

As of November 2011, the GLONASS constellation includes 23 usable spacecrafts (`new.glonass-iac.ru`). The completely deployed GLONASS constellation will be composed of 24 satellites in three orbital planes, whose ascending nodes are 120° apart (Fig. 1.17). GLONASS satellites operate in circular 19.100 Km orbits at an inclination 64.8° and each satellite completes the orbit in approximately 11 hours 15 minutes. The spacing of the satellites allows providing continuous and global coverage of the terrestrial surface and the near-Earth space (GLONASS SIS ICD).

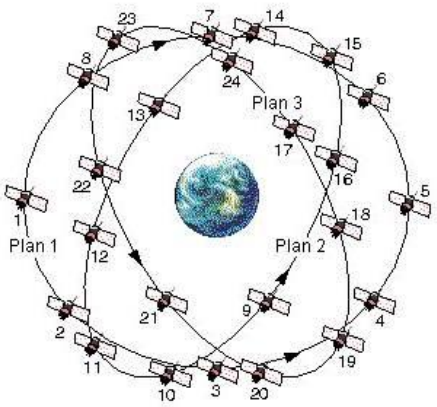

Figure 1.17: *GLONASS space segment.*

The GLONASS control segment includes the System Control Center and the network of the Command and Tracking Stations, that are located throughout the territory of Russia (Fig. 1.18). The control segment provides monitoring of GLONASS constellation status, correction to the orbital parameters and navigation data uploading.

GLONASS provides high-accuracy signal for military use and a standard-accuracy signal for civil use free of charge. Since its FOC in 1996, GLONASS satellites emit the standard-accuracy signal modulated on the carrier frequency G1 and the high-accuracy signal on G1 and G2 (Tab. 1.6). However, with the first GLONASS-M satellite, the standard-accuracy signal is also modulated on G2. The modernized GLONASS-K satellites will provide a third frequency, denoted as G3. GLONASS implements the Frequency Division Multiple Access (FDMA) to differentiate signals between satellites. With this technique, the carrier frequencies are derived from the fundamental frequencies in the form

$$\begin{aligned} f_{1k} &= 1602.000 + 0.5625k \\ f_{2k} &= 1246.000 + 0.4375k \\ f_{3k} &= 1204.704 + 0.4230k \end{aligned} \tag{1.1}$$

where k differentiates the frequency channels (Hofmann-Wellenhof et al., 2008). A different triple of frequencies is assigned to every GLONASS satellite, allowing them to be identified by the receiver. After 2005, the satellites have been transmitting on frequency channels $k = -7, -6, ..., +5, +6$, where channel numbers $+5$ and $+6$ are reserved for technical purposes. The limitation of 12 channels has been possible by assigning satellites in antipodal position within the same orbital plane the same channel number. However, the new block GLONASS-K will introduce the new civil signals G3PT, G1CR and G5R, modulated with the CDMA technique in order to be interoperable with GPS and Galileo.

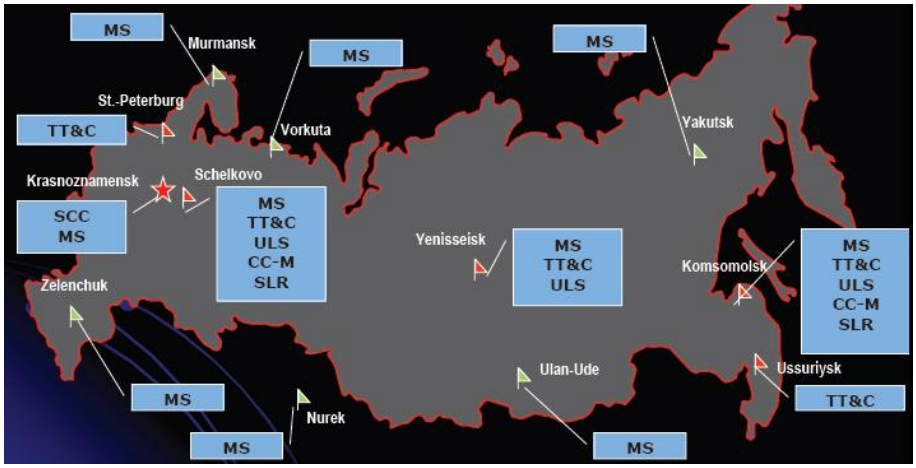

Figure 1.18: *GLONASS ground segment. Source: Revnivykh (2007).*

Signal	Carrier Frequency (MHz)
G1	1602.000
G2	1246.000
G3	1204.704

Table 1.6: *GLONASS fundamental frequencies.*

GLONASS time is generated on a base of GLONASS Central Synchronizer time and the broadcast ephemeris describe a position of the transmitting antenna phase center of a given satellite in the Parametri Zemli 1990 (PZ-90) Earth-Centered Earth-Fixed (ECEF) reference frame. Within the modernization plans, the switch to a geodetic reference frame PZ-90, better aligned to ITRF was carried out in September 2007 and the GLONASS Time System (GLoTS) was better adjusted to the UTC in order to increase the interoperability between GLONASS, GPS and Galileo.

Updated information about the status of the GLONASS system can be found in `www.glonass-ianc.rsa.ru`, `www.m2m-t.ru` and `www.bnavigator.ru`.

1.5. BEIDOU-2 / COMPASS

Beidou-2/COMPASS is a navigation satellite system developed by the Chinese Academy of Space Technology whose primary mission is the military one (Chong (2009), `www.beidou.gov.cn`). It has been conceived as a global expansion of the former Beidou-1, which uses satellites in geostationary orbit. The first three Beidou-1 experimental satellites, Beidou 1A, 1B and 2A, were launched between 2000 and 2003 (van Haaften, 2007). Then, Beidou-1 demonstration system was completed in 2003 and is available for civil users since 2004 (Chong, 2009).

Beidou-2 or COMPASS is under construction since 2005 and the complete system will contain 35 satellites, including 5 GEOstationary (GEO) satellites, 3 Inclined GeoSynchronous Orbit (IGSO) satellites and 27 MEO satellites (Fig. 1.19). The first COMPASS satellite was launched in April, 2007, followed by a second launch in April 2009. During 2010, 5 COMPASS satellites were put into orbit (Barbosa, 2010a,b) and the last launches took place in April and July, 2011 (`www.insidegnss.com`). As of September 2011, COMPASS is formed by 4 GEO satellites, 4 IGSO and 1 MEO (Tab. 1.7), covering the region bounded by longitude 70° to 140° and latitude 5° to 55°. It will ultimately offer complete coverage of the globe before 2020 (Chong, 2009).

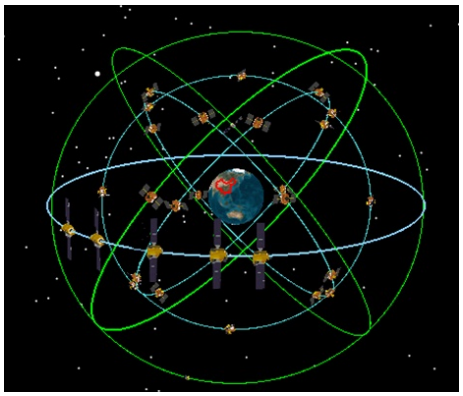

Figure 1.19: *Beidou-2/COMPASS space segment. Source: Chong (2009).*

Launch date	Satellite	Orbit
14-04-2007	COMPASS-M1	MEO (testing)
14-04-2009	COMPASS-G2	GEO 38° E
17-01-2010	COMPASS-G1	GEO 144.5° E
02-06-2010	COMPASS-G3	GEO 84° E
01-08-2010	COMPASS-IGS1	IGSO 118° E
01-11-2010	COMPASS-G4	GEO 160° E
18-12-2010	COMPASS-IGS2	IGSO
09-04-2011	COMPASS-IGS3	IGSO
26-07-2011	COMPASS-IGS4	IGSO

Table 1.7: *Beidou-2/COMPASS satellites (September 2011). Source: Barbosa (2010a).*

The COMPASS ground segment consists of one Master Control Station, two upload stations and 30 monitor stations. According to Chong (2009), four frequencies are currently transmitted by COMPASS and other three will be used in the future, Tab. 1.8. Some of the signals overlay the Galileo PRS band and the GPS M-code. These signals are modulated in phase and in quadrature using the QPSK technique although, in the future, the modulation scheme will be changed to the BOC, AltBOC and MBOC, giving place to new signals (Chong, 2009). The signals B1-C, B2a and B2b have been designed to enhance the interoperability between COMPASS and Galileo.

COMPASS/BeiDou uses China Geodetic System 2000 (CGS2000), coincident with ITRF within a few cm, and the COMPASS/BeiDou Time (BDT) is synchronized with UTC within 100 ns (Chong, 2009). The offset between BDT and GPST/GST will be measured and broadcast.

COMPASS will offer two levels of service: a free service for those in China and a licensed service for the military. The free service will have a 10 m location-

	Current	Future
B1	1561.098	1575.42
B1-2	1589.742	
B2	1207.14	1191.75
B3	1268.52	1268.52

Table 1.8: *Current and future COMPASS frequencies (MHz). Source: Chong (2009).*

tracking accuracy, will synchronize clocks with an accuracy of 50 ns and will measure velocity within 0.2 m/s. The licensed service, more accurate than the free service, can be used for communication and will supply information about system status to the users.

The official web site of the Beidou-2/COMPASS programme is `www.beidou.gov.cn` (in chinese).

1.6. Satellite-Based Augmentation Systems (SBAS)

The increasing requirements imposed by the administration and the users to the navigation systems has led to the development of additional satellite-based infrastructures, to support and augmentate the current global systems and ensure the availability and reliability of the GNSS services, specially for civil aviation (Zaidman, 2008). The SBAS have been designed for that purposes, enhancing the GNSS systems performance and providing additional information necessary in space-based positioning, navigation and timing.

The SBAS systems count on, at least, two geostationary satellites and a network of terrestrial monitoring stations (Hofmann-Wellenhof et al., 2008). Such stations are continuously tracking the GNSS signal and sending data to the master stations, where the correction parameters for the satellite orbits, clocks and the ionospheric influence are generated. The corrections, as well as the integrity information, are transmitted to the geostationary satellites, which modulate such information on a GNSS-like signal and broadcast it. This GNSS-like signal can also be used by the users as an additional observation for positioning.

Some of the current SBAS systems are the american WAAS, the European EGNOS, the japanese Multifunctional transport Satellite Augmentation System (MSAS) or the indian GAGAN.

1.6.1. WAAS

WAAS is operated by the U.S. Federal Aviation Administration (FAA) (`www.faa.gov`). It was created to enhance GPS performance across North America and provide civil aviation the additional accuracy, availability, continuity and integrity necessary to rely on the GPS for all phases of flight (Zaidman (2008), `www.gps.gov/systems/augmentations`). Moreover, its capabilities are broadly used in many other applications because their GPS-like signals can be processed by simple receivers without additional equipment.

WAAS is based on two geostationary satellites and a network of 38 reference stations, strategically positioned across the U.S., including Alaska, Hawaii, Puerto Rico, Canada and Mexico (Fig. 1.20). From November 2010, the third WAAS geosynchronous satellite was declared operational (`www.nstb.tc.faa.gov`). The GPS satellite data is collected and sent to master stations, where the corrections are calculated. Then, the correction data is broadcast to users through the two geostationary satellite communication links (`www.faa.gov`).

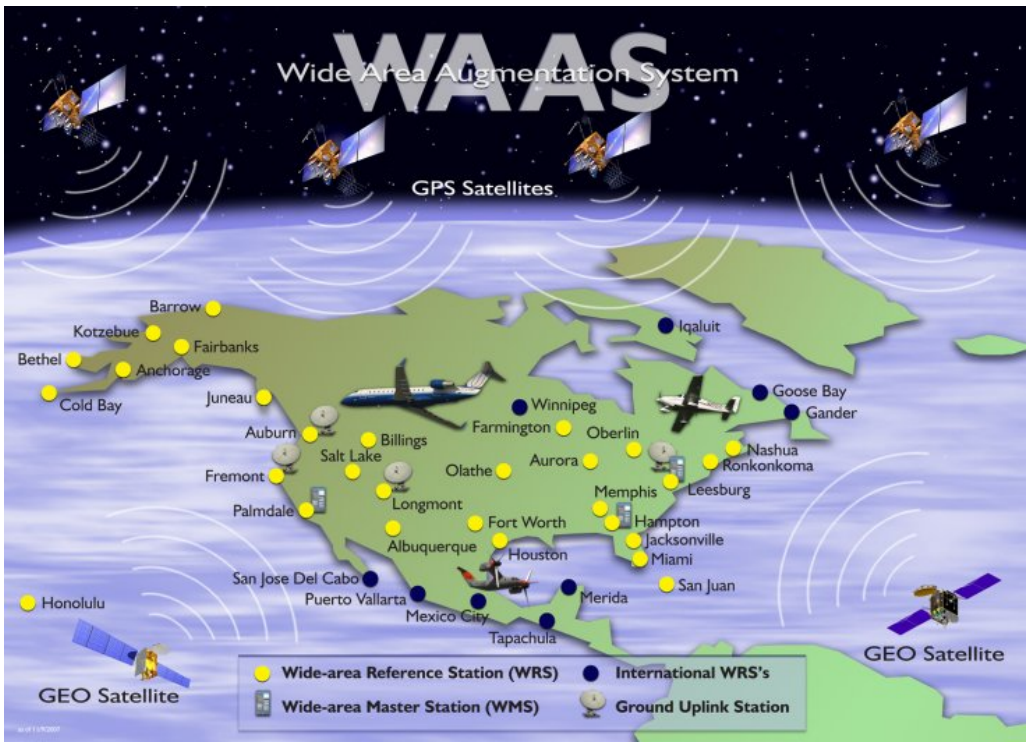

Figure 1.20: *WAAS space and ground segments. Source:* `www.nstb.tc.faa.gov`.

The FAA approved WAAS for aviation use in all weather conditions throughout the continental U.S. and most of Alaska in July 2003. Until then, no other navigation system could provide so highly precise horizontal and vertical navigation. The plans for WAAS development continue to improve the coverage and reliability of the service. WAAS coverage can be consulted in real-time in the site `www.nstb.tc.faa.gov/RT_VerticalProtectionLevel.htm`, where figures are updated every 3 minutes.

1.6.2. EGNOS

EGNOS is the Europe's first venture into satellite navigation, built to improve the public open service offered by Galileo and GPS over the European continent (`www.egnos-portal.gsa.europa.eu`). The development of EGNOS arose from a tripartite agreement between ESA, EC and Eurocontrol, the European Organisation for the Safety of Air Navigation.

EGNOS' infrastructure comprises a ground network of 34 Ranging and Integrity Monitoring Stations (RIMS), 6 Navigation Land Earth Stations (NLES), 4 mission control centres and signal transponders on 3 geostationary satellites (Artemis, Inmarsat AOR-E and Inmarsat IOR-W, Fig. 1.21). EGNOS permanent stations in Europe are presented in Fig. 1.22. The signal coverage area includes most European countries.

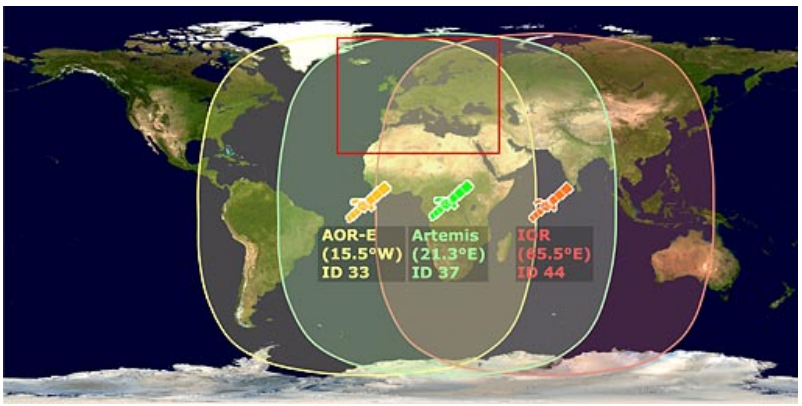

Figure 1.21: *EGNOS geostationary satellites.*

EGNOS has an enormous potential in several applications such as air and maritime navigation, commerce, traffic control, precise timing, etc. In a near future, EGNOS will offer three different services (`www.egnos-portal.gsa.europa.eu`):

- an OS: provided free of charge without any guarantee or resulting liability,
- a SoL service: including a valuable integrity message to warn the user of any malfunction of the GPS signal within 6 seconds, and
- a CS: the terrestrial commercial data service, called the EGNOS Data Access Service (EDAS), disseminates EGNOS data in real time generated by the EGNOS infrastructure.

Figure 1.22: *EGNOS stations in Europe. Source:* `www.egnos-pro.esa.int`.

The first experimental signals of EGNOS were transmitted starting in 2000, as part of the EGNOS system test bed. EGNOS IOC was reached in 2005 and, the 1^{st} of October of 2009, the EC declared operational the EGNOS OS (`www.gsa.europa.eu/go/home/egnos/news`). Since end of November 2010, the EGNOS programme entered its last preparatory phase before the SoL declaration and, on 2 March 2011, the EGNOS SoL signal was formally declared available to aviation (`www.esa.int/esaNA/SEM98MUTLKG_egnos_0.html`).

The EGNOS signal is available more than 99% of the time and its continuous monitoring improves the accuracy of GPS to within 1 to 2 metres (Ventura-Traveset and Flament, 2006). EGNOS currently provides correction and integrity information about the GPS system, making it suitable for safety-critical applications, such as flying aircraft or navigating ships through narrow channels, improving the existing services and developing a wide range of new applications.

Information on the availability of the geostationary satellites is supplied on the ESSP User Support Website, `egnos-user-support.essp-sas.eu/egnos_ops/index.php`. Moreover, real time EGNOS performance in-

formation can be accessed through www.egnos-pro.esa.int/IMAGEtech/imagetech_realtime.html.

1.6.3. Other SBAS

The Japanese augmentation system (MSAS, www.jma.go.jp/jma) is a payload of the Multifunctional Transport Satellites (MTSAT). The first satellite in the MSAS space segment (MTSAT-1R) went into orbit in 2005 and the second (MTSAT-2) in 2006 (www.insidegnss.com). MSAS operates in a similar fashion as WAAS and provides a service comparable to EGNOS. Besides the L-band broadcasts, MTSAT provides voice and data communications over Ku- and Ka-band frequencies. MTSAT-2 will also serve as a weather observatory for Japanese forecasters.

On the other hand, GAGAN is the SBAS system developed by the Indian Space Research Organization (ISRO) (isro.org) and the Airports Authority of India. The space segment of GAGAN is a dual frequency (L1 & L5) GPS compatible payload on INMARSAT-4F1 (Jain, 2008). The ground segment consists of 8 INdian REference Stations (INRES), 1 INdian Master Control Centre (INMCC) and 1 INdian Land Uplink Station (INLUS).

Other countries are also interested in providing SBAS services over their regions, although their plans are less advanced. The Canadian Wide Area Augmentation System (CWAAS) is based on an extension of the U.S. WAAS, the Republic of China is deploying its Satellite Navigation Augmentation System (SNAS) and the Russian Federal Space Agency has launched a project for the development of the System for Differential Correction and Monitoring (SDCM) (www.sdcm.ru), expected to be operational by 2011. Some of the current and future SBAS systems are schematically represented in Fig. 1.23.

1.7. Ground-Based Augmentation Systems (GBAS)

The Ground-Based Augmentation Systems (GBAS) combine ground stations and pseudolites in order to augment GNSS satellite performance for aiding aircraft landing systems (Murphy, 1998).

The ground stations receive the GNSS signal and compute the error associated to the pseudoranges as the deviation between the measures and the known distances. Then, a datalink signal containing the error information is transmitted to the aircrafts, for them to correct its own pseudoranges to every satellite. On the other hand, the pseudolite transmit GNSS-like signals in such a way that

Figure 1.23: *Current and future SBAS systems. Source:* `www.egnos-portal.gsa.europa.eu`.

an aircraft can combine the satellite range measurements with range measurements from pseudolite signals (Hofmann-Wellenhof et al., 2008). Furthermore, the pseudolite signals are not affected by ionospheric errors and the tropospheric influences are reduced. In this way, the accuracy is increased by the additional signal and, in particular, by the differential corrections.

GBAS yield the extremely high accuracy, availability and integrity necessary for the established precision approaches and provide the ability for flexible, curved approach paths.

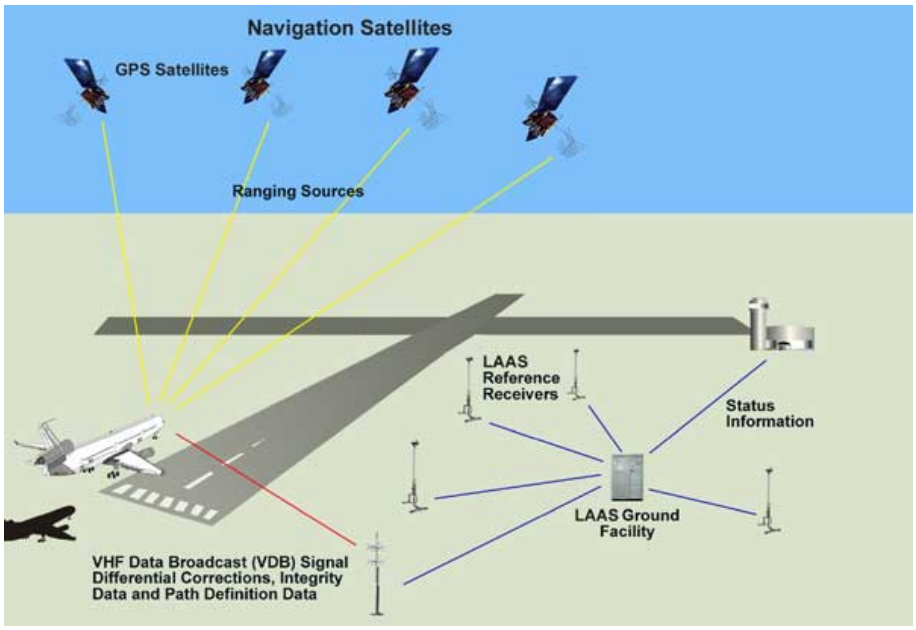

Figure 1.24: *U.S. Local-Area Augmentation System scheme. Source:* `www.faa.gov`.

The Local-Area Augmentation System (LAAS) (Fig. 1.24) is the U.S. GBAS for GPS, which focuses its service on the airport area (approx. a 45 Km radius), for precision approach, departure and terminal area operations (`www.faa.gov`). A reference network on ground of four or more redundant receivers computes differential corrections and broadcast them via a Very High Frequency (VHF) radio datalink from a ground-based transmitter. LAAS has already demonstrated accuracy below one metre in both the horizontal and vertical axis.

Chapter 2

GNSS Observables and Error Sources

A GNSS receiver is in charged of measuring the time elapsed between the signal transmission and reception epochs. For that purpose, the received signal is compared with a signal internally generated by the receiver. Thus, the main GNSS observables are the time delay of the received code with respect to an internal copy and the phase difference between the received signal and the locally generated frequency. Such measurements are converted into the satellite-receiver distance, or range, by multiplying by the speed of light and by the corresponding wavelength. Then, the receiver position and time can be determined from the measured ranges through a simple geometrical relation.

However, from its transmission to its reception, the GNSS signal is affected by several physical and geometrical effects, which introduce errors in the measured distances and must be carefully tackled. The GNSS observables and the different error sources affecting the observations are detailed in this chapter. Further information can be found in El-Rabbany (2002); Seeber (2003); Leick (2004); Hofmann-Wellenhof et al. (2008), among others.

2.1. The measure of ranges from the GNSS signal

The signal travel time is determined within the receiver by means of the alignment of the received modulating code with an internally-generated copy. Such alignment is carried out through the analysis of the maximum correlation peak.

Both, the transmitted and the internal codes are generated by satellite and receiver clocks, respectively, and therefore, the range measurements are affected by their instabilities in time. As a result, the signal travel time (Δt) is determined as

$$t_r(rec) - t^s(sat) = (t_r + dt_r) - (t^s + dt^s) = \Delta t + (dt_r - dt^s) \tag{2.1}$$

where $t_r(rec)$ is the epoch of the signal reception in the receiver time system, $t^s(sat)$ is the epoch of signal transmission in the satellite time system and dt_r and dt^s are the receiver and satellite clock offsets with respect to a common time system. When multiplying by the speed of light the distance (or range) is obtained,

$$P_r^s = c \cdot (t_r(rec) - t^s(sat)) = c\Delta t + c\,(dt_r - dt^s)\,. \tag{2.2}$$

In order to determine the true range, the satellite and receiver clock offsets must be known. The satellite oscillators are very stable in time and their corrections (predicted) are transmitted in the navigation message with a precision of 5 to 10 ns. Moreover, the precise (estimated) corrections are provided by different GNSS Analysis Centers (ACs) with a precision of about 0.2 ns. In contrast, the receiver clock in very instable and its offset has to be determined at every epoch.

Traditionally, the precision in the measure of the code delay has been the 1% of the chip length and, therefore, it depends on the code used (Hofmann-Wellenhof et al., 2008). In this way, the codes with shorter chip length will be the most precise. For instance, a GPS C/A code with a chip length of 300 metres will provide a precision of 3 m, while a P code with a length of 30 metres will result in a precision of about 30 cm.

On the other hand, in the precise positioning the phase differences between the received carrier wave and an internally-generated frequency are also used. In the same way as with the code measurements, the satellite and receiver oscillators are involved in the frequencies generation and thus, the offsets introduced by them have to be taken into account. Therefore, the phase difference is obtained as

$$\phi_r - \phi^s = f \cdot (\Delta t + (dt_r - dt^s)) \tag{2.3}$$

where ϕ_r and ϕ^s are the receiver and satellite signal phases with respect to a common time system and f is the carrier frequency in Hz. However, since

the phase differences take values from -1 to 1 cycles, an ambiguity of an integer number of cycles emerges, N. Thus,

$$\phi_r^s = \phi_r - \phi^s + N = f \cdot (\Delta t + (dt_r - dt^s)) + N. \tag{2.4}$$

This ambiguity is unknown and remains constant during a continuous observation period. When multiplying the phase difference by the corresponding wavelength, Λ, the satellite-receiver distance is obtained,

$$L_r^s = c\Delta t + c\,(dt_r - dt^s) + \Lambda N. \tag{2.5}$$

Since it is possible to measure the phase of an electromagnetic wave with a precision of 0.01 cycles, the precision of range measurements from carrier frequencies is of the order of millimetres (Hofmann-Wellenhof et al., 2008). However, the determination of the initial phase ambiguity is required, what can take several minutes of continuous observation and, in case of signal loss of lock or reinitialization of the phase counter, a new ambiguity has to be determined.

2.2. Relativistic Effects

In order to determine the true satellite-receiver distance from the GNSS observations some relativistic effects must be taken into account. In first place, since different time systems are involved in the ranges measurement, a rotating system over the Earth surface and an accelerated system fixed to every satellite, the special relativity theory must be applied. Moreover, the Earth's gravity field causes relativistic perturbations in the satellite orbits and clocks and the curvature of the space-time, which must be corrected according to the general relativity theory. An overview of all these effects can be found in Zhu and Groten (1988).

2.2.1. Relativistic effects on the satellite clocks

According to the general and special relativity theories, clocks moving with high velocity run slower than clocks with smaller relative velocity and clocks at high altitudes above the Earth run faster than clocks on its surface. The corresponding effects on GNSS clocks are small and can be linearly superposed.

In order to compensate these effects, a correction is applied to the original frequency generated in the satellites ($f_0 = 10.23$ MHz). Such correction has been derived for circular orbits, being $df \approx -4.5674 \cdot 10^{-3}$ Hz for GPS and $df \approx -5 \cdot 10^{-3}$ Hz for Galileo (Hofmann-Wellenhof et al., 2008).

However, the slight eccentricity of each orbit causes a periodic error in the satellite clock, which varies with the satellite position (Ashby, 2003) and, therefore, the GNSS observations must be corrected according to the expression

$$\delta^{rel} = -\frac{2}{c^2}\boldsymbol{\rho^s} \cdot \boldsymbol{\dot{\rho}^s} \tag{2.6}$$

where $\boldsymbol{\rho^s}$ and $\boldsymbol{\dot{\rho}^s}$ are the instantaneous satellite position and velocity vectors, respectively.

This relativistic effect is included in the clock polynomial correction broadcast via the navigation message and thus, (2.6) must not be applied when the satellite clock offsets are computed from the navigation message.

2.2.2. Relativistic effects on the signal propagation

During the GNSS signal propagation, the satellite and the receiver position varies due to the movement of the satellite in its orbit and to the Earth rotation. Therefore, the distance traveled by the signal between the satellite and the receiver does not correspond to the distance at the transmission epoch. This effect is known as Sagnac effect and, according to Su (2001), can be modeled as

$$\delta^{rel} = \frac{1}{c}\ (\boldsymbol{\rho_r} - \boldsymbol{\rho^s}) \cdot (\boldsymbol{\omega_e} \times \boldsymbol{\rho_r}) \tag{2.7}$$

where $\boldsymbol{\rho_r}$ is the instantaneous receiver position vector and $\boldsymbol{\omega_e}$ is the Earth rotation vector.

On the other hand, the gravitational field of the Earth gives rise to a space-time curvature that is reflected in longer distance measurements than those expected in Euclidean spaces. This effect is modeled as

$$\delta^{rel} = -2\frac{\mu}{c^2} ln \frac{\rho^s + \rho_r + \rho_r^s}{\rho^s + \rho_r - \rho_r^s} \tag{2.8}$$

where μ is the Earth gravitational constant, ρ^s and ρ_r are the geocentric distances to the satellite and the receiver and ρ_r^s is the satellite-receiver distance (Holdridge, 1967). The maximum range error due to the space-time curvature is about 18.6 mm.

Another relativistic effect affecting the signal propagation is known as Shapiro delay and it is caused by light velocity changes in presence of the Earth gravitational field. However, this effect for a satellite is less than 2 cm and for most purposes can be neglected, Ashby (2003).

2.2.3. Relativistic effects on the receiver clock

A clock located on the Earth surface is rotating with respect to the resting reference system at the geocenter. The associated linear velocity at the equator is 0.5 Km/s, yielding an error of 10 ns after 3 hours (Hofmann-Wellenhof et al., 2008). Moreover, moving users or fixed users at some altitude above the Earth surface have to make additional corrections caused by their velocity and height above the ground. However, these effects will be absorbed by the estimation of the receiver clock offset and no corrections are needed.

2.3. Ionospheric Effects

The ionosphere is the part of the atmosphere which extends, approximately, from 50 to 2000 Km above the Earth's surface and it is ionized enough as to affect radio signals propagating through it (Hargreaves, 1992). As it can be seen in Fig. 2.1, the ionosphere is divided in different layers which vary greatly between day and night (McNamara, 1991). The lowest layers are denoted as D and E. They come out with the solar radiation and disappear during the night, extending from 50 to 160 Km, with nominal peak heights at 90 and 110 Km, respectively. The F layer extends from 160 Km up and is divided into two regions, F1 and F2, with nominal peak heights at 200 and 300 Km. The topside starts at the height of the maximum density of the F2 layer and extends upward with decreasing density to a transition height, which seldom drops below 500 Km at night or 800 Km in the daytime, although it may lie as high as 1100 Km. Above the transition height, the weak ionization has little influence on radio signals.

The ionization observed in the ionosphere is mainly produced by the ultraviolet radiation and solar X-rays. The free electrons obtained in the ionization processes cause radio waves to reflect off different layers of the ionosphere or

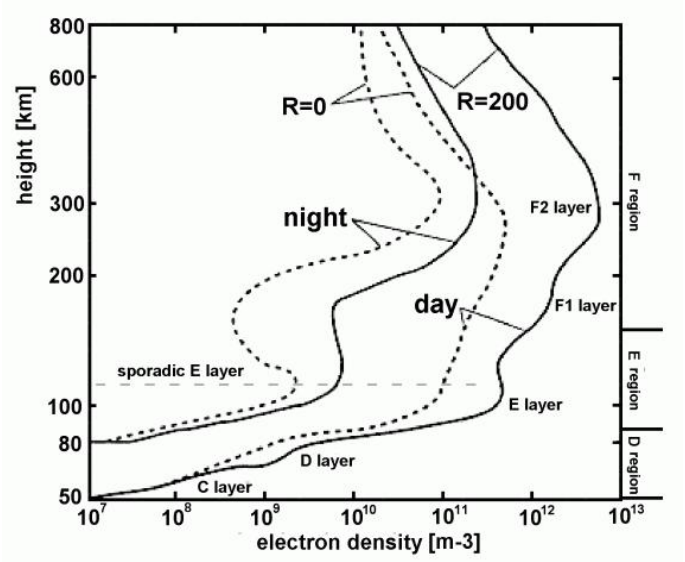

Figure 2.1: *Ionosphere layers. Source: Instituto Nazionale di Geofisica e Vulcanologia (`www.ingv.it`). The dashed line corresponds to the sunspot minimum and the continue line to the maximum. R represents the monthly mean solar index.*

travel straight through them, depending upon frequency and angle of transmission (Jakowski et al., 2008).

The ionization levels are quantified by means of the Total Electron Content (TEC), defined as the total number of electrons present in a column of 1 m^2 along the straight line between two points,

$$TEC = \int N_e ds_0 \tag{2.9}$$

where N_e denotes the number of electrons per m^3, i.e. is the electron density along the path, and s_0 is the measured range. TEC units are electrons/m^2, where 10^{16} electrons/m^2 = 1 Total Electron Content Unit (TECU).

The refraction of a radio wave with frequency f is described by the refractive index n, which in case of GNSS frequencies can be approximated by

$$n = 1 - \frac{f_p^2}{2f^2} \pm \frac{f_p^2 f_g}{2f^3} cos\Theta - \frac{f_p^4}{8f^4} \tag{2.10}$$

where Θ is the angle between the ray path and the geomagnetic field, f_p denotes the plasma frequency,

$$f_p^2 = \frac{e_-^2 N_e}{4\pi^2 m_e \epsilon_0} \tag{2.11}$$

and f_g is the gyro frequency of the electron,

$$f_g = \frac{e_- B_{gm}}{2\pi m_e}. \tag{2.12}$$

The parameter ϵ_0 is the free space permittivity, B_{gm} is the geomagnetic induction and e_- and m_e are the electron charge and mass, respectively (Jakowski et al., 2008).

The ionosphere produces a group delay and phase advance of the GNSS signals, whose magnitude, J, depends on the frequency, is proportional to the TEC along the propagation path and can be approximated by taking into account only the first two terms of (2.10),

$$J = \frac{40.3}{f^2} TEC. \tag{2.13}$$

The ionospheric error in the GNSS observations can reach cents of metres in periods of intense solar activity and for satellites at low elevation. However, it can be eliminated to a first order approximation by forming the ionofree linear combination of dual-frequency observations,

$$P_{IF} = \frac{f_1^2 P_1 - f_2^2 P_2}{f_1^2 - f_2^2}; \quad L_{IF} = \frac{f_1^2 L_1 - f_2^2 L_2}{f_1^2 - f_2^2} \tag{2.14}$$

where P_i and L_i represent the GNSS code and phase observations in the frequency f_i, $i = 1, 2$. The ionospheric error is the main reason why the GNSS systems started to transmit two different frequencies simultaneously.

On the other hand, single-frequency users can reduce the ionospheric delay by applying a model, such as the Klobuchar or NeQuick models, or use the values computed by the AC for either a global or a regional ionosphere.

In fact, the Center for Orbit Determination in Europe (CODE), through the IGS network of GNSS permanent stations, provides Global Ionospheric Maps (GIMs) containing values of vertical Total Electron Content (vTEC) in a grid of $5^\circ \times 5^\circ$ and $2.5^\circ \times 2.5^\circ$, every 2 hours (`www.aiub.unibe.ch/ionosphere`). The vTEC is modeled in a solar-geomagnetic reference frame using a spherical harmonics expansion up to degree and order 15. Moreover, the instrumental biases, P1-P2 DCB for all GPS satellites and ground stations are estimated at the meantime as constant values for each day. The DCB datum is defined by a zero-mean condition imposed on the satellite bias estimates and the P1-C1 bias corrections are taken into account if needed.

To convert line-of-sight TEC into vTEC, a modified single-layer model (M-SLM) mapping function is adopted (Fig. 2.2, Schaer (1997)). It employs the elevation angle at the Ionospheric Piercing point (IP), which is the point of intersection of the signal ray with the ionosphere, concentrated in a single layer of infinitesimal thickness. Such elevation angle can be obtained by

$$sinz' = \frac{R}{R_E + H} sinz \tag{2.15}$$

where R is the geocentric distance to the station, R_E is the Earth's radius, H is a mean value of the height of the ionosphere (typically 350 Km), z' and z are the satellite zenith angles at the IP and at the observing site, respectively. In this way the vTEC is associated to the geocentric coordinates of the IP.

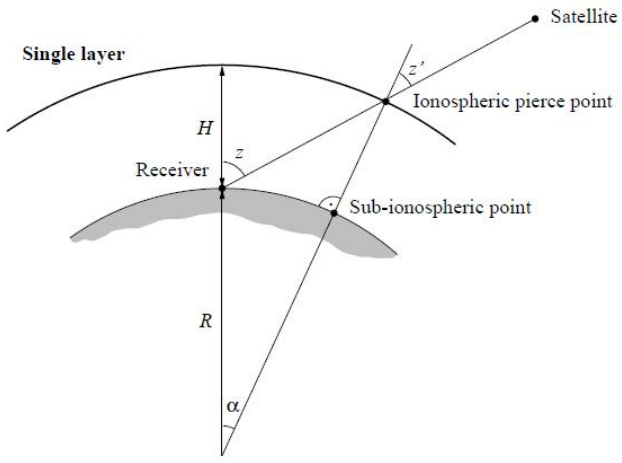

Figure 2.2: *Single-layer model mapping function. Source: Schaer (1997).*

An example of the vTEC values computed by CODE is presented in Fig. 2.3. It reproduces several features of the TEC global distribution: the peak TEC values at low latitudes and the diurnal variation, that is maximum around 2 pm local time decaying to a minimum just prior to sunrise. A TEC depletion at about $60°$ latitude in the local time range 21:00-02:00 is in the location for the mid-latitude trough. Moreover, the characteristic double-hump structure of the Equatorial Anomaly (EA) appears at low latitudes. Further information about CODE GIMs can be found in `aiuws.unibe.ch/ionosphere/index.html` and they can be download from `ftp.unibe.ch/aiub/`. Since 1995, CODE also provides regional maps over Europe (`www.aiub.unibe.ch/ionosphere`).

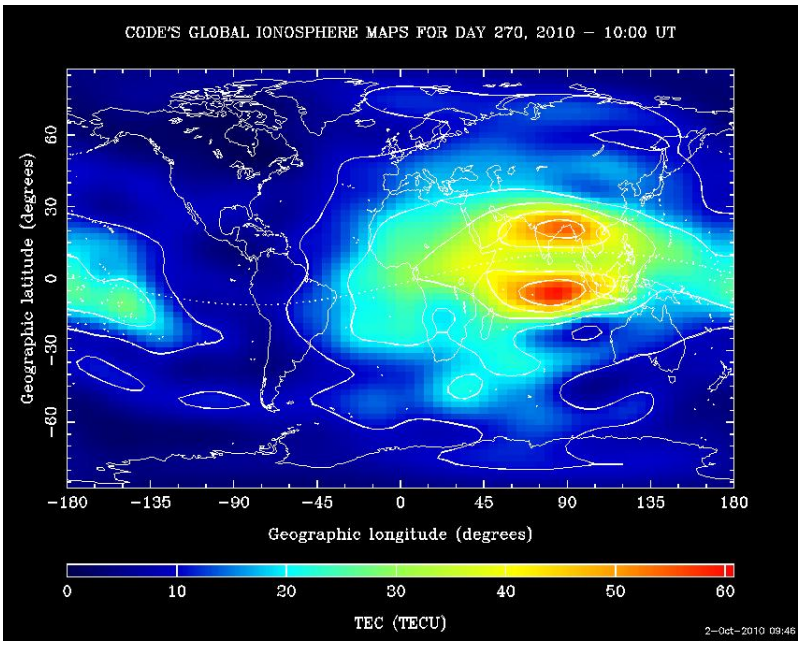

Figure 2.3: *GIM provided by CODE for 10:00 UT in day 270, 2010. Source:* `aiuws.unibe.ch/ionosphere/index.html`.

On the other hand, the National Oceanic and Atmospheric Administration (NOAA) computes real-time TEC maps over the north american continent from ground-based GPS dual frequency receivers (US TEC service). NOAA maps are given every 15 minutes for vertical and slant TEC in a grid of $1°$ resolution in latitude and longitude. Further details about the US TEC service can be found in `www.ngdc.noaa.gov/stp/IONO/USTEC/`.

2.3.1. Klobuchar model

The Klobuchar model (Klobuchar, 1986) approximates the vertical time delay for code measurements by introducing the coefficients transmitted in the GPS navigation message in the expression

$$\Delta t^{Iono} = A_1 + A_2 cos\left(\frac{2\pi(t - A_3)}{A_4}\right), \tag{2.16}$$

where

$$\begin{aligned} &A_1 = 5 \text{ ns}, \\ &A_2 = \alpha_1 + \alpha_2\varphi_{IP}^m + \alpha_3\varphi_{IP}^{m2} + \alpha_4\varphi_{IP}^{m3}, \\ &A_3 = 14^h, \\ &A_4 = \beta_1 + \beta_2\varphi_{IP}^m + \beta_3\varphi_{IP}^{m2} + \beta_4\varphi_{IP}^{m3}. \end{aligned} \tag{2.17}$$

The coefficients α_i and β_i are uploaded to the GPS satellites and broadcast to the user. The parameter t is the local time of the IP and can be derived by

$$t = \frac{\lambda_{IP}}{15} + t_{UT} \tag{2.18}$$

where λ_{IP} is the IP geomagnetic longitude (positive to east) and t_{UT} is the observation epoch in Universal Time (UT). Finally, φ_{IP}^m is the spherical distance between the geomagnetic pole and the IP. Denoting the coordinates of the geomagnetic pole by φ_P, λ_P and those of the ionospheric point by φ_{IP}, λ_{IP},

$$\cos\varphi_{IP}^m = \sin\varphi_{IP} \sin\varphi_P + \cos\varphi_{IP} \cos\varphi_P \cos(\lambda_{IP} - \lambda_P) \tag{2.19}$$

where the coordinates of the geomagnetic pole are

$$\begin{aligned} \varphi_P &= 78.3^\circ N \\ \lambda_P &= 291.0^\circ E. \end{aligned} \tag{2.20}$$

2.3.2. NeQuick model

The NeQuick model is a three-dimensional, time-dependent ionospheric electron density model developed by Radicella and Leitinger (2001). It gives an analytical representation of the vertical profile of electron density and has been adopted by the ITU has a suitable method for TEC modeling. Moreover, it has been proposed by the Galileo project for the ionospheric delay correction in single-frequency positioning. With the NeQuick model, the correction of the ionospheric delay is driven by an "effective ionisation level", Az, valid for the whole world and applicable for a period of 24 hours. Az is defined as

$$Az(\nu) = a_0 + a_1\nu + a_2\nu^2 \tag{2.21}$$

where ν is the modified magnetic dip (inclination), computed from the true magnetic dip, I, and the latitude of the site, φ, by

$$\tan \nu = \frac{I}{\sqrt{\cos \varphi}}. \tag{2.22}$$

From the Galileo navigation message, the users will extract the coefficients a_i, $i = 0, 1, 2$. An example of a navigation message header is shown in Fig. 2.4 (Gurtner and Estey, 2007). Klobuchar and NeQuick coefficients are given for GPS and Galileo users. Furthermore, the format rinex 3.00 is designed to include the ionospheric delay correction derived from a model as a pseudo-observable.

```
     3.00           Navigation data     G                   RINEX VERSION / TYPE
sbf2rin                                 20100120 143727 LCL PGM / RUN BY / DATE
GPSA   4.6566E-09  1.4901E-08 -5.9605E-08 -5.9605E-08       IONOSPHERIC CORR
GPSB   7.9872E+04  6.5536E+04 -6.5536E+04 -3.9322E+05       IONOSPHERIC CORR
GAL    1.0000E+02  0.0000E+00  0.0000E+00  0.0000E+00       IONOSPHERIC CORR
GPUT  0.0000000000E+00 0.000000000E+00 536576 1392          TIME SYSTEM CORR
     0                                                      LEAP SECONDS
                                                            END OF HEADER
```

Figure 2.4: *GNSS navigation message header in rinex 3.00 format. Source: Gurtner and Estey (2007). The Klobuchar and NeQuick coefficients are given for GPS and Galileo single-frequency users.*

2.3.3. Ionospheric scintillation

The complex processes taking place within the ionosphere give place to the appearance of irregularities of different scales in the TEC distribution. Such irregularities may degrade the radio signals propagating through the ionosphere, producing variations in their amplitude, phase and Faraday rotation angle (Basu et al., 1986). These effects are known as scintillation and they are characterised by a rapid fluctuation and fading of the received signal intensity. Scintillation can produce a decrease in the Signal to Noise Ratio (SNR), an increase in the number of cycle slips and even the complete signal loss of lock by the receiver. In presence of scintillation the carrier phase measurements result more affected than code pseudoranges and the observations in L2 more affected than in L1 (Dubey et al., 2005).

The degree of ionospheric scintillation is evaluated by the indexes S_4 and $\sigma_{\delta\phi}$ (Dierendonck, 1999). S_4 is the amplitude scintillation index and can be obtained as the standard deviation of the received signal power divided by its mean value,

$$S_4 = \sqrt{\frac{\langle SI^2 \rangle - \langle SI \rangle^2}{\langle SI \rangle^2}}, \tag{2.23}$$

where SI is the signal intensity and $\langle\ \rangle$ is the average value during the interval of interest. If $S_4 > 0.1$, it is claimed that scintillation exists and, if $S_4 > 0.8$, the scintillation is considered strong. On the other hand, $\sigma_{\delta\phi}$ is the phase scintillation index obtained as the standard deviation of the signal phase measurements. A value of $\sigma_{\delta\phi} \geq 1.0$ rad indicates strong scintillation.

Scintillation may be particularly intense at low magnetic latitude and its intensity and occurrence are greatest immediately after sunset and around the equinoxes. An example of the effect of phase scintillation on L2 can be observed in Fig. 2.5. The observations correspond to the GPS satellite PRN14 observed from the permanent station DOUA, in the African equatorial region. The maximum scintillation is observed after the local sunset.

2.4. Tropospheric Effects

The neutral (non-ionized) atmosphere is an approximately spherical shell extending outward from the Earth's surface to about 100 km above it. The first

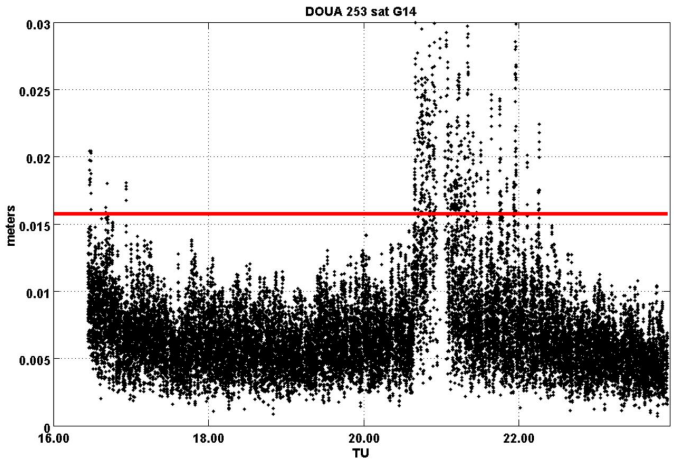

Figure 2.5: *Effect of the phase Scintillation on L2. The observations correspond to the GPS satellite PRN14 observed from the permanent station DOUA at the end of day 253 of 2004.*

50 Km contain the 99.9% of the total atmospheric mass (Kertz, 1971) and consist of the troposphere (0-10 km), in which temperature decreases with height, the tropopause (10 km), at which temperature remains constant, and the stratosphere (10-50 km), in which temperature increases with height (Fig. 2.6).

Unlike the ionosphere, the neutral atmosphere is a non-dispersive medium for GNSS carrier frequencies. However, it produces a reduction in the velocity of the signal transmission and the curvature of its trajectory, constituting one of the dominant error sources in GNSS positioning.

The main effect of the neutral atmosphere on the GNSS observations is known as tropospheric delay, although it is also due to the presence of the stratosphere. The tropospheric delay is frequency-independent and can not be eliminated via dual-frequency observations. It depends on the temperature, pressure and humidity and is divided into a wet and a dry (or hydrostatic) part. The hydrostatic fraction is mostly due to dry gases and contributes approximately 90% of the total tropospheric refraction, whereas the wet component is a result of water vapor and constitutes the other 10% (Hofmann-Wellenhof et al., 2008). The total effect is around 2.23 metres, although it can reach up to 10 metres in humid and warm climates and for satellites at low elevations.

The tropospheric zenith delay for the wet and hydrostatic parts, ZWD and ZHD, can be approximated by means of different models, such as the Hopfield or Saastamoinen ones, which will be detailed below. These troposphere models need the values of the atmospheric pressure, temperature and humidity of the

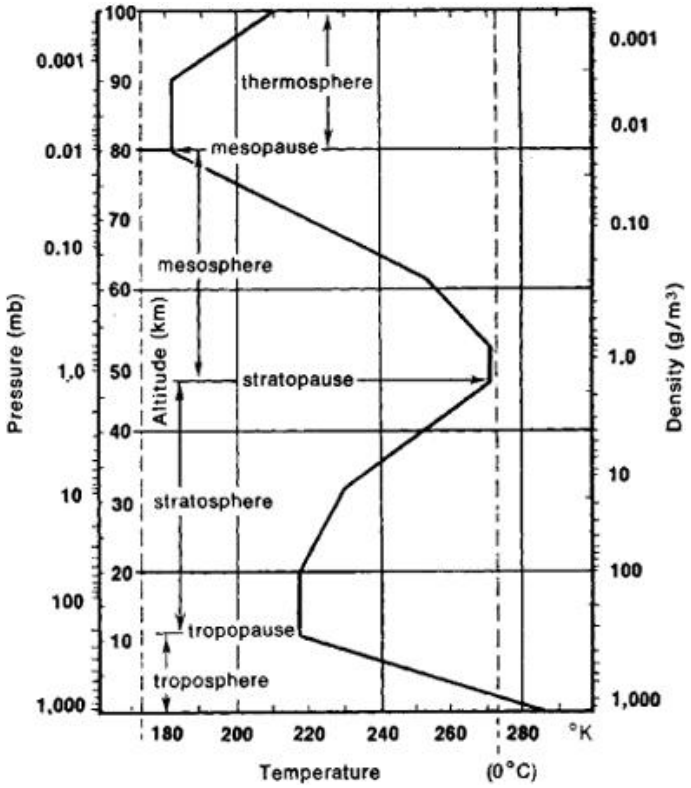

Figure 2.6: *Vertical distribution of temperature in the neutral atmosphere. Source:* `encyclopedia2.thefreedictionary.com`.

observing site. In case that the actual meteorological parameters are not available, they can be taken from the Standard Atmosphere or from the Minimal Operation Performance System (MOPS).

Moreover, in order to project the zenith delay correction into the satellite-receiver direction, mapping functions for the wet and dry components are needed. One of the most used mapping functions is the Niell Mapping Function (NMF). Such function was designed considering exclusively satellite elevation angles and, therefore, an azimuthal symmetry of the troposphere is implicitly assumed (Chen and Herring, 1997). Azimuthally inhomogeneous mapping functions have been proposed as early as 1977 (Gardner, 1977) but have never been used in routine GNSS geodesy. However, the horizontal gradients emerging of the simplifications of the mapping functions can be estimated in the observations processing, along with the rest of parameters.

On the other hand, Sansó (2006) derived an expression to approximate the error in the GNSS range due to the ray curvature along its path through the troposphere, δl. The magnitude of this term for different satellite zenith angles is

shown in Tab. 2.1. Although the error of curvature can reach a few cm, its correction is normally discarded in the GNSS observations processing.

As a result, the complete expression for the tropospheric effect on GNSS observations is

$$\begin{aligned} Trop = \; & m_h(E)ZHD + m_w(E)ZWD \\ & + m_\nabla(E)cotgE\,(\nabla_{NS}\,cosA + \nabla_{EW}\,sinA) + \delta l \end{aligned} \tag{2.24}$$

where m_h, m_w are the mapping functions of the hydrostatic and wet zenith delays, respectively; m_∇ is the horizontal gradient mapping function, ∇_{NS} and ∇_{EW} are the tropospheric delay horizontal gradients in the north-south and east-west directions and E and A are the satellite elevation and azimuth (measured eastward from north). The large difference between gradient mapping functions at low elevation angles might be significant, however the wet or dry mapping functions can be used for the gradient mapping.

z (°)	δl (mm)
60	1.1
65	1.9
70	3.9
75	9.5
80	32.6

Table 2.1: *Tropospheric ray curvature error in GNSS ranges for different satellite zenith angles. Source: Sansó (2006).*

2.4.1. Hopfield model

Hopfield developed empirically a troposphere model using worldwide data (Hopfield, 1969). The Hopfield model applies a single-layer polytropic atmosphere model, ranging from the Earth's surface to altitudes of about 11 and 40 Km for the wet and dry layers, respectively. Hopfield expressions for the dry and wet vertical delays are

$$ZHD(E) = \frac{10^{-6}}{5}\frac{77.64}{sin\sqrt{E^2+6.25}}\frac{p}{T}\left[40136+148.72\left(T-273.16\right)\right]$$
$$ZWD(E) = \frac{10^{-6}}{5}\frac{-12.96T+3.71810^5}{sin\sqrt{E^2+2.25}}\frac{e}{T^2}11000 \tag{2.25}$$

where p, T and e are the atmospheric pressure (mb), the temperature (K) and the partial pressure of water vapor (mb).

A modified Hopfield model can also be used to compute the wet and hydrostatic tropospheric path delay in the satellite-receiver direction (Hopfield, 1972). The needed expressions are

$$ZD_i(z) = 10^{-6}N_i\sum_{k=1}^{9}\frac{f_{k,i}}{k}r_i^k \quad i=H,W. \tag{2.26}$$

where $r_i = \sqrt{\left(R_E+h_i\right)^2 - R_E^2 sin^2 z} - R_E cosz$,

$$\begin{array}{ll} f_{1,i}=1 & f_{2,i}=4a_i \\ f_{3,i}=6a_i^2+4b_i & f_{4,i}=4a_i(a_i^2+3b_i) \\ f_{5,i}=a_i^4+12a_i^2b_i+6b_i^2 & f_{6,i}=4a_ib_i(a_i^2+3b_i) \\ f_{7,i}=b_i^2(6a_i^2+4b_i) & f_{8,i}=4a_ib_i^3 \\ f_{9,i}=b_i^4 & \end{array} \tag{2.27}$$

and

$$\begin{array}{ll} a_i=-\frac{cosz}{h_i}, & b_i=-\frac{sin^2 z}{2h_iR_E} \\ h_h=40136+148.72\left(T-273.16\right) & (m), \\ h_w=11000 & (m), \\ N_h=\frac{77.64p}{T} & (mbK^{-1}), \\ N_w=-\frac{12.96e}{T}+\frac{3.71810^5e}{T^2}, & \\ R_E=6378137 & (m). \end{array} \tag{2.28}$$

2.4.2. Saastamoinen model

The Saastamoinen model was derived from the Gas laws and the conception of the atmosphere as a mixture of two ideal gases (dry air and water vapor), Saastamoinen (1973). Thus, the tropospheric delay in the satellite-receiver direction according to Saastamoinen model is

$$Trop(z) = \frac{0.002277}{cosz}\left[p + \left(\frac{1255}{T} + 0.05\right)e - B_{Saas}tan^2 z\right] + \delta R \tag{2.29}$$

where B_{Saas} and δR are correction terms depending on the height of the observing site. They are shown in Tabs. 2.2 and 2.3.

Height (Km)	B_{Saas} (mb)
0.0	1.156
0.5	1.079
1.0	1.006
1.5	0.938
2.0	0.874
2.5	0.813
3.0	0.757
4.0	0.654
5.0	0.563

Table 2.2: *Correction term B_{Saas} to the Saastamoinen model.*

2.4.3. Mapping functions

Some troposphere models provide the tropospheric delay for the zenithal direction and then, the projection of such delay to the receiver-satellite direction is needed. In this case, a mapping function must be used. The mapping functions, $m(E)$, are defined as the ratio of the electrical path length through the atmosphere at geometric elevation E, to the electrical path length in the zenith direction (Niell, 1996).

Marini (1972) showed that the elevation angle dependence of any horizontally stratified atmosphere could be approximated by a continue fraction in terms of $1/sin(E)$ as

Zenith	Station Height above sea level (Km)							
angle	0	0.5	1.0	1.5	2.0	3.0	4.0	5.0
60° 00′	0.003	0.003	0.002	0.002	0.002	0.002	0.001	0.001
66° 00′	0.006	0.006	0.005	0.005	0.004	0.003	0.003	0.002
70° 00′	0.012	0.011	0.010	0.009	0.008	0.006	0.005	0.004
73° 00′	0.020	0.018	0.017	0.015	0.013	0.011	0.009	0.007
75° 00′	0.031	0.028	0.025	0.023	0.021	0.017	0.014	0.011
76° 00′	0.039	0.035	0.032	0.029	0.026	0.021	0.017	0.014
77° 00′	0.050	0.045	0.041	0.037	0.033	0.027	0.022	0.018
78° 00′	0.065	0.059	0.054	0.049	0.044	0.036	0.030	0.024
78° 30′	0.075	0.068	0.062	0.056	0.051	0.042	0.034	0.028
79° 00′	0.087	0.079	0.072	0.065	0.059	0.049	0.040	0.033
79° 30′	0.102	0.093	0.085	0.077	0.070	0.058	0.047	0.039
79° 45′	0.111	0.101	0.092	0.083	0.076	0.063	0.052	0.043
80° 00′	0.121	0.110	0.100	0.091	0.083	0.068	0.056	0.047

Table 2.3: *Correction term δR to the Saastamoinen model.*

$$m(E) = \frac{1 + \dfrac{a}{1 + \dfrac{b}{1 + c}}}{sin(E) + \dfrac{a}{sin(E) + \dfrac{b}{sin(E) + c}}}. \tag{2.30}$$

The mapping function parameters, a, b, c, are normally involved with temperature, pressure and relative humidity. In the design of the mapping functions, azimuthal symmetry is usually assumed and the corrections due to the horizontal gradients can be added or estimated.

The NMF (Niell, 1996) for the hydrostatic and wet atmosphere path delays are based on the Marini's expression (2.30) and depend on the latitude and height of the observing site above sea level and on the day of the year. The hydrostatic component of the mapping function is related to the geopotential height of the 200 mb isobaric pressure level above the site and the wet component is calculated from the vertical profile of wet refractivity at the site. The coefficients of the dry and wet NMF are obtained by applying the expression

$$a(\varphi, t) = a_{avg}(\varphi) + a_{amp}(\varphi) cos\left[2\pi \frac{t - t_0}{365.25}\right] \tag{2.31}$$

where φ is the station latitude, t_0 corresponds to January 28th and t is the time from January 0.0 expressed in UT days. If the station is located in the southern hemisphere an increment of $365.25/2$ days must be added to t. The parameters a_{avg}, a_{amp} for the dry NMF must be obtained by interpolating the values given in Tab. 2.4.

			Latitude		
Coefficient	15°	30°	45°	60°	75°
			Average		
a_{avg}	1.2769934e-3	1.2683230e-3	1.2465397e-3	1.2196049e-3	1.2045996e-3
b_{avg}	2.9153695e-3	2.9152299e-3	2.9288445e-3	2.9022565e-3	2.9024912e-3
c_{avg}	62.610505e-3	62.837393e-3	63.721774e-3	63.824265e-3	64.258455e-3
			Amplitude		
a_{amp}	0.0	1.2709626e-5	2.6523662e-5	3.4000452e-5	4.1202191e-5
b_{amp}	0.0	2.1414979e-5	3.0160779e-5	7.2562722e-5	11.723375e-5
c_{amp}	0.0	9.0128400e-5	4.3497037e-5	84.795348e-5	170.37206e-5
			Height correction		
a_{ht}			2.53e-5		
b_{ht}			5.49e-3		
c_{ht}			1.14e-3		

Table 2.4: *Coefficients of the Niell Hydrostatic Mapping Function.*

On the other hand, the coefficients of the wet mapping function are obtained by interpolating the values from Tab. 2.5.

			Latitude		
Coefficient	15°	30°	45°	60°	75°
a	5.8021897e-4	5.6794847e-4	5.8118019e-4	5.9727542e-4	6.1641693e-4
b	1.4275268e-3	1.5138625e-3	1.4572752e-3	1.5007428e-3	1.7599082e-3
c	4.3472961e-2	4.6729510e-2	4.3908931e-2	4.4626982e-2	5.4736038e-2

Table 2.5: *Coefficients of the Niell Wet Mapping Function.*

The resulting values can be used in (2.30) to obtain the wet and dry NMF. A correction for the station height must be applied to the dry mapping function, which can be obtained as

$$\delta^{dmf} = \left[\frac{1}{sin(E)} - \frac{1 + \dfrac{a_{ht}}{1 + \dfrac{b_{ht}}{1 + c_{ht}}}}{sin(E) + \dfrac{a_{ht}}{sin(E) + \dfrac{b_{ht}}{sin(E) + c_{ht}}}} \right] H \cdot 10^{-3} \tag{2.32}$$

where H is the station height in metres.

2.4.4. Meteorological parameters

In the troposphere models, either measured values of pressure, temperature and humidity or the values derived from a model may be used. The values of the Standard Atmosphere are shown in Tab. 2.6.

Parameter	value	units
Temperature (T)	291.16	(K)
Pressure (p)	1013.25	(mb)
Humidity (R)	50	(%)

Table 2.6: *Standard Atmosphere temperature, pressure and humidity.*

To transform the unit of temperature from Celsius to Kelvin one can use $T(K) = T(^{\circ}C) + 273.16$.

Moreover, the MOPS (`www.rtca.org/comm/Committee.cfm?id=14`) for Airborne Navigation Equipment Using the Global Positioning System provides a tropospheric delay correction defined through a fairly simple model using estimated receiver position, satellite elevation and day of year. The meteorological parameters provided by MOPS are obtained by interpolating the values in Tabs. 2.7 and 2.8 and applying

$$\psi(\varphi, t) = \psi_0(\varphi) - \Delta\psi_0(\varphi) cos\left[2\pi \frac{t - t_0}{365.25}\right], \tag{2.33}$$

where t_0 corresponds to January 28th in the northern hemisphere and t is the day of the year.

However, the meteorological parameters given by the Standard Atmosphere model and MOPS correspond to the sea level and must be projected to

Latitude	p_0 (mb)	T_0 (K)	e_0 (mb)
$\leq 15°$	1013.25	299.65	26.31
30°	1017.25	294.15	21.79
45°	1015.75	283.15	11.66
60°	1011.75	272.15	6.78
$\geq 75°$	1013.00	263.65	4.11

Table 2.7: *Meteorological Parameters given by MOPS.*

Latitude	p_0 (mb)	T_0 (K)	e_0 (mb)
$\leq 15°$	0.00	0.00	0.00
30°	-3.75	7.00	8.85
45°	-2.25	11.00	7.24
60°	-1.75	15.00	5.36
$\geq 75°$	-0.50	14.50	3.39

Table 2.8: *Correction to MOPS Meteorological Parameters.*

the station altitude, H. The height-dependent values of the meteorological parameters can be obtained by using the expressions

$$\begin{aligned} p &= p_0 \left[1 - 0.0000226 \left(H - H_0\right)\right]^{5.225} \\ T &= T_0 - 0.0065 \left(H - H_0\right) \\ R &= R_0 e^{-0.0006396(H - H_0)} \end{aligned} \tag{2.34}$$

where p_0, T_0, R_0 are the values at the reference height, H_0, and R is the relative humidity at the station altitude. The partial pressure of water vapour is obtained as

$$e = Re^{-37.2465 + 0.213166T - 0.000256908T^2}. \tag{2.35}$$

2.5. Antennas Phase Center Offset and Variation (PCO/V)

As it was mentioned above, the code and phase observations approximately correspond to the geometric receiver-satellite distance, which must be corrected of relativistic and atmospheric errors. More specifically, these observations refer to the distance between the satellite and receiver antenna phase centers, which

vary with the frequency and the receiver-satellite direction (Mader, 1999). However, the satellite precise coordinates are given for the satellite mass center and the station coordinates are generally referred to a reference point located out of the antenna. Therefore, the reduction of the GNSS observations to both, satellite and receiver reference points is needed.

For the receiver antennas calibration, a reference point is defined as the intersection of the vertical axis and the bottom of the antenna and denoted as Antenna Reference Point (ARP) (Fig. 2.7). Then, the mean position of the electrical phase center is determined for every frequency and their location with respect to the ARP in a local reference system is denoted as Phase Center Offset (PCO). However, the signal can be received at any point of the surface of the antenna, depending on the frequency and the satellite-receiver direction. The deviation from the mean phase center is known as Phase Center Variation (PCV).

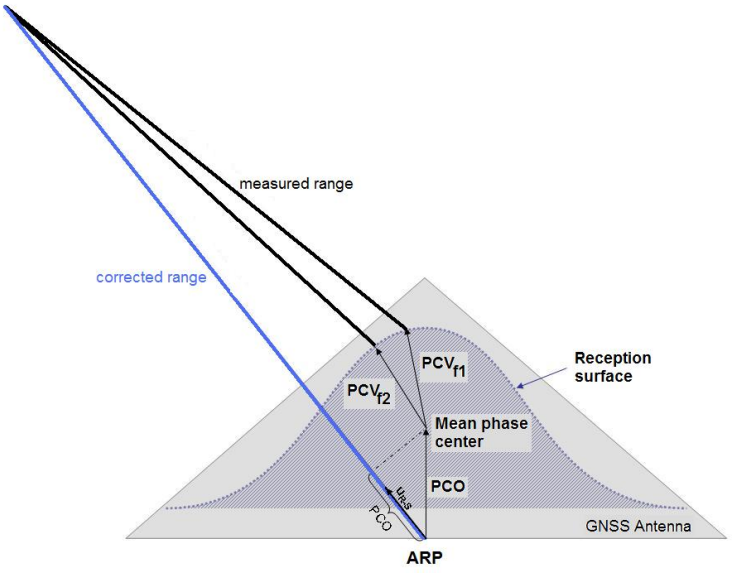

Figure 2.7: *Antenna PCO/V correction.*

For every frequency, the antenna phase center error correction is carried out in two steps. First, the PCV with respect to the mean phase center are added to the up component of the PCO and, second, this PCO is projected into the satellite-receiver direction and added to the ranges,

$$\delta_{PCO} = \boldsymbol{u_{rs}} \cdot \boldsymbol{a_{ri}} \tag{2.36}$$

where $\boldsymbol{u_{rs}}$ is the unit vector in the receiver-satellite direction in a local reference system and $\boldsymbol{a_{ri}}$ represents the receiver antenna phase center eccentricity for the frequency f_i. Then, the observations are referred to the antenna ARP.

The same approach must be used for the correction of satellite antenna PCO/V. Whereas the satellite zenith angle at the receiver ranges from $0°$ to $90°$, the corresponding nadir angle of the receiver as seen from the satellite only varies between $0°$ and $15°$ (Rothacher, 2001). The nadir angle at the satellite, z', is related to the zenith angle at the receiver, z, by

$$sin(z') = \frac{R}{r} sin(z) \tag{2.37}$$

where R is the Earth's radius and r the geocentric distance of the satellite, Fig. 2.8.

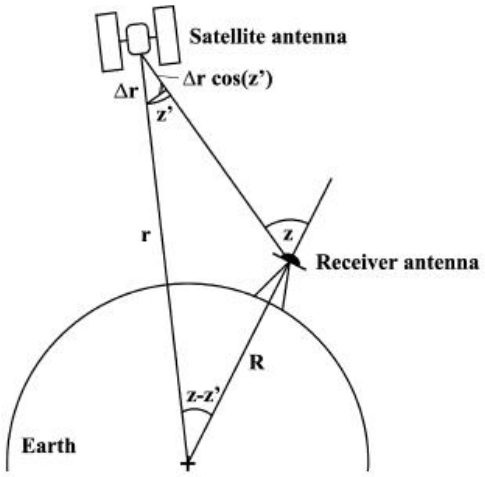

Figure 2.8: *Relation between satellite and receiver zenith and nadir angles. Source: Rothacher (2001).*

It is important to remember that the origin of the satellite coordinate system is at the mass center, the z-axis points toward the Earth center, the y-axis points along the solar panel axis and the x-axis completes the right-handed coordinate system. However, by convention, the GPS IIR, IIF blocks and Galileo vehicles x and y-axis point in the opposite direction.

Each individual antenna must be calibrated to obtain its phase center corrections. Relative antenna phase center models have been used within the IGS

for a long time (IGS01 calibration). In the relative calibration, one antenna type, the AOAD/M_T without radome, was assumed to represent a perfect antenna without any direction dependence of the phase center (Mader, 1999). However, the simplifications assumed in the relative calibration result in the introduction of systematic errors and therefore, the IGS switched to an absolute antenna phase center model (IGS05) in the GPS week 1400 (2006-Nov-05, Gendt (2006)). The absolute calibration is based on a set of robot-calibrated receiver antenna PCV that consider also the azimuthal dependence (Wübbena et al., 2000). At the same time, the satellite antenna PCV are considered in a nadir-dependent model and are different for every satellite (Schmid and Rothacher, 2003). The IGS05 calibration is consistent with IGS05 products (orbits, clocks, etc) and must be used together. Moreover, in April 2011, the IGS has adopted a new reference frame (IGS08, Schmid (2011)) and the IGS products in this reference frame must be used together with the new IGS08 absolute calibration, an updated set of receiver and satellite antenna phase center corrections.

The IGS calibrations of the GPS and GLONASS antennas and IGS stations can be downloaded from `igscb.jpl.nasa.gov/pub/station/general`. However, the IGS calibration only comprises PCO/V values for the GPS frequencies L1 and L2, and not for the modernized L5, already transmitted by block IIF satellites.

The values of the PCO corrections in the z-axis direction for the GIOVE satellites are given in Tab. 2.9. GIOVE antennas PCV are not known for the time being. Moreover, the Galileo experimental antennas of the GESS stations have been calibrated but the values are still preliminary. GPC provides PCO/V corrections for the GESS experimental antennas, which are consistent with the IGS absolute calibration of the GPS satellites. However, only the most recent antennas present PCO/V values for the GIOVE frequencies.

Satellite	PCO z-axis [m]
Giove-A (E01)	0.771
Giove-B (E16)	1.347

Table 2.9: *GIOVE antennas PCO. Source: Zandbergen and Navarro (2006).*

2.6. Satellite and Receiver Electronic Delays

The GNSS signal is generated within the satellite and travels through its circuitries to reach the antenna phase center, from where it is transmitted. Later, this signal is received at the receiver antenna and travels through the receiver circuitries before being processed. Thus, satellite and receiver circuitries introduce time delays in the measured ranges, which differ for every frequency and every modulating code. These delays are known as instrumental or electronic biases. Whereas for carrier phase observations the instrumental delays are absorbed by the initial ambiguities, the error introduced in code observations can reach several ns.

Although instrumental errors cannot be determined in an absolute sense, monthly DCB for GPS and GLONASS satellites and for some IGS stations are provided by CODE (`www.aiub.unibe.ch/ionosphere`). They can be downloaded from `ftp.unibe.ch/aiub/CODE/`. Satellite DCBs between GPS codes are defined as

$$\begin{aligned} B^s_{P1-P2} &= B^s_{P1} - B^s_{P2} \\ B^s_{P1-C1} &= B^s_{P1} - B^s_{C1} \\ B^s_{P2-C2} &= B^s_{P2} - B^s_{C2}. \end{aligned} \tag{2.38}$$

B^s_{P1-P2} values are computed while solving for the ionosphere parameters from the geometry-free linear combination (Dach et al., 2007) and B^s_{P1-C1} are obtained in the course of a global GNSS clock analysis (Schaer, 2000). It must be mentioned that it is common practice to impose a zero-mean condition on the set of DCB estimates (with respect to each GNSS system) for datum definition. This implies that DCB results may be shifted by a common offset value. Although satellite DCBs are not constant, they are very stable in time, since the day-to-day reproducibility is observed around 0.05 ns RMS (Dach et al., 2007). As an example, B^s_{P1-P2} values obtained by CODE for GPS and GLONASS satellites in May, 2010 are shown in Fig. 2.9. Moreover, the B_{rP1-P2} obtained for some IGS stations in the same month are shown in Fig. 2.10.

On the other hand, it must be taken into account that IGS precise satellite clocks are estimated from the ionofree combination of phase and code observations in $P1$ and $P2$ and, therefore, they contain the ionofree combination of the satellite electronic biases, B^s_{P1} and B^s_{P2}, i.e., Dach et al. (2007),

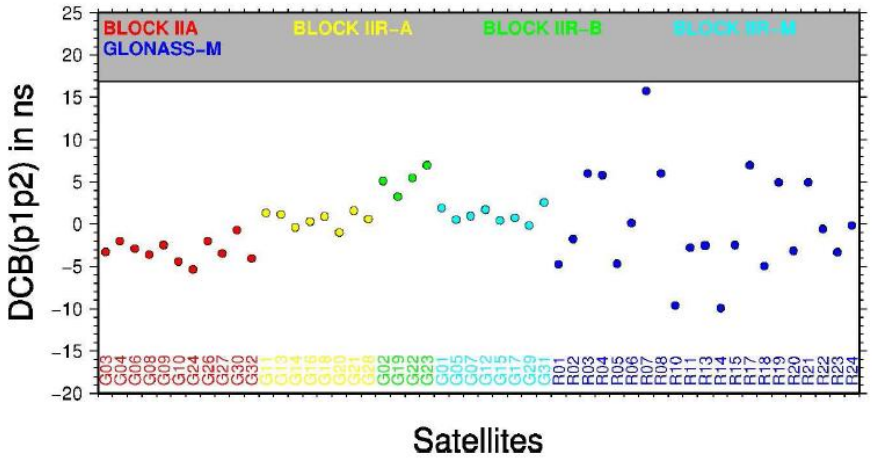

Figure 2.9: *Satellite P1-P2 DCB values for May, 2010. Source: Schaer and Dach (2010).*

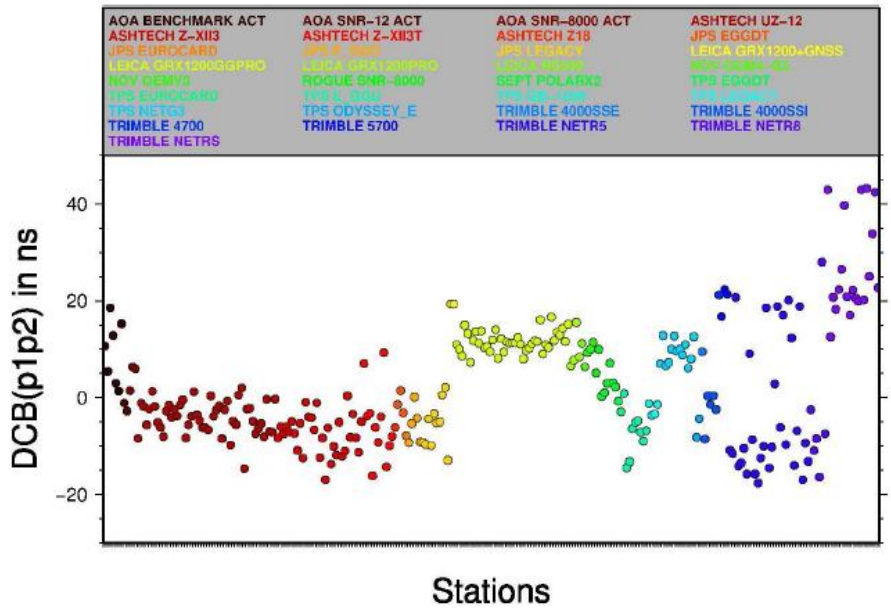

Figure 2.10: *IGS station P1-P2 DCB for May, 2010. Source: Schaer and Dach (2010).*

$$dt^s_{IGS} = dt^s - (2.55B^s_{P1} - 1.55B^s_{P2}). \tag{2.39}$$

The same is also true with regard to the broadcast satellite clock information. This implies that clock corrections have to be consistent with the code observations, in such a way that the electronic biases cancel out during the data processing.

When double differences are formed, satellite and receiver DCBs cancel out but, in other cases, estimated DCBs may be used to correct code observations to become consistent with satellite clocks. This practice can not be ignored in point positioning applications where DCB do not cancel by differencing. The correction for 5 different linear combinations are given in Tab. 2.10. As expected, no DCB correction is needed for the ionofree linear combination of $P1/P2$ code data.

L. C.	$P1/P2$	$C1/P2$	$C1/C2$
$P1/C1$	$1.546B_{P1-P2}$	$1.546B_{P1-P2} + B_{P1-C1}$	$1.546B_{P1-P2} + B_{P1-C1}$
$P2$	$2.546B_{P1-P2}$	$2.546B_{P1-P2}$	$2.546B_{P1-P2} + B_{P2-C2}$
Ionofree	0	$2.546B_{P1-C1}$	$2.546B_{P1-C1} - 1.55B_{P2-C2}$
Geomfree	-B_{P1-P2}	$-B_{P1-P2} + B_{P1-C1}$	$-B_{P1-P2} + B_{P1-C1} + B_{P2-C2}$
Widelane	$-1.984B_{P1-P2}$	$-1.984B_{P1-P2} + 4.529B_{P1-C1}$	$-1.984B_{P1-P2} + 4.529B_{P1-C1} - 3.53B_{P2-C2}$

Table 2.10: *DCB correction for different linear combinations. Source: Dach et al. (2007).*

The ionofree linear combination is given in (2.14), the geometry-free is formed as $P1 - P2$ and the widelane linear combination of code observations is

$$P_{wl} = \frac{1}{f_1 - f_2}(f_1 P1 - f_2 P2). \tag{2.40}$$

The receiver DCBs are different for GPS and GLONASS observations and should not exceed a few tens of ns. There is not a way to correct the errors caused by receiver code biases in point positioning and when analyzing doubly differenced data from more than one receiver class, the effect of B_{rP1-C1} does not either cancel out.

Furthermore, when observations from different satellite systems are processed together, the ISB introduced by the receiver must also be taken into ac-

count. This ISB emerges due to the fact that signals from different satellite systems are processed in different parts of the receiver. The ISB estimated by CODE for some types of GPS/GLONASS receivers is shown in Fig. 2.11.

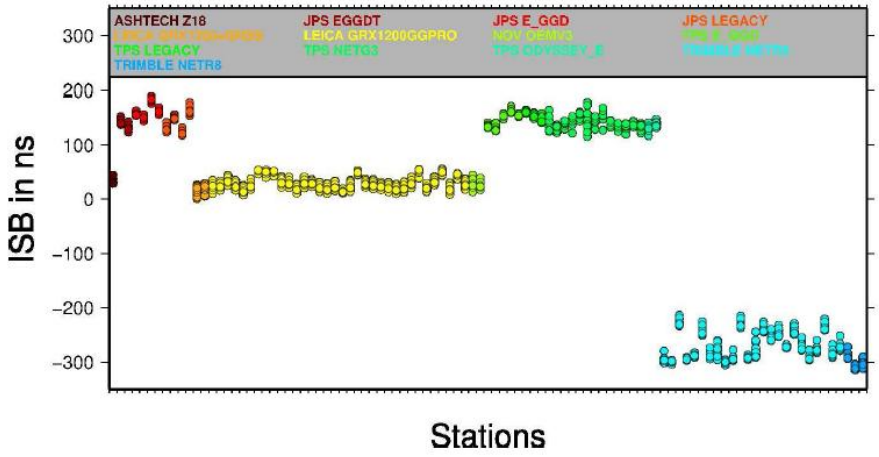

Figure 2.11: *GPS/GLONASS InterSystem Biases by CODE. Source: Schaer and Dach (2010).*

In the permanent GESS network, the ISB are obtained as the difference between GPS $P1-P2$ IFB and GIOVE $C1C-C7Q$ IFB, as it was seen in the section 1.3. GESS mean values of $P1-P2$ and $C1C-C7Q$ IFB, as well as ISB are obtained weekly by GPC (Fig. 1.16, `www.giove.esa.int`). The experimentation has also provided estimations of the GIOVE IFB between signals in E1 and E5 (Tab. 2.11). Similarly to GPS clocks, the GIOVE clocks are estimated from the ionofree combination of phase and code observations in $C1C$ and $C7Q$ and, therefore, they contain the ionofree combination of the satellite electronic biases, B^s_{C1} and B^s_{C7},

$$dt^s_{GPC} = dt^s - (2.42B^s_{C1} - 1.42B^s_{C7}). \tag{2.41}$$

Satellite	IFB (ns)
GIOVE-A	921.829
GIOVE-B	909.139

Table 2.11: *GIOVE E1-E5 IFB obtained by GPC. Source: Personal communication.*

2.7. Phase Wind-Up Effect

GNSS satellites transmit right circularly polarized radio waves and a rotation of either the receiver or the satellite antenna around its axis will change the carrier phase measurement, L_r^s, up to one cycle. This effect is denoted as phase wind-up and is associated with the mutual antenna orientation at the satellite and the receiver. Wu et al. (1993) derived the phase wind-up correction for a crossed dipole antenna, which consists of two equal-gain dipole elements perpendicular to each other, as in Fig. 2.12. This correction is applicable to more general cases.

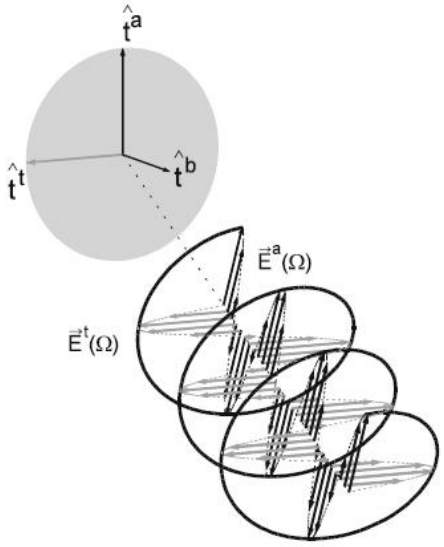

Figure 2.12: *Electric fields transmitted by two dipoles oriented at $\hat{t}^a$ and $\hat{t}^t$. Source: Beyerle (2009).*

According to Wu et al. (1993), the variation in the measured phase due to phase wind-up can be obtained by

$$\Delta\phi = sign(\zeta) cos^{-1}\left(\frac{\boldsymbol{D'}\cdot\boldsymbol{D}}{|\boldsymbol{D'}|\,|\boldsymbol{D}|}\right) \tag{2.42}$$

where $\zeta = \boldsymbol{u_{sr}}\cdot(\boldsymbol{D'}\times\boldsymbol{D})$, $\boldsymbol{u_{sr}}$ is the satellite to receiver unit vector and $\boldsymbol{D'}$ and $\boldsymbol{D}$ are the effective dipole vectors of the satellite and receiver. They are computed from the satellite coordinate unit vectors $(\boldsymbol{x'}, \boldsymbol{y'}, \boldsymbol{z'})$, as defined in section 2.5, and the local receiver unit vectors $(\boldsymbol{x}, \boldsymbol{y}, \boldsymbol{z})$, forming a direct reference system (i.e., north, west, up),

$$\begin{aligned} \boldsymbol{D'} &= \boldsymbol{x'} - \boldsymbol{u_{sr}}(\boldsymbol{u_{sr}} \cdot \boldsymbol{x'}) - \boldsymbol{u_{sr}} \times \boldsymbol{y'} \\ \boldsymbol{D} &= \boldsymbol{x} - \boldsymbol{u_{sr}}(\boldsymbol{u_{sr}} \cdot \boldsymbol{x}) + \boldsymbol{u_{sr}} \times \boldsymbol{y}. \end{aligned} \tag{2.43}$$

Continuity between consecutive phase observation segments must be ensure by adding full cycle terms of 2π to the correction.

This effect is quite significant for un-differenced positioning when fixing satellite clocks, since most of the IGS AC apply the phase wind-up correction and, therefore, neglecting it would result in positioning errors at the decimetre level.

2.8. Other error sources

There exist some error sources for GNSS observations which can not be either modeled or predicted, such as the multipath, cycle slips or clock jumps, which degrade significantly the position determination if they are not properly handled. Moreover, the periods of satellite maneouvres, shadow crossing or satellite failure may give place to erroneous observations and products, which must be discarded from the processing. These error sources are introduced in the following.

2.8.1. Multipath

The multipath effect is due to the reflection of the GNSS signal in different surfaces during its propagation, producing a superposition of signals from different paths (Fig. 2.13). The main multipath error is introduced by surfaces near the receiver antenna, although some effects are also due to reflections at the satellite.

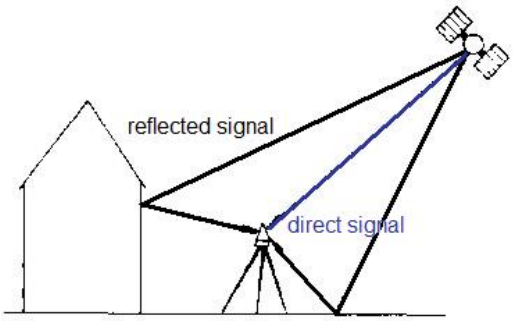

Figure 2.13: *Multipath effect.*

Multipath varies greatly depending upon a variety of factors, such as the receiver-satellite-surface geometry or the strength and the delay of the reflected signal compared to the direct one. There is not a general model of the multipath effect and therefore, it is considered one of the major limitations imposed on the accuracy of the observations. Multipath affects code observations in a higher measure than phases, reaching magnitudes of some metres. In severe cases of multipath these errors can reach up to 100 m and the loss of lock may occur (Nee, 1991).

In order to reduce the multipath effects various methods have been developed, such as the introduction of choke ring antennas (Moelker, 1997), the use of antennas that take advantage of the polarization of the signal (Aloi and van Graas, 2004), the narrow correlation spacing technology (Dierendonck and Braasch, 1997), the exploration of the SNR (Comp and Axelrad, 2002) or the smoothing of the carrier phases, among others. Beyond that, during the processing of the observations, the satellites at very low elevations must be discarded by imposing an elevation cut-off angle and the observations must also be properly weighted.

2.8.2. Cycle slips

During the observation period the GNSS signal is continuously tracked by the receiver, which includes an internal counter of the integer number of cycles of the received carrier wave. In this way, the initial ambiguities remain constant during a continuous observation period.

However, in some situations, the receiver can lose the lock of the phase lock loop, due to a low SNR, a severe multipath, strong ionospheric scintillation, very fast acceleration changes or a failure in the receiver software (Hofmann-Wellenhof et al., 2008). In these events, the counter is reinitialized causing a jump of an integer number of cycles in the instantaneous accumulated phase, which is denoted as cycle slip. In Fig. 2.14 it is observed that the phase measurements are represented by a fairly smooth curve and, in case of a cycle slip, a jump appears in the plotted curve.

After every interruption a new ambiguity should be estimated, although, in practice, it is only introduced if the pause is very long, while in the rest of the cases the cycle slip is repaired.

For the detection of the cycle slip epochs, the Melbourne-Wübbena (MW) linear combination is frequently used,

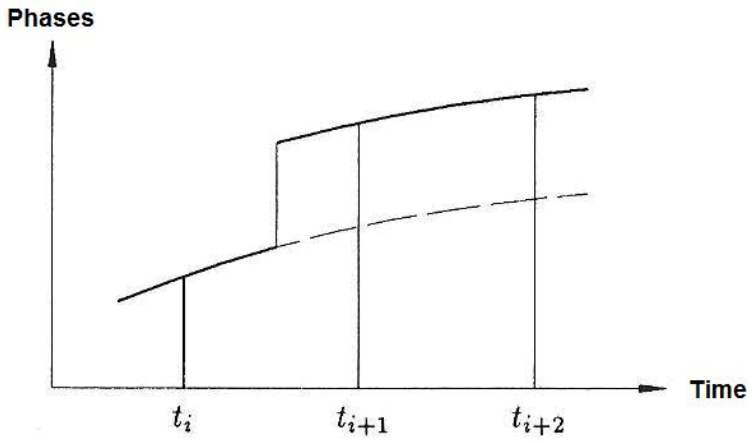

Figure 2.14: *Cycle slip schematic representation. Source: Hofmann-Wellenhof et al. (2008).*

$$L_{MW} = \frac{f_1 L_1 - f_2 L_2}{f_1 - f_2} - \frac{f_1 P_1 + f_2 P_2}{f_1 + f_2}, \tag{2.44}$$

given that most error terms in GNSS observations are canceled out. Thus, the variation in time of the MW should be random noise and, if the noise of the MW is below 0.5 widelane cycles (43 cm), then it is almost trivial to detect all cycle slips and outliers (Dach et al., 2007). However, in the unlikely case that the integer number of slips in the two frequencies are identical, no cycle slips will be detected by the analysis of the MW.

Moreover, the MW does not allow to determine which frequency contains the jump and an additional quantity must be checked. In this case, the geometry-free linear combination of phase measurements ($L_1 - L_2$) can be applied, by carefully considering the time variation of the ionospheric delay. Other recent techniques are based on analysing the variation in time of TEC, which can be estimated only from phases (Liu, 2011). The application of the Kalman filtering for cycle slip detection was also proven by Bastos and Landau (1988) and a solution based on the Bayesian approach to detect and determine the size of cycle slips in undifferenced observations was proposed by de Lacy et al. (2008b).

On the other hand, the introduction of a third frequency by the GNSS systems will facilitate the detection and repair of cycle slips. To tackle the cycle slip problem for triple-frequency GPS observations, two geometry-free phase combinations have been applied by Dai et al. (2009).

2.8.3. Receiver clock jumps

In order to compensate high clock offset drifts, most GNSS receivers introduce clock jumps periodically. As an example, Fig. 2.15 shows the clock offset of a GNSS receiver, which introduces a jump of about 1000 ms every 200 observation epochs.

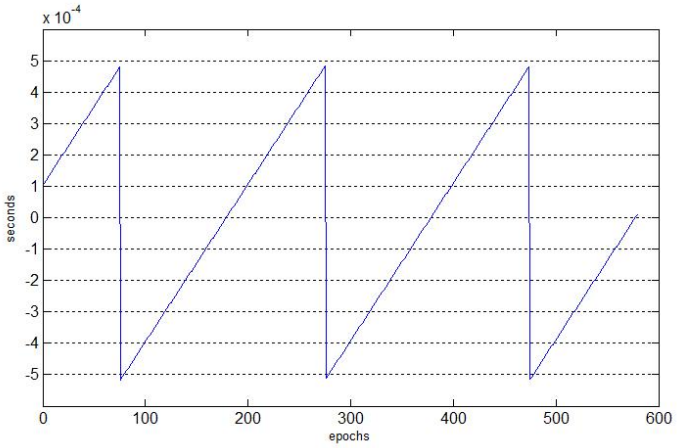

Figure 2.15: *Receiver clock offset and clock jumps.*

These clock jumps show magnitudes of an integer number of ms and affect all observables in the same way. Thus, they can not be detected with the analysis of geometry-free linear combinations, but they are observed as huge cycle slips in phase observations. In positioning techniques with undifferenced data, the receiver clock offsets do not cancel out and, therefore, correcting all clock events is mandatory, given that the errors introduced in the ranges are in the order of thousands of metres (1 ms $\approx$ 300 m).

2.8.4. Satellite eclipse periods

GNSS satellites orientation in space depends on the position of the satellite with respect to the Sun and the Earth mass center, since the satellite z-axis points towards the Earth center and the y-axis must remain perpendicular to the satellite-Sun direction, in order for the solar panels to receive the highest amount of sunlight possible. The eclipses take place when the Sun, the Earth and the satellite are collinear (Fig. 2.16). Moreover, orbit noon is defined as the point on the orbit that is closest to the Sun and orbit midnight as the point farthest from the Sun.

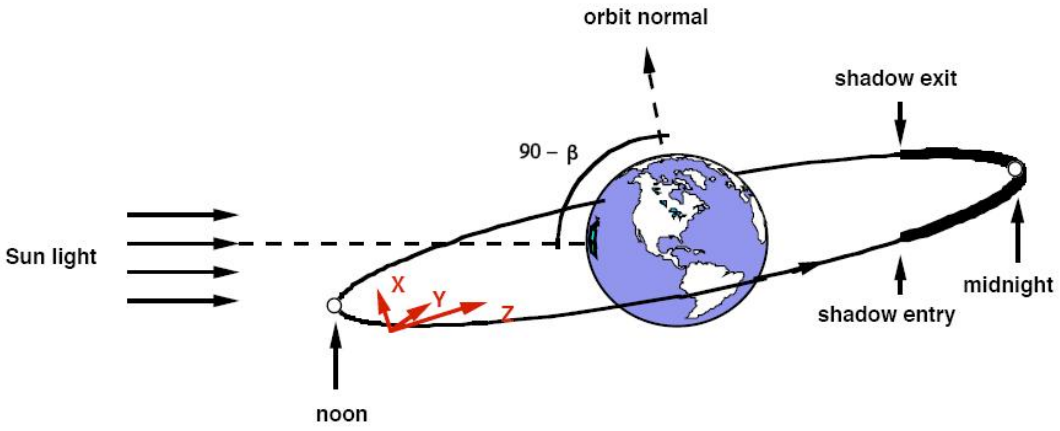

Figure 2.16: *Satellite eclipse periods, orbit noon and midnight. Source: Bar-Sever (1997).*

During the eclipse periods, the GNSS satellites can lose their orientation. The problems derived from the disorientation and reorientation of the satellites after the eclipse period are related to solar pressure modeling, determination of the antenna phase center position in space, sudden variations of the phase wind-up, etc. The largest error can exceed 10 cm and is caused by the block II/IIA antenna phase center eccentricity.

GPS block II/IIA satellites display a non-nominal attitude behavior during eclipse season, which happens during every shadow crossing and up to 45 minutes thereafter, and in the vicinity of orbit noon at low Sun angles ($\beta < 5°$) for up to 30 minutes. Typically, it takes about 1 hour to cross the Earth shadow for a block II/IIA satellite and the 45-min post-shadow recovery period cannot be accurately modeled and should be excluded from precise global GPS analyses, Bar-Sever (1996).

On the other hand, the block IIR satellites have significantly smaller errors caused by an incorrect yaw-attitude control, since they have no antenna phase center eccentricity in the x- or y-axis. Furthermore, the block IIR satellites maintain the nominal yaw attitude except for the noon and shadow midnight turn maneuvers, both of which can be controlled by using the constant hardware yaw rate of $0.20°/s$ and last up to 15 min, Kouba (2009b). The duration of the block IIR noon and midnight turns are significantly shorter than for the block II/IIA and they have no post-shadow recovery. Therefore, block IIR yaw-attitude control reduces to a noon and midnight turn maneuvers that typically last less than 15 min.

For high-precision applications it is essential that users implement a yaw-attitude model which is consistent with the generation of the satellite clocks. An improper yaw-attitude modeling can cause small errors of a few cm in position, troposphere and clock solutions, Bar-Sever (1996). A possible remedy is to delete the data of eclipsing satellites for intervals during the noon turns, shadow crossings and the subsequent recovery periods. This works well for static PPP, since it can almost instantly recover from data outages of a single satellite, Kouba (2009b).

According to Kouba (2009b), the starting time of a turn maneuver is

$$t_s = t_m - \sqrt{\beta_0|\beta| - \beta^2}/\dot{\mu} \tag{2.45}$$

where t_m is the middle time of the nominal yaw-attitude turn, β is the Sun angle with respect to the orbital plane (Fig. 2.16), β_0 represent the maximum β angle ($\beta_0 = 4.9°$ for block II/IIA and $\beta_0 = 2.4°$ for block IIR satellites) and $\dot{\mu} = 0.00836°/s$ is the average orbital angular velocity.

The Sun angle can be obtained as

$$cos(90 - \beta) = (\boldsymbol{v^s} \times \boldsymbol{u^s}) \cdot \boldsymbol{u_S} \tag{2.46}$$

where $\boldsymbol{u^s}$ and $\boldsymbol{v^s}$ are the satellite position and velocity unit vectors and $\boldsymbol{u_S}$ is the Sun position unit vector in an ECEF reference system.

For all epochs before the middle of a turn,

$$t_m = t + \sqrt{\Gamma^2 - \beta^2}/\dot{\mu} \tag{2.47}$$

and after the middle,

$$t_m = t - \sqrt{\Gamma^2 - \beta^2}/\dot{\mu} \tag{2.48}$$

where Γ is the satellite-Earth-Sun angle,

$$\Gamma = acos(\boldsymbol{u_S} \cdot \boldsymbol{u^s}), \tag{2.49}$$

which for the noon and midnight turns is β. It is not necessary to worry about noon or midnight turns of a satellite if β angle is higher that the maximum established for its block.

For shadow crossing of block II/IIA satellites a special yaw attitude model is needed. All satellites with $|\beta| < 13.5^\circ$ will experience an eclipsing period. The start and exit times are

$$t_s = t_m - \sqrt{\Gamma_{sh}^2 - \beta^2}/\dot{\mu} \tag{2.50}$$

$$t_e = t_m + \sqrt{\Gamma_{sh}^2 - \beta^2}/\dot{\mu} \tag{2.51}$$

where $\Gamma_{sh} = 13.5^\circ$. The observation period when $t_e < t < t_e + 30$ min should be discarded in precise analysis.

2.8.5. Satellite problems

The satellite problems derived from maneuver processes or satellite failures are recorded in the files *SAT_yyyy.CRX* (for GPS and GLONASS) and *GPS_yyyy.CRX* (with GLONASS deactivated), which are daily updated based on data problems or maneuvers identified in the CODE routine processing. These files must be used to avoid problems with misbehaving satellites. The observations must be treated accordingly by removing the affected observations (Dach et al., 2007). These files are available at `www.aiub.unibe.ch/download/BSWUSER50/GEN`.

2.9. Complete expression of the GNSS observables

Taking into account all error sources presented above, for a fixed GNSS receiver and satellite and for a fixed epoch, the complete expressions of the GNSS observables are

$$\begin{aligned} P_i &= \rho + c\,(dt_r - dt^s) + Trop^s + k_{1i}J_1 + c\,(B_i^s + B_{ir}) + \boldsymbol{u_{rs}} \cdot (\boldsymbol{a_i^s} - \boldsymbol{a_{ri}}) \\ &\quad + M^s + M_{ri} + \nu_{Pi} \\ L_i &= \rho + c\,(dt_r - dt^s) + Trop^s - k_{1i}J_1 + c\,(b_i^s + b_{ir}) + \boldsymbol{u_{rs}} \cdot (\boldsymbol{a_i^s} - \boldsymbol{a_{ri}}) \\ &\quad + L_{i0} + N_i\Lambda_i + m^s + m_{ri} + \nu_{Li}. \end{aligned} \tag{2.52}$$

In these expressions, P_i and L_i are the code and phase observations in the frequency f_i, expressed in distance units and for $i = 1, 2, 3, \ldots$. The geometric part is conformed by the satellite-receiver distance, ρ, the receiver and satellite clock error terms, dt_r and dt^s, and the tropospheric delay, $Trop^s$. The term $Trop^s$ includes the zenith wet and dry tropospheric delay, mapped to the receiver-satellite direction, the horizontal gradients and the correction due to the curvature of the signal. The ionospheric group delay in f_1 in a first order approximation is denoted by J_1 and $k_{1i} = (f_1/f_i)^2$. The terms B_i^s, B_{ir}, b_i^s and b_{ir} correspond to the code and phase electronic delays introduced by the receiver and the satellite at frequency f_i in seconds. The vectors $\boldsymbol{a_i^s}$ and $\boldsymbol{a_{ri}}$ represent the satellite and receiver antenna phase center eccentricities, respectively, and $\boldsymbol{u_{rs}}$ is the receiver-satellite direction unit vector in a local reference system. The values of the initial phases are denoted by L_{i0} (in meters) and the carrier phase ambiguities by N_i (in cycles), multiplied by the corresponding wave length, Λ_i. M^s, M_{ri}, m^s and m_{ri} are the code and phase multipath at the satellite and at the receiver. Finally, ν_{Pi} and ν_{Li} represent the measurement noise of code and phase observations, respectively.

The relativistic effects and phase wind-up can be reduced by means of the models shown above and, for the sake of simplicity, these terms have been excluded from (2.52).

As a summary of the effects presented above, the different error sources in the GNSS ranges and their magnitudes are shown in Tab. 2.12. The maximum values of the PCO/V corrections have been taken from the IGS05 calibration.

Effect	Magnitude (m)
Sagnac effect	≈ 23
Orbit eccentricity	≈ 15
Space curvature	< 0.018
Shapiro	< 0.02
Phase wind-up	< 0.12
Ionospheric delay	< 100
Tropospheric delay	≈ 2.23
Troposphere curvature	< 0.03
GPS satellite PCO	< 2.7
GPS satellite PCV	< 0.01
Receiver PCO	< 0.12
Receiver PCV	< 0.02
Satellite DCB	< 2
Receiver DCB	< 14

Table 2.12: *Magnitude of the different errors on GNSS ranges.*

Chapter 3

GNSS data processing in Precise Point Positioning

The position determination with GNSS techniques is generally based on the simultaneous use of various GNSS receivers, like in the relative positioning, or the reception of corrections from reference stations in real time, like in the differential positioning. These techniques can provide results at the millimetre-level accuracy for a static receiver and at centimetre-level in real-time kinematic mode (Gao et al., 2002).

However, with the transmission of two different frequencies by the GNSS satellites and the improvement in the precision of the satellite ephemeris and clocks, accurate positioning with a single receiver is now feasible after short observation periods. In fact, one of the most studied techniques nowadays is known as PPP, a single-receiver positioning technique providing precise receiver position and clock offset from undifferenced code and carrier phase observations and accurate satellite products.

Generally, PPP is able to reach a few cm-level accuracy in static positioning and decimetre-level in kinematic mode (Bisnath and Gao, 2007). It can be performed in any part of the world, being especially interesting in isolated regions as well as far offshore. Thus, due to its great operational flexibility and high-accurate results, PPP has been studied by several authors such as Kouba and Héroux (2001); Le and Tiberius (2007); Shen and Gao (2006); Mireault et al. (2008); Bisnath and Gao (2009); Geng et al. (2009); Banville et al. (2009); Moreno et al. (2009), among others. Moreover, some researchers have shown the benefits of the combined use of differential GNSS and PPP (Wübbena et al., 2005; Geng et al., 2010) and the potential of PPP to replace other positioning techniques was analysed in Ebner and Featherstone (2008).

In this chapter, the main features, achievements and limitations of the PPP technique are presented and the strategies used in the processing of the GNSS observations in PPP are also detailed.

3.1. Precise Point Positioning (PPP)

PPP is a stand-alone positioning technique aimed at estimating precise receiver position from undifferenced GNSS code and carrier phase observations and precise products. It was first introduced by Zumberge et al. (1997) for the reduction of the computational burden reached in the analysis of large GPS networks, in which station coordinates and satellite ephemeris and clocks must be estimated. However, PPP has been widely studied by several authors ever since, given that it offers great operational flexibility and provides high accuracy estimations.

Some of the first uses of PPP were the post-processing of static geodetic data, crustal deformation monitoring or precise orbit determination of Low Earth Orbit (LEO) satellites. Currently, some authors are studying the PPP capabilities in atmosphere remote sensing or precise time transfer (Orgiazzi and Tavella, 2005).

Since PPP only requires the use of one GNSS receiver and internet connection to download satellite products from the AC, it is a very cost-effective technique and can be applied in the most isolated parts of the world, far offshore and in underdeveloped countries, which do not count on GNSS permanent networks and must minimize costs. The main commercial applications of PPP so far have been in precision farming, marine applications, seafloor mapping, etc.

In the PPP process, satellite orbits and clocks are fixed and therefore, the receiver position and time are obtained in the same reference systems (Fig. 3.1). As a consecuence, the best results are obtained when precise (final) satellite products are used. Since the final products are delivered with some days delay, the most accurate PPP can be achieved in post-processing mode. There are different ACs providing GPS, GLONASS and GIOVE ephemeris and clocks, such as CODE, IGS, JPL or GPC, whose precise products present 3-6 cm accuracy (Kouba and Héroux, 2001). Nevertheless, the dissemination of precise products in increasingly shorter periods of time is improving considerably the real-time PPP capabilities (Héroux et al., 2004; Wübbena et al., 2005; Geng et al., 2010).

As it was shown in chapter 2, the largest error in GNSS ranging is due to the ionospheric refraction, which is removed to a first order approxima-

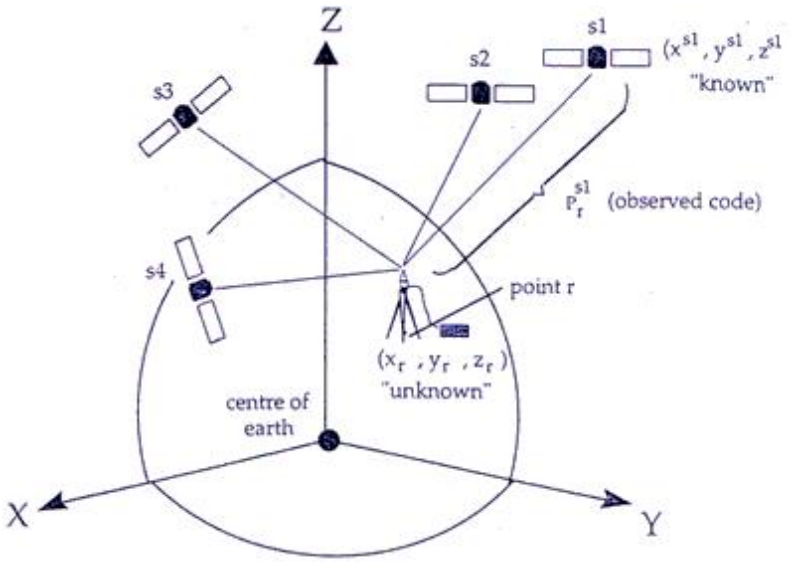

Figure 3.1: *Point position determination. In point positioning only one GNSS receiver is required and the satellite ephemeris and clocks are fixed. Source: Kumar (2001).*

tion (99%, Seeber (2003)) by forming the ionofree linear combination of dual-frequency observations (2.14). However, single-frequency receivers are cheaper than dual-frequency ones and are commonly used in georeferencing applications and precise farming. That is why, single-frequency PPP has also been studied by many authors, such as Gao et al. (2006); Keshin et al. (2006); Le and Tiberius (2007), etc. In static point positioning with single-frequency observations, Le and Tiberius (2007) confirmed the 0.5 m accuracy level in the horizontal plane and 1 m in the vertical, without depending on receiver dynamics, by using a phase-adjusted pseudorange algorithm (Teunissen, 1991), precise satellite orbits and clocks, GIMs and improved tropospheric models.

Nevertheless, in PPP the errors introduced by the satellites and the receiver in the observations do not cancel out by means of the double differences and therefore, the receiver clock offset has to be estimated at every observation epoch and the initial ambiguities are biased by satellite and receiver electronic delays and are not integer. Furthermore, accurate physical models must be applied in the correction of relativistic errors, phase wind-up and tropospheric delay and the problems derived from the satellites reorientation during and after eclipses must be accounted for. The antennas PCO/V must be corrected with consistent IGS calibration values and a correction to the tropospheric zenith delay must be estimated together with the rest of parameters, at least, every two hours. The estimation of tropospheric delay horizontal gradients can also improve the PPP estimates (Bar-Sever et al., 1998). In addition, the instrumental delays between

code observations (DCB) must be corrected, when necessary, and the use of a proper stochastic model is essential. Finally, in order to achieve high-accuracy results and to be consistent with the satellite products reference systems, the site displacements due to the effect of the Earth tide, ocean loading and pole tide must be taken into account.

Therefore, the main features of the PPP processing are:

- Undifferenced code and phase observations from a single receiver are processed.
- Precise satellite products are needed (3-5 cm accuracy).
- Dual-frequency observations are necessary to remove the ionospheric delay to a first order approximation.
- Antennas PCO/V must be corrected with consistent calibration values (IGS).
- Receiver and satellite electronic delays (DCB, IFB, ISB) must be corrected when necessary.
- Satellite problems, maneuver and eclipsing periods must be discarded.
- The receiver clock offset must be estimated at every observation epoch.
- A correction to the tropospheric zenith delay must be estimated, at least, every 2 hours.
- The initial ambiguities are estimated as real values.
- Accurate physical models for the relativistic effects, phase wind-up, tropospheric delay, Earth and pole tide and ocean loading are required.

PPP can be used in either static or kinematic mode, both in real time and in post-processing, providing different levels of accuracy. Generally, PPP is able to provide few cm-level accuracy in position estimation in static mode and dm-level in kinematic mode (Bisnath and Gao, 2007). Moreover, mm positioning accuracy can be reached with daily observations in static PPP (Geng et al., 2009). Figures 3.2 and 3.3 show some results obtained in PPP with the online program CSRS-PPP, both in static and kinematic modes. It can be observed that it takes less that 1 hour to reach the 10 cm accuracy level in static PPP, less than 2 hours to reach 5 cm and the estimations improve until the mm level is reached. In kinematic mode, CSRS-PPP uses a backward sequential filter and therefore it is not possible to observe the convergence time in Fig. 3.3, but only the accuracy reached, which is well below 30 cm in the 6 hours period.

The primary factors that limit PPP accuracy are the precision of the orbit and clock products, the effects of the unmodelled error sources and the quality of the code observations.

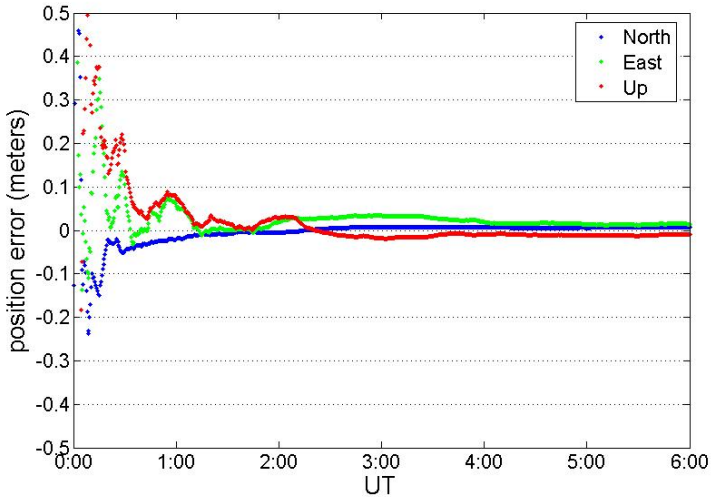

Figure 3.2: *PPP convergence time and position accuracy in static mode. Solution obtained with CSRS - PPP.*

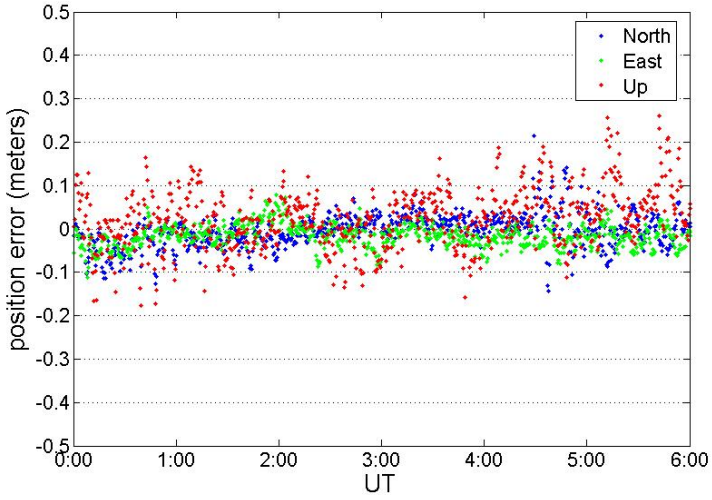

Figure 3.3: *PPP position accuracy in kinematic mode. Solution obtained with CSRS - PPP.*

The repeatability of the estimated parameters is better when a joint network adjustment is done, in which common errors are neglected by the use of double differences. In particular, the accuracy and repeatability of the east component in the PPP solution can still be improved by the use of estimated phase delays and integer ambiguity fixing (Ge et al., 2008). Moreover, the covariance matrices obtained in the PPP adjustment do not reflect the actual quality of the results, given that their nonzero elements are independent on the receiver location (Zumberge et al., 1997). In addition, the classical weighting in PPP position determination considers observations as uncorrelated with each other, when actually temporal correlations occur caused by slowly varying influences of the atmosphere and multipath, and spatial correlations exist between different satellite observations at one station (Schön and Brunner, 2006).

One of the main limiting factors of the PPP technique is the initialization time required until the carrier phase ambiguities converge to constant values. Given that ambiguities in PPP are biased by satellite and receiver hardware delays, the ambiguity resolution techniques can not benefit from their integer properties. The initial solutions rely almost exclusively on noisy pseudorange measurements, whose uncertainties are magnified via the ionofree linear combination (Bisnath and Gao, 2007). Typically, the convergence period to reach a dm-level position solution in static mode is about 30 minutes under normal conditions, taking much longer to obtain a cm-level solution (Gao and Shen, 2001). This period is determined by the number and the geometry of the visible satellites and the redundancy and quality of the observations. In this respect, signal losses of lock constitute a serious threat for PPP, given that the process must be reinitialized, resulting in tens of minutes of greater than dm error solutions. This constraint limits the utility of PPP to environments with continuous open sky coverage. The main advantages and limitations of the PPP technique are summarised in Tab. 3.1.

Advantages	Limitations
Cost-effectiveness	Required convergence time (> 30 min)
Operational flexibility	Bad repeatability of the estimations
High-accuracy results	Too optimistic precision

Table 3.1: *PPP advantages and limitations.*

However, a way to reduce the convergence time and improve the repeatability was introduced by Ge et al. (2006, 2008), who estimated the fractional part

of the uncalibrated hardware delays within a network of stations and used them as ambiguity corrections, so that initial ambiguities can be reduced to integer values. This technique also improves the estimation of the east component. Based on this method, Geng et al. (2009) has obtained a PPP positioning accuracy of 0.5 cm in the horizontal plane and 1.5 cm in the vertical direction after 1 hour observations. On the other hand, Collins et al. (2008) proposed a decoupled clock model for the GPS observations, which accelerate the convergence time to the cm-level horizontal accuracy after 1 hour or less.

3.2. Current PPP Programs

Different GNSS data processing softwares have incorporated the PPP technique with slight variations. Among them:

- **Bernese GPS software (BSW) Version 5.0** (`www.bernese.unibe.ch`), developed at the Astronomical Institute of the University of Berne (AIUB), applies a LSA for receiver position and clock offset estimation in the PPP mode (Dach et al., 2007). The PPP process provides position at cm-level accuracy, receiver clock offset, TEC information and receiver DCB in P1-P2. The main limitation of BSW PPP is that satellite clock offsets are not interpolated to the observation epochs, but used as provided, what reduces the processing to the time rate of the clock corrections file. Moreover, GLONASS observations can not be processed by BSW in PPP mode, given that the corresponding frequency dependent receiver biases are not yet considered in the processing.
- **Automatic Point Positioning Service (APPS)** (`apps.gdgps.net/apps/index.php`) is a free online service by JPL that uses GYPSI-OASIS v.5 software to compute PPP solutions (Zumberge, 1999). APPS employs JPL's final GPS orbit and clock products, possessing a User Range Error (URE) of roughly 3 cm RMS. It provides receiver position and clock offset, zenith wet tropospheric delay and gradients.
- **CSRS - PPP** (`www.geod.nrcan.gc.ca`) is an online PPP post-processing service developed at Natural Resources of Canada (NRCan). It applies a sequential filter to estimate receiver position and clock offset, tropospheric zenith delay and ionofree ambiguities (Kouba and Héroux, 2001; Mireault et al., 2008). The accuracy of the position provided by CSRS-PPP when processing 24-hours of dual-frequency observations with IGS precise products is about 0.67 cm in horizontal and 1.13 cm in vertical (Mireault et al., 2008).

- **MagicGNSS** (magicgnss.gmv.es) is the PPP online service developed by the company GMV and computes a PPP solution based on a batch least-squares algorithm. It can process GPS-only, GPS+GLONASS and GLONASS-only data. MagicGNSS includes part of the software of ODTS, used by GPC to compute GESS station coordinates and satellite orbits and clocks.

Moreover, the precise point positioning software center has been created under the auspices of the Geomatics for Informed Decisions Network of Centres of Excellence to provide a comparison between the PPP solutions obtained by the online services CSRS-PPP, APPS and MagicGNSS. This service can be accessed through gge.unb.ca/Resources/PPP/index.htm. The three online programs support both static and kinematic modes, however APPS and CSRS - PPP only can process GPS data.

3.3. Precise Satellite Products

In the PPP process, satellite orbits and clocks are fixed and, as a consecuence, the best results are obtained when precise (final) satellite products are used. There are different ACs providing GPS, GLONASS and GIOVE ephemeris and clocks, such as CODE , IGS, JPL or GPC.

The IGS is a voluntary collaboration of more than 200 contributing organizations in more than 80 countries (igscb.jpl.nasa.gov). The IGS global tracking network consists of more than 300 permanent, continuously-operating GNSS stations globally distributed, Fig. 3.4.

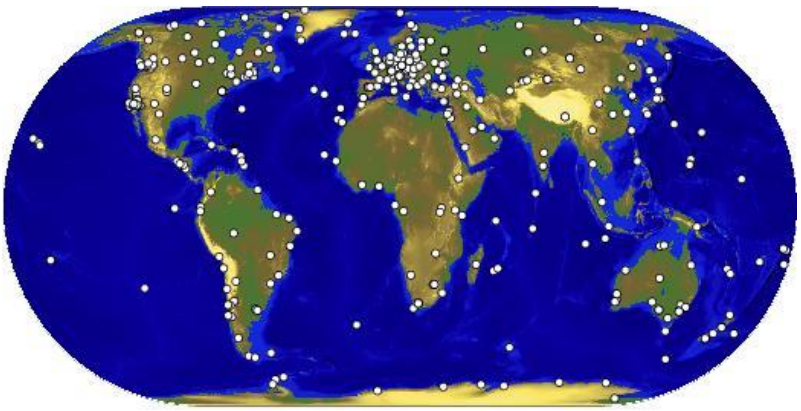

Figure 3.4: *IGS tracking network. Source: igscb.jpl.nasa.gov.*

IGS generates rapid and precise ephemeris for the satellites and clock corrections, together with Earth Orientation Parameters (EOP). Currently, up to 8

IGS ACs contribute daily Ultra-rapid, Rapid and Final GPS orbit and clock solutions to the IGS combinations. The main features of the IGS precise (final) satellite products are shown in Tab. 3.2. Accurate GNSS satellite orbit and clock solutions are obtained the latter with delays of 11 days (final products). Typical accuracies of the final products are 3 cm and 0.1 ns for orbits and clocks. GPS final orbits are given with 15 minutes sampling rate and clocks every 5 minutes, however, starting with GPS Week 1410 (January 14, 2007) the IGS final clock combinations also include additional clock files with 30 s sampling. Moreover, CODE computes satellite clocks every 5 s.

	Accuracy	Sample Interval	Latency	Updates
Orbits	2.5 cm	15 min	12 - 18 days	every Thursday
Clocks	20 ps	30 s		

Table 3.2: *IGS precise (final) satellite ephemeris and clocks characteristics. Source:* `igscb.jpl.nasa.gov`.

IGS orbits are computed in the IGS reference system, which is consistent with the current ITRF. The ITRF has been established by the International Earth Rotation Service (IERS) and is frequently updated according to the new data obtained from various geodetic observation systems, thus producing a time series of reference frames. The transformation from one reference frame to another is generally accomplished with a seven-parameter Helmert transformation. The ITRF represents the ITRS, which has an origin at the mass center of the whole Earth that takes the oceans and the atmosphere into account, it is realized by estimates of the coordinates and velocities of a set of IERS observing stations and uses International Standard (SI) metre for its length unit, defined in a local Earth frame in the meaning of a relativistic theory of gravitation (Petit and Luzum, 2010). According to the resolutions by the International Astronomical Union (IAU) and the International Union of Geodesy and Geophysics (IUGG), the orientation of the ITRS axes is consistent with that of the Bureau International de l'Heure (BIH) System at 1984.0 within ± 3 milli-arc-second (mas) and the time evolution in orientation of ITRS has no residual rotation relative to Earth's crust (Boucher and Altamimi, 1996).

In general, all AC solutions and thus, IGS combined products follow the current IERS conventions (Petit and Luzum, 2010). The only exceptions are the atmospheric and snow loading effects, which are currently neglected by all ACs in the satellite and station coordinates estimation.

Positioning and GNSS analysis that constrain or fix orbit and clock solutions need to apply consistent conventions, orbit/clock weighting and models. IGS orbit and clock products imply positioning, orientation and scale of the ITRF so that PPP solutions are directly in this reference frame. Since February 2000, when the SINEX and EOP combinations became official, all the IGS final products are also fully consistent with respect to IGS position and velocity coordinate solutions of a set of 50 reference frame stations. Moreover, the IGS precise clocks contain the ionofree linear combination of the satellite DCB in P1 and P2, which must be taken into account when other observables are used or single-frequency positioning is carried out.

On the other hand, the GPC, located at ESA/ESTEC in Noordwijk, conducts experimentation activities using GIOVE's two satellites, collecting data through the GESS data servers and computing the near real-time orbit and clock information by means of the E-OSPF, Fig. 3.5. Each GESS station integrates the GETR, the Galileo antenna (Fig. 3.6), an atomic clock and a core computer to collect GIOVE/GPS data and make them available for archiving in the DSF.

Figure 3.5: *Orbit and Synchronisation Process Facility.*

Figure 3.6: *GESS antenna and cabinet.*

Integrated in E-OSPF is the ODTS module, which determines station position, satellite orbits and clocks in a single batch least squares adjustment (Píriz, 2007). The final station position takes into account the tidal uplift due to the Earth tide and it is referred to the antenna phase center. The satellite orbits and clocks are obtained in two different processes. First, products are predicted and second, they are restituted with the values obtained in the orbit determination process. Restituted clocks (or precise) are given every 5 minutes and the orbits every 15 minutes. The GGTO is also determined by the E-OSPF, as well as stations ISB and IFB.

According to Tobías et al. (2009), the difference between the IGS and GPC orbits and clocks are typically 8 cm and 0.3 ns, which is considered quite good given the limited size and distribution of the GESS tracking network. Moreover,

the uncertainty in the estimation of the GGTO is around 2 ns. Trusted users can access the GESS observations, GPC products and reports through the website `www.giove.esa.int`.

The GPC products are given in the IGS reference frame and in the GST. In the future, the GGSP (`www.ggsp.eu/ggsp_home.html`) will provide satellite products in the GTRF and GST. The GGSP will include the generation of precise products that are needed by the advanced Galileo geodetic user community to get full access to the GTRF. These products will comprise of:

- precise Galileo satellite orbit and clock estimates,
- EOP and
- GTRF data and information for the users.

On the other hand, GNSS orbits and clocks are provided by the ACs at a nominal epoch and, as a consequence, their interpolation is needed to obtain the satellite position and clock correction at the transmission epochs. The Lagrange method can be applied in the orbits interpolation, whereas clocks can be linearly interpolated with enough accuracy.

It must also be noted that IGS satellite clocks are referred to the IGS time, and GPC clocks to the GST. Then, the correction of GGTO must be done when satellite clocks from different ACs are used in position determination.

Moreover, there is an additional offset between the GPST and the IGS realization. Its values are given by IGS in the precise clock files, along with the satellites and IGS station clock offsets. Thus, the GGTO correction for GIOVE satellite clocks is given by

$$dt^s_{IGS} = dt^s_{GPC} - GGTO + GPST. \tag{3.1}$$

3.4. Data Preprocessing

Since PPP is very sensitive to outliers, cycle slips and low quality data, it is most important to make a good preprocessing of the observations. As it was shown in section 2.8.2, the MW (2.44) may be screened for outliers and cycle slips detection, given that most terms are canceled out and the remaining ones are the widelane ambiguity,

$$\Lambda_{wl} N_{wl} = \frac{c}{f_1 - f_2}(N_1 - N_2) \tag{3.2}$$

and the noise of the linear combination. The MW standard deviation is

$$s_{MW} = \sqrt{\frac{f_1^2 \sigma_{P1}^2 + f_2^2 \sigma_{P2}^2}{f_1^2 + f_2^2}}. \tag{3.3}$$

Thus, the variation in time of the MW should be random noise with mean equal to 0 and standard deviation $\sqrt{2} s_{MW}$. If the noise of the MW is below 0.5 widelane cycles, then it is almost trivial to detect all cycle slips and outliers (Dach et al., 2007). However, in the unlikely case where the number of slips on the two frequencies are identical, no cycle slips will be detected.

In the preprocessing carried out by BSW, the MW is formed in continuous observation periods as long as possible, denoted by arcs, and the RMS of the arcs are compared against a threshold (Dach et al., 2007). If the RMS exceeds this threshold, the observation arc is screened for cycle slips. Then the initial arc is divided into two equal subintervals and their RMS are checked again. The arc with the highest RMS is assumed to contain the cycle slip and the arc splitting step is repeated until the epoch of the cycle slip is found. When all cycle slips are found, the arcs before and after the cycle slip epochs are screened for outliers, by using an outlier level 4 times the maximum RMS of the arcs. Then, the detected outliers are temporarily deleted to compute the difference between the two arcs and connect them. The RMS of the connected arc is recomputed to check whether there are more cycle slips. After the detection of all cycle slips, the observations are again screened for outliers until the RMS of the arc is below the specified maximum, typically 0.4-0.6 widelane cycles (34-52 cm). If an outlier is detected, the observations at that epoch are discarded and if cycle slips are detected and not corrected, new ambiguities must be set up.

It must taken into account that the noise in the observations increases at low elevations and, therefore, it will be more difficult to detect outliers and cycle slips for satellites at low elevations.

Sometimes the MW linear combination is not able to detect systematic errors due to the filtering of the observations by the receiver and therefore, an additional screening is needed. For that purpose, BSW analyses the difference be-

tween the ionofree linear combination of codes and phases ($L_{IF} - P_{IF}$). In this case, the residual should consist only of noise computed by

$$s = \sqrt{\frac{f_1^4 \sigma_{P1}^2 + f_2^4 \sigma_{P2}^2}{(f_1^2 - f_2^2)^2}}. \tag{3.4}$$

The disadvantage of this linear combination is the amplified noise, about 3 times the noise in P_1. When the RMS of an arc is larger than a threshold (typically 1.6-1.8 m), it is assumed that there are outliers in the arc, which is divided into two equal parts until they are located and removed.

The limitations of the RMS screening are due to the use of code observations, which implies that small outliers in the phase cannot be detected. For instance, with a typical RMS of 0.5 cycles for the MW combination, the outlier rejection level is about 160 cm. All carrier phase outliers below this level will not be detected and therefore a post-fit residual screening is highly recommended and even mandatory when undifferenced observations are used (in PPP). The post-fit residuals screening must be carried out in combination with the estimation of the parameters as an iterative process until all outliers have been found.

An additional screening of code observations may be done by forming the difference between the observed and calculated ranges, introducing satellite orbits, clocks and a priori station coordinates. Then, the receiver clock offset can be estimated at every observation epoch and the residuals analysed for outliers. If the biggest residual is smaller than a threshold, all observations at this epoch are accepted. Otherwise, the RMS of all residuals but the biggest one is computed and a limit of 4 or 5 times the new RMS is chosen to either reject the biggest residual or not.

The same screening may be performed with the phases by analysing the observed minus computed quantities. It is expected that these quantities are smooth functions of time with random errors of a few cm. This is checked by computing the variation in time of the observed minus computed values q times and analysing if such differences are zero within 3 times its RMS error. If the condition is met, all observations are accepted and if not, the last observation is marked and replace by the following one.

On the other hand, receiver clock jumps affect the observation epoch, the code and the phase measurements in the same way (section 2.8.3). The linear combinations shown above are geometry free and, therefore, they can not be used

to detect clock jumps. Instead, receiver clock jumps can be detected after differencing in time an a priori receiver clock offset estimated from undifferenced code observations. In the receiver clock estimation usually the ionofree linear combination of the codes is used (2.14), along with satellite coordinates and clocks. The station coordinates may be estimated as well and the estimations improved by an iterative process. When observations from different satellite systems are processed the offset between time systems must be also estimated. Then, the differences in time of the estimated receiver clock offset may be compared to a threshold in microseconds (1 ms $= 10^{-6}$ s). If variations larger than the threshold are found, the corresponding epochs are marked. Then, the estimated clock offset may be adjusted in short intervals before and after the possible jump epochs by means of 1^{st} or 2^{nd}-order polynomials. The differences between the polynomials evaluated at jump epochs would correspond to the jump sizes, computed as an integer number of ms. If the jump sizes are larger than the fixed threshold, the observables and the a priori clock offset are corrected by adding the jump size.

The strategies presented here for the detection of outliers, cycle slips and clock jumps have been implemented within the preprocessing part of the PCube software.

3.5. Receiver Position and Clock Offset Estimation

In addition to the outliers and cycle slips removal, the models presented in chapter 2 must be applied in order to correct the relativistic and geometrical errors. Then, the ionofree linear combination may be formed so that the ionospheric delay is removed to a first order, although other methods can be also applied, like the one proposed in this thesis. The disadvantage of the ionofree is its high noise, about 3 times the noise in P_1.

The station position and its clock offset can be determined from the ionofree observations by means of different techniques, such as a LSA or a sequential filter. In both cases, it is necessary to define a functional and a stochastic model. The functional model describes the mathematical relationship between the observations and the unknowns, while the stochastic model reflects the statistical characteristics of the observations and depends on the functional model.

3.5.1. Mathematical and stochastic models in PPP

The mathematical model for the estimation of the receiver coordinates and clock offset from the ionofree linear combination of the observables is obtained from the equations

$$\begin{aligned} P_{IF} &= \rho + c\,(dt_r - dt^s) + m_w^s ZWD + \nu_{P_{IF}} \\ L_{IF} &= \rho + c\,(dt_r - dt^s) + m_w^s ZWD + N_{IF}^s + \nu_{L_{IF}} \end{aligned} \tag{3.5}$$

for a fixed epoch, where $\rho = \sqrt{(X_r - X^s)^2 + (Y_r - Y^s)^2 + (Z_r - Z^s)^2}$ is the geometric distance, P_{IF} and L_{IF} are the ionofree combination of code and phase measurements, m_w^s is a mapping function for a correction of the tropospheric Zenith Wet Delay (ZWD) and N_{IF}^s are the ionofree ambiguities in distance units. The terms containing the electronic biases have not been considered in (3.5). The horizontal gradients of the tropospheric delay can also be added to (3.5).

Linearizing in an a priori position, $\boldsymbol{X}_0$, the mathematical model for an observation period of n epochs and n_s observed satellites can be expressed in the matrix form $A\boldsymbol{x} - \boldsymbol{y} = \boldsymbol{v}$, where

$$A = \begin{pmatrix}
\frac{-\left(X^1(t_1)-X_0\right)}{\rho_0^1(t_1)} & \frac{-\left(Y^1(t_1)-Y_0\right)}{\rho_0^1(t_1)} & \frac{-\left(Z^1(t_1)-Z_0\right)}{\rho_0^1(t_1)} & 1 & \dots & 0 & m_w^1(t_1) & 0 & \dots & 0 \\
\vdots & \vdots & \vdots & & \ddots & & \vdots & & & \\
\frac{-\left(X^1(t_n)-X_0\right)}{\rho_0^1(t_n)} & \frac{-\left(Y^1(t_n)-Y_0\right)}{\rho_0^1(t_n)} & \frac{-\left(Z^1(t_n)-Z_0\right)}{\rho_0^1(t_n)} & 0 & \dots & 1 & m_w^1(t_n) & 0 & \dots & 0 \\
\frac{-\left(X^1(t_1)-X_0\right)}{\rho_0^1(t_1)} & \frac{-\left(Y^1(t_1)-Y_0\right)}{\rho_0^1(t_1)} & \frac{-\left(Z^1(t_1)-Z_0\right)}{\rho_0^1(t_1)} & 1 & \dots & 0 & m_w^1(t_1) & 1 & \dots & 0 \\
\vdots & \vdots & \vdots & & \ddots & & \vdots & \vdots & & \\
\frac{-\left(X^1(t_n)-X_0\right)}{\rho_0^1(t_n)} & \frac{-\left(Y^1(t_n)-Y_0\right)}{\rho_0^1(t_n)} & \frac{-\left(Z^1(t_n)-Z_0\right)}{\rho_0^1(t_n)} & 0 & \dots & 1 & m_w^1(t_n) & 1 & \dots & 0 \\
 & \vdots & & & \vdots & & \vdots & & & \\
\frac{-(X^{n_s}(t_1)-X_0)}{\rho_0^{n_s}(t_1)} & \frac{-(Y^{n_s}(t_1)-Y_0)}{\rho_0^{n_s}(t_1)} & \frac{-(Z^{n_s}(t_1)-Z_0)}{\rho_0^{n_s}(t_1)} & 1 & \dots & 0 & m_w^{n_s}(t_1) & 0 & \dots & 0 \\
\vdots & \vdots & \vdots & & \ddots & & \vdots & & & \\
\frac{-(X^{n_s}(t_n)-X_0)}{\rho_0^{n_s}(t_n)} & \frac{-(Y^{n_s}(t_n)-Y_0)}{\rho_0^{n_s}(t_n)} & \frac{-(Z^{n_s}(t_n)-Z_0)}{\rho_0^{n_s}(t_n)} & 0 & \dots & 1 & m_w^{n_s}(t_n) & 0 & \dots & 0 \\
\frac{-(X^{n_s}(t_1)-X_0)}{\rho_0^{n_s}(t_1)} & \frac{-(Y^{n_s}(t_1)-Y_0)}{\rho_0^{n_s}(t_1)} & \frac{-(Z^{n_s}(t_1)-Z_0)}{\rho_0^{n_s}(t_1)} & 1 & \dots & 0 & m_w^{n_s}(t_1) & 0 & \dots & 1 \\
\vdots & \vdots & \vdots & & \ddots & & \vdots & & & \vdots \\
\frac{-(X^{n_s}(t_n)-X_0)}{\rho_0^{n_s}(t_n)} & \frac{-(Y^{n_s}(t_n)-Y_0)}{\rho_0^{n_s}(t_n)} & \frac{-(Z^{n_s}(t_n)-Z_0)}{\rho_0^{n_s}(t_n)} & 0 & \dots & 1 & m_w^{n_s}(t_n) & 0 & \dots & 1
\end{pmatrix} \tag{3.6}$$

$$\boldsymbol{y} = \begin{pmatrix} P_{IF}^1(t_1) - \rho_0^1(t_1) + cdt^1(t_1) - Trop^1(t_1) \\ \vdots \\ P_{IF}^1(t_n) - \rho_0^1(t_n) + cdt^1(t_n) - Trop^1(t_n) \\ L_{IF}^1(t_1) - \rho_0^1(t_1) + cdt^1(t_1) - Trop^1(t_1) \\ \vdots \\ L_{IF}^1(t_n) - \rho_0^1(t_n) + cdt^1(t_n) - Trop^1(t_n) \\ \\ \vdots \\ \\ P_{IF}^{n_s}(t_1) - \rho_0^{n_s}(t_1) + cdt^{n_s}(t_1) - Trop^{n_s}(t_1) \\ \vdots \\ P_{IF}^{n_s}(t_n) - \rho_0^{n_s}(t_n) + cdt^{n_s}(t_n) - Trop^{n_s}(t_n) \\ L_{IF}^{n_s}(t_1) - \rho_0^{n_s}(t_1) + cdt^{n_s}(t_1) - Trop^{n_s}(t_1) \\ \vdots \\ L_{IF}^{n_s}(t_n) - \rho_0^{n_s}(t_n) + cdt^{n_s}(t_n) - Trop^{n_s}(t_n) \end{pmatrix} \tag{3.7}$$

and

$$\boldsymbol{x} = \begin{pmatrix} \Delta X \\ \Delta Y \\ \Delta Z \\ c\Delta dt_r(t_1) \\ \vdots \\ c\Delta dt_r(t_n) \\ ZWD \\ N_{IF}^1 \\ \vdots \\ N_{IF}^{n_s} \end{pmatrix}. \tag{3.8}$$

It can be observed that a clock offset value is estimated at every epoch and the initial ambiguities have been considered constant during the whole observation period, what must be assured by correcting the cycle slips during the preprocessing. Moreover, if the period is longer than 2 hours, a new unknown for the ZWD estimation should be added.

In this model, A is the design matrix, $\boldsymbol{y}$ contains the observations corrected with the a priori distance and satellite clocks, $\boldsymbol{x}$ is the unknowns vector and $\boldsymbol{v}$ is the residuals vector. The observation noise is assumed to be Gaussian normally distributed with zero mean, i.e., $\boldsymbol{y} \approx N(A\boldsymbol{x}, C_{\boldsymbol{yy}})$, where the stochastic model of the observations is

$$C_{\boldsymbol{yy}} = \sigma_0^2 Q_{\boldsymbol{yy}}, \tag{3.9}$$

being σ_0^2 the a priori variance of unit weight and $Q_{\boldsymbol{yy}}$ the observations cofactor matrix.

For the estimation of additional parameters it is necessary to add more columns in (3.6), containing the corresponding coefficients. Thus, the ISB can be estimated by including the coefficients: 0 if observations correspond to GPS satellites, and 1 if correspond to GIOVE (or Galileo) satellites. It must be remarked that the ISB estimated in this way does not correspond to the one obtained by GPC, which is obtained as the difference between the estimated receiver IFB.

3.5.2. Least squares theory

The least squares theory provides expressions for the parameters estimation and their covariance matrix,

$$\hat{\boldsymbol{x}} = \left(A^T P A\right)^{-1} A^T P \boldsymbol{y} = N^{-1}\boldsymbol{d} \tag{3.10}$$

$$C_{\hat{\boldsymbol{x}}\hat{\boldsymbol{x}}} = \hat{\sigma}_0^2 \left(A^T P A\right)^{-1} = \hat{\sigma}_0^2 N^{-1} \tag{3.11}$$

where $P = Q_{\boldsymbol{yy}}^{-1}$ is the weight matrix and $N = A^T P A$ is the normal matrix (Sevilla, 1987). Moreover, the residuals are obtained as

$$\begin{aligned} \hat{\boldsymbol{v}} &= A\hat{\boldsymbol{x}} - \boldsymbol{y} \\ C_{\hat{\boldsymbol{v}}\hat{\boldsymbol{v}}} &= \hat{\sigma}_0^2 Q_{\hat{\boldsymbol{v}}\hat{\boldsymbol{v}}} \\ Q_{\hat{\boldsymbol{v}}\hat{\boldsymbol{v}}} &= \left(Q_{\boldsymbol{yy}} - AN^{-1}A^T\right) \end{aligned} \tag{3.12}$$

where

$$\hat{\sigma}_0^2 = \frac{\hat{\boldsymbol{v}}^T P \hat{\boldsymbol{v}}}{r - m} \tag{3.13}$$

is the a posteriori variance of unit weight, with r the number of observations and m the number of unknowns.

3.5.3. Sequential filter

In order to fasten the process, a sequential filter may be used (Kouba and Héroux, 2001). The mathematical model is given by (3.5) and the unknowns variation in time is modeled by a stochastic process, with which the covariance information is propagated from one epoch to the next. The process noise may be represented by the matrix

$$C_{\epsilon\epsilon} = \begin{pmatrix} C_\epsilon x & & & & & & & \\ & C_\epsilon y & & & & & & \\ & & C_\epsilon z & & & & & \\ & & & C_\epsilon dt_r & & & & \\ & & & & C_\epsilon ZWD & & & \\ & & & & & C_\epsilon N_{IF}^1 & & \\ & & & & & & \ddots & \\ & & & & & & & C_\epsilon N_{IF}^n \end{pmatrix} \tag{3.14}$$

where the station coordinates variation noise is given by the values $C_\epsilon x$, $C_\epsilon y$ and $C_\epsilon z$ and must be set to zero in static positioning and adapted to the receiver velocity in kinematic mode. The clock drift noise, $C_\epsilon dt_r$, may be set to 1 mm/epoch, but a better modeling of the clock offset can significantly improve the estimations. The tropospheric variation may be approximated as $C_\epsilon ZWD = 2 - 5\,\text{mm}/\sqrt{h}$ and the ambiguities variation is zero (Kouba and Héroux, 2001).

Then, the unknowns and their covariance matrices are obtained in a sequential way by means of the expressions

$$\begin{aligned}
\hat{\boldsymbol{x}}_i &= \boldsymbol{x}_{i-1} + \hat{\boldsymbol{\delta}}_i \\
\hat{\boldsymbol{\delta}}_i &= \left(P_{0i} + A_i^T P_i A_i\right)^{-1} A_i^T P_i \boldsymbol{y_i} \\
C_{\hat{\boldsymbol{x}}_i \hat{\boldsymbol{x}}_i} &= \hat{\sigma}_{0i}^2 \left(P_{0i} + A_i^T P_i A_i\right)^{-1}
\end{aligned} \tag{3.15}$$

where subscript $i-1$ refers to the previous epoch and $P_{0i} = \left(C_{\hat{\boldsymbol{x}}_{i-1}\hat{\boldsymbol{x}}_{i-1}} + C_{\epsilon\epsilon}\right)$.

Finally, the a posteriori variance of unit weight is determined by

$$\hat{\sigma}_{0i}^2 = \frac{\hat{\boldsymbol{\delta}}_i^T P_{0i} \hat{\boldsymbol{\delta}}_i + \hat{\boldsymbol{v}}_i^T P_i \hat{\boldsymbol{v}}_i}{r - m} \tag{3.16}$$

where r is the number of observations and m is the number of effective unknowns, computed as the dimension of the parameter vector $\boldsymbol{x}_i$, minus the trace of P_{0i}.

The sequential filter presented above has been implemented within the PCube software for the estimation of the receiver position, clock offset, correction to the ZWD, etc.

3.5.4. Observations weighting

The election of a proper stochastic model allows to further improve the accuracy and reliability of the positioning estimations, particularly in the up component.

The stochastic model is formed by the variance-covariance matrix of the observations, which describes the statistical properties of the GNSS observations,

$$C_{\boldsymbol{yy}} = \begin{pmatrix}
\sigma_1^2 & \sigma_{12}\sigma_1\sigma_2 & \cdots & \sigma_{1n_s}\sigma_1\sigma_{n_s} \\
\sigma_{12}\sigma_1\sigma_2 & \sigma_2^2 & \cdots & \sigma_{2n_s}\sigma_2\sigma_{n_s} \\
\vdots & \vdots & \ddots & \vdots \\
\sigma_{1n_s}\sigma_1\sigma_{n_s} & \sigma_{2n_s}\sigma_2\sigma_{n_s} & \cdots & \sigma_{n_s}^2
\end{pmatrix} \tag{3.17}$$

where σ_i is the standard deviation of the observation of satellite i and σ_{ij} is the correlation coefficient between observations of satellites i and j. The elements

in the diagonal describe the observations precision and the elements outside the diagonal, the relation between observations of different satellites.

Commonly, the observations between different epochs, satellites and stations are considered uncorrelated, thus the covariance matrix becomes diagonal, being the code pseudoranges noise about 100 times the phase observations noise,

$$C_{\boldsymbol{yy}} = \begin{pmatrix} \sigma_P^2 & & & & \\ & \sigma_L^2 & & & \\ & & \ddots & & \\ & & & \sigma_P^2 & \\ & & & & \sigma_L^2 \end{pmatrix}. \tag{3.18}$$

Nevertheless, the noise of the observations increases at low elevation angles, due to the increase of the multipath error and the atmospheric influence on the GNSS signal, and therefore, the stochastic model should take into account the satellite elevation, E_i. In this way, the covariance matrix may be

$$C_{\boldsymbol{yy}} = \begin{pmatrix} \sigma_P^2 cos^2(E_1) & & & & \\ & \sigma_L^2 cos^2(E_1) & & & \\ & & \ddots & & \\ & & & \sigma_P^2 cos^2(E_{n_s}) & \\ & & & & \sigma_L^2 cos^2(E_{n_s}) \end{pmatrix}. \tag{3.19}$$

Moreover, the SNR provided by modern GNSS receivers can be used to form the stochastic model. The SNR characterizes the quality of the received signal and its difference with the minimal reference, scaled with the maximal range, can be used in the observations weighting,

$$w = \frac{SNR - SNR^{min}}{SNR^{max} - SNR^{min}}. \tag{3.20}$$

The SNR weighting method adjusts well the observation properties, providing better weighting values than the elevation dependent one (Beckheinrich, 2008). Nevertheless, Satirapod and Wang (2000) compared the modeling tech-

niques based on SNR and satellite elevation and concluded that, in some cases, both failed to reflect the true data quality.

In addition, temporal correlations occur between observables, caused by slowly varying influences of the atmosphere and multipath, and spatial correlations occur between observations of different satellites at one station and observations of one satellite at different stations. Some stochastic modeling techniques have been proposed to accommodate the correlation between GNSS observations. The Minimum Norm Quadratic Unbiased Estimation (MINQUE) procedure was suggested by Wang et al. (1998), but it is only applicable to the static positioning. An exponential function was developed by El-Rabbany (1994) to model temporal correlations and an iterative stochastic assessment taking into account all the error features was proposed by Wang et al. (2002).

3.5.5. Statistical analysis of the residuals

The final PPP solution is obtained after the screening of the adjustment residuals, when the last outliers are detected, the corresponding observations eliminated and the unknowns estimated from cleaned observations. In order to identify the remaining outliers, different statistical tests must be applied to the residuals.

First, the global test of the mathematical model must be applied, which assures that the model used is *'correct and complete'* and, therefore, the observations are not affected by systematic errors, outliers or mismodelling errors (Sansó, 1996). This test is based on the hypothesis

$$H_0 : E\left[\hat{\sigma}_0^2\right] = \sigma_0^2 \tag{3.21}$$

where σ_0^2 is the a priori variance and $\hat{\sigma}_0^2$ is the a posteriori variance obtained in the adjustment. If H_0 is true, the estimator

$$T = (r - m)\frac{\hat{\sigma}_0^2}{\sigma_0^2} \tag{3.22}$$

follows a χ^2_{r-m} distribution, with r the number of observations and m the number of unknowns.

Providing that the global test is not passed, the existence of possible systematic errors is checked by means of a second statistical test. In this case, the null hypothesis is

$$H_0 : \bar{u} = 0 \tag{3.23}$$

where $\bar{u}$ is the mean value of the typified residuals,

$$u_i = \frac{v_i}{\sigma_0 \sqrt{q_i}}. \tag{3.24}$$

for $i = 1, \ldots, r$, being v_i the residuals obtained in the adjustment and q_i the diagonal elements of the residuals cofactor matrix, $Q_{\hat{v}\hat{v}}$. Then, the estimator used is

$$T = \frac{\bar{u}}{\sigma_u} \tag{3.25}$$

which follows a t_{r-1} distribution if H_0 is true, being σ_u the residuals standard deviation. If this test is passed, it is assumed that there are not systematic errors and the existence of outliers must be checked. In this case, the null hypothesis is

$$H_0 : E[u_i] = 0 \quad i = 1, \ldots, r. \tag{3.26}$$

If σ_0 is known, the Baarda test (Baarda, 1968) can be used to check for high values among the residuals, which could correspond to outliers. It is based on that the typified residuals (3.24) follow a $N(0, 1)$ distribution if (3.26) is true. In case that the Baarda test is not passed, the observation with the largest typified residual is removed and the adjustement is performed once more. If now the global test is fullfiled, the identified observation could be an outlier and, if it is not, the observation with the second largest typified residual is moved out this time. This process is repeated until either all residuals that did not pass the Baarda test are removed one by one or the global test is fulfilled.

On the other hand, if σ_0 is not known, the Pope test is then applied (Pope, 1976). In this case, $\hat{\sigma}_0$ is used in (3.24), which now follow a τ distribution with $r - m$ degrees of freedom.

Given that it is not worth eliminating observations if they are not really outliers, to finally corroborate that the detected outlier is actually an outlier a last test is checked. In this case, the null hypothesis is that *'the possible outlier is not an outlier'* and the estimator used is

$$W_0 = y_0 - A_0 \hat{x}_{r-1} \tag{3.27}$$

where y_0 is the identified observation, A_0 is the row of the design matrix A corresponding to y_0 and $\hat{x}_{r-1}$ is the estimation obtained from the other $r - 1$ observations. W_0 follows a Normal distribution with zero mean and $\sigma^2(W_0) = \sigma_0^2 \left(Q_{y_0 y_0} + A_0 N_{r-1}^{-1} A_0^t\right)$, being $Q_{y_0 y_0}$ the variance of y_0 and N_{r-1}^{-1} the inverse of the normal matrix obtained from the $r - 1$ observation equations.

However, it can happen that neither outliers nor systematic errors are identified and the global test of the model is not fullfiled, what can be due to that the observations precision has been overestimated. This is common in GNSS data processing, since the stochastic model only considers the receiver noise, assumed to be in the order of cm for the codes and of mm for the phases, weighted with the satellite elevation. However, this model is not realistic enough due to the large multipath errors, the mismodelling in the ionospheric and tropospheric delays correction and the spatial and temporal correlations existent between the observations.

3.6. Site Displacement Corrections

The effects of the solid Earth tide, pole tide and ocean loading can reach a few dm and have to be considered in the PPP processing (Kouba and Héroux, 2001). The needed corrections must be taken from the last IERS conventions (Petit and Luzum, 2010), given that the reference systems and procedures of the IERS are based on the resolutions of international scientific unions. The physical models for the correction of the site displacements due to the Earth and pole tide and ocean loading are presented in the following. Such models allow to reach few mm-level accuracy in the position determination in PPP and have been implemented within the PCube software.

3.6.1. Earth tide

The Earth tides are similar to ocean tides, however the latter are strongly affected by coastal geography and ocean topography. There are four measurable Earth tide constituents, large enough for geodetic consideration: the lunar diurnal, the lunar semidiurnal, the solar diurnal and the solar semidiurnal tides. Diurnal tides have a period of about 1-day (24 hours and 50 minutes) whereas semidiurnal tides are about half a day (12 hours and 25 minutes).

The periodic vertical and horizontal site displacements caused by tides are represented by spherical harmonics of degree and order (n, m), characterized by the Love and Shida numbers, h_{nm} and l_{nm}. The effective values of these numbers depend on station latitude (ϕ) and tidal frequency (Wahr, 1981).

The computation of the position variations due to solid Earth tides is done by means of the expression in the time domain for the full degree 2 and 3 tidal potential and nominal values for the Love and Shida numbers.

Thus, the site displacement vector in Cartesian coordinates, $\Delta\mathbf{r}$, due to second degree tides is

$$\Delta\boldsymbol{r} = \sum_{j=2}^{3} \frac{GM_j R_e^4}{GM_e R_j^3} \left\{ h_2 \boldsymbol{r} \left(\frac{3}{2} \left(\boldsymbol{R_j} \cdot \boldsymbol{r} \right)^2 - \frac{1}{2} \right) + 3 l_2 \left(\boldsymbol{R_j} \cdot \boldsymbol{r} \right) \left(\boldsymbol{R_j} - \left(\boldsymbol{R_j} \cdot \boldsymbol{r} \right) \boldsymbol{r} \right) \right\} \quad (3.28)$$

where GM_j are the gravitational parameters for the Moon ($j = 2$) and the Sun ($j = 3$), GM_e is the gravitational parameter of the Earth, $\boldsymbol{R_j}$, R_j are the unit vector and the magnitude of the geocentric Moon and Sun position, R_e is the Earth's equatorial radius, $\boldsymbol{r}$, r are the unit vector and the magnitude of the geocentric station position (Petit and Luzum, 2010). Moreover, h_2 and l_2 are the nominal values of the Love and Shida numbers of degree 2, computed as

$$\begin{aligned} h_2 &= h^{(0)} + h^{(2)}(\tfrac{3}{2} sin^2\phi - \tfrac{1}{2}) \\ l_2 &= l^{(0)} + l^{(2)}(\tfrac{3}{2} sin^2\phi - \tfrac{1}{2}) \end{aligned} \quad (3.29)$$

where

$$\begin{aligned} h^{(0)} &= 0.6078 \quad & l^{(0)} &= 0.0847 \\ h^{(2)} &= -0.0006 \quad & l^{(2)} &= 0.0002. \end{aligned} \quad (3.30)$$

Note that the part proportional to h_2 gives the radial component of the tide-induced displacement and the terms in l_2 give the perpendicular displacement. The tidal correction can reach up to 30 cm in the radial and 5 cm in the horizontal directions.

Similarly, the displacement vector due to degree 3 tides is then given by

$$\begin{aligned}\Delta \boldsymbol{r} = \sum_{j=2}^{3} \frac{GM_j R_e^5}{GM_e R_j^4} \Big\{ & h_3 \boldsymbol{r} \left(\frac{5}{2} \left(\boldsymbol{R_j} \cdot \boldsymbol{r} \right)^3 - \frac{3}{2} \left(\boldsymbol{R_j} \cdot \boldsymbol{r} \right) \right) \\ & + l_3 \left(\frac{15}{2} \left(\boldsymbol{R_j} \cdot \boldsymbol{r} \right)^2 - \frac{3}{2} \right) \left[\boldsymbol{R_j} - \left(\boldsymbol{R_j} \cdot \boldsymbol{r} \right) \boldsymbol{r} \right] \Big\}\end{aligned} \tag{3.31}$$

The Love numbers of the degree 3 tides may be taken as real and constant,

$$h_3 = 0.292 \quad l_3 = 0.015. \tag{3.32}$$

The radial part of this displacement can reach 1.7 mm. Additional corrections due to the contributions of the $l^{(1)}$ term to the transverse displacement caused by the diurnal and semidiurnal tides must be applied, which can reach up to 1 mm. Moreover, the error introduced by neglecting the imaginary parts of $h_{2m}^{(0)}$ and $l_{2m}^{(0)}$ due to mantle anelasticity, ocean tidal loading and centrifugal perturbations due to the Nearly Diurnal Free Wobble resonance must be taken into account. In addition, corrections to the results obtained above are needed to take account of the frequency-dependent deviations of the Love and Shida numbers from their respective nominal values, and also to compute the out-of-phase contributions from the zonal tides. The needed expressions are given in Petit and Luzum (2010).

The tidal model described here in principle contains a time-independent part so that the coordinates obtained by taking into account this model will be *'conventional tide free'*.

The University of Bern generates plots of Earth tides vertical displacements by following McCarthy (1989) (`www.aiub.unibe.ch/content/services/earth_tides/index_eng.html`). As an example, the vertical displacement in the IGS station CHPI during day 120 of 2010 is shown in Fig. 3.7.

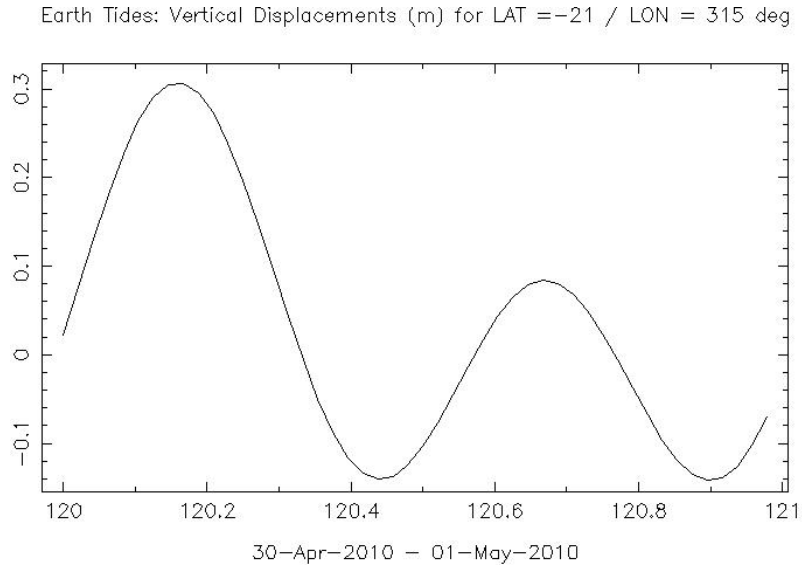

Figure 3.7: *Vertical displacement in CHPI during day 120, 2010 due to the Solid Earth Tide computed by the University of Bern. Source:* `www.aiub.unibe.ch/content/services/earth_tides/index_eng.html`.

3.6.2. Ocean loading

The Ocean loading tide is the deformation of the sea floor and adjacent land responding to the redistribution of seawater due to the ocean tide. The pure ocean tide can primarily be measured by using tide gauges, whereas altimeters measure the sum of ocean, loading and Earth body tides.

Ocean tide loading is the largest perturbation in the solid Earth tide predictions. Both amplitude and phase of ocean loading effects are heavily station and frequency dependent and can reach 100 mm (Petit and Luzum, 2010), where the vertical displacement is approximately three times larger than the horizontal components.

A site displacement component Δc (radial, west, south) at time t can be written as

$$\Delta c = \sum_{j=1}^{11} A_{cj} cos(\chi_j(t) - \Phi_{cj}) \tag{3.33}$$

where $\chi_j(t)$ is the astronomical argument of the tidal wave component j, which can be evaluated directly with the routine ARG2.f, available at `ftp://maia.usno.navy.mil/conventions/chapter7`. The station specific am-

plitudes A_{cj} and phases Φ_{cj}, for the radial, south (positive) and west (positive) directions are computed by convolution of the Green functions from global ocean tide models, such as FES2004, GOT00.2, CSR4.0, etc, as well as a refined coastline database. The use of the most recent of these models is recommended. These coefficients can be obtained electronically through the ocean loading service at `froste.oso.chalmers.se/loading`.

With the introduction of the ITRF2005 a mean geocenter was adopted, which includes the geocenter variations. This new convention, after counting for all the loading effects, provides an ITRF realization of stable station positions at the mm level. The geocenter movements are included in the ocean loading effect and its correction is mandatory in the GNSS data processing for all stations, even those far from the coast.

The current IGS convention requires that sub-daily center of mass is included in ocean loading corrections when generating IGS orbits and clocks. Consequently, when using IGS products directly in ITRF, like in PPP, the ocean loading correction to the estimated position should be done with the FES2004 model without the center of mass (Gendt, 2006).

3.6.3. Pole tide

The variation of the Earth's spin axis with respect to the crust is known as pole tide and causes periodical station position deformations due to small changes in the Earth centrifugal potential. The motion of the Earth rotation axis relative to the crust is represented by the EOP, X_p and Y_p. In the terrestrial frame, the equatorial coordinates of the pole are X_p and $-Y_p$. The pole tide has two major components: (i) a free oscillation with period about 435 days (Chandler wobble) and (ii) an annual oscillation forced by the seasonal displacement of air and water masses beating which each other (`www.iers.org`). The position of the Earth pole over the period 2001-2006 is shown in Fig. 3.8.

Using the second degree Love numbers, the corrections to the latitude, longitude (+east) and height, in mm, are given by

$$\begin{aligned} \Delta\phi &= -9\ \cos 2\phi(m_1\ \cos\lambda + m_2\ \sin\lambda) \\ \Delta\lambda &= \ 9\ \cos\ \phi(m_1\ \sin\lambda - m_2\ \cos\lambda) \\ \Delta h &= -33\ \sin 2\phi(m_1\ \cos\lambda + m_2\ \sin\lambda) \end{aligned} \tag{3.34}$$

where

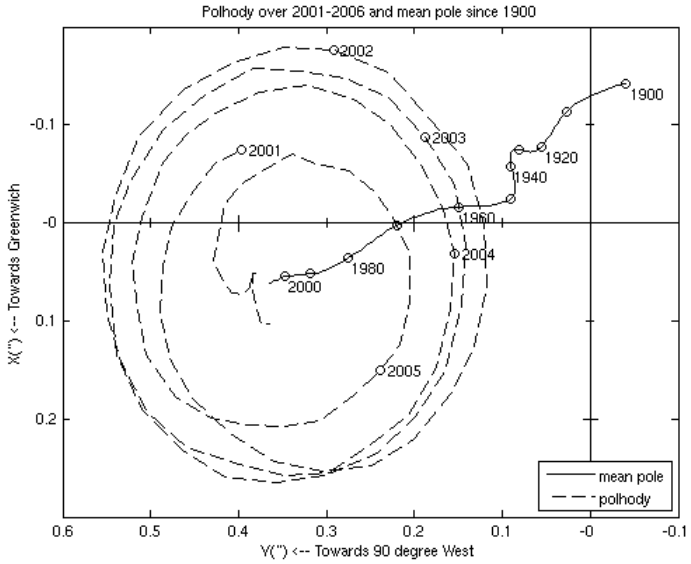

Figure 3.8: *Polar motion over the period 2001-2006. Solid line: mean pole displacement 1900-2006. Source:* `www.iers.org`.

$$m_1 = X_p - \bar{x}_p, \quad m_2 = -(Y_p - \bar{y}_p). \tag{3.35}$$

The pole position coordinates, X_p and Y_p, are given in arcseconds. The current version of the conventional mean pole is composed of a cubic model valid over the period 1976.0-2010.0 and a linear model for extrapolation after 2010.0,

$$\bar{x}_p(t) = \sum_{i=0}^{3} (t - t_0)^i \bar{x}_p^i \quad \bar{y}_p(t) = \sum_{i=0}^{3} (t - t_0)^i \bar{y}_p^i \tag{3.36}$$

where $t_0 = 2000.0$ and the coefficients $\bar{x}_p^i$ and $\bar{y}_p^i$ are given in Tab. 3.3 (Petit and Luzum, 2010).

	Until 2010.0		After 2010.0	
Degree i	$\bar{x}_p^i$	$\bar{y}_p^i$	$\bar{x}_p^i$	$\bar{y}_p^i$
0	55.974	346.346	23.513	358.891
1	1.8243	1.7896	7.6141	-0.6287
2	0.18413	-0.10729	0.0	0.0
3	0.007024	-0.000908	0.0	0.0

Table 3.3: *IERS (2010) coefficients of the mean pole model in mas/yr^i. Source: Petit and Luzum (2010).*

Most ACs are utilizing this correction when generating their orbit/clock solutions. Therefore, the above corrections must be subtracted from the solution to be consistent with ITRF.

The maximum displacement due to the pole tide can reach about 25 mm in the height and 7 mm in the horizontal direction. If X, Y and Z are the cartesian coordinates of a station in a right-handed equatorial coordinate system, their variation due to polar motion is computed as

$$[dX, dY, dZ]^T = R^T[\Delta\phi, \Delta\lambda, \Delta h]^T \tag{3.37}$$

where

$$R = \begin{pmatrix} \cos\phi\cos\lambda & \cos\phi\sin\lambda & -\sin\phi \\ -\sin\lambda & \cos\lambda & 0 \\ \sin\phi\cos\lambda & \sin\phi\sin\lambda & \cos\phi \end{pmatrix}. \tag{3.38}$$

3.6.4. Earth Orientation Parameters (EOP) variation

IGS precise products are given in the ECEF reference system ITRF, however many GNSS softwares compute satellite coordinates by propagating the orbit in an inertial reference system. The parameters required for the transformation between reference systems are the EOP, i.e., the pole position (X_p, Y_p) and $UT1 - UTC$, along with conventions for sidereal time, precession and nutation.

Some ACs do not employ the sub-daily EOP in the computation of the satellite orbits and clocks and, in order to be consistent, the users of such orbits must have it into account, especially when processing observation periods much shorter than 24 hours or when the tropospheric delay or the clock offset are required with significant accuracy.

According to Kouba and Héroux (2001), the needed corrections to the conventional ITRF coordinates evaluated from the instantaneous sub-daily EOP corrections are

$$\begin{aligned} \delta x &= \ y\delta UT1 + z\delta X_p \\ \delta y &= -x\delta UT1 - z\delta Y_p \\ \delta z &= -x\delta X_p + y\delta Y_p. \end{aligned} \tag{3.39}$$

However, GNSS users fixing IGS orbits and working directly in ITRF do not need to worry about EOP, since the IGS orbits are derived with the complete EOP, so that no sub-daily EOP is required in ITRF (Kouba, 2009a).

3.6.5. Other effects

In addition to the effects described above, Petit and Luzum (2010) propose models and corrections for the displacements due to the diurnal and semidiurnal atmospheric pressure loading and the loading caused by the ocean pole tide.

The diurnal heating of the atmosphere causes surface pressure oscillations at diurnal, semidiurnal and higher harmonics, which induce periodic motions of the Earth's surface. The amplitude of such displacements can reach up to 15 mm in the radial direction and the horizontal deformations are a factor of 10 smaller in amplitude (Ray and Ponte, 2003).

On the other hand, the ocean pole tide is generated by the centrifugal effect of polar motion on the oceans, dominated by the 14-month Chandler wobble and annual variations. The load deformation is typically no larger than about 1.8 mm in the radial direction and 0.5 mm in the horizontal component, but it may occasionally be larger. The IERS recommends the use of the model by Desai (2002) to correct this effect.

However, the GNSS ACs do not include corrections for these effects in their routine generation of the satellite products. Other surface loads due to changes in the snow and ice cover, soil moisture and groundwater, as well as ocean-bottom pressure also contribute to surface displacements. However, no sufficient models for these phenomena exist at this time.

Chapter 4

Multi-frequency Algorithms for PPP: MAP3

The state of the art of the PPP, its main features and limitations were presented in the previous chapter, as well as some techniques used in the PPP data processing and the physical models needed to reach the mm-level accuracy. The classical PPP strategy is based on applying either a LSA or a sequential filter to the ionofree linear combination of dual-frequency code and phase observations, in order to estimate the receiver position and its clock offset.

However, the characteristics of the future GNSS scenario will enable to optimise the PPP technique in several aspects. In particular, the combined use of GPS and Galileo multi-frequency signals will increase largerly the redundancy of observations and a higher number of visible satellites will optimise the configuration geometry. Moreover, more frequencies will enable to estimate the ionospheric delay to a second order without recursing to the ionofree linear combination, which increases the noise of the observations approximately three times. The new linear combinations will fasten the ambiguity resolution techniques and improve the detection and correction of cycle slips. As it is shown in Cai and Gao (2007), the combination of GPS and GLONASS in PPP greatly improves position accuracy and time convergence, and Shen and Gao (2006) proved that the combined use of modernized GPS and Galileo systems can reduce the convergence time in PPP in more than half compared to the GPS alone system.

For the time being, the existing PPP softwares only are able to process GPS and GLONASS dual-frequency observations and, therefore, further research is needed in order to develop new PPP algorithms ready to work with the future multi-frequency observations from the arriving satellite systems.

In this work, a new and original PPP strategy able to process multi-system, multi-frequency GNSS observations and determine precise position in static

mode has been developed. The new approach is based on the model for undifferenced GNSS observations proposed by Euler and Goad (1991) and, in the design of the algorithms, the least squares theory has been applied twice to obtain explicit expressions for the ionospheric delay, initial carrier phase ambiguities and smoothed pseudodistances estimation, in first place, and finally to recover the receiver position and its clock offset.

The new multi-frequency algorithms have been called MAP3 and have been integrated within a PPP software, known as PCube. In this chapter, the MAP3 algorithms are introduced.

4.1. The Euler-Goad model

The GNSS observables depend on the satellite-receiver distance, atmospheric effects, satellite and receiver offsets and phase ambiguities, as well as satellite and receiver equipment delays (2.52). Euler and Goad (1991) assumed some approximations in the general model of the GPS observables in order to express them in a more suitable form. Taking these simplifications into account, the mathematical model of undifferenced carrier phase and pseudorange observables for a fixed epoch, t, is

$$\begin{aligned} P_i(t) &= \tilde{\rho}(t) + k_{1i} J_1(t) + \nu_{P_i} \\ L_i(t) &= \tilde{\rho}(t) - k_{1i} J_1(t) + \beta_i + \nu_{L_i} \end{aligned} \tag{4.1}$$

where subscript $i = 1, 2$ denotes the frequency, the geometric part

$$\tilde{\rho}(t) = \rho(t) + c\,(dt_r(t) - dt^s(t)) + Trop(t) \tag{4.2}$$

is conformed by the satellite-receiver geometric distance $\rho(t)$, the receiver and satellite clock terms $dt_r(t)$ and $dt^s(t)$, and the tropospheric delay $Trop(t)$. The term β_i corresponds to the carrier phase initial ambiguity in the frequency f_i, in metres, biased by receiver and satellite initialization constants and therefore, not integer,

$$\beta_i = L_{i0} + N_i \Lambda_i. \tag{4.3}$$

The electronic delays were not considered in Euler and Goad (1991). The antennas PCO/V can be corrected according to section 2.5 and the multipath is assumed to be included in the noise terms, ν_{P_i} and ν_{L_i}.

Then, the mathematical model (4.1) can be written in matrix form as

$$\begin{aligned} \boldsymbol{P}(t) &= A_1\boldsymbol{\xi}(t) + \boldsymbol{\nu_P} \\ \boldsymbol{L}(t) &= A_2\boldsymbol{\xi}(t) + \boldsymbol{\beta} + \boldsymbol{\nu_L} \end{aligned} \tag{4.4}$$

where

$$\boldsymbol{P}(t) = \begin{pmatrix} P_1(t) \\ P_2(t) \end{pmatrix} \quad \boldsymbol{L}(t) = \begin{pmatrix} L_1(t) \\ L_2(t) \end{pmatrix} \tag{4.5}$$

$$A_1 = \begin{pmatrix} 1 & 1 \\ 1 & k_{12} \end{pmatrix} A_2 = \begin{pmatrix} 1 & -1 \\ 1 & -k_{12} \end{pmatrix} \tag{4.6}$$

and

$$\boldsymbol{\beta} = \begin{pmatrix} \beta_1 \\ \beta_2 \end{pmatrix} \quad \boldsymbol{\xi}(t) = \begin{pmatrix} \tilde{\rho}(t) \\ J_1(t) \end{pmatrix} \tag{4.7}$$

contain the unknowns to be estimated. These expressions are valid only if carrier phase observations are free of cycle slips and, therefore, initial ambiguities are constant during the whole observation period.

Thus, the unknown parameters are:

1. the carrier phase initial ambiguity at every frequency, β_1 and β_2, which are constant over the observation period, and
2. the smoothed pseudorange and ionospheric delay at every epoch, $\tilde{\rho}(t)$ and $J_1(t)$.

On the other hand, the stochastic model can be formed as

$$C = \sigma_0^2 \begin{pmatrix} Q_P & 0 \\ 0 & Q_L \end{pmatrix} \tag{4.8}$$

where Q_P and Q_L are the cofactor matrix of the code and phase measurements, respectively, and σ_0^2 represents the a priori variance of unit weight. By hypothesis, it is considered that (4.8) is diagonal and the standard deviations for the carrier phase and pseudorange observations are at the order of millimetres and decimetres, respectively.

Euler and Goad (1991) applied a sequential Bayes filter to (4.4) in order to determine the relative coordinates of a moving receiver. However, this approach can be used for relative and absolute positioning and does not depend on the receiver kinematics.

4.2. MAP3 1. Smoothed Pseudodistances, Ionospheric Delay and Carrier Phase Ambiguities Estimation

The Euler-Goad model presented above can be applied in a multi-frequency scenario by adding more observations, i.e.,

$$\boldsymbol{P}(t) = \begin{pmatrix} P_1(t) \\ P_2(t) \\ P_3(t) \end{pmatrix} \quad \boldsymbol{L}(t) = \begin{pmatrix} L_1(t) \\ L_2(t) \\ L_3(t) \end{pmatrix}, \tag{4.9}$$

$$A_1 = \begin{pmatrix} 1 & 1 \\ 1 & k_{12} \\ 1 & k_{13} \end{pmatrix} A_2 = \begin{pmatrix} 1 & -1 \\ 1 & -k_{12} \\ 1 & -k_{13} \end{pmatrix} \tag{4.10}$$

and

$$\boldsymbol{\beta} = \begin{pmatrix} \beta_1 \\ \beta_2 \\ \beta_3 \end{pmatrix} \quad \boldsymbol{\xi}(t) = \begin{pmatrix} \tilde{\rho}(t) \\ J_1(t) \end{pmatrix}. \tag{4.11}$$

Then, for an observation period of n_t epochs, the design matrix may be formed as

$$A = \begin{pmatrix} A_1 & 0 & \dots & & 0 \\ A_2 & 0 & & & I_3 \\ 0 & A_1 & & & 0 \\ 0 & A_2 & & & I_3 \\ \vdots & & \ddots & & \vdots \\ & & & A_1 & 0 \\ 0 & & & A_2 & I_3 \end{pmatrix}, \tag{4.12}$$

the observation vector is

$$\boldsymbol{y} = \begin{pmatrix} \boldsymbol{P}(t_1) \\ \boldsymbol{L}(t_1) \\ \boldsymbol{P}(t_2) \\ \boldsymbol{L}(t_2) \\ \vdots \\ \boldsymbol{P}(t_{n_t}) \\ \boldsymbol{L}(t_{n_t}) \end{pmatrix} \tag{4.13}$$

and the stochastic model,

$$C_{\boldsymbol{yy}} = \sigma_0^2 \begin{pmatrix} Q_P & & & & & & \\ & Q_L & & & & & \\ & & Q_P & & & & \\ & & & Q_L & & & \\ & & & & \ddots & & \\ & & & & & Q_P & \\ & & & & & & Q_L \end{pmatrix} = \sigma_0^2 Q_{\boldsymbol{yy}}. \tag{4.14}$$

It is also considered that the covariance matrix of the observations, $C_{\boldsymbol{yy}}$, is diagonal and the standard deviations of the carrier phase measurements and pseudoranges are of the order of millimetres and decimetres, respectively. In spite of this hypothesis, it is important to remember that some receivers filter the observations in order to reduce the measurement noise and this procedure causes correlations between the observables (Bona, 2000). For the time being, the same noise is considered for all satellites and all observation epochs, what is not realistic and must be improved by means of the introduction of an elevation weighting scheme.

Then, applying the least squares theory (section 3.5.1), explicit expressions for the parameters estimation and their covariance matrices can be obtained. Thus,

$$\begin{pmatrix} \hat{\boldsymbol{\xi}}(t_1) \\ \hat{\boldsymbol{\xi}}(t_2) \\ \vdots \\ \hat{\boldsymbol{\xi}}(t_{n_t}) \\ \hat{\boldsymbol{\beta}} \end{pmatrix} = \bar{N}^{-1}\boldsymbol{d} \tag{4.15}$$

where

$$\bar{N} = A^T Q_{\boldsymbol{yy}}^{-1} A = \begin{pmatrix} N & & & & A_2^T Q_L^{-1} \\ & N & & & A_2^T Q_L^{-1} \\ & & \ddots & & \vdots \\ & & & N & A_2^T Q_L^{-1} \\ Q_L^{-1}A_2 & Q_L^{-1}A_2 & \dots & Q_L^{-1}A_2 & n_t Q_L^{-1} \end{pmatrix} \tag{4.16}$$

is the normal matrix, $N = A_1^T Q_P^{-1} A_1 + A_2^T Q_L^{-1} A_2 = M + A_2^T Q_L^{-1} A_2$ is a 2×2 matrix and

$$\boldsymbol{d} = \begin{pmatrix} A_1^T Q_P^{-1} \boldsymbol{P}(t_1) + A_2^T Q_L^{-1} \boldsymbol{L}(t_1) \\ A_1^T Q_P^{-1} \boldsymbol{P}(t_2) + A_2^T Q_L^{-1} \boldsymbol{L}(t_2) \\ \vdots \\ A_1^T Q_P^{-1} \boldsymbol{P}(t_{n_t}) + A_2^T Q_L^{-1} \boldsymbol{L}(t_{n_t}) \\ Q_L^{-1} \sum_{i=1}^{n_t} \boldsymbol{L}(t_i) \end{pmatrix}. \tag{4.17}$$

N^{-1} always exists and presents the form (Koch, 1999)

$$N^{-1} = M^{-1} - M^{-1} A_2^T Q_L^{-1} \left(I_3 + A_2 M^{-1} A_2^T Q_L^{-1} \right)^{-1} A_2 M^{-1}. \tag{4.18}$$

In order to invert (4.16), it is expressed as a block matrix,

$$\bar{N} = \begin{pmatrix} \tilde{N} & E \\ E^T & F \end{pmatrix}, \tag{4.19}$$

where

$$\tilde{N} = \begin{pmatrix} N & & & \\ & N & & \\ & & \ddots & \\ & & & N \end{pmatrix}, \tag{4.20}$$

$$E = \begin{pmatrix} A_2^T Q_L^{-1} \\ A_2^T Q_L^{-1} \\ \vdots \\ A_2^T Q_L^{-1} \end{pmatrix} \tag{4.21}$$

and

$$F = n_t Q_L^{-1}. \tag{4.22}$$

Taking into account that the inverse of a block matrix is another block matrix (Koch, 1999),

$$\bar{N}^{-1} = \begin{pmatrix} \Gamma & \Delta \\ \Delta^T & \gamma \end{pmatrix}, \tag{4.23}$$

the equation system

$$\begin{cases} \tilde{N}\Gamma + E\Delta^T = I_{2n_t} \\ \tilde{N}\Delta + E\gamma = 0 \\ E^T\Delta + F\gamma = I_3 \end{cases} \tag{4.24}$$

is obtained. Then, from the second equation we know that

$$\Delta = -\tilde{N}^{-1}E\gamma, \tag{4.25}$$

substituting (4.25) into the third equation and operating

$$\gamma = \left(F - E^T\tilde{N}^{-1}E\right)^{-1} \tag{4.26}$$

is obtained and, from the first equation,

$$\Gamma = \tilde{N}^{-1}\left(I_{2n_t} - E\Delta^T\right). \tag{4.27}$$

Then, substituting (4.20) - (4.22) into (4.26) and operating,

$$\gamma = \left(n_t Q_L^{-1} - \begin{pmatrix} Q_L^{-1}A_2 & Q_L^{-1}A_2 & \dots & Q_L^{-1}A_2 \end{pmatrix} \begin{pmatrix} N^{-1}A_2^T Q_L^{-1} \\ N^{-1}A_2^T Q_L^{-1} \\ \vdots \\ N^{-1}A_2^T Q_L^{-1} \end{pmatrix} \right)^{-1}$$
$$= \left(n_t Q_L^{-1} - n_t Q_L^{-1} A_2 N^{-1} A_2^T Q_L^{-1} \right)^{-1} = \frac{1}{n_t} \left(I_3 - A_2 N^{-1} A_2^T Q_L^{-1} \right)^{-1} Q_L$$

and denoting $D = I_3 - A_2 N^{-1} A_2^T Q_L^{-1}$,

$$\gamma = \frac{1}{n_t} D^{-1} Q_L. \tag{4.28}$$

In the same way, substituting (4.21) and (4.28) into (4.25),

$$\Delta = \frac{-1}{n_t} \begin{pmatrix} N^{-1} & & & \\ & N^{-1} & & \\ & & \ddots & \\ & & & N^{-1} \end{pmatrix} \begin{pmatrix} A_2^T Q_L^{-1} \\ A_2^T Q_L^{-1} \\ \vdots \\ A_2^T Q_L^{-1} \end{pmatrix} D^{-1} Q_L$$

and then,

$$\Delta = -\frac{1}{n_t} \begin{pmatrix} N^{-1} A_2^T Q_L^{-1} D^{-1} Q_L \\ N^{-1} A_2^T Q_L^{-1} D^{-1} Q_L \\ \vdots \\ N^{-1} A_2^T Q_L^{-1} D^{-1} Q_L \end{pmatrix}. \tag{4.29}$$

Finally, substituting (4.21) and (4.29) into (4.27),

$$\Gamma = \tilde{N}^{-1} + \frac{1}{n_t} \begin{pmatrix} N^{-1} A_2^T D^{-1} Q_L^{-1} A_2 N^{-1} & \dots & N^{-1} A_2^T D^{-1} Q_L^{-1} A_2 N^{-1} \\ \vdots & & \vdots \\ N^{-1} A_2^T D^{-1} Q_L^{-1} A_2 N^{-1} & \dots & N^{-1} A_2^T D^{-1} Q_L^{-1} A_2 N^{-1} \end{pmatrix}$$

and simplifying,

$$\Gamma = N^{-1} \otimes I_{n_t} + \frac{1}{n_t} N^{-1} A_2^T D^{-1} Q_L^{-1} A_2 N^{-1} \otimes \boldsymbol{e} \cdot \boldsymbol{e}^T \tag{4.30}$$

where $\boldsymbol{e} = (1, 1, 1, \ldots, 1)^T$ and $\otimes$ represents the tensorial product. The inverse matrix of D always exists, since

$$\begin{aligned}
A_2 N^{-1} A_2^T Q_L^{-1} = & \; A_2 \left(M^{-1} - M^{-1} A_2^T Q_L^{-1} \left(I_3 + A_2 M^{-1} A_2^T Q_L^{-1} \right)^{-1} A_2 M^{-1} \right) A_2^T Q_L^{-1} \\
= & \; A_2 M^{-1} A_2^T Q_L^{-1} \left(I_3 - \left(I_3 + A_2 M^{-1} A_2^T Q_L^{-1} \right)^{-1} A_2 M^{-1} A_2^T Q_L^{-1} \right) \\
\overset{*}{=} & \; A_2 M^{-1} A_2^T Q_L^{-1} \left(I_3 + A_2 M^{-1} A_2^T Q_L^{-1} \right)^{-1} \\
= & \; I_3 - I_3 + A_2 M^{-1} A_2^T Q_L^{-1} \left(I_3 + A_2 M^{-1} A_2^T Q_L^{-1} \right)^{-1} \\
\overset{*}{=} & \; I_3 - \left(I_3 + A_2 M^{-1} A_2^T Q_L^{-1} \right)^{-1}
\end{aligned}$$

where, in * the identity $I_3 = \left(I_3 + A_2 M^{-1} A_2^T Q_L^{-1} \right)^{-1} \left(I_3 + A_2 M^{-1} A_2^T Q_L^{-1} \right)$ has been replaced. Thus, $D = I_3 - A_2 N^{-1} A_2^T Q_L^{-1} = \left(I_3 + A_2 M^{-1} A_2^T Q_L^{-1} \right)^{-1}$ and

$$D^{-1} = I_3 + A_2 M^{-1} A_2^T Q_L^{-1}. \tag{4.31}$$

By forming (4.23) with the expressions (4.28), (4.29) and (4.30) and substituting in (4.15), along with (4.17), the explicit expressions of the first part of the MAP3 algorithms are obtained. In particular, the initial ambiguities are estimated by

$$\begin{aligned}
\hat{\boldsymbol{\beta}} = & \; \frac{1}{n_t} D^{-1} \sum_{i=1}^{n_t} \boldsymbol{L}(t_i) - \frac{1}{n_t} \sum_{i=1}^{n_t} Q_L D^{-1} Q_L^{-1} A_2 N^{-1} \left(A_1^T Q_P^{-1} \boldsymbol{P}(t_i) + A_2^T Q_L^{-1} \boldsymbol{L}(t_i) \right) \\
= & \; D^{-1} \bar{\boldsymbol{L}} - Q_L D^{-1} Q_L^{-1} A_2 N^{-1} \left(A_1^T Q_P^{-1} \bar{\boldsymbol{P}} + A_2^T Q_L^{-1} \bar{\boldsymbol{L}} \right) \\
= & \; \left(D^{-1} - Q_L D^{-1} Q_L^{-1} A_2 N^{-1} A_2^T Q_L^{-1} \right) \bar{\boldsymbol{L}} - Q_L D^{-1} Q_L^{-1} A_2 N^{-1} A_1^T Q_P^{-1} \bar{\boldsymbol{P}}
\end{aligned} \tag{4.32}$$

where $\bar{\boldsymbol{P}}$ and $\bar{\boldsymbol{L}}$ are the arithmetic mean of the pseudorange and phase measurements over the observation period, respectively. The smoothed pseudorange and ionospheric delay at epoch t are given by

$$\begin{aligned}\hat{\boldsymbol{\xi}}(t) = \begin{pmatrix} \hat{\tilde{\rho}}(t) \\ \hat{J}_1(t) \end{pmatrix} &= N^{-1}\left(A_1^T Q_P^{-1}\boldsymbol{P}(t) + A_2^T Q_L^{-1}\boldsymbol{L}(t)\right) \\ &+\frac{1}{n_t}N^{-1}A_2^T D^{-1}Q_L^{-1}A_2 N^{-1}\left(A_1^T Q_P^{-1}\sum_{i=1}^{n_t}\boldsymbol{P}(t_i) + A_2^T Q_L^{-1}\sum_{i=1}^{n_t}\boldsymbol{L}(t_i)\right) \\ &-\frac{1}{n_t}N^{-1}A_2^T Q_L^{-1}D^{-1}\sum_{i=1}^{n_t}\boldsymbol{L}(t_i) \\ = \; & N^{-1}A_2^T D^{-1}Q_L^{-1}A_2 N^{-1}\left(A_1^T Q_P^{-1}\bar{\boldsymbol{P}} + A_2^T Q_L^{-1}\bar{\boldsymbol{L}}\right) \\ &+N^{-1}\left(A_1^T Q_P^{-1}\boldsymbol{P}(t) + A_2^T Q_L^{-1}\boldsymbol{L}(t)\right) - N^{-1}A_2^T Q_L^{-1}D^{-1}\bar{\boldsymbol{L}}.\end{aligned} \tag{4.33}$$

The covariance matrices of the estimated ambiguities, the smoothed pseudorange and ionospheric delay at epoch t are

$$C_{\hat{\boldsymbol{\beta}}\hat{\boldsymbol{\beta}}} = \hat{\sigma}_0^2\frac{1}{n_t}D^{-1}Q_L \tag{4.34}$$

$$C_{\hat{\boldsymbol{\xi}}(t)\hat{\boldsymbol{\xi}}(t)} = \hat{\sigma}_0^2\left(N^{-1} + \frac{1}{n_t}N^{-1}A_2^T D^{-1}Q_L^{-1}A_2 N^{-1}\right) \tag{4.35}$$

where $\hat{\sigma}_0^2$ is the a posteriori variance obtained in the LSA. Moreover, the covariance matrix of the smoothed pseudoranges and ionospheric delay during the complete observation period is

$$C_{\hat{\boldsymbol{\xi}}\hat{\boldsymbol{\xi}}} = \hat{\sigma}_0^2\Gamma. \tag{4.36}$$

4.3. MAP3 2. Receiver Position and Clock Offset Estimation

In the new approach the least squares theory is applied once more in order to estimate the receiver position and its clock offset. In the same way as in (3.5), for a satellite s, the mathematical model at any epoch t is given by

$$\tilde{\rho}^s(t) = \rho^s(t) + c\left(dt_r(t) - dt^s(t)\right) + m_w^s(t)ZWD + \nu \tag{4.37}$$

where $\tilde{\rho}^s(t)$ are the smoothed pseudodistances obtained with (4.33), dt^s is corrected by using final satellite clocks and m_w^s is a mapping function for the ZWD. The dry component of the tropospheric delay composes the 90% and can be corrected by means of a model. Finally, ν is the noise of the smoothed pseudodistances, about 5 mm.

Thus, considering an observation period of n_t epochs $(t_1, \ldots, t_{n_t})$, in which n_s satellites have been observed, and linearizing (4.37) in an a priori solution, $\boldsymbol{X}_0$, the mathematical model can be written as

$$\begin{pmatrix} \boldsymbol{y^1} \\ \boldsymbol{y^2} \\ \vdots \\ \boldsymbol{y^{n_s}} \end{pmatrix} = \begin{pmatrix} I_{n_t} & \tilde{G}^1 & M_w^1 \\ I_{n_t} & \tilde{G}^2 & M_w^2 \\ \vdots & \vdots & \vdots \\ I_{n_t} & \tilde{G}^{n_s} & M_w^{n_s} \end{pmatrix} \begin{pmatrix} c \cdot \boldsymbol{dt_r} \\ \delta X \\ \delta Y \\ \delta Z \\ \boldsymbol{ZWD} \end{pmatrix} - \begin{pmatrix} \boldsymbol{v^1} \\ \boldsymbol{v^2} \\ \vdots \\ \boldsymbol{v^{n_s}} \end{pmatrix} \tag{4.38}$$

where the vector of unknowns is formed by the receiver clock offset in metres, $c \cdot \boldsymbol{dt_r}$, the corrections to the a priori receiver position (δX, δY, δZ) and a correction to the ZWD for every 2-hours period, $\boldsymbol{ZWD}$. The observation vector, $\boldsymbol{y}$, is formed from the smoothed pseudodistances of every satellite ($s = 1, \ldots, n_s$), corrected with a priori values of the distance, $\rho_0^s(t_i)$, the precise satellite clock offsets $dt^s(t_i)$ and the tropospheric delay by means of a model, i.e.,

$$\boldsymbol{y^s} = \begin{pmatrix} \tilde{\rho}^s(t_1) - \rho_0^s(t_1) + cdt^s(t_1) - Trop^s(t_1) \\ \tilde{\rho}^s(t_2) - \rho_0^s(t_2) + cdt^s(t_2) - Trop^s(t_2) \\ \vdots \\ \tilde{\rho}^s(t_{n_t}) - \rho_0^s(t_{n_t}) + cdt^s(t_{n_t}) - Trop^s(t_{n_t}) \end{pmatrix}. \tag{4.39}$$

For every satellite s, the matrices $\tilde{G}^s$ and M_w^s are

$$\tilde{G}^s = \begin{pmatrix} \left.\frac{-(X^s - X_0)}{\rho_0^s}\right|_{t_1} & \left.\frac{-(Y^s - Y_0)}{\rho_0^s}\right|_{t_1} & \left.\frac{-(Z^s - Z_0)}{\rho_0^s}\right|_{t_1} \\ \left.\frac{-(X^s - X_0)}{\rho_0^s}\right|_{t_2} & \left.\frac{-(Y^s - Y_0)}{\rho_0^s}\right|_{t_2} & \left.\frac{-(Z^s - Z_0)}{\rho_0^s}\right|_{t_2} \\ \vdots & \vdots & \vdots \\ \left.\frac{-(X^s - X_0)}{\rho_0^s}\right|_{t_{n_t}} & \left.\frac{-(Y^s - Y_0)}{\rho_0^s}\right|_{t_{n_t}} & \left.\frac{-(Z^s - Z_0)}{\rho_0^s}\right|_{t_{n_t}} \end{pmatrix} \tag{4.40}$$

and

$$M_w^s = \begin{pmatrix} m_w^s(t_{11}) & 0 & \dots & 0 \\ \vdots & \vdots & & \\ m_w^s(t_{1q}) & 0 & & \\ 0 & m_w^s(t_{21}) & & \\ \vdots & \vdots & & \\ 0 & m_w^s(t_{2q}) & & \\ \vdots & & \ddots & \\ 0 & & & m_w^s(t_{p1}) \\ \vdots & & & \vdots \\ 0 & & & m_w^s(t_{pq}) \end{pmatrix}, \tag{4.41}$$

where the observation period has been divided in p subintervals 2-hours long and q is the number of observations in any of such intervals. Finally, I_{n_t} is the identity matrix of dimension n_t and $\boldsymbol{v^s}$ is the residuals vector for the satellite s.

Then, the design matrix may be formed as

$$A = \begin{pmatrix} I_{n_t} & G^1 \\ I_{n_t} & G^2 \\ \vdots & \vdots \\ I_{n_t} & G^{n_s} \end{pmatrix} \tag{4.42}$$

where, for the sake of simplicity, the matrices $\tilde{G}^s$ and M_w^s have been joined in the way

$$G^s = \begin{pmatrix} \tilde{G}^s & M_w^s \end{pmatrix}. \tag{4.43}$$

The stochastic model employed in this second part is given by a block matrix conformed by the covariance matrices of the observation vectors of every satellite,

$$C_{\boldsymbol{yy}} = \begin{pmatrix} C_{\boldsymbol{y}^1\boldsymbol{y}^1} & & & \\ & C_{\boldsymbol{y}^2\boldsymbol{y}^2} & & \\ & & \ddots & \\ & & & C_{\boldsymbol{y}^{n_s}\boldsymbol{y}^{n_s}} \end{pmatrix}. \tag{4.44}$$

Every block in the diagonal of $C_{\boldsymbol{yy}}$ can be obtained from (4.36) by discarding the ionospheric delay variance and covariance terms. Thus, for every satellite and every continuous arc, a matrix

$$Q_{\boldsymbol{yy}} = \begin{pmatrix} d+a & a & \dots & a \\ a & d+a & & \vdots \\ \vdots & & \ddots & a \\ a & \dots & a & d+a \end{pmatrix} = dI_n + a\boldsymbol{e}\boldsymbol{e}^T \tag{4.45}$$

can be formed, being d the first element of the matrix N^{-1} and a the first element of the matrix $N^{-1}A_2^T D^{-1} Q_L^{-1} A_2 N^{-1}$ divided by the number of observations in the arc, n. I_n is the $n \times n$ identity matrix and $\boldsymbol{e} = (1, 1, 1, \dots, 1)^T$. Moreover, this matrix must be multiplied by the corresponding a posteriori variance obtained in the adjustement of the arc. It must be mentioned that (4.45) is a simplification of the true covariance matrix, since the ionospheric delay variance terms have been discarded. However, this simplification gives place to a full variance-covariance matrix with a known inverse,

$$Q_{\boldsymbol{yy}}^{-1} = \frac{1}{d}\left(I_n - \frac{a}{d+na}\boldsymbol{e}\boldsymbol{e}^T\right). \tag{4.46}$$

The fact that a complete covariance matrix is used improves the estimations that are obtained with a diagonal one. Moreover, the computational time is reduced significantly when the matrices inversion is avoided.

The weight matrix is obtained by inverting (4.44) and the unknown parameters in (4.38) are estimated by

$$\begin{pmatrix} c \cdot \boldsymbol{dt_r} \\ \delta X \\ \delta Y \\ \delta Z \\ \boldsymbol{ZWD} \end{pmatrix} = N^{-1}\boldsymbol{d}, \tag{4.47}$$

where N is a block matrix,

$$N = \begin{pmatrix} \tilde{N} & E \\ E^T & F \end{pmatrix}, \tag{4.48}$$

with

$$\begin{aligned} \tilde{N} &= \sum_{s=1}^{n_s} C^{-1}_{\boldsymbol{y^s y^s}}, \\ E &= \sum_{s=1}^{n_s} C^{-1}_{\boldsymbol{y^s y^s}} G^s, \\ F &= \sum_{s=1}^{n_s} G^{sT} C^{-1}_{\boldsymbol{y^s y^s}} G^s \end{aligned} \tag{4.49}$$

and

$$\boldsymbol{d} = \begin{pmatrix} d_1 \\ d_2 \end{pmatrix} = \begin{pmatrix} \sum_{s=1}^{n_s} C^{-1}_{\boldsymbol{y^s y^s}} \boldsymbol{y}^s \\ \sum_{s=1}^{n_s} G^{sT} C^{-1}_{\boldsymbol{y^s y^s}} \boldsymbol{y}^s \end{pmatrix}. \tag{4.50}$$

Analogously to section 4.2, the inverse of N can be expressed as another block matrix (4.23), where

$$\begin{aligned}\gamma &= \left(F - E^T \tilde{N}^{-1} E\right)^{-1}, \\ \Delta &= -\tilde{N}^{-1} E \gamma, \\ \Gamma &= \tilde{N}^{-1}\left(I_{n_t} - E\Delta^T\right).\end{aligned} \tag{4.51}$$

Thus, the second part of the MAP3 algorithms is given by

$$\boldsymbol{\delta\hat{X}} = \begin{pmatrix} \delta\hat{X} \\ \delta\hat{Y} \\ \delta\hat{Z} \\ \boldsymbol{Z\hat{W}D} \end{pmatrix} = \Delta^T d_1 + \gamma d_2 \tag{4.52}$$

and

$$c \cdot \boldsymbol{d\hat{t}_r} \quad = \Gamma d_1 + \Delta d_2. \tag{4.53}$$

The covariance matrix of the estimated parameters is given by

$$C_{\boldsymbol{d\hat{t}_r \delta\hat{X} d\hat{t}_r \delta\hat{X}}} = \hat{\sigma}^2 N^{-1}, \tag{4.54}$$

where $\hat{\sigma}^2$ is the a posteriori variance of the second LSA.

The proposed method can be adapted to work with observations from different satellite systems by taking into account the offset introduced by the circuitries of the receiver in the observations (ISB). The ISB can be modeled as the time difference between observations from different satellite systems and considered constant all through the observation period. However, it is important to stress that the ISB estimation carried out by the GPC is obtained as the difference between the ionofree code delays of the different satellite systems, estimated in a network adjustment (section 1.3).

Then, the mathematical model presented above has to be modified in the following way. Assuming that the first m observed satellites correspond to a determined system, such as GPS, and the rest belong to another satellite system, for example Galileo, (4.38) changes to

$$\begin{pmatrix} \boldsymbol{y^1} \\ \vdots \\ \boldsymbol{y^m} \\ \boldsymbol{y^{m+1}} \\ \vdots \\ \boldsymbol{y^{n_s}} \end{pmatrix} = \begin{pmatrix} I_{n_t} & G^1 & \mathbf{0} \\ \vdots & \vdots & \vdots \\ I_{n_t} & G^m & \mathbf{0} \\ I_{n_t} & G^{m+1} & \mathbf{1} \\ \vdots & \vdots & \vdots \\ I_{n_t} & G^{n_s} & \mathbf{1} \end{pmatrix} \begin{pmatrix} c \cdot \boldsymbol{dt_r} \\ \delta X \\ \delta Y \\ \delta Z \\ \boldsymbol{ZWD} \\ ISB \end{pmatrix} - \begin{pmatrix} \boldsymbol{v^1} \\ \vdots \\ \boldsymbol{v^m} \\ \boldsymbol{v^{m+1}} \\ \vdots \\ \boldsymbol{v^{n_s}} \end{pmatrix} \tag{4.55}$$

where $\mathbf{0}$ and $\mathbf{1}$ are column vectors of length n_t conformed by 0 and 1, respectively. Including the last column within the matrices G^s, the same expressions for the least-squares estimators and covariance matrices, (4.52), (4.53) and (4.54), are obtained.

4.4. Satellite Elevation Weighting

The stochastic model presented above (4.14) does not take into account the increase of the observations noise at low satellite elevations and assigns the same weights to the observations in all epochs and for all satellites. This weighting scheme is too simple and does not reflect the real statistical properties of the GNSS observables.

However, this stochastic model can be improved by including the satellite elevation at every epoch and a matrix of the type (3.19) can be used instead of (4.14). In fact, as it will be seen in chapter 5, the estimations obtained with MAP3 improve significantly when the satellite elevation is considered in the observations weighting scheme.

4.5. Correction of Electronic Delays

In previous analysis of the MAP3 algorithms it has been observed that the presence of satellite and receiver electronic biases do not affect the position estimations from GPS dual-frequency observations, but the phase delays are absorbed by the initial ambiguities estimations and the code delays affect mainly the estimation of the ionospheric delay. However, when the ionospheric delay is wanted the correction of the code electronic delays is required.

The satellite code delays between $P1$ and $P2$ can be completely removed from the observations by using the corresponding DCB provided by CODE, $B^s_{P1-P2} = c\,(B^s_{P1} - B^s_{P2})$ (section 2.6). The needed correction can be applied in

two steps. First, the value B^s_{P1-P2} is added to P_2 and thus, the remaining satellite electronic delay in both code observations is equal to B^s_{P1}. And second, since precise satellite clocks obtained by IGS contain the ionofree linear combination of B^s_{P1} and B^s_{P2}, $dt^s_{IGS} = dt^s - (2.55B^s_{P1} - 1.55B^s_{P2})$ (Dach et al., 2007), by adding $1.55B^s_{P1-P2}$ to the clock corrections we obtain

$$dt^s_{IGS} + 1.55B^s_{P1-P2} = dt^s - B^s_{P1}. \tag{4.56}$$

and therefore, when the observations are corrected with the precise satellite clocks, the term B^s_{P1} cancels out. This correction will affect the phase observations but it will be fully absorbed by the estimated ambiguities.

When either $C1$ or $C2$ code observations are processed instead of $P1$ or $P2$, the corresponding offsets B^s_{P1-C1} and B^s_{P2-C2} should be added first to $C1$ and $C2$, therefore obtaining the same electronic delay in C as we would have in P. Then, the same procedure can be followed.

Moreover, receiver electronic delays can be reduced by using CODE monthly DCB values obtained for IGS stations. Since $B_{rP1-P2} = B_{r1} - B_{r2}$, by adding this quantity to P_2, the remaining delay due to the receiver should be the same for both code observations and equal to B_{r1}. The same should be done with $C1$ and B_{rP1-C1}. In consequence, a remainder of the receiver instrumental bias in $P1$ will still be present in both code observations for all satellites and it will be absorbed by the receiver clock offset estimations.

When GIOVE observations are processed, the delay between the different frequencies can be corrected with the IFB values provided by GPC (B^s_{C1-C7}, Tab. 2.11). Since the GIOVE clocks computed at GPC contain a combination of the code delays in $C1C$ and $C7Q$, the correction of the satellite electronic delays would be

$$dt^s_{GPC} + 1.42B^s_{C1-C7} = dt^s - B^s_{C1}. \tag{4.57}$$

Moreover, GPC also provides IFB values for the GESS stations (B_{rP1-P2}, B_{rC1-C7}, Fig. 1.16), which can be used in the correction of GPS and GIOVE observations taken at these stations. Therefore, GPS and GIOVE observations will present the same delay in both frequencies, B_{r1}, which will be fully absorbed by the receiver clock offset estimations.

4.6. Implementation of MAP3

The main advantage of the MAP3 algorithms with respect to the classic PPP is that they are able to deal with multi-frequency observations from different satellite systems, what will be very beneficial in the future GNSS scenario.

Moreover, the ionofree linear combination employed in the classical PPP is avoided, obtaining smoothed pseudodistances with a noise of a few mm. In Figs. 4.1 and 4.2, the noise of the smoothed pseudodistances obtained with MAP3 and the noise of the ionofree linear combination of code observations are shown. The large difference in the y-axis scale must be noticed. The noise of the smoothed pseudodistances is around 5 mm, while the noise of the ionofree is about 77 cm. Only satellites at elevation higher than 10° have been considered.

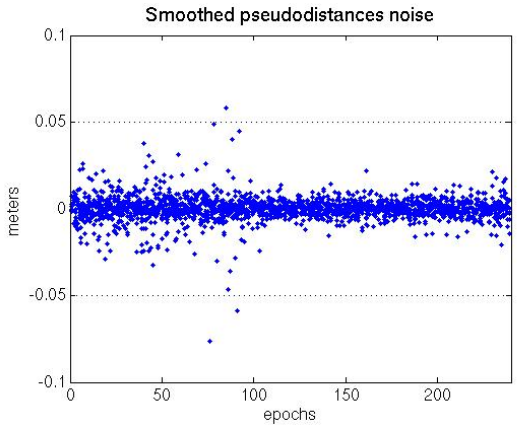

Figure 4.1: *Noise of the smoothed pseudodistances obtained with MAP3.*

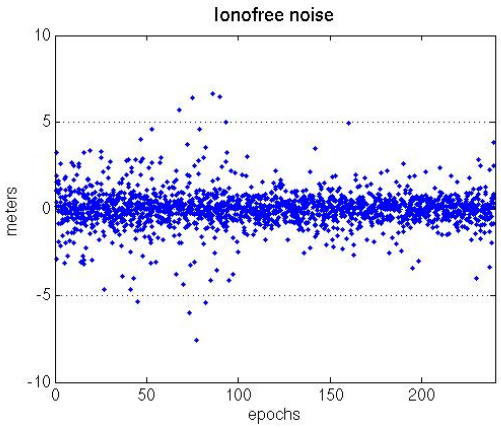

Figure 4.2: *Noise of the Ionofree linear combination of codes.*

It must be beard in mind that the accuracy of the solutions obtained with MAP3 depends on the goodness of the smoothed pseudodistances estimated in the first part of the processing, which are affected by the noise of the observations. Therefore, it is expected that the best results will be obtained from observations with the lowest noise. Moreover, as it will be seen in the following chapter, a good choice of the elevation cut-off angle and the introduction of a satellite elevation weighting scheme improves significantly the estimations.

MAP3 have been integrated within a PPP software named PCube and developed in collaboration with scientific staff of ESA. PCube has been implemented in Matlab and is able to process modernized GPS and Galileo/GIOVE observations along with, either IGS, GPC or the combination of both sets of prod-

ucts, by taking into account the corresponding offsets. The main PCube flow chart is shown in Fig. 4.4.

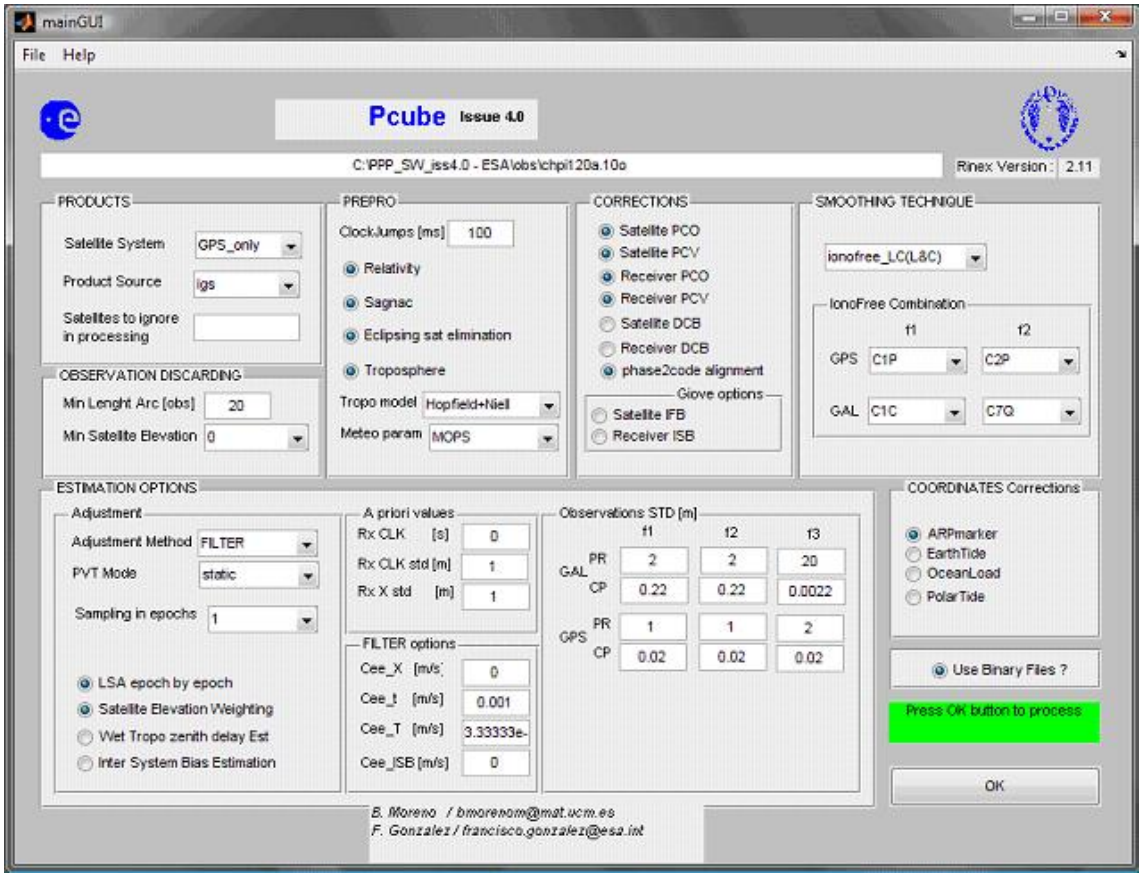

Figure 4.3: *PCube GUI.*

PCube contains the models and techniques presented in chapter 2 for the correction of the relativistic effects, the tropospheric delay, the antennas PCO/V, the electronic delays and the phase wind-up. Moreover, the detection of outliers, cycle slips and clock jumps within PCube is carried out with the methods shown in the section 3.4. The correction of the electronic delays is done by means of the strategy proposed in the section 4.5 and for the estimation of the receiver position and its clock offset, either the new MAP3 algorithms or the sequential filter presented in the section 3.5.1 can be used. Finally, the physical models introduced in the section 3.6, which take into account the site displacement effects, can be applied. Therefore, the accuracy of PCube is at few mm-level.

The different settings used in the processing can be set up by the user by means of the GUI (Fig. 4.3). It is possible to choose the observations to be included in the processing among GPS-only, Galileo-only or both, and the type of satellite

products. Moreover, the needed corrections to the observations can be selected and different estimation techniques can be used. In case that the filter is applied, the ionofree linear combination must be formed. Finally, the corrections to the position due to the site displacement effects can also be activated.

In the numerical tests of the PCube software, it has been observed that the estimations provided by MAP3 and the sequential filter from GPS dual-frequency observations are very similar, although, in short observation periods MAP3 provides more accurate estimations. The results obtained in the numerical tests of MAP3 are presented in the chapter 5 and, for completeness, some results obtained with the sequential filter have been attached as an appendix.

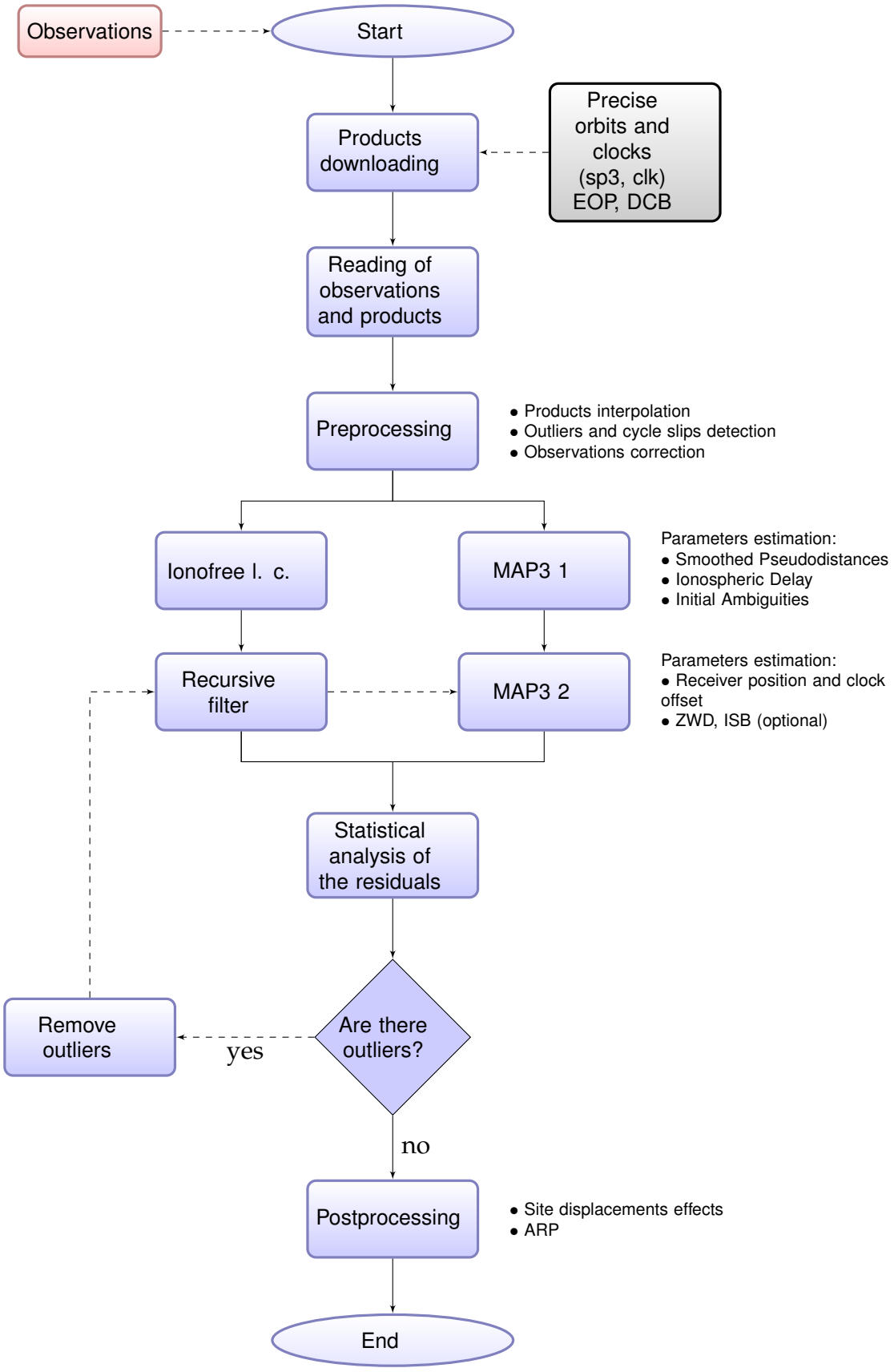

Figure 4.4: *PCube flow chart*

Chapter 5

Numerical Tests

In order to assess the goodness of the MAP3 algorithms, different numerical tests have been accomplished. In first place, real GPS dual-frequency data have been processed with MAP3 and the obtained results have been compared with other PPP programs. Then, MAP3 has been applied to real GIOVE and GPS triple-frequency observations, although, for the time being, only two GIOVE satellites and one GPS transmitting the L5 signal are available. In fact, the main problem found in the testing of the multi-frequency algorithms was the lack of real multi-frequency observations, what has been overcome by the use of a GNSS signal simulator. Thus, the performance of MAP3 in the modernized GPS and Galileo scenario has been analysed through the processing of simulated observations, which were kindly provided by ESA. These observations were obtained with a SimGEN simulator, developed by Spirent Communications, and collected with a Septentrio Test User Receiver (TUR). Nevertheless, the simulated data are far from the real observations, since they lack antennas and multipath errors, realistic ionospheric and tropospheric delays, etc, and definitive conclusions about the performance of MAP3 in the future scenario can not be drawn from these tests.

The MAP3 algorithms have been tested with the help of PCube (section 4.6). In the processing, the observations are cleaned of outliers, cycle slips and clock jumps, the relativistic errors and the phase wind-up are corrected, the absolute calibration for the antennas PCO/V is applied, the tropospheric delay is reduced with the modified Hopfield model and a correction to the tropospheric ZWD is estimated every 2 hours. Since the electronic delays do not influence the position estimation, the DCB are not corrected. Finally, the site displacement effects corrections are also applied.

5.1. Data and Products

In order to perform numerical tests of the MAP3 algorithms, the following datasets have been gathered:

1. Real GPS dual-frequency observations.
2. Real GPS and GIOVE triple-frequency observations.
3. Simulated Galileo and modernized GPS multi-frequency observations.

Although every set of observations presents different code noises, depending on the signals and the receiver, the same values have been used in all the numerical tests. Such code noises have been deduced from the literature and are shown in Tab. 5.1. On the other hand, the noise of the carrier phase measurements has been set to 2 mm.

GPS Code	Noise	Galileo Code	Noise
L1C/A	30	E1 BOC	20
L2C	30	E5a QPSK	15
P	15	E5b QPSK	15
L5C	15	E5 AltBOC	10

Table 5.1: *Code noise used in the numerical tests of MAP3 (cm).*

In the processing, precise satellite coordinates and clocks from IGS (Dow et al., 2009) and GPC (Tobías et al., 2009) have been used in the different tests. Since IGS and GPC orbits are given in IGS05, the PPP solutions are also in the same reference system. In agreement with IGS orbits and clocks, the FES2004 model has been used for the ocean loading correction. GPC and IGS precise products can be combined in the same processing, as long as the GGTO is taken into account, however this does not happen in the numerical tests carried out here.

In the correction of satellite and receiver PCO/V, the IGS absolute calibration for GPS satellites and IGS stations has been used. This calibration is consistent with IGS and GPC precise products, although it only comprises the corrections for GPS frequencies L1-L2 and the modernized L5 is not yet included.

For the time being there is not calibration of the GIOVE satellites antennas PCV and only the PCOs in the z-axis direction are known (Tab. 2.9). The GPC coordinates of the GESS stations are given in the mean phase center and, therefore, the station PCO must not be applied. Regarding the GESS antennas PCV correction, errors of some cm in the estimated position have been observed when the

PCVs of the type-2 antennas have been corrected and, therefore, this calibration is not used in the numerical tests.

Moreover, the introduction of GIOVE observations requires the correction of the electronic biases between the different GIOVE signals, for what the GPC IFB values obtained in the experimentation can be used (Fig. 1.16 and Tab. 2.11). In addition, the ISB between the GPS and GIOVE observations must be estimated when observations from the two satellite systems are processed together.

5.1.1. Real GPS dual-frequency observations

In the first test, real GPS dual-frequency observations taken at the IGS station USN3 from April 20^{th} to May 10^{th} of 2010 have been processed. USN3 station has been chosen since it is connected to the H-Maser defined as the primary realization of UTC (USNO) and a good clock behaviour and data quality are expected. In fact, the estimated noise in the code observations of this station is low, about 15 cm for the P code. The precise coordinates of USN3 in IGS05 are shown in Tab. 5.2.

X	Y	Z
1112162.0576	-4842853.5341	3985496.0235

Table 5.2: *USN3 precise coordinates (m) in IGS05 at epoch April 28^{th}, 2010.*

5.1.2. Real GPS and GIOVE triple-frequency observations

In order to include real GPS and GIOVE triple-frequency observations in the numerical tests, two different sets of observations have been compiled:

- GIOVE observations taken at some stations of the GESS network (section 1.2) and
- GPS triple-frequency observations taken by UNAVCO (`www.unavco.org`).

The GIOVE observations collected at the GESS stations can be accessed by authorised users through `www.giove.esa.int`. Every GESS station can support up to 3 receivers and 2 different antennas but, for the time being, they only integrate a GETR receiver and an experimental antenna. The dataset used in this work corresponds to part of November 1^{st}, 2009 (Day of Year (DOY) 305). The precise coordinates of the selected GESS stations in IGS05 are shown in Tab. 5.3.

Station	X	Y	Z
GVES	1974177.8873	87480.6834	-6045329.0681
GMAL	4865386.3873	4110717.8372	-331129.0351
GWUH	-2267733.4054	5009167.6152	3221289.9923
GIEN	4476536.1285	600429.0322	4488762.9989
GNNO	-2414193.1554	4907785.6032	-3270594.1054

Table 5.3: *GESS precise coordinates (m) in IGS05 at epoch November 1st, 2009.*

In order to analyse the quality of the observations used in this test, the noise of the code pseudoranges at the selected GESS stations has been estimated and it is shown in Tab. 5.4, although these noise values will not be used in the numerical tests. As an example, the code noise of the GVES observations is displayed in Fig. 5.1. It can be observed that the estimated noise of the GPS P-code observations at GESS stations is very low (between 2 and 7 cm) and the noise in $P1$ is a little higher than in $P2$. However, the estimated code noise in E1 ($E1BOC$) and E5b ($E5bQPSK$) is much larger than the GPS P-code noise; in fact, the noise in $E1BOC$ is up to 13 times the noise in $P1$. This is due to a lower strength of the GIOVE signal with respect to the GPS one, what will be overcome with the advent of the Galileo satellites (Crisci et al., 2007). However, as it can be observed, the E5 is a low-noise signal and hence, its noise is at the same level as the GPS one. Moreover, the noise in $E1BOC$ is higher than in $E5bQPSK$ and $E5AltBOC$, since in the GESS network, the E5 band shows a higher signal strength (Simsky et al., 2008a).

Furthermore, the quality of the GIOVE-B observations is better than those of GIOVE-A, due to the GIOVE-B E1 signal presents a higher overall power than that of GIOVE-A and the CBOC modulation used by GIOVE-B produces a better multipath suppression than the BOC(1,1) used by GIOVE-A.

Station	GPS $P1$	GPS $P2$	GIOVE $E1BOC$	GIOVE $E5bQPSK$	GIOVE $E5AltBOC$
GVES	6.7	5.8	21.3	10.7	2.9
GMAL	2.2	1.8	10.8	6.7	1.3
GWUH	3.4	4.5	23.2	18.7	6.4
GIEN	2.1	1.8	26.1	13.4	3.1
GNNO	3.0	2.3	24.9	16.0	4.5

Table 5.4: *GESS stations estimated code noise (cm).*

It is important to mention that, in the first analysis of the GIOVE signal tracked at GESS stations, Crisci et al. (2007) have detected large systematic eleva-

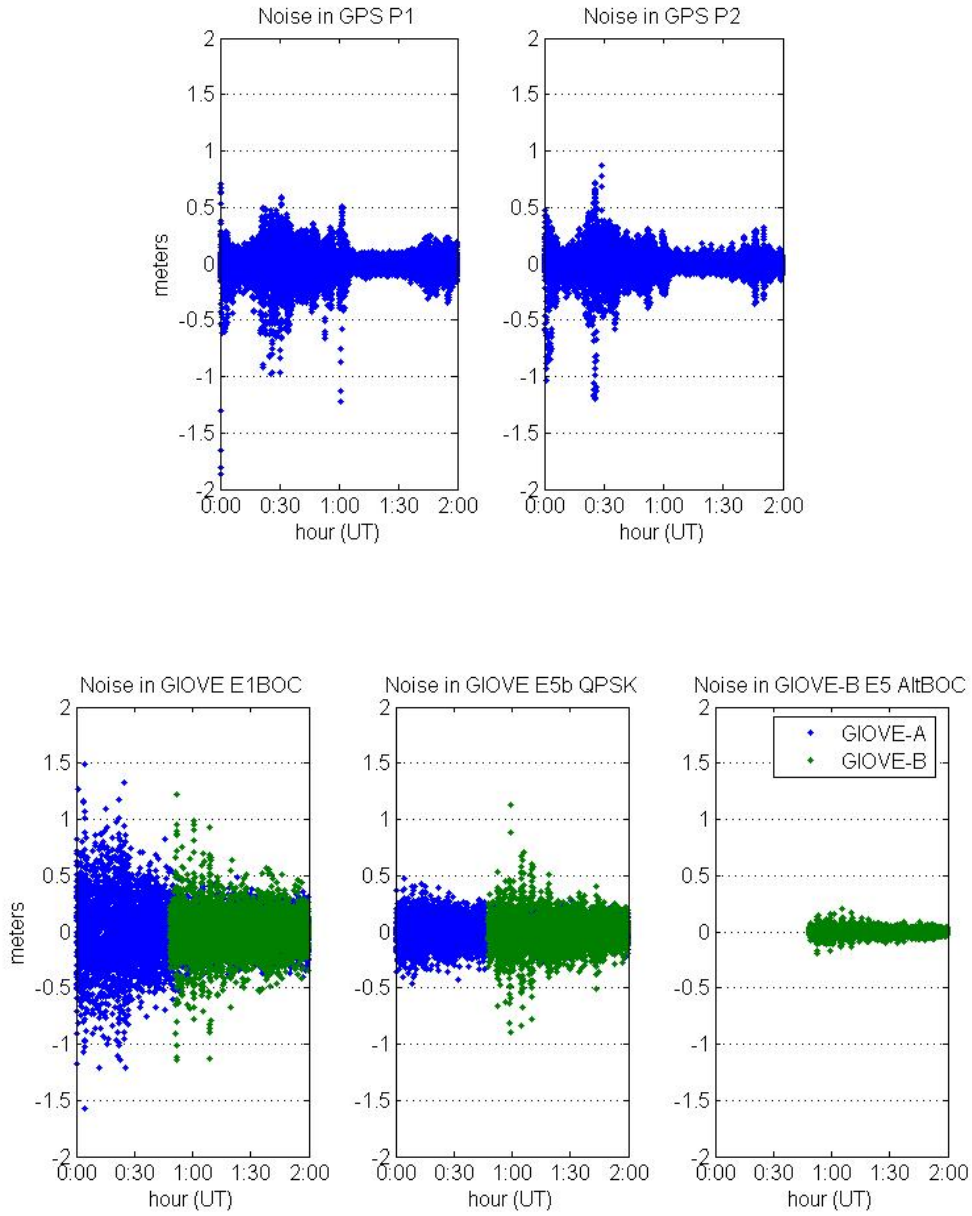

Figure 5.1: *GPS and GIOVE code noise at GVES station.*

tion, azimut and signal dependent group delay variations and a significant bias at high satellite elevations. According to Tobías et al. (2009), this effect is due to a code/phase incoherence generated at the station antenna and will be solved with the installation of calibrated antennas. This bias has been also observed by other authors, such as Simsky et al. (2008a) and de Bakker et al. (2011), together with a low multipath rejection level by the antennas, what will give place to degraded position estimations.

In Fig. 5.2 the multipath error of the GIOVE code observations used in these numerical tests is shown. In agreement with Simsky et al. (2008a), the average multipath error in E1C reaches up to 1 m, the error in E5b is slightly smaller and the best reduction of the multipath is observed with the E5 signal. Moreover, the GPS observations in $P1$ and $P2$ also present strong code multipath variations, especially in stations GVES and GWUH, as it is shown in Fig. 5.3. These problems will be reflected in the positioning with GESS observations, since only low-accuracy solutions can be obtained.

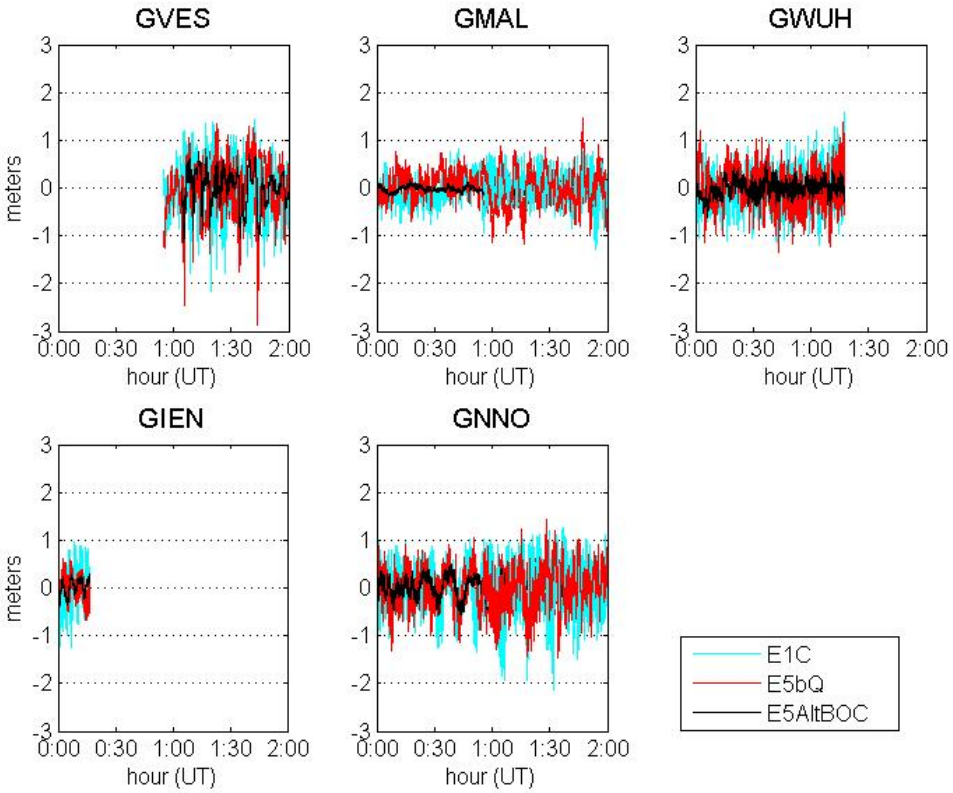

Figure 5.2: *Code multipath error of the GIOVE-A and B signals at GESS stations. Only elevations higher than 10° have been considered.*

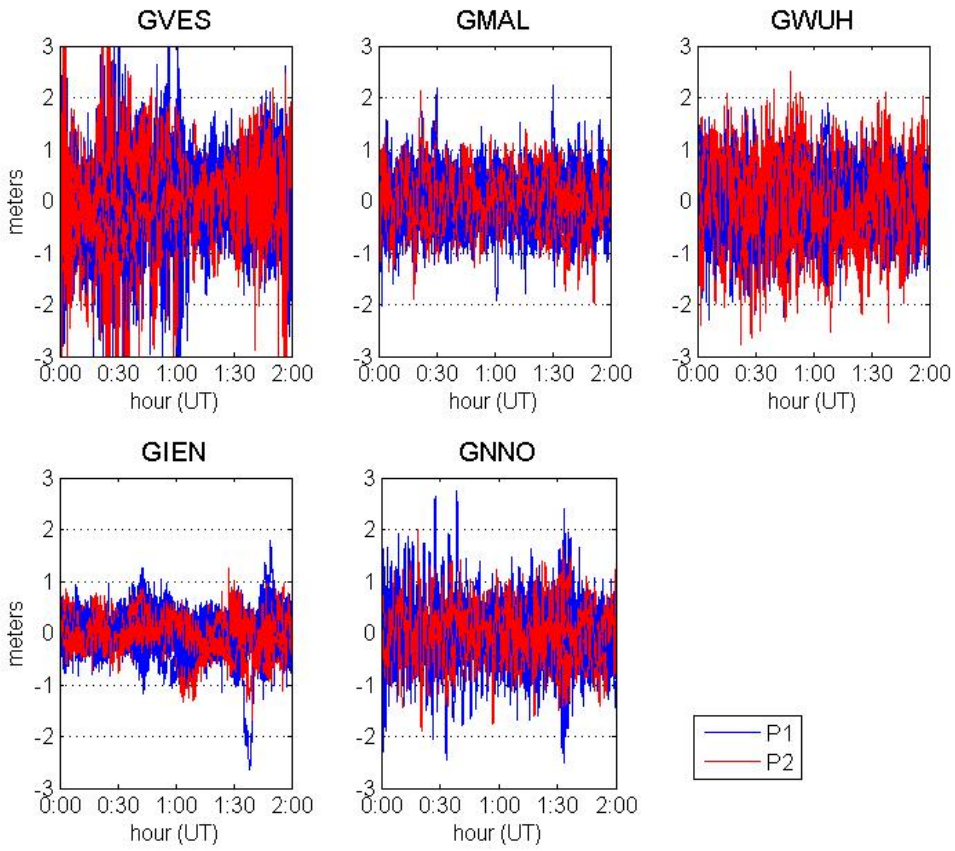

Figure 5.3: *Code multipath error of the GPS P1-P2 signals at GESS stations. Only elevations higher than 10° have been considered.*

On the other hand, GPS observations including the new L2C and L5 signals transmitted by SVN62/PRN25 can be accessed via `ftp://cddis.gsfc.nasa.gov/pub/gps/data/l5test/`. The L5 signal of the new block IIF satellite (SVN62/PRN25) shows a favorable signal strength, somewhere between L1 and L2C, and the PRN25 measurements demonstrate a good tracking quality (Montenbruck et al., 2010). The observation files used in the numerical tests belong to one of the UNAVCO stations, with a TRIMBLE antenna and receiver. The estimated code noise of the UNAVCO observations are quite high, as it shown in Tab. 5.5, about 40 cm for the C code and 30 cm for the P and L5C codes.

Code	Noise
GPS L1C/A	40.4
GPS L2C	37.7
GPS P	28.5
GPS L5C	30.9

Table 5.5: *UNAVCO station estimated code noise (cm).*

5.1.3. Simulated Galileo and modernized GPS observations

The Radio Navigation Laboratory of ESA offers a number of tools and facilities to Navigation projects. Among them, the GNSS RF Signal Generator (SimGEN), developed by Spirent Communications, generates the physical output signal of a GNSS satellite and offers a complete and flexible scenario generation capability. On the other hand, the Galileo TUR is a fully stand-alone, multi-frequency, multi-constellation receiver unit developed by Septentrio for the verification of the Galileo IOV constellation. TUR can receive all the Galileo signals and GPS L1+L5 (Simsky et al., 2005).

Two datasets of Galileo and modernized GPS multi-frequency observations simulated with the help of SimGEN and TUR and provided by ESA have been used in the analysis of MAP3 performance in the future GNSS scenario. In the simulations, neither satellite electronic delays nor antenna PCO/V have been considered, the tropospheric delay was obtained by means of the model given in NATO (1993) and the ionospheric errors are introduced by using the Klobuchar model, for GPS observations, and the NeQuick model for Galileo signals. The observation files were provided along with satellite products and navigation files obtained in the simulation.

The first dataset comprises 3 hours of GPS L1 and Galileo E1, E5a and E5b observations and the second one also contains GPS L5 data. The estimated noise of the code observations is very low (Tab. 5.6) due to that the output of the simulator is directly connected to the receiver and therefore, the observations are not affected by multipath, interferences and antenna errors.

Code	Noise
GPS	5.8
Galileo E1C	2.6
Galileo E5a	1.3
Galileo E5b	1.4

Table 5.6: *TUR estimated code noise (cm).*

5.2. The Results

5.2.1. Scenario I: GPS dual-frequency

A first test of MAP3 has been carried out from real GPS dual-frequency observations taken at USN3 station during days 110 to 130 of 2010. The performance of MAP3 in short and long observation periods has been analysed and the obtained results have been compared with other PPP programs. The convergence time of MAP3 and the influence of the DCB correction on the estimations has been also studied.

5.2.1.1. Test 1. Short observation periods

In first place, the accuracy of the position estimations in short observation periods (2 hours) and under different circumstances is studied.

5.2.1.1.1. Elevation angle and observations weighting In order to analyse the influence of the code noise on the performance of MAP3, three different cases have been considered:

(a) An elevation cut-off angle of 7° is imposed.
(b) An elevation cut-off angle of 7° is imposed and a satellite elevation weighting scheme is applied.
(c) An elevation cut-off angle of 10° is imposed and a satellite elevation weighting scheme is applied.

MAP3 positioning errors obtained in these three cases are presented in Fig. 5.4 and the RMS of such errors is shown in Tab. 5.7. In the case (a) the maximum error in the east and up components reaches up to 5 and 6 cm, respectively, and the error RMS is about 7 mm for the north, 2.5 cm for the east and 3.6 for the up. In case (b) the maximum error is 5 cm for the east and 8 cm for the up (only one day) although the RMS is smaller than in the case (a), 6 mm for the north, 2 cm for the east and 3.1 cm for the up. Therefore, the introduction of a satellite elevation weighting scheme improves significantly the estimations (in total a 14.7%). However, the best results are obtained in case (c), when a higher elevation cut-off angle is imposed (10°), since the most noisy observations due to the low elevations are discarded. In that case the maximum errors are about 4 cm in the east and up components and the RMS is about 6 mm for the north, 1.4 cm for the east and 2 cm for the up. The total improvement in the accuracy with respect to case (b) is about 33.56%. However, a higher elevation cut-off angle may degrade the position estimations, especially in the altitude.

Case	cut-off angle	Weighting	N	E	U	3D
(a)	7°	No	0.69	2.51	3.57	4.42
(b)	7°	Yes	0.61	1.99	3.14	3.77
(c)	10°	Yes	0.57	1.41	1.98	2.50

Table 5.7: *MAP3 positioning error RMS (cm) in short observation periods (2 hours) for the different studied cases.*

The precision (standard deviation) of the position estimations in case (c) is smaller than 4 mm. However, as occurs in PPP, this value is too optimistic and does not reflect the real precision of the estimations. On the other hand, the error in the USN3 estimated clock offset has been obtained by comparison with the receiver clocks provided by IGS and it is shown in Fig. 5.5, being the RMS 0.122 ns.

For comparison, the same observation files have been processed with the online programs CSRS-PPP, MagicGNSS and APPS and also with BSW v 5.0. The programs CSRS-PPP, magicGNSS and BSW use IGS final products to estimate the receiver position and APPS uses JPL precise products. In the processing, an elevation cut-off angle of 10° has been used and corrections of the tropospheric delay have been estimated at every epoch with the online programs and one correction for the complete period has been estimated with BSW. The positioning errors of

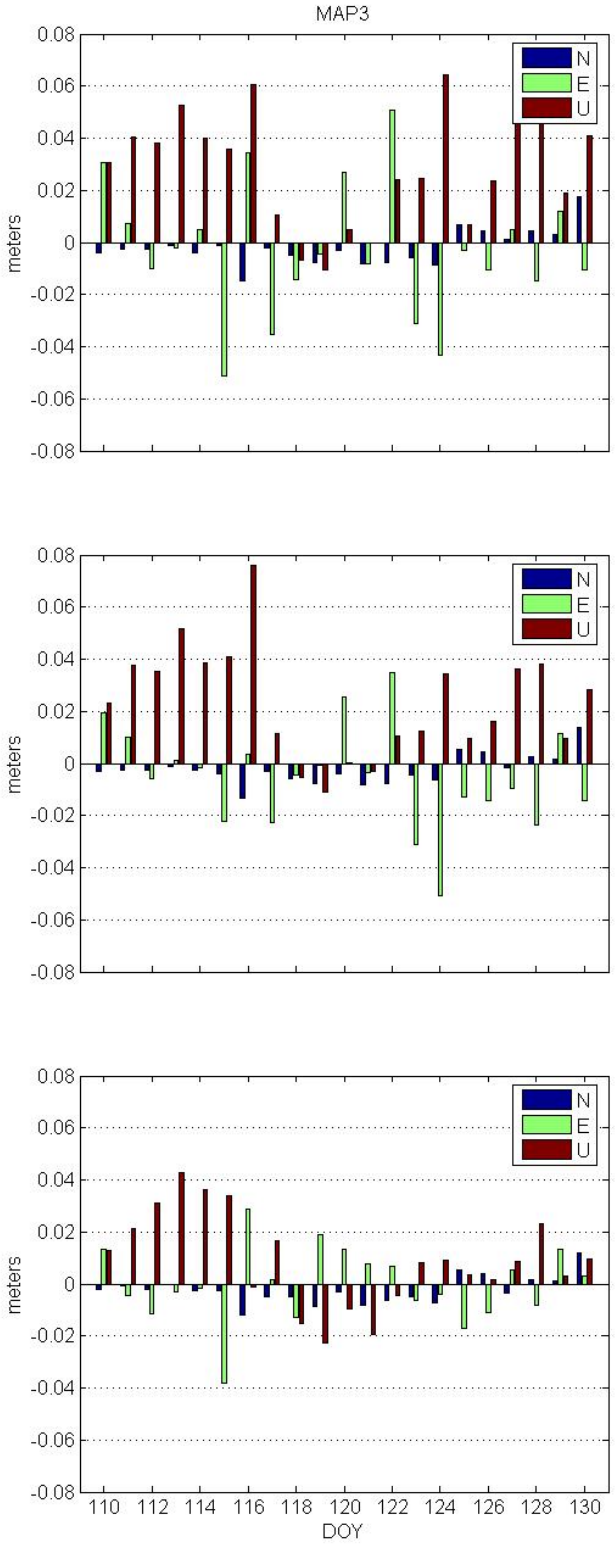

Figure 5.4: *MAP3 positioning error in short observation periods (2 hours) in days 110 to 130, 2010 for the different studied cases: (a) - top, (b) - middle and (c) - bottom.*

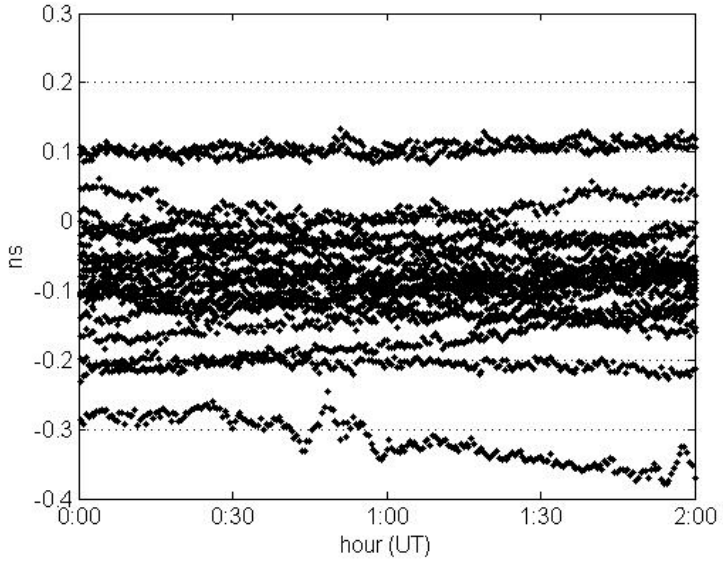

Figure 5.5: *MAP3 estimated clock offset error in short observation periods (2 hours) in days 110 to 130, 2010.*

these programs in short observation periods (2 hours) are shown in Figs. 5.6 and 5.7 and the error RMS is in Tab. 5.8.

The maximum positioning errors of CSRS-PPP and MagicGNSS are about 4 cm in the east and up components, similarly to the results obtained with MAP3, and the error obtained with APPS is slightly larger, up to 6 cm. The least accurate results are obtained with the BSW software, since the error in the up reaches up to 7 cm. In general, with the three online programs the error RMS is smaller than 1 cm in the north, 2.3 cm in the east and 2.8 cm in the up, higher than the mean error obtained with MAP3. Only the north component seems slightly better estimated with the program CSRS-PPP. Therefore, the accuracy reached with the MAP3 software in the position estimation in short observation periods (2 hours) is better than that of the online programs, with a difference of about 7 mm with respect to the next best solution.

Program	N	E	U	3D
MAP3	0.6	1.4	2.0	2.5
CSRS-PPP	0.4	1.5	2.8	3.2
magicGNSS	1.0	2.3	2.3	3.4
APPS	0.7	2.1	2.4	3.3
BSW	1.0	2.0	4.1	4.7

Table 5.8: *MAP3, CSRS-PPP, magicGNSS, APPS and BSW positioning error RMS (cm) in short observation periods (2 hours).*

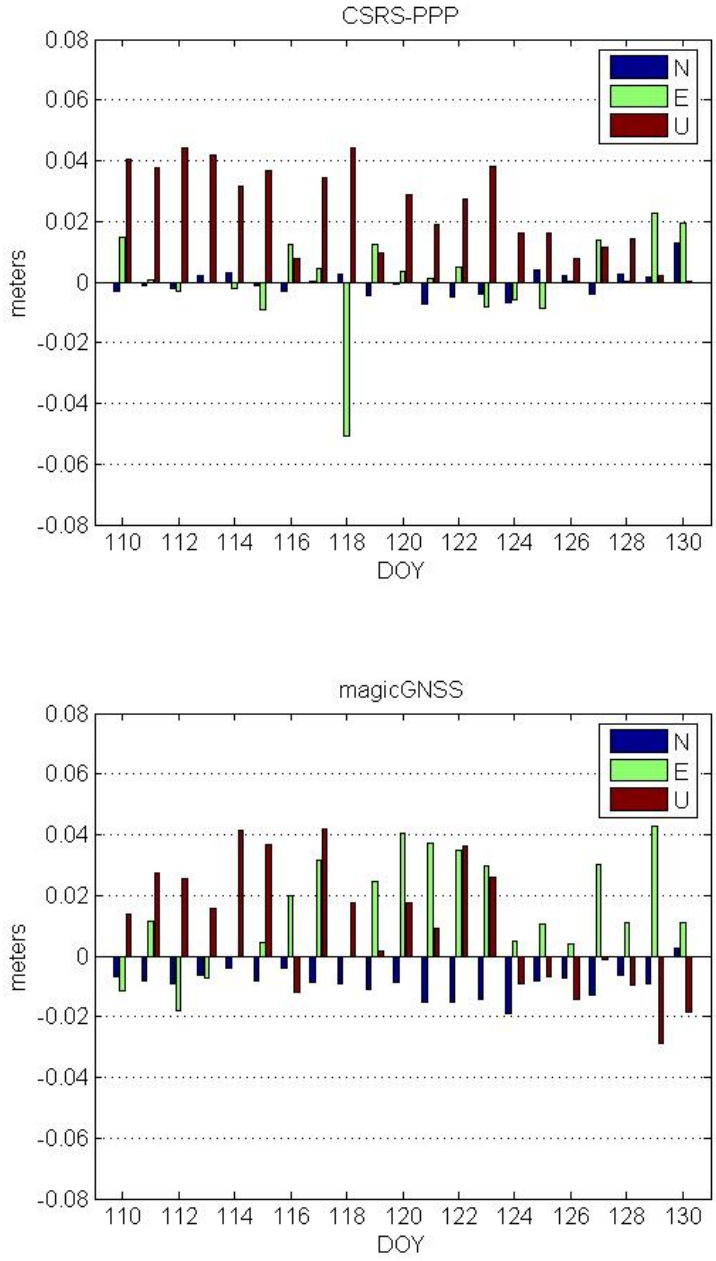

Figure 5.6: *CSRS-PPP and MagicGNSS positioning error in short observation periods (2 hours). USN3 observations during days 110 to 130, 2010 have been processed.*

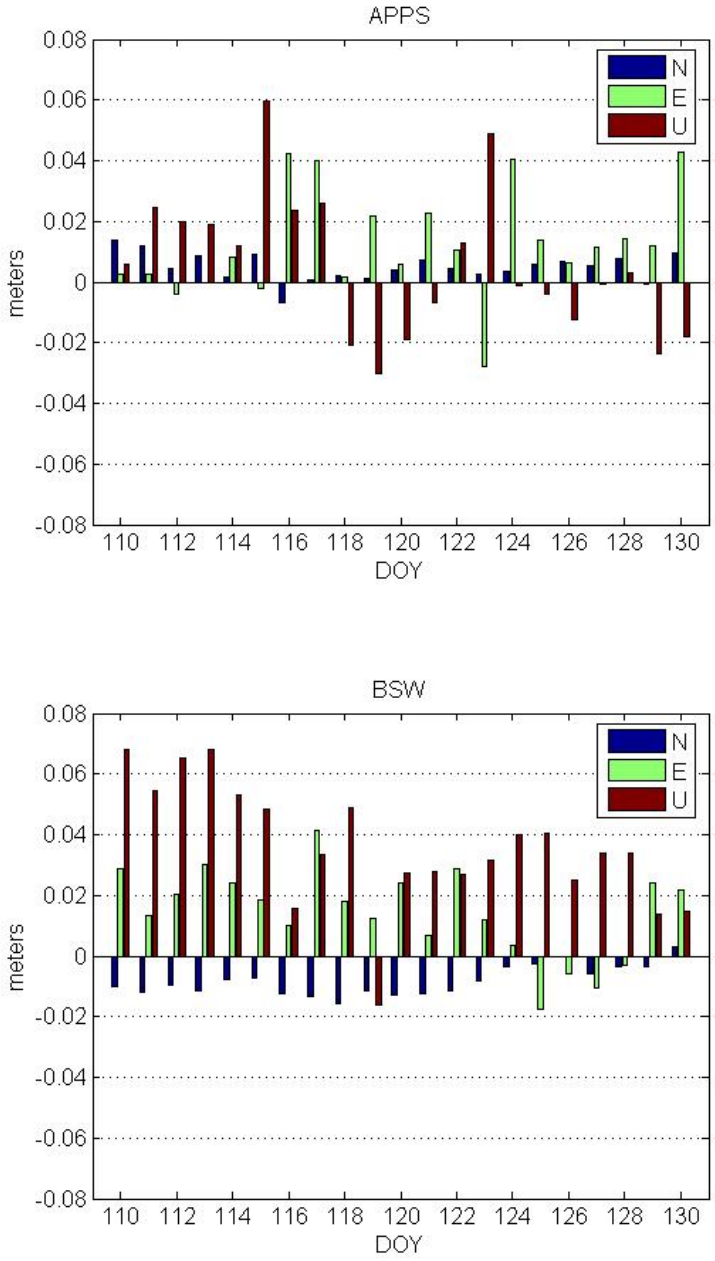

Figure 5.7: *APPS and BSW positioning error in short observation periods (2 hours). USN3 observations during days 110 to 130, 2010 have been processed.*

5.2.1.1.2. Observations sampling rate MAP3 has also been tested with observations at different sampling rates, since a more dense dataset facilitates the detection of outliers and cycle slips, increases the redundancy of observations and, therefore, should provide better estimations. For this study, 2-hours observation files at 1 and 30 s sampling rate, taken in days 120 and 121, have been processed. However, the results obtained at 1 s and 30 s sampling rate are very similar and both solutions only differ in 1-1.5 mm (Tab. 5.9). Therefore, it can be concluded that, in 2-hours observation, a sampling rate of 30 s gives enough accuracy.

Sampling rate	N	E	U	N	E	U
30 s	-0.32	1.34	-0.96	-0.82	0.76	-1.92
1 s	-0.31	1.50	-1.03	-0.82	0.81	-1.78
Doy	120			121		

Table 5.9: *MAP3 positioning error (cm) in short observation periods (2 hours) with different sampling rate.*

5.2.1.2. Test 2. Long observation periods

Secondly, the performance of MAP3 in long observation periods (24 hours) has been studied. In this test, a minimum elevation angle of 10° has been used and the elevation weighting scheme has been applied. MAP3 positioning errors after 24 hours observation are shown in Fig. 5.8. It can be observed that the maximum error in the north component is about 4 mm, 7 mm in the east and 1.4 cm in the up (only in 2 cases).

For comparison, the observation files have been processed with the PPP programs CSRS-PPP, magicGNSS, APPS and BSW and the positioning errors are shown in Figs. 5.9 and 5.10.

The maximum error obtained with CSRS-PPP is about 5 mm in the horizontal plane and 1.3 cm in the up. The error with magicGNSS is about 8 mm in the horizontal and 1 cm in the up and the programs APPS and BSW provide less accurate estimations. The north and up components are more affected with APPS, reaching errors of up to 7 mm and 1.6 cm, respectively. The worst results have been obtained with BSW, up to 1 cm error in the north and more than 2 cm in the east and up components.

The RMS of the positioning errors obtained with MAP3 and the other programs are shown in Tab. 5.10. In general, CSRS-PPP and magicGNSS can estimate the horizontal components at the 2-3 mm accuracy level and the vertical at 5-7

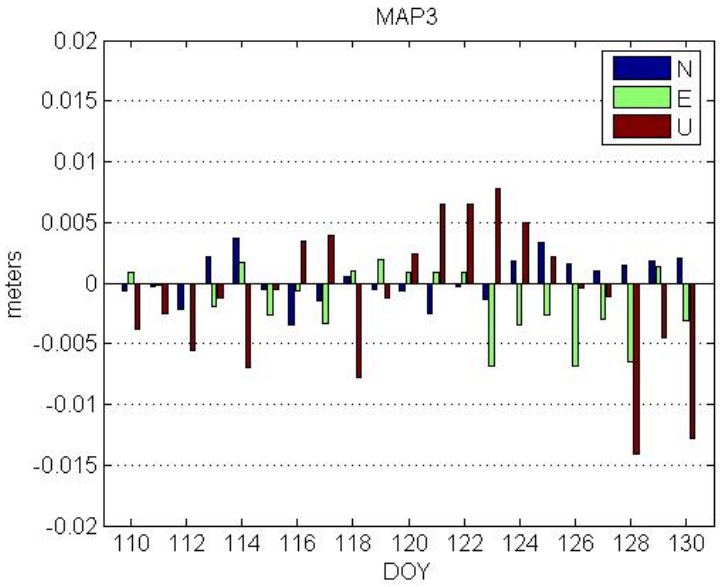

Figure 5.8: *MAP3 positioning error in long observation periods (24 hours). Observations at 30 s sampling rate during days 110 to 130, 2010 have been processed.*

mm level. These results are in accordance with Mireault et al. (2008), where it is shown that the accuracy of the position provided by CSRS-PPP when processing 24 hours of dual-frequency observations with IGS precise products is about 0.67 cm in horizontal and 1.13 cm in vertical. The APPS results are at about 6 mm accuracy level in the north and 9 mm in the up, but the east component is accurately estimated with an error of only 2 mm. Finally, the accuracy achieved with BSW in 24-hours observations is about 1 and 1.7 cm in the east and up components, respectively, and the error in the north is only 4 mm.

In conclusion, the position estimated with MAP3 in long observation periods (24 hours) is at the same accuracy level as the online programs CSRS-PPP and magicGNSS, about 7 mm, only the east component is better estimated with CSRS-PPP and the up component with magicGNSS. Moreover, APPS programs provides less accurate solutions in the north and up components and the worst results are obtained with BSW. It must be said that Dach et al. (2007) recomends to use BSW PPP only to obtain a priori values of the receiver coordinates.

Moreover, the error RMS of the estimated clock offset with MAP3 when daily files are processed is about 0.08 ns and the precision (standard deviation) of the estimated position is around 0.5 mm.

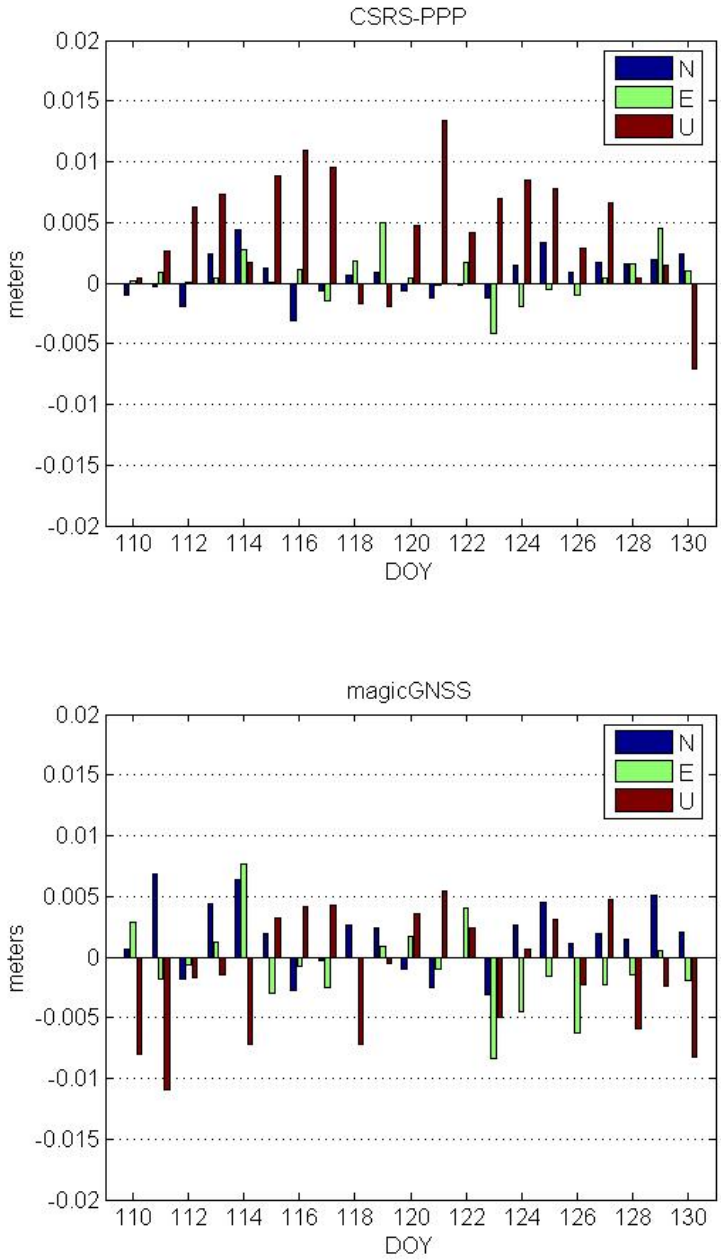

Figure 5.9: *CSRS-PPP and magicGNSS positioning error in long observation periods (24 hours). USN3 observations during days 110 to 130, 2010 have been processed.*

Program	N	E	U	3D
MAP3	0.19	0.31	0.60	0.70
CSRS-PPP	0.19	0.21	0.66	0.72
magicGNSS	0.32	0.35	0.52	0.70
APPS	0.58	0.23	0.91	1.10
BSW	0.40	1.09	1.67	2.03

Table 5.10: *MAP3, CSRS-PPP, magicGNSS, APPS and BSW positioning error RMS (cm) in long observation periods (24 hours).*

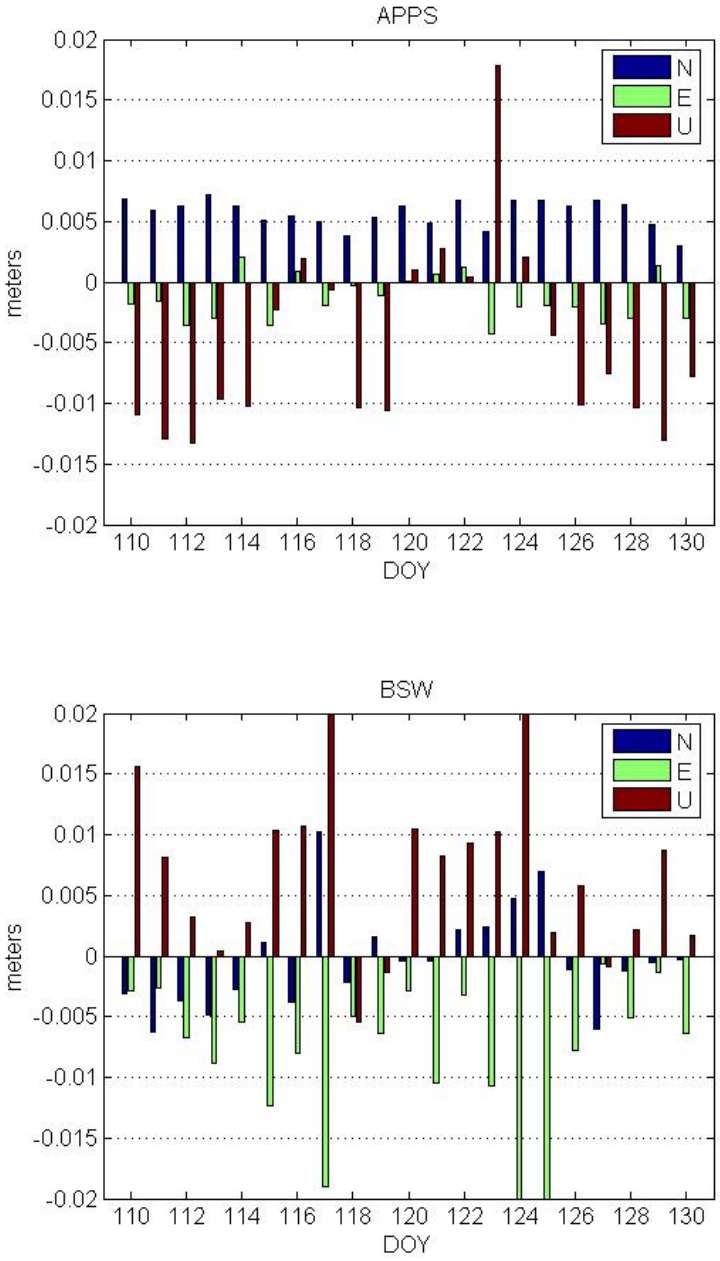

Figure 5.10: *APPS and BSW positioning error in long observation periods (24 hours). USN3 observations during days 110 to 130, 2010 have been processed.*

5.2.1.3. Test 3. Convergence time

In order to assess the convergence time of MAP3, the positioning error obtained in periods of increasing length has been analysed. USN3 observations in days 110 to 130 have been divided in intervals increased by 2 hours every time and the results of the processing are shown in Fig. 5.11 and Tab. 5.11. It can be observed that the north component is at 6 mm level accuracy from the first 2 hours observation and improves to the couple of mm after 18-20 hours. The east component is about 1.5 cm accurate from the first 2 hours, improves to the 5 mm after 10 observation hours and reaches 3-4 mm in one day. Finally, the up component is at 2 cm level accuracy after 2 hours, improves to about 8 cm in 10 hours and reaches the 5 mm level after 18 hours observation.

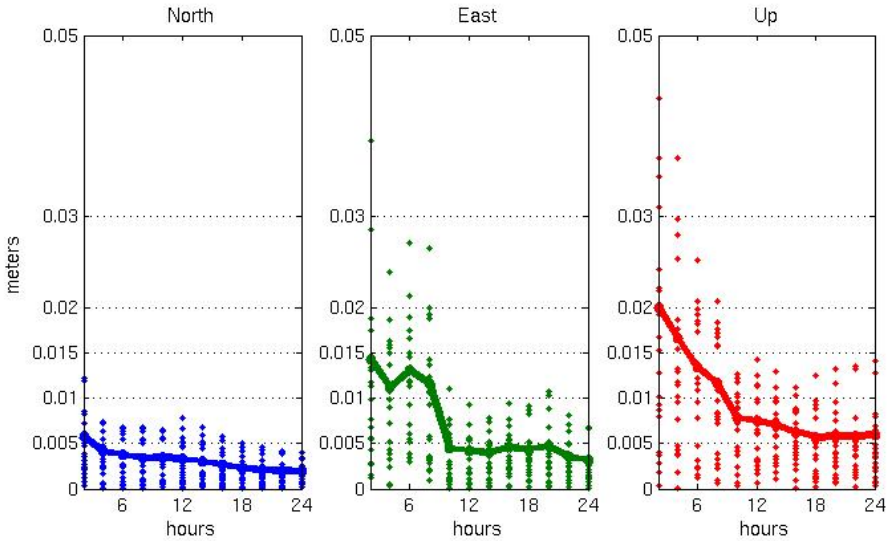

Figure 5.11: *MAP3 convergence time. The USN3 positioning error in the components North, East and Up obtained in observation periods of increasing length in days 110 to 130 is shown. The solid line correspond to the error RMS.*

Length (hours)	Accuracy (cm) N	E	U
2	0.6	1.4	2.0
12	0.4	0.5	0.7
18	0.3	0.5	0.6
24	0.2	0.3	0.6

Table 5.11: *MAP3 convergence time.*

5.2.1.4. Test 4. Influence of the electronic delays on the estimations

As it was observed in previous analysis of the MAP3 algorithms, the satellite and receiver electronic delays do not affect the position determination from GPS dual-frequency observations, but they are absorbed by the ionospheric delay and the initial ambiguities estimations. Nevertheless, it is mandatory to correct the electronic delays when the ionospheric delay is wanted.

However, the receiver electronic delay can not be completely removed and a remainder is still present in the observations, which will be absorbed by the receiver clock offset estimations. To ilustrate this result, the short observation periods of USN3 observations have been processed again with MAP3 and the electronic biases have been corrected. The errors in the estimated clock offset are shown in Fig. 5.12. It can be observed that the clock offset error has increased approximately 14.5 ns with respect to Fig. 5.5, where the DCB correction was not applied.

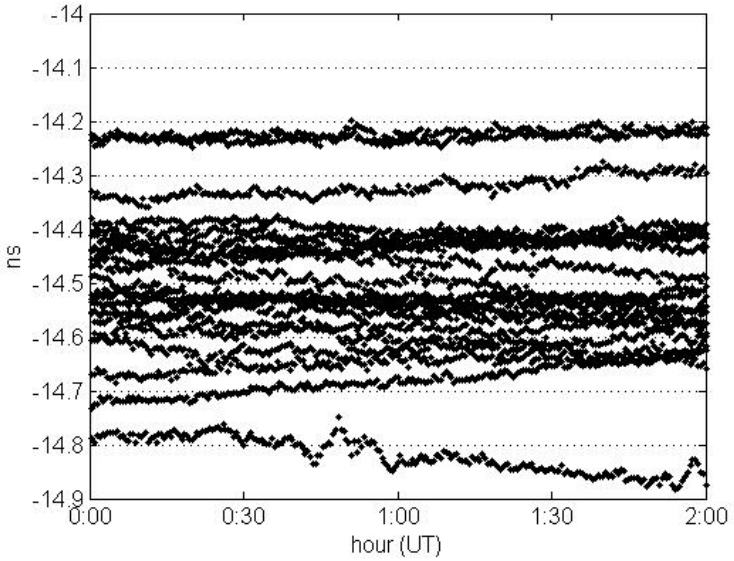

Figure 5.12: *MAP3 estimated clock offset error in days 110 to 130 (2010) when the electronic delays are corrected.*

On the other hand, the ionospheric delay obtained with MAP3 in DOY 120 has been converted to vTEC and compared with the corresponding GIM (CODE) and NOAA products (USTEC service, `www.swpc.noaa.gov/ustec`). The vTEC has been computed by mapping the estimated slant Total Electron Content (sTEC) to the vertical direction in the IP. MAP3 vTEC values, the GIM and

NOAA products are shown in Fig. 5.13. It can be observed that MAP3 vTEC are closer to the NOAA values than to the GIM, being the highest difference about 5 TECU. For satellites G16, G07 and G08, the estimated vTEC is within the NOAA error limits, while for the rest it is close to these limits. However, the GIM is global and its values are smoother, therefore the differences with the estimated values are higher, reaching up to 6 TECU. These differences reflect that the vTEC estimations obtained with MAP3 must still be improved.

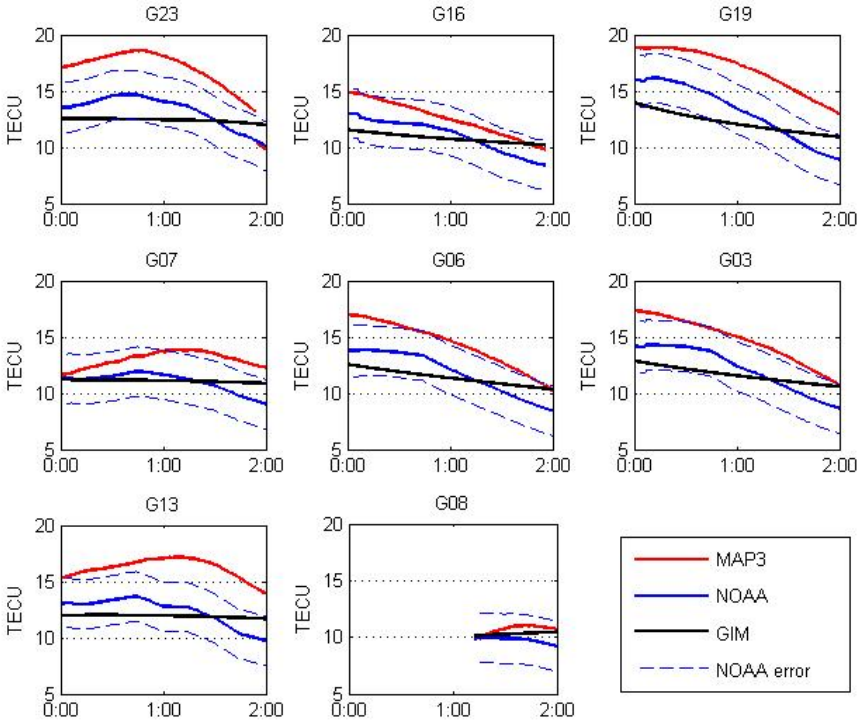

Figure 5.13: *MAP3 estimated vTEC and NOAA (USTEC) and CODE (GIM) products.*

5.2.2. Scenario II: GPS and GIOVE

The performance of MAP3 with real GPS and GIOVE triple-frequency observations has been analysed. In particular, 2-hour observation files taken at some GESS stations during the 1^{st} of November of 2009 have been processed along with GPC products. Since, for the time being, there is not exist any other PPP program able to work with GIOVE data, the results obtained in this scenario can not be compared with other softwares.

In this test GPS $P1$, $P2$ and GIOVE $E1BOC$, $E5bQPSK$, $E5AltBOC$ observations have been processed, the elevation cut-off angle is 10° and the satellite elevation weighting is applied. The GIOVE antennas PCO provided by GPC are corrected and the ISB is estimated when GPS and GIOVE observations are processed together.

It must be remembered that the GIOVE antennas PCV are unknown and, since the GESS coordinates (Tab. 5.3) are given at the antenna phase center, the receiver PCO correction is not applied. Moreover, the PCV values provided by GPC for GESS type-2 antennas introduce errors in the estimated positions and, therefore, the station PCV are not corrected. Finally, the ocean loading coefficients are not known for these stations and the correction is not applied.

Different tests have been run within this second scenario:

Test 1 GPS-only observations are processed.
Test 2 GPS and GIOVE observations are processed.
Test 3 GPS and GIOVE observations are processed and the satellite and receiver electronic biases are corrected.

5.2.2.1. Test 1. GPS-only observations

In order to analyse the achievable accuracies when processing GESS observations, in a first test only GPS observations have been considered. The MAP3 positioning errors are shown in Fig. 5.14.

Although an accuracy of about 2-3 cm in the estimated position is expected, errors of up to 15 cm are observed, what reflects the problems inherent to this data, such as the large code multipath variations registered in the GPS observations (Fig. 5.3), especially for stations GVES, GWUH and GNNO, where the errors are higher.

5.2.2.2. Test 2. GPS+GIOVE observations

In the second case, GPS and GIOVE observations have been processed together. The received GIOVE frequencies are E1 and E5b, transmitted by both GIOVE satellites, and E5 (E5a+b) transmitted only by GIOVE-B. The positioning error of the MAP3 algorithms with GPS+GIOVE observations is shown in Fig. 5.15.

It can be observed that the introduction of GIOVE observations does not influence significantly the estimations, only the accuracy of the north component improves in GVES and GNNO stations. The estimated coordinates of GIEN and

GWUH have not varied, since, for these two stations, only GIOVE-B observations have been included in the processing. The RMS of the positioning error is presented in Tab. 5.12, where it can be observed that the introduction of GIOVE observations increases the position errors in a few mm.

However, high GIOVE-B residuals have been observed (Fig. 5.17), which are due to the presence of the large IFB (Tab. 2.11). As a consequence, a third test has been carried out by considering the electronic delays in the processing.

5.2.2.3. Test 3. GPS+GIOVE observations and electronic delays correction

In a third test the GIOVE IFB are corrected and, for completeness, the GPS satellites DCB and station IFB have also been considered in the processing. The GPC estimations of the GESS and GIOVE IFB were presented in Fig. 1.16 and Tab. 2.11.

The positioning error obtained in this test is shown in Fig. 5.16. It can be observed that, when the electronic delays are taken into account, the GPS+GIOVE observations provide more accurate estimations than the GPS-only solution, especially for GNNO. However, the error in the east component in GVES and GMAL has increased, what can be due to the large multipath errors detected in the GIOVE observations (Fig. 5.2). The positioning error RMS is presented in Tab. 5.12. In general, the positioning accuracy with GPS+GIOVE observations improves almost 2 cm in the north and east components and 1.5 cm in the up with respect to the GPS-only solution. It can be also observed that the clock offset estimation has absorbed the residual part of the electronic biases correction.

The residuals obtained in this test are shown in Fig. 5.18. In this case, the GIOVE residuals are close to zero and, therefore, the IFB have been correctly removed from the observations.

Test	N	E	U	clk
		(cm)		(ns)
1. GPS-only	6.84	11.68	8.56	0.31
2. GPS+GIOVE	6.46	11.82	9.09	0.33
3. GPS+GIOVE (DCB, IFB)	5.09	9.93	7.00	32.49

Table 5.12: *MAP3 positioning error RMS with GPS-only and GPS+GIOVE observations.*

It must be also remembered that, for the time being, only two GIOVE satellites are available and therefore, the ISB estimation absorbs the mismodelled er-

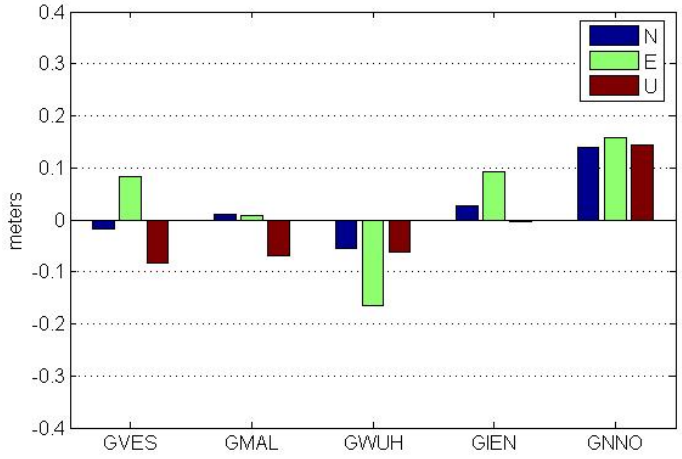

Figure 5.14: *MAP3 positioning error with GPS-only observations*

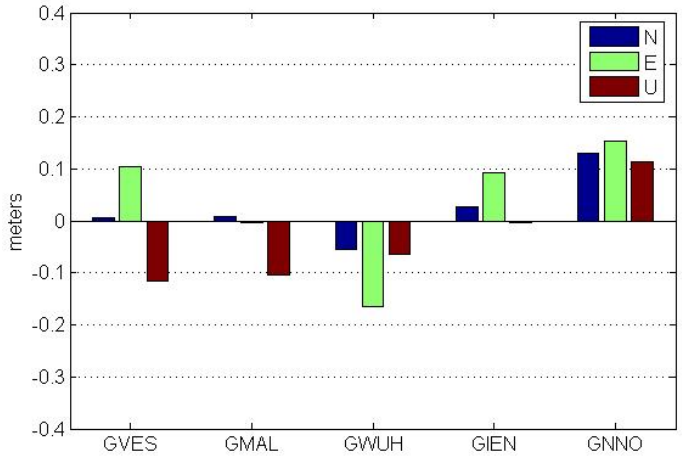

Figure 5.15: *MAP3 positioning error with GPS+GIOVE observations.*

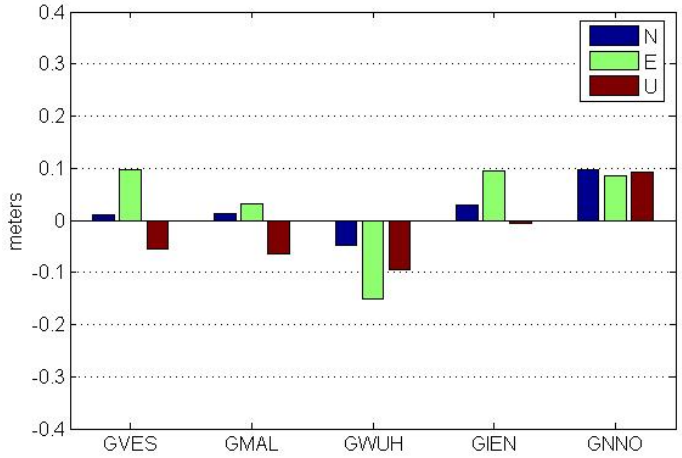

Figure 5.16: *MAP3 positioning error with GPS+GIOVE observations when the electronic delays are corrected.*

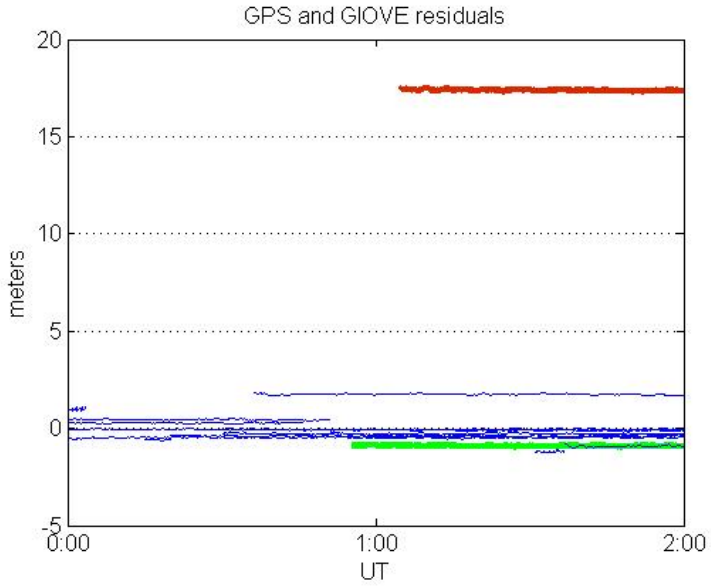

Figure 5.17: *GPS and GIOVE residuals. The blue lines correspond to GPS satellites, the red line to GIOVE-B (E16) and the green one to GIOVE-A (E01) residuals.*

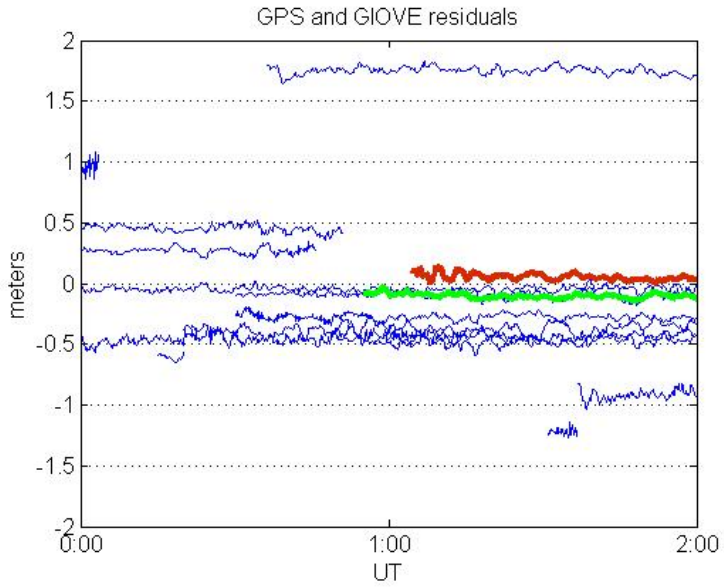

Figure 5.18: *GPS and GIOVE residuals after the electronic delays correction. The blue lines correspond to GPS satellites, the red line to GIOVE-B (E16) and the green one to GIOVE-A (E01) residuals.*

rors in the GIOVE observations. The ISB estimations obtained with MAP3 are presented in Tab. 5.13, along with the values provided by GPC. The absolute values of the ISB are of the same order of magnitude, but for GWUH and GIEN. For these stations only GIOVE-B signal was included in the processing and, therefore, the ISB estimation has absorbed all mismodelled errors in the GIOVE-B observations. GMAL and GNNO have tracked the GIOVE signal for a longer period, however, the large GIOVE-A multipath error (Fig. 5.2), especially in GNNO, limits the ISB estimation. It must be also said that better ISB estimations will be obtained when more Galileo satellites are available.

Station	Estimated ISB	ISB by GPC
GVES	20.80	-27
GMAL	24.30	-33
GWUH	64.61	-37
GIEN	216.01	-27
GNNO	26.33	-42

Table 5.13: *GESS stations estimated ISB (ns).*

5.2.3. Scenario III: GPS triple-frequency

The first GPS satellites transmitting the L5 signal are SVN49/PRN01 and SVN62/PRN25, however, before October of 2011, only SVN62/PRN25 could be used for positioning. In this scenario, some GPS data collected at UNAVCO station and including PRN25 triple-frequency observations, have been processed.

The PRN25 signals tracked were L1C/A, L2C and L5C and the observations of the rest of GPS satellites correspond to L1C/A and L2P. A set of 5 daily files from the 1^{st} to the 5^{th} of November, 2010 has been processed with MAP3, along with IGS precise products, and the estimated position has been compared to the mean estimated coordinates, since the precise coordinates of the station are not known.

The differences of the estimated positions with respect to the mean are shown in Fig. 5.19. It can be observed that, the estimations obtained in the five days agree within 2 mm, 9 mm and 4 mm in the north, east and up components. The worse repeatability in the east can be explained by the high noise level of the observations (Tab. 5.5).

It has been also observed that the differences between the triple-frequency solution and the L1-L2 solution are about 6 mm, what is maybe due to that the

antennas PCV and electronic delays for L5 signal are not yet available. This is confirmed by the residuals of satellite PRN25 when the L5 signal is included, which are slightly higher than those of the rest of satellites (Fig. 5.20).

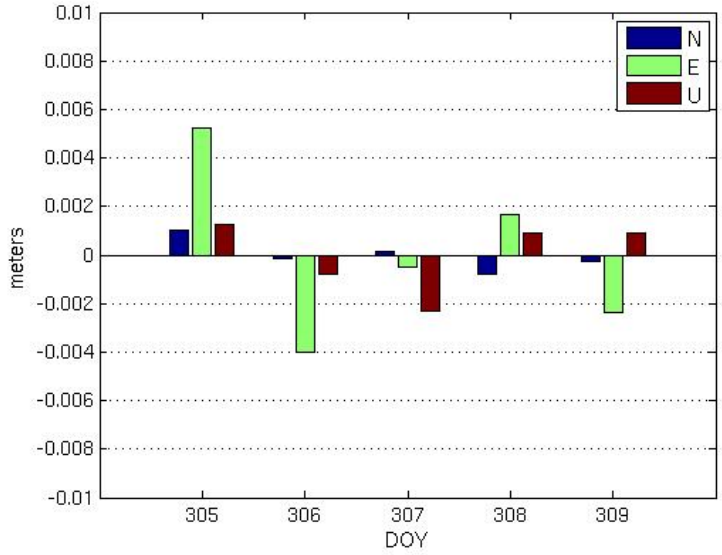

Figure 5.19: *MAP3 solution from GPS L1, L2 and L5 signals. The variation of the UNAVCO estimated position with the respect to the mean estimated coordinates is shown.*

5.2.4. Scenario IV: Modernized GPS and Galileo

The performance of the MAP3 algorithms in the modernized GPS and Galileo scenarios has been analysed through the processing of simulated data provided by ESA. In the simulation of the data, the errors due to satellite and receiver PCO/V, DCB, phase wind-up, Earth tide and other site displacement effects have not been considered and, therefore, no models to correct these effects have been applied in the processing of the observations. Moreover, since the observations are not affected by multipath or high noise at low elevations, a low elevation cut-off angle has been set.

Nevertheless, it must be stressed here that the observations provided by the simulations are not realistic, since they lack proper ionospheric and tropospheric delay, multipath and other errors which are present in the real GNSS observations. Therefore, definitive conclusions can not be drawn from the results obtained in this scenario.

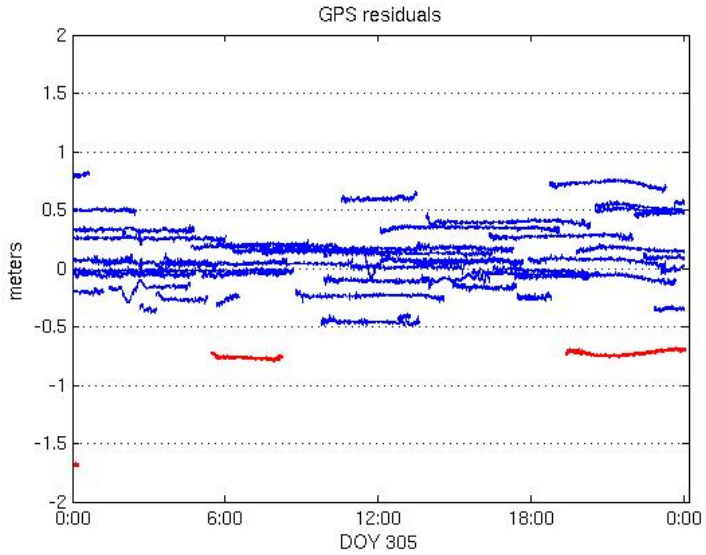

Figure 5.20: *SVN62/PRN25 residuals. The red line corresponds to satellite SVN62/PRN25 and the blue lines to the rest of GPS satellites.*

5.2.4.1. Test 1. Galileo-only observations

In first place, a test with 3 hours of simulated Galileo-only observations belonging to the OS frequencies E1-E5a-E5b, has been performed. In particular, a dataset consisting of 3 periods of 1 hour, 2 periods of 2 hours and 1 period of 3 hours at 1 s sampling rate have been processed. For comparison, tests with two of the three frequencies have also been run. The errors in the position estimation are displayed in Fig. 5.21. It can be observed that accuracies at 2 cm level are obtained in the first hour of observation and the results with frequencies E1-E5a and E1-E5a-E5b are identical down to the mm level. The most accurate results with 2 and 3 hours observation are obtained with the frequencies E5a-E5b. It has also been noticed that the estimated positions are not affected by the presence of the receiver IFB.

5.2.4.2. Test 2. Modernized GPS and Galileo observations

In a second test, an observation file with about 3 hours of GPS L1-L5 and Galileo E1-E5a-E5b observations has been used. The errors in the estimated position with GPS-only, Galileo-only and GPS+Galileo observations are shown in Fig. 5.22. The estimations obtained with GPS-only observations seem more accurate than those obtained with Galileo-only data, although the Geometric Dilution of Precision (GDOP) in the Galileo-only scenario is higher during the first part of the observation period, what limits the accuracy of the estimations. Another reason of the worse results obtained in the Galileo-only scenario may lie in the

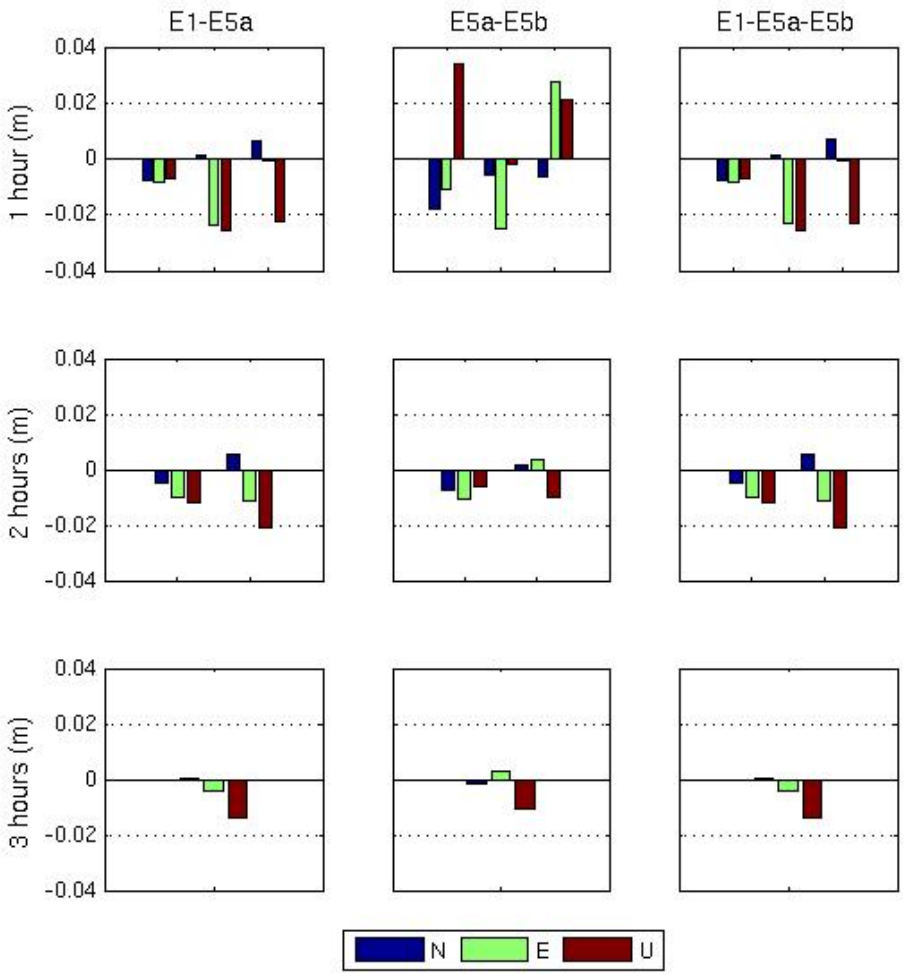

Figure 5.21: *MAP3 positioning error with simulated Galileo observations.*

navigation file used to compute Galileo satellites positions and clocks, since different navigation files are created for GPS and Galileo during the simulation and their accuracy is intentionally degraded by the simulator. On the other hand, the best GDOP and the most accurate solution are obtained in the combined GPS and Galileo scenario, as it was expected.

It has also been noticed that the estimated positions are not affected by the presence of the receiver IFB, which is about 3.89 m for GPS signals and 5.28 m for the Galileo frequencies. Finally, the estimated ISB is about 1.72 $\cdot 10^4$ ns.

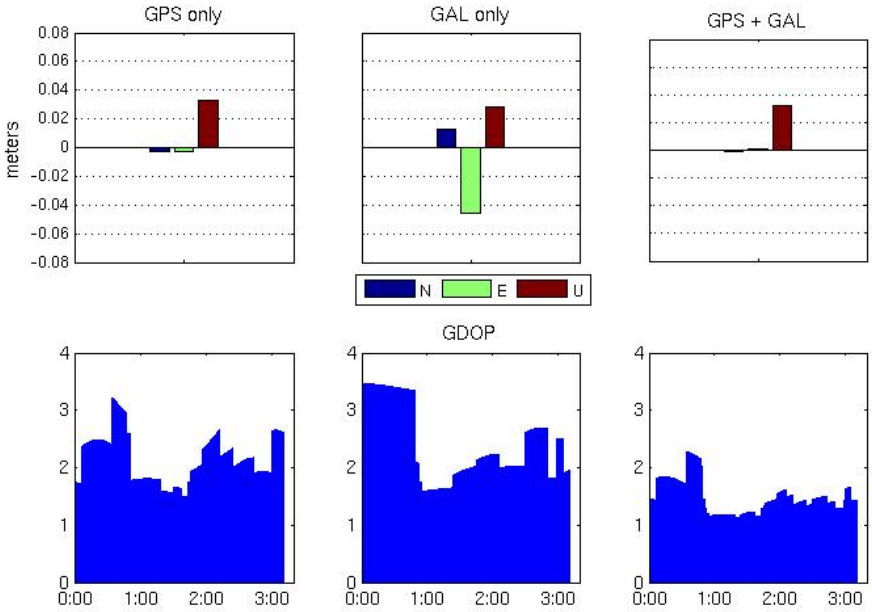

Figure 5.22: *MAP3 positioning error with simulated modernized GPS and Galileo observations.*

Chapter 6

Analysis of the Influence of Ionospheric Disturbances on Position Determination

The ionosphere constitutes one of the major error sources in positioning with GNSS techniques, not only due to the fact that the ionospheric refraction introduces errors of several metres in the measured ranges, but also the irregularities in the plasma density distribution can give place to a significant degradation of the transmitted signal (Jakowski et al., 2008). The GNSS signals affected by ionospheric irregularities may suffer strong variations in their amplitude, phase and Faraday rotation angle (Basu et al., 1986).

As a consecuence, it is most important to make a deep study about the features of the complex processes taking place within the ionosphere and their possible effects on GNSS positioning. Since strong variations in the ionospheric plasma density distribution are more frequent and intense in the proximity of the magnetic equator, the positioning techniques can be more affected in equatorial regions.

On the grounds of that, the MAP3 algorithms have been applied in the analysis of the possible effects of the equatorial ionospheric disturbancies on the single-epoch PPP. In this work, the possible relation between large Rate of TEC (ROT), observed at equatorial latitudes during post-sunset hours, and PPP estimate errors from dual-frequency observations has been investigated.

6.1. Introduction

As it was seen in the section 2.3, the ionosphere is the part of the atmosphere which extends, approximately, from 50 to 2000 Km above the Earth's surface and

it is ionized enough as to affect radio signals propagating through it (Hargreaves, 1992). The ionization observed in this region is produced mainly by the ultraviolet radiation and solar X-rays. At mid latitudes, this ionization is removed by chemical recombination processes, which involve the neutral atmosphere and ionized species. These processes also take place in high and low latitudes, however in such regions additional processes can be observed.

Over the magnetic equator the conductivity is exceptionally large due to the vertical limitation of the conducting layer, giving place to an enhanced current denoted as equatorial electrojet. Such current flows horizontally along the geomagnetic equator at E region height, eastward by day and westward by night. As it can be observed in Fig. 6.1, the equatorial electrojet, $\boldsymbol{E}$, combined with the north-south magnetic field of the Earth, $\boldsymbol{B}$, generate a drift of electrons to elevated heights in the ionosphere (fountain effect, Rishbeth (2000)). Then, electrons are forced to diffuse pole-ward along the geomagnetic field lines, producing a trough of electron concentration at the geomagnetic equator and two crests north and south at about 15° of geomagnetic dip latitudes, the EA.

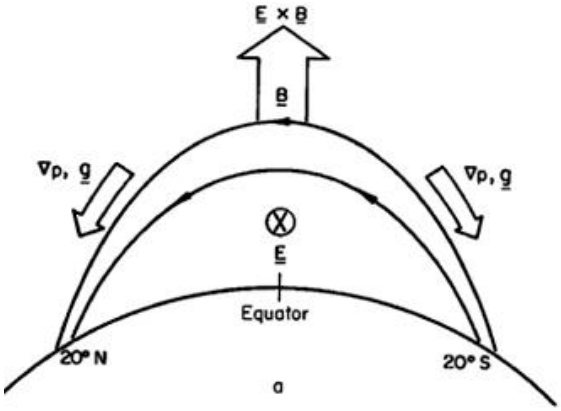

Figure 6.1: *Fountain Effect. Equatorial Anomaly formation process.*

Moreover, there are several phenomena which can produce the appearance of ionospheric plasma irregularities. For instance, large post-sunset vertical drifts can cause the resurgence of the equatorial fountain effect by reducing the ionization near the magnetic equator and, simultaneously increasing the ionization at higher latitudes, resulting in the development of plasma irregularities. These irregularities manifest as Equatorial Plasma Bubble (EPB) and scintillation of radio signals.

According to Tsunoda (1985), plasma bubbles are large-scale (10 to 100 km) depletions which form on the bottomside of the F-layer in the night-time equatorial ionosphere from irregularities and evolve following the Rayleigh-Taylor instability. EPBs present a cylindrical shape, extending in the south-north direction along the geomagnetic field lines and their electron density is inferior than the environmental one. They have been investigated by some authors such as Tsunoda (1985); Huang et al. (2001), who observed that EPBs were frequent during geomagnetic storms, Sobral et al. (2002); Abdu et al. (2003) analysed the climatology of EPBs in the Brazilian region and Portillo et al. (2008) studied the occurrence of EPBs in the African region.

On the other hand, the largest error in GNSS ranging is due to the ionospheric refraction of the signal, which can reach up to cents of metres in periods of intense solar activity and for satellites at low elevation. However, this ionospheric bias in the measured satellite-receiver distance is proportional to the integrated electron density along the ray path (TEC) and can be determined to a first order approximation from dual-frequency observations, what enables to eliminate almost completely (in a 99% (Seeber, 2003)) the ionosphere as a source of error.

The remaining error in GNSS observations due to the ionosphere may reach several centimetres and depends on the trajectory orientation and geophysical conditions (Brunner and Gu, 1991). The effects of higher-order terms on receiver position estimation have been studied by several authors, such as Bassiri and Hajj (1993); Fritsche et al. (2005); Munekane (2005); Hoque and Jakowski (2007); Hernandez-Pajares et al. (2007). In particular, Kedar et al. (2003) shown that the correction of the second-order term in PPP causes a latitudinal shift of about 0.1 - 0.5 cm with strong diurnal, seasonal and decadal signatures. The triple-frequency signals used by the future modernized GPS and Galileo systems will enable the determination of higher-order ionospheric terms (Kim and Tinin, 2007).

Moreover, ionospheric plasma irregularities can produce variations in the ionospheric delay of some centimetres (Kim and Tinin, 2007) and when the GNSS signal traverses an EPB it is affected by the sudden decrease in the plasma density within the bubble, what is reflected in a reduction of the measured pseudodistances. These density decreases generate rapid changes in amplitude and phase of radio signals propagating through the EPB and can produce the biggest ionospheric scintillations. As an example, Figs. 6.2 and 6.3 show the estimated sTEC and the corresponding scintillation index of GPS observations affected by an EPB (Panadero et al., 2010). The observations correspond to satellite PRN08 and were

taken at the Tucumán station on 7th December, 2000. As it can be observed, the scintillation period starts with the sudden decrease of the estimated sTEC values, i.e. under the influence of the bubble, and the maximum scintillation is observed from 5:00 UT on, i.e. when the signal was leaving the bubble.

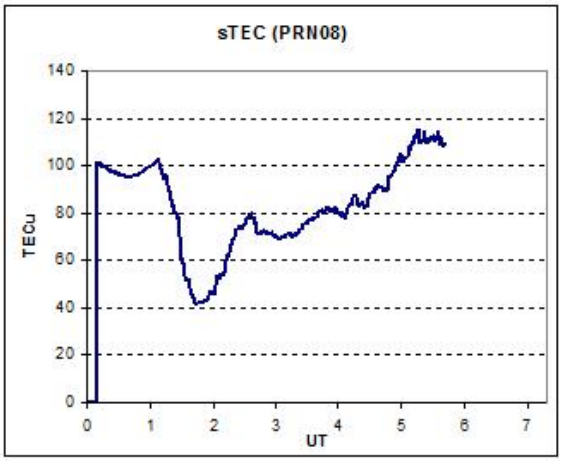

Figure 6.2: *Estimated sTEC at Tucumán station.*

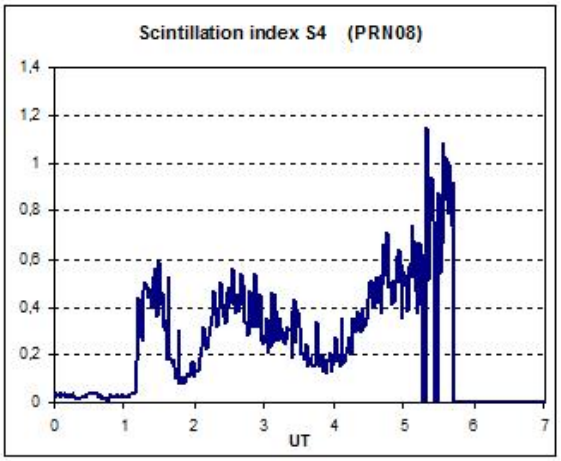

Figure 6.3: *Scintillation index S4 at Tucumán station.*

All these phenomena alter the plasma density distribution and can significantly affect position estimations with GNSS techniques, as proven by Tiwari et al. (2009) and Bergeot et al. (2010) for the case of geomagnetic storms.

6.2. The Methodology

The effect of the ionospheric irregularities on GNSS signals can be investigated by means of TEC estimations from dual-frequency observations. At mid-latitudes and quiet periods, TEC values are expected to vary gradually as a function of time, while, in the equatorial region, large ROT and pronounced TEC depletions associated to plasma bubbles are frequently observed (Portillo et al., 2008).

The MAP3 algorithms, presented in chapter 4, have been applied to GPS observations taken in the African equatorial region in order to estimate smoothed pseudodistances and ionospheric delay for every observed satellite. In the preprocessing of the observations the tropospheric delay has been reduced by using the Hopfield model and Niell mapping functions, the term due to the signal curvature produced by the troposphere has been neglected, satellite and receiver DCBs have been corrected with the monthly values given by CODE by following

the indications in section 4.5, satellite and receiver PCO/V given in the absolute calibration have been applied and the phase wind-up has been corrected by means of Wu et al. (1993) model.

Then, sTEC values have been obtained from the estimated ionospheric delays by means of (2.13) and the satellite elevation dependency has been removed by multiplying with the sine of the satellite elevation, therefore obtaining vTEC estimates. The ROT is then computed as the difference between 2 consecutive vTEC values. As an example, the ROT obtained in MALI during a part of the day 108 of 2004 is shown in Fig. 6.4.

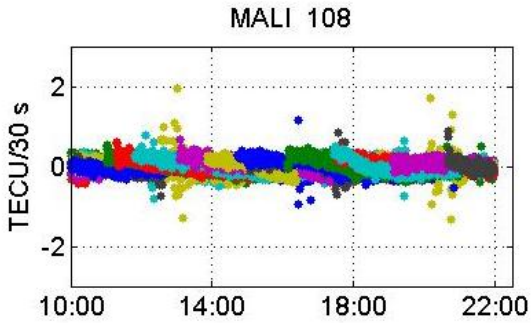

Figure 6.4: *ROT obtained at MALI station during day 108 of 2004.*

The smoothed pseudodistances estimated for the different satellites have been used to determine the station position and clock offset in a single-epoch LSA (section 3.5.1). Since our tests are carried out at IGS stations, IGS precise satellite orbits have been used (Dow et al., 2009) and precise coordinates and clock offsets computed by IGS are considered as a priori values.

Given that poor satellite geometries give rise to degraded position estimations, the satellite configuration geometry becomes an important factor. A measure of the satellite geometry effect on positioning is given by the Dilution of Precision (DOP), which is a function of satellites and receiver position and, therefore, varies with time. The GDOP can be computed as the square root of the trace of the inversed normal matrix obtained in the LSA, $N = A^t \cdot P \cdot A$, when the weight matrix is the identity matrix, $P = I$, so that higher GDOP values correspond to weaker geometry. In case that unexpected loss of lock of a tracked satellite weakens the geometry considerably, it would be reflected in a sudden GDOP increase. Typical GDOP factors range from 2 to 3, but can become 10 or higher in poor

viewing conditions. In this work, the GDOP values obtained vary in the range from 2 to 15, given a cut-off elevation angle of $15°$.

In order to reduce and smooth the effect of poor satellite geometry and sudden loss of lock on the estimation, a weighting function depending on GDOP has been defined. This function assigns values within the interval (0, 1) to the instantaneous GDOP in such a way that lower weights correspond to higher GDOP values. Thus, the weight function used is

$$w(GDOP) = \frac{maxGDOP - GDOP}{maxGDOP - minGDOP} \tag{6.1}$$

where the values used were $maxGDOP = 15$ and $minGDOP = 2$. Then, the differences of the estimated and precise IGS station coordinates at every epoch are multiplied with the corresponding weights given by the function.

6.3. Data Analysis

This study is based on the analysis of GPS observations taken at the IGS permanent station MALI (Malindi, Kenya) during the year 2004. This station belongs to the IGS permanent network and is located in the African region affected by the ionospheric EA .

The days of April 18-22, 2004 (DOY 109-112) were of particular interest in the MALI location because high TEC gradients have been observed in GPS observations repeatedly during these days. Such variations cannot be associated with a high geomagnetic activity, as it is seen in the Disturbance storm-time (Dst) shown in Fig. 6.5. The time period chosen for this study was geomagnetically quiet.

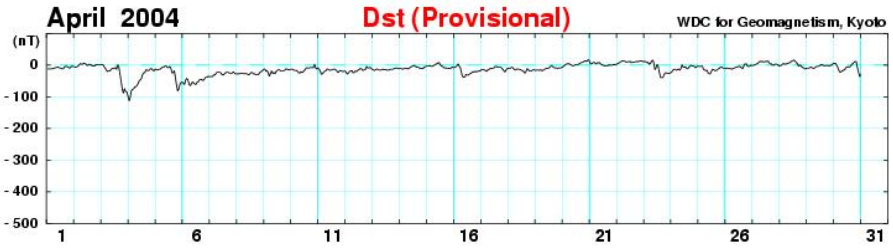

Figure 6.5: *Dst provisional index obtained by Kyoto University for April, 2004.* `http://wdc.kugi.Kyoto-u.ac.jp`.

However, some plasma depletions had been detected by Portillo et al. (2008) from sTEC values obtained at the MALI station around local sunset in days 109 to 113, whose average duration was 80 minutes and average TEC decrease was 9 TECU. These depletions indicate the presence of ionospheric irregularities associated with the EA formation processes.

For comparison, April 17, 2004 (DOY 108) has also been studied in this research, since no significant TEC gradients have been detected in MALI observations during this day. Moreover, two IGS stations located at mid-latitudes and, therefore, outside the region affected by the EA, have been added to the analysis. Observations taken at MAS1 (Mas Palomas, Spain) and PRE1 (Pretoria, South Africa) during the same days have been analyzed. The location of the three IGS stations is shown in Fig. 6.6 and Tab. 6.1.

In particular, the analyzed dataset consists of undifferenced GPS dual-frequency code and carrier phase observations, at 30 s sampling rate, taken by the IGS stations MALI, PRE1 and MAS1. The observation period is from 10:00 to 22:00 UT in days 108, 109 and 112 of 2004.

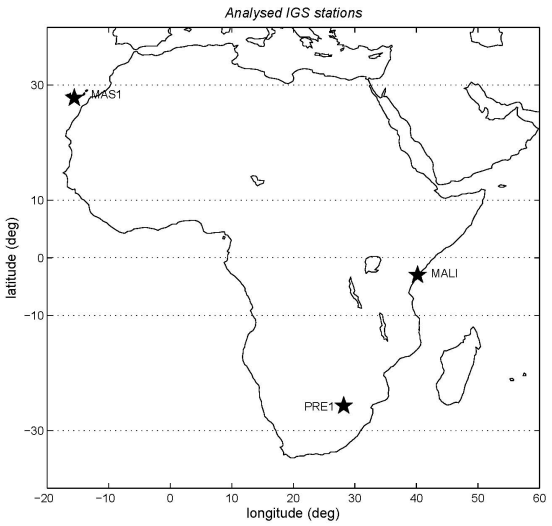

Figure 6.6: *Location of the analysed IGS stations.*

Station name	latitude (deg)	longitude (deg)	altitude (m)	DIP (deg)
MALI	-3.0	40.2	22.7	-26.6
MAS1	27.75	-15.6	197.3	37.4
PRE1	-25.7	28.2	1416.4	-61.1

Table 6.1: *Geographic coordinates of stations and geomagnetic DIP.*

6.4. Numerical Tests

First, MALI observations have been processed by the method described above and the ROT is computed as the difference between 2 consecutive estimated TEC values. Figure 6.7 shows the ROT obtained for satellites over 15° elevation for days 108 to 113 of 2004. It can be observed here that the TEC over the MALI station varies less than 1 TECU/30 s during most of the observed periods, especially during day 108, which was a quiet day and taken as reference. Larger variations of up to 3 TECU/30 s are observed during the periods from 17:00 to 22:00 UT in days 109 to 113. The large ROT reflects alterations in the received signal of different satellites, which could lead to degraded position estimations.

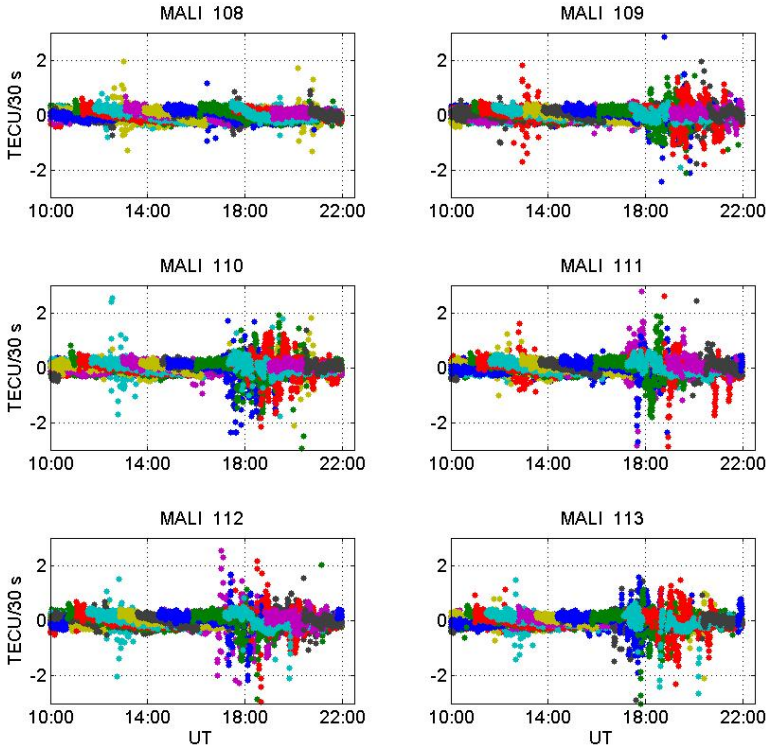

Figure 6.7: *ROT (TECU/30 s) obtained in MALI station for satellites over 15° elevation during 10:00 to 22:00 UT in days 108-113 of 2004.*

The coordinates of MALI have been estimated by means of a single-epoch LSA. Fig. 6.8 shows the differences between the MALI a priori and estimated altitude for the period 10:00 to 22:00 UT in days 108, 109 and 112; similar results have been obtained for the perturbed days. Given that positioning has being

carried out epoch by epoch, altitude variations up to 1 m are expected. However, large variations up to 4 m can be observed in days 109 and 112 during the periods from 17:00 to 22:00 UT, i.e. when large ROT have been registered, while during the first observation period and in day 108 the altitude variations remain within ± 1.5 m.

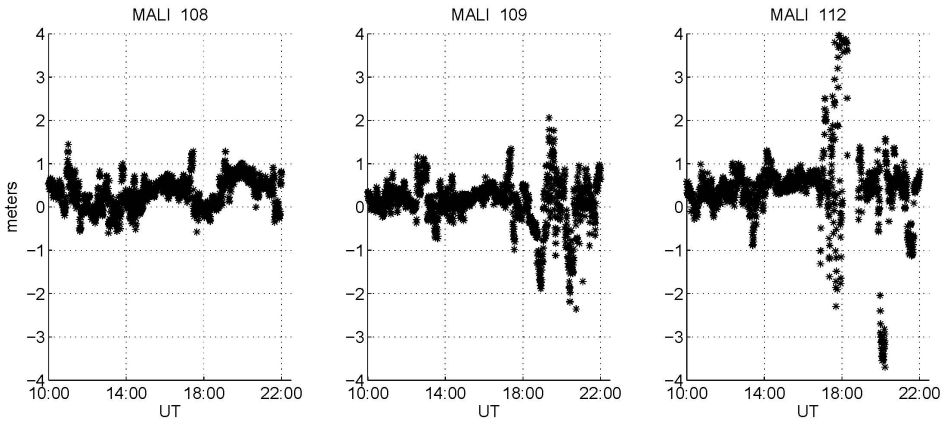

Figure 6.8: *Estimated altitude of MALI station in a single-epoch adjustment in days 108, 109 and 112 of 2004. The difference with respect to IGS05 position is shown.*

In order to eliminate the effect of weak satellite geometry as a possible cause of these abrupt variations, the altitude estimates have been smoothed by means of the GDOP weighting described above. The weighted altitude differences obtained for MALI in days 108, 109 and 112 are presented in Fig. 6.9. Due to the weighting, most of the small peaks observed in Fig. 6.8 have disappeared. Nevertheless, large variations of up to 4 m in altitude can still be observed in days 109 and 112 during the period from 17:00 to 22:00. On the other hand, the repeated loss of signal would mean degradation in the quality of the smoothed pseudodistances. However, no significant changes in satellite geometry have taken place during the period with largest positioning errors, as it can be seen in Fig. 6.10, although in day 109 a total loss of signal is observed at 18:19 UT. Therefore, the effect of the geometry can be discarded as a possible source of the detected errors in position estimation.

The same analysis has been performed for IGS stations MAS1 and PRE1, which are located at mid-latitudes and therefore outside the influence of the EA . Figure 6.11 shows the ROT obtained for satellites over 15° elevation at the stations MAS1, MALI and PRE1 during days 108, 109 and 112. Here, it can be seen that the ROT remains below 0.5 TECU/30 s most of the time for MAS1 and MALI, while

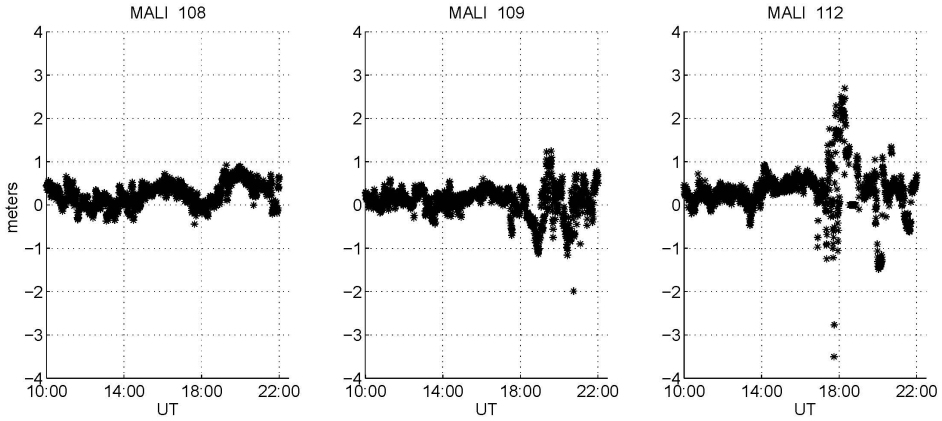

Figure 6.9: *Estimated altitude of MALI station weighted with GDOP values. The difference with respect to IGS05 position is shown.*

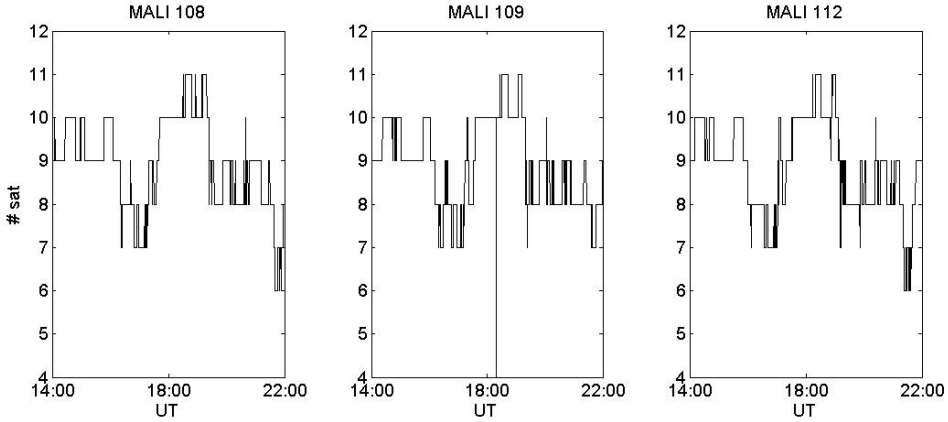

Figure 6.10: *Number of observed satellites in MALI station during period 14:00 - 22:00 of the days studied. The average number of satellites observed in the period 17:00 - 21:00 is very similar for the three days.*

in PRE1 it reaches 1 TECU/30 sec. This is due to a higher noise level introduced by the PRE1 receiver in the GPS observations. Contrary to the MALI station, MAS1 and PRE1 show a constant ROT for the three days analyzed.

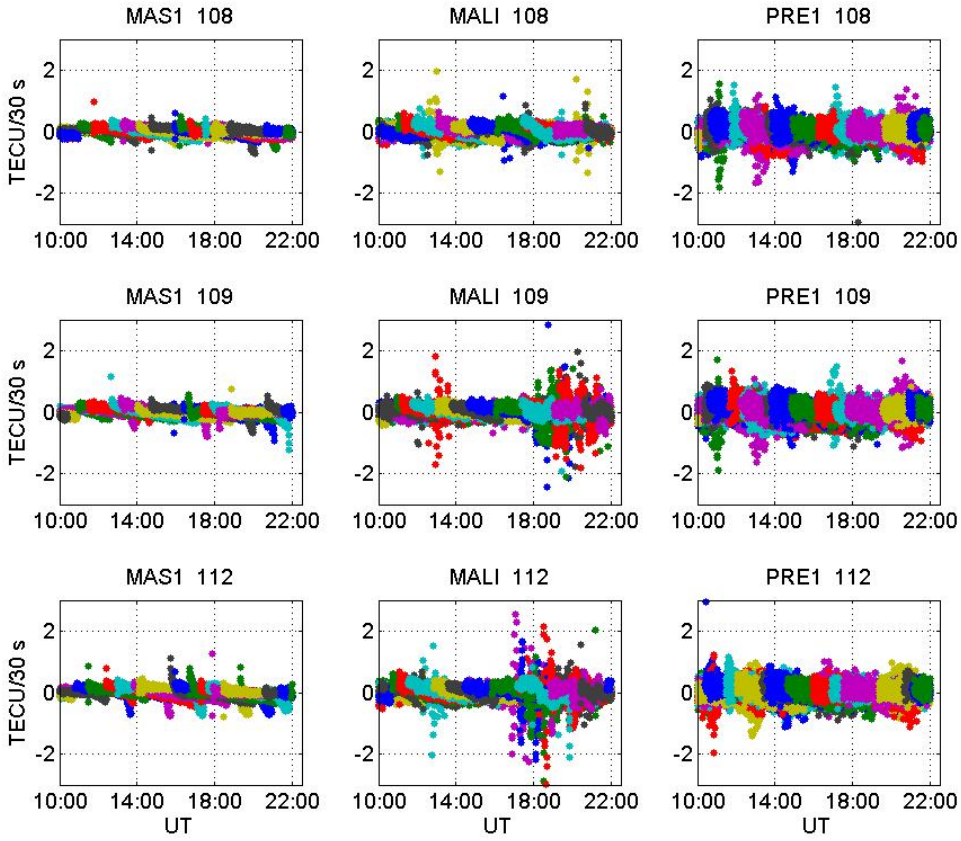

Figure 6.11: *ROT (TECU/30 s) obtained in MAS1, MALI and PRE1, for satellites over* 15° *elevation.*

In the same way, the positions of MAS1 and PRE1 have been estimated during these periods. The weighted differences in altitude with respect to IGS05 precise coordinates are shown in Fig. 6.12. The MAS1 clock offset computed by IGS was used as a priori value; however, neither the PRE1 clock offset nor the station DCB were available for the observation period. The figure shows that the MAS1 estimated altitudes are very close to each other and the weighted differences remain below 1 m. The PRE1 estimated altitudes present a higher noise level, in agreement with the TEC noise observed in Fig. 6.11, although no abrupt variations are seen. However, as mentioned above, the MALI altitudes show large

variations from 17:00 to 22:00 UT in days 109 and 112. On the contrary, the MALI weighted altitudes in day 108 vary slightly.

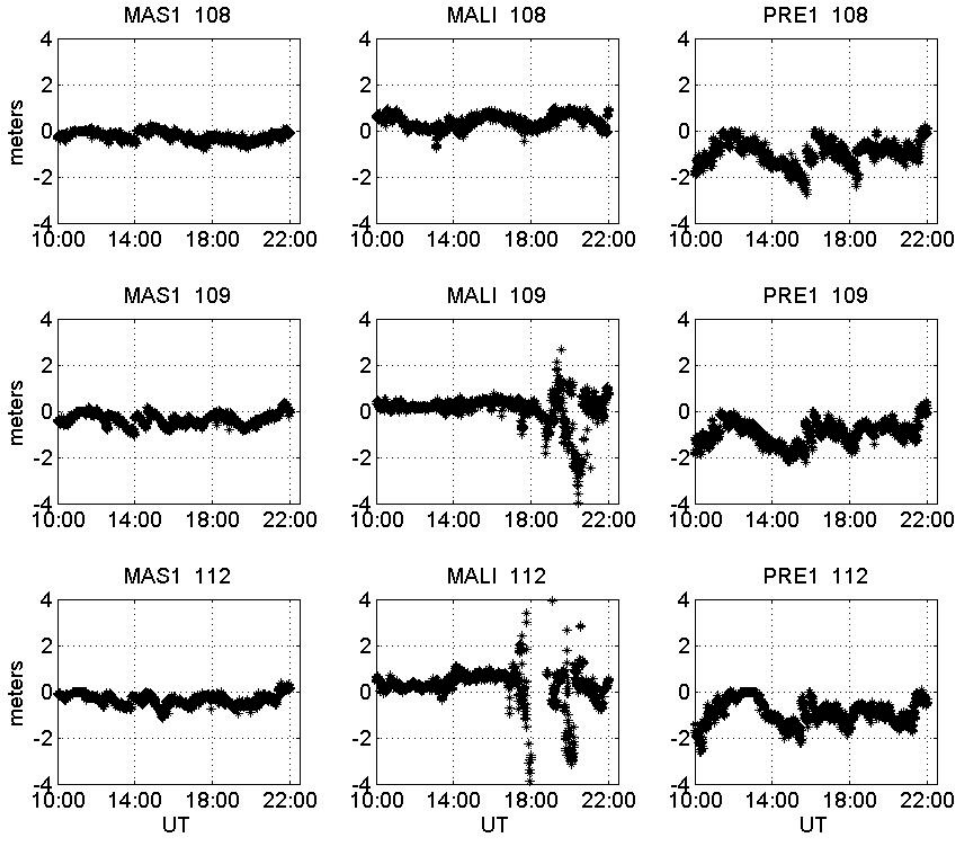

Figure 6.12: *Weighted altitude differences obtained in MAS1, MALI and PRE1.*

Once altitude variations have been analyzed, GDOP-weighted longitude and latitude of MAS1, MALI and PRE1 are studied. The differences with respect to a priori values are shown in Figs. 6.13 and 6.14. The longitude and latitude estimations present variations below 0.5 m for the MAS1 station, as well as for MALI during day 108. The PRE1 longitude and latitude errors remain below 1 m in all cases, without showing significant increases. However, there is a large error in the MALI longitude and latitude estimates from 17:00 to 22:00 UT in days 109 and 112.

In order to confirm the results obtained with the single-epoch PPP, the same observation files were processed in kinematic mode with the online program CSRS-PPP (section 3.1). The MALI coordinates were estimated by CSRS-PPP and

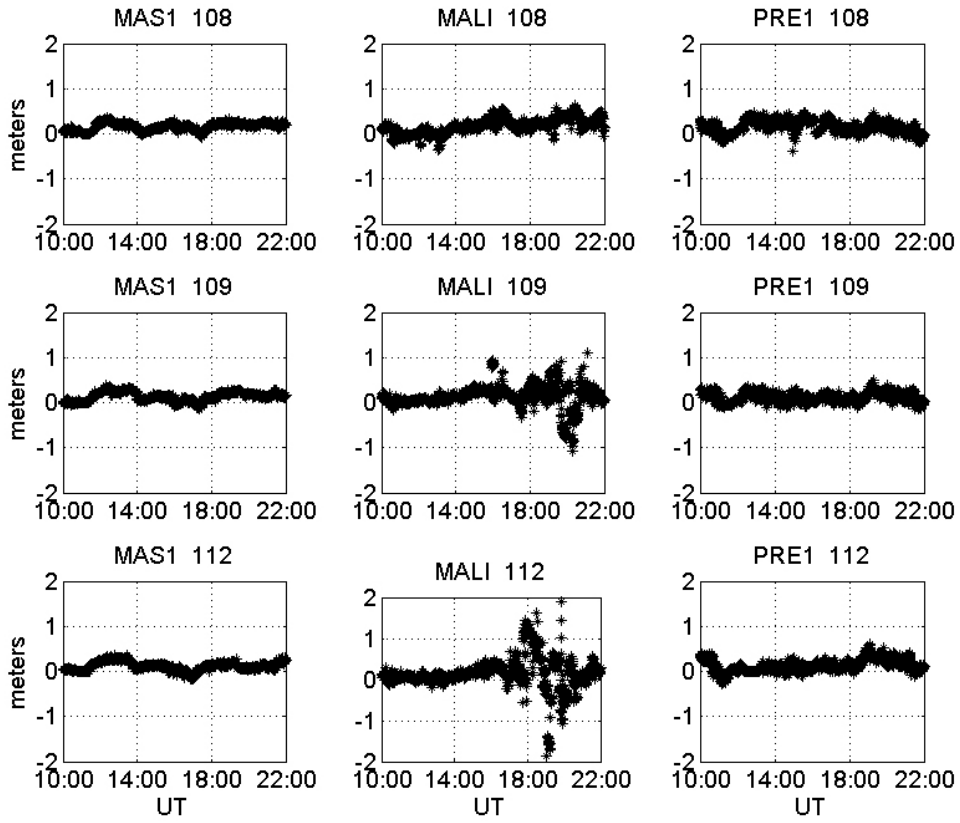

Figure 6.13: *Weighted longitude differences obtained in MAS1, MALI and PRE1.*

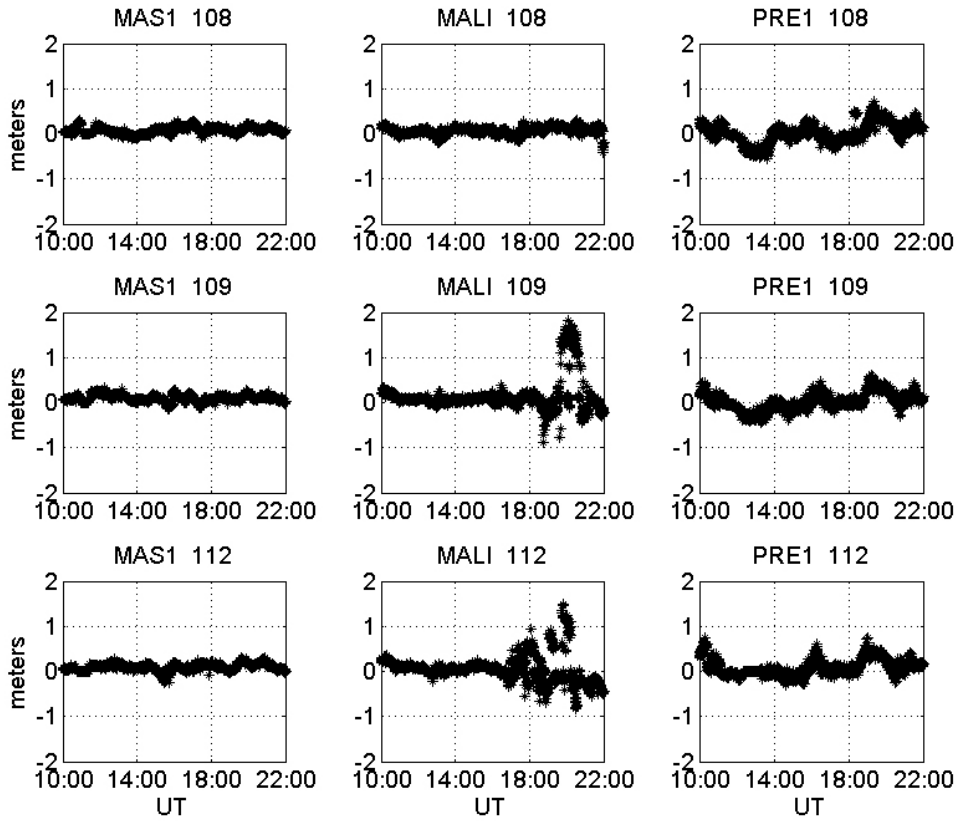

Figure 6.14: *Weighted latitude differences obtained in MAS1, MALI and PRE1.*

the difference with respect to a priori values are shown in Fig. 6.15. The solution provided by CSRS-PPP is smoother since a backward sequential filter is applied in kinematic mode. In agreement with the results obtained with the single-epoch LSA, during day 108 the differences between MALI position estimates and a priori values vary slightly during the observation period and remain below 0.5 m. However, large variations with respect to a priori values can be observed in days 109 and 112, especially in altitude. These errors reach 2 m on day 109 at about 20:00 and are higher than 20 m on day 112.

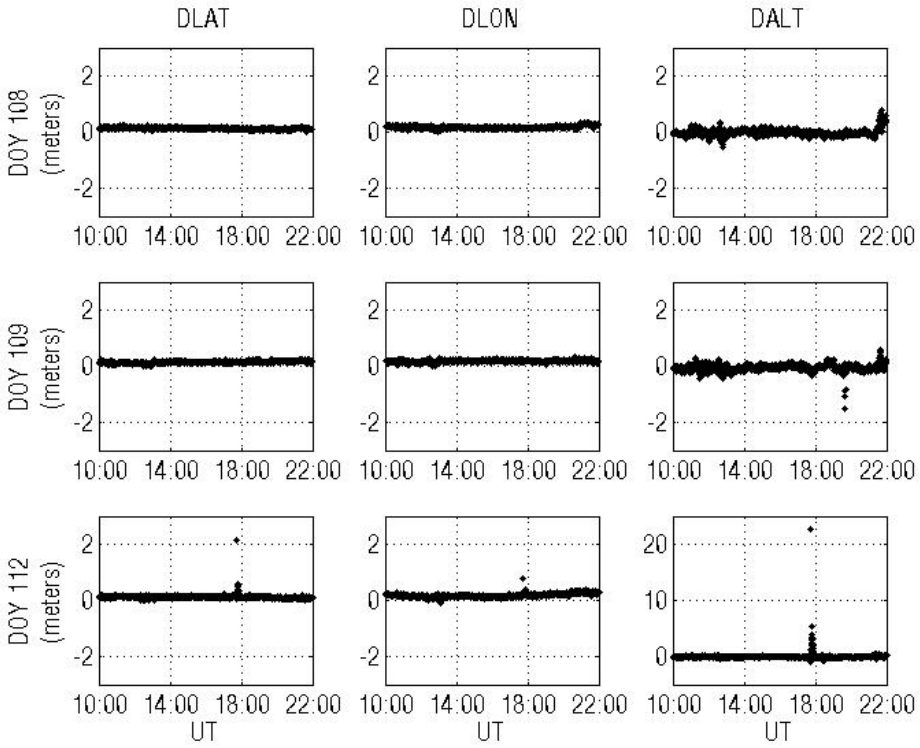

Figure 6.15: *MALI estimated coordinates (latitude, longitude, altitude) obtained with CSRS-PPP. The difference with respect to MALI a priori position is shown.*

In addition, the differences between PRE1 and MAS1 estimated coordinates with CSRS-PPP and their a priori positions have been obtained. These figures have been not included in the text given that they do not add relevant information. The estimates do not present large variations, but they remain within 0.5 m during the whole observation period for the three days, with the exception of a single jump of 1 m observed in the MAS1 estimated altitude in day 108 at about 11:30.

Chapter 7

Conclusions and Future Work Lines

The main objective of this thesis was the introduction of new positioning algorithms able to work in the future GNSS scenario, which will count on the modernized GPS and Galileo systems. In particular, the new MAP3 algorithms have been presented, which allow to perform static PPP from the future multi-system and multi-frequency observations.

MAP3 constitutes a new and original PPP strategy in which the least squares theory is applied to estimate the ionospheric delay, initial ambiguities and smoothed pseudodistances, which in turn are used to recover the receiver position and its clock offset.

The main advantage of MAP3 is its flexibility to combine multi-frequency observations from different satellite systems, in contrast to the classic PPP technique, which is limited to the use of dual-frequency observations. Moreover, MAP3 is prepared to deal with observations from the future modernized GPS and Galileo systems, while most of the current PPP programs can only work with GPS data and only a few support GLONASS observations.

The least squares theory applied by MAP3 provides covariance matrices of the estimated parameters, which are propagated from one step to the other to give place to complete weight matrices, accounting for temporal correlations between observations of the same satellite. Although this stochastic model is a simplification of the true covariance matrices, its use improves the estimation of the receiver position and its clock offset, with respect to the solution obtained with a model of uncorrelated observations. Moreover, the existence of an expression for the inverse of the covariance matrix reduces the computational time.

In the numerical tests of MAP3, it has been concluded that the accuracy reached in the position estimation in short and long observation periods (2 and 24 hours) is at the same level as the online programs CSRS-PPP and magicGNSS, about 2.5 cm position accuracy in 2 hours and 7 mm in 1 day (Tabs. 5.8 and 5.10).

It is important to stress that, in short observations periods, MAP3 has provided the most accurate estimations, with a difference of 7 mm with respect to the next best solution.

The precision provided by MAP3 is at few-mm level after 2 hours and at sub-mm level in 24 hours. However, it is well known that the precision of the PPP technique is too optimistic, given that the stochastical model is still too simple and the actual error and correlations between the observations are not considered.

The convergence time in the positioning with MAP3 has been also analysed and, generally, the 2 cm-level accuracy is reached with 2 hours of observation, 1 cm-level after 12 hours and 7 mm-level after 24 hours (Tab. 5.11).

In addition, it has been seen that it is neccessary to correct satellite and receiver electronic biases when the ionospheric delay is required or when GIOVE observations are processed. In that case, a remainder of the receiver delay will bias the observations and will be absorbed by the receiver clock estimation. Nevertheless, a deeper research on the effects and correction of the electronic delays in multi-system and multi-frequency observations must be carried out in the future, when more satellites are available.

On the other hand, the main problem found in the testing of the multi-frequency MAP3 algorithms has been the lack of real multi-frequency observations, since, for the time being, only two GIOVE satellites and two GPS satellites transmitting the L5 signal are available.

In the numerical tests performed with GIOVE triple-frequency observations collected at the GESS network, it has been shown that the presence of systematic code variations in the GESS observations gives place to errors in the position determination of up to 15 cm after 2 hours observation, when a 2 cm-level accuracy was expected. A remarkable result is that, when GPS and GIOVE observations are combined in the same processing, the position accuracy improves almost 2 cm in the every component with respect to the GPS-only solution. It has been also proven that the GIOVE IFB correction is always required and the ISB estimation absorbs the mismodelled errors in the GIOVE observations, especially when only one of the two GIOVE satellites is included in the processing.

In view of these results, it is planned to continue analysing the benefits of the introduction of the Galileo satellites in the positioning techniques, especially after the arrival of the first four Galileo satellites in the next months. This will also allow to study the influence of the offsets between GPS and Galileo reference

frames, to improve the estimation of the receiver ISB and to analyse the precision of the GPC satellite products.

In the numerical tests performed with GPS triple-frequency observations from satellite SVN62/PRN25, it has been observed that the introduction of a third frequency varies the estimated position in about 6 mm, what is due to the lack of the antennas PCV correction and the electronic delays for the L5 frequency. Moreover, the estimations obtained in the five analysed days agree within 2 mm, 9 mm and 4 mm in the north, east and up components and the worse repeatability in the east can be explained by the high noise level of the observations.

MAP3 performance in the modernized GPS and Galileo scenario has been analysed through simulated observations, kindly provided by ESA. As it was expected, the most accurate solutions were obtained in the GPS+Galileo scenario, where the lowest GDOP factors can be reached. On the other hand, in the Galileo-only scenario the most accurate results were obtained by processing observations in the frequencies E5a-E5b. Nevertheless, the simulated observations used in the numerical tests lack of proper ionospheric and tropospheric delays, multipath and other errors which are present in real GNSS observations and, therefore, reliable and definitive conclusions on the PPP performance in the future GNSS scenario can not be drawn from the results obtained in this work.

This fact reveals the need of developing a simulator of GNSS signal, able to generate realistic GNSS observations from the future multi-system, multi-frequency scenario, on which we are currently working.

Finally, the MAP3 algorithms have been applied in the analysis of the influence of equatorial ionospheric disturbances on point positioning. In this study it has been shown that, although the ionospheric delay is removed to a first order by means of the combination of dual-frequency observations, the position estimations at low latitudes present significant errors during the periods when large ROT is registered. The altitude is especially affected, reaching errors of several meters for a single-epoch positioning, although variations of a few meters can also be observed in the horizontal components. By contrast, during periods with small ROT at low and mid latitudes, no significant errors in the position estimation have been observed. The sudden satellite geometry changes have been discarded as possible cause of such errors by means of a GDOP weighting of the estimated coordinates and, as a consequence, it has been concluded that the presence of large ROT, observed at equatorial latitudes, reflects a significant degradation of dual-frequency point positioning estimations.

However, these results must be generalised to a higher number of stations and observation periods. In particular, it is planned to study the periods of large ROT during years of different solar activity (2001, 2004 and 2008), in order to detect some periodicity in the possible errors and anticipate the less favorable observation periods for the positioning at low latitudes. Moreover, the physical explanation of why a large ROT is accompanied by positioning degradation is not yet clear and further research will be carried out.

Appendix A

Numerical Tests of the Sequential Filter

The PCube software allows to choose among the MAP3 algorithms and a sequential filter to estimate the receiver position. The results obtained in the numerical tests of the MAP3 algorithms have been shown in the chapter 5 and the results provided by the sequential filter in short and long observation periods with data from USN3 station are presented here. It can be observed that, from dual-frequency observations both techniques provide very similar results although, in short observation periods, MAP3 still provides more accurate estimations.

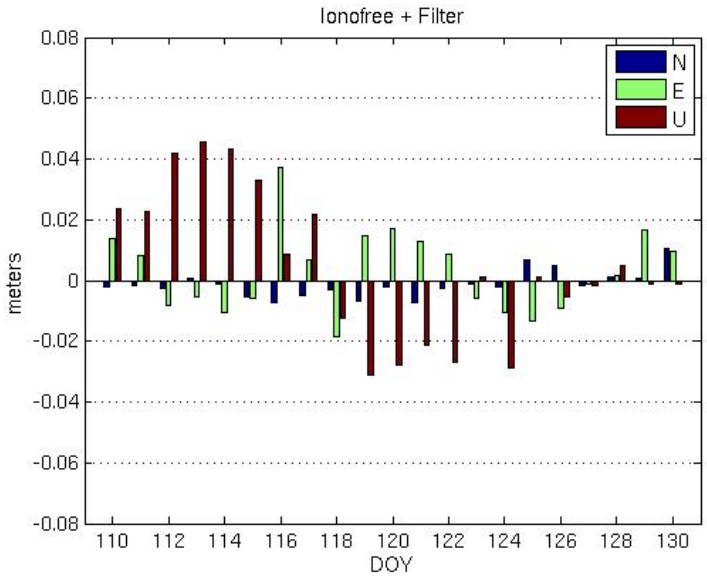

Figure A.1: *Sequential Filter positioning error in short observation periods (2 hours) in days 110 to 130, 2010.*

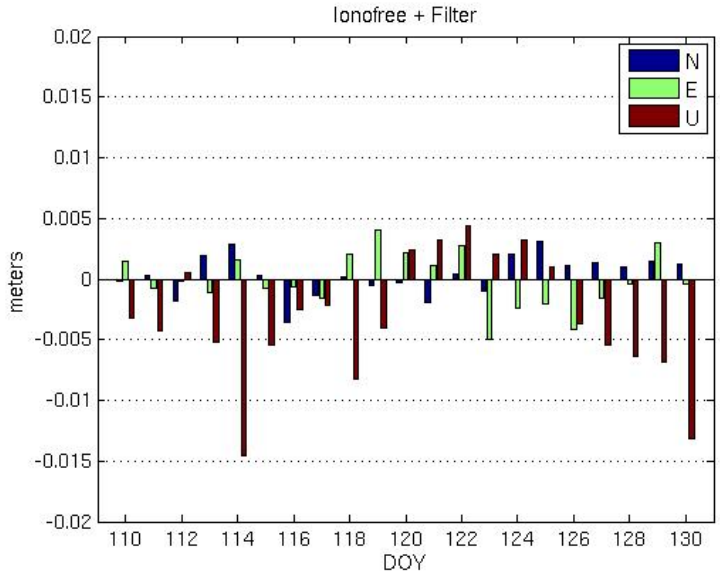

Figure A.2: *Sequential Filter positioning error in long observation periods (24 hours) in days 110 to 130, 2010.*

	2 hours				24 hours			
Technique	N	E	U	3D	N	E	U	3D
MAP3	0.6	1.4	2.0	2.5	0.19	0.31	0.60	0.70
Filter	0.5	1.4	2.4	2.8	0.16	0.25	0.61	0.68

Table A.1: *MAP3 and Sequential Filter positioning error RMS (cm) in short and long observation periods (2 and 24 hours).*

Appendix B

MAP3 Source Code in Matlab

```
function [E, B, C_EtEt, C_BB, Sroro, sig2pos] = MAP3_1(OBS, ...
                     freq, Var, cslips, SatEleWeighting, elev)

% ------------------------------------------------------------------ %
% MAP3_1
% ------------------------------------------------------------------ %
% Estimation of smoothed pseudodistances, initial ambiguities and
%      ionospheric delay from multi-frequency undifferenced code
%                     and phase observations
%
% ------------------------------------------------------------------ %
%
% input:
% ---------------
%   OBS              = (n,m) Code and phase observations          [m]
%                            to be used
%                            n: num. of epochs,
%                            m: num. of observables
%   freq             = [struct] .f1, f2, f3,.. : frequencies     [Hz]
%   Var              = [struct] .C1, C2, C3,.. : observations
%                                                noise^2        [m^2]
%   cslips           = epochs of detected cycle slips
%   SatEleWeighting  = %b if elevation weighting is to be applied
%   elev             = sat elevation                             [rad]
%
% output:
% ---------------
%   E                  = (n,2) estimated smoothed pseudodistances
%                               and ionospheric delay            [m]
%   B                = (n,m/2) estimated ambiguities              [m]
%   C_EtEt           = (n,2) estimated smoothed pseudodistances
%                       and ionospheric delay variance  [m^2]
```

```
%   C_BB            = (n,m/2,m/2) estimated ambiguities variance
%   S_roro          = (1,2)  a and d for pseudodistances
%                            weighting
%   sig2pos         = (n,1) a posteriori variance of unit weight
%
%
%   programmed by: bmorenom@mat.ucm.es
% ------------------------------------------------------------------ %


%% 1. INITIALIZE
nt = size(OBS,1);     % nt = # observations
nf = size(OBS,2)/2;   % nf = # frequencies

Lt = OBS(:,2:2:end); % Lt = phase meas. [m]
Ct = OBS(:,1:2:end); % Ct = code meas.  [m]


%% 2. ARCS CREATION
EmptObL   = [1; sum(isnan(OBS),2)~=0 ; 1]; % find empty epochs
Int_edge  = find( diff(EmptObL) ~= 0 );     % arc borders

% Consider observations in the same arc if the gap between
%          intervals is smaller than 3 epochs
smallgap = zeros(1,length(Int_edge));
for kext = 2:2:length(Int_edge)-1,
    if Int_edge(kext+1)-Int_edge(kext)< 3,
       smallgap(kext:kext+1) = 1;
    else smallgap(kext:kext+1) = 0;
    end
end
Int_edge  = Int_edge(~smallgap);

% add cycle slip epochs to split arcs
for kext = 1:length(cslips)
    if cslips(kext) > Int_edge(1) && cslips(kext) < Int_edge(end)
        Int_edge = sort([Int_edge; cslips(kext); cslips(kext)+1]);
    end
end


%% 3. MATRICES
%  3.1 Design matrix A
for kf = 1:nf
   k12 = ( freq.f1/freq.(['f',num2str(kf)]) )^2;
   A1(kf,:)  = [ 1 k12 ];
```

```
   A2(kf,:)  = [ 1 -k12];
end

%  3.2 Weight matrix : P = inv(Q)
for kf = 1:nf
   qc_kf = Var.L1/Var.(['C',num2str(kf)]);
   ql_kf = Var.L1/Var.(['L',num2str(kf)]);
   invQp(kf,kf) = qc_kf;
   invQl(kf,kf) = ql_kf;
   Ql(kf,kf)    = 1/ql_kf;
end

% 3.3 Normal Matrix : N = A1'Qp-1 A1 + A2' A2
N       = A1'*invQp*A1 + A2'*invQl*A2; % (nf x nf)
invN    = inv(N);

% 3.4 Coefficients
I_nf    = eye(nf);
D       = I_nf - A2*invN*A2'*invQl; % (nf x nf)
invD    = inv(D);

COEF_B_codes  = Ql*invD*invQl*A2*invN*A1'*invQp;
COEF_B_phases = invD - Ql*invD*invQl*A2*invN*A2'*invQl;
COEF_B_phases = I_nf;  % affected by rounding

NA2DA2N        = invN*A2'*invD*invQl*A2*invN;
COEF_E_code    = NA2DA2N *A1'*invQp;
COEF_E_phase   = NA2DA2N *A2'*invQl - invN*A2'*invQl*invD;
COEF_E_code_t  = invN*A1'*invQp;
COEF_E_phase_t = invN*A2'*invQl;


%% 4. ESTIMATION OF PARAMETERS
%  4.1 Initialize matrices
E       = zeros(nt,2)*NaN;
B       = zeros(nt,nf);
Ecte    = zeros(2,nt)*NaN;
C_EtEt  = zeros(nt,2)*NaN;
C_BB    = zeros(nt,nf,nf)*NaN;
sig2pos = zeros(nt,1);

% 4.2 Least Squares Adjustment in every arc
Ltaux = Lt;

for kl = 1:2: length(Int_edge)
```

```
% interval
ObsInt = (Int_edge(kl):Int_edge(kl+1)-1);

% Remove nan observations in the interval
ObsInt = ObsInt(~isnan(Ct(ObsInt,1)));

% interval length
len_ObsInt = length(ObsInt);
if len_ObsInt < 5, continue, end

% observations weighting
 sumKei   = sum( cos(pi/2-elev(ObsInt)).^2 ) ;
 if SatEleWeighting
     meanP = cos(pi/2-elev(ObsInt)).^2' / sumKei * Ct(ObsInt,:) ;
 else
     meanP = mean(Ct(ObsInt,:));
 end

 % 4.2.1 estimate ambiguities
 while 1,
    if SatEleWeighting
       meanL = cos(pi/2-elev(ObsInt)).^2' / sumKei * ...
          Ltaux(ObsInt,:);
    else
       meanL = mean(Ltaux(ObsInt,:));
    end

    ambig = [];
    ambig = repmat( ( COEF_B_phases*meanL' - COEF_B_codes * ...
       meanP')', len_ObsInt, 1 ); % row

    % update phases, Lt
    Ltaux(ObsInt,:)= Ltaux(ObsInt,:) - ambig;
    % save ambiguities in B
    B(ObsInt,:)    = ambig + B(ObsInt,:) ;
    % iterate until convergence
    if abs(ambig(1,1)) < 1e-7 && abs(ambig(1,2)) < 1e-7, break,end
 end

 % 4.2.2 estimate smoothed pseudodistances and ionospheric delay

 % observations weighting
 if SatEleWeighting
    meanL = cos(pi/2-elev(ObsInt)).^2' / sumKei * Ltaux(ObsInt,:);
 else
    meanL = mean(Ltaux(ObsInt,:));
```

```
end

% compute coefficient
Ecte(:,ObsInt) = repmat( COEF_E_code  * meanP' + COEF_E_phase * ...
    meanL', 1, len_ObsInt ); % column


sumv = 0;
for kt =1:len_ObsInt
    t = ObsInt(kt);

    % estimation
    E(t,:) = (COEF_E_code_t*Ct(t,:)' + ...
        COEF_E_phase_t*Ltaux(t,:)' + Ecte(:,t) )';    % E = [ro J]

    % Residuals
    v_C1 = A1*E(t,:)' - Ct(t,:)';
    v_L1 = A2*E(t,:)' - Ltaux(t,:)';%+ B(t,:)'


    if SatEleWeighting
        v2 = cos(pi/2-elev(t))^2 *(v_C1'*invQp*v_C1 + ...
            v_L1'*invQl*v_L1);
        CETET =  1/cos(pi/2-elev(t))^2 * invN + 1/sumKei* NA2DA2N;
    else
        v2 = v_C1'*invQp*v_C1 + v_L1'*invQl*v_L1;
        CETET = invN + 1/len_ObsInt * NA2DA2N; % 2x2
    end
    sumv = sumv + v2;
    C_EtEt(t,1) = CETET(1,1);
    C_EtEt(t,2) = CETET(2,2);

 end

 % 4.3 A posteriori sigma
 m = 2*nf*len_ObsInt;  % # observations
 r = 2*len_ObsInt + nf;% # unknowns

 s2post = sumv/(m - r);% a posteriori sigma of unit weight
 sig2pos(ObsInt,1) = s2post;

% 4.4 Covariance Matrices
%  Ambiguities
if SatEleWeighting
    C_BB(ObsInt(1),:,:)    = s2post * invD*Ql / sumKei;
else
```

```
        C_BB(ObsInt(1),:,:)    = s2post * invD*Ql /len_ObsInt;
    end
    %  Smoothed Pseudodistances and Ionospheric Delay
    C_EtEt(ObsInt,1) = s2post *C_EtEt(ObsInt,1); % ro
    C_EtEt(ObsInt,2) = s2post *C_EtEt(ObsInt,2); % J1

end

%% 5. SAVE COEFFICIENTS
d_        = invN(1,1);
a_        = NA2DA2N(1,1);
Sroro     = [a_, d_];
```

```
function [EstPos,StdPos,res_sat] = MAP3_2( SatList, sp3i, ...
     pseud, apriori, Tgps, TropoZenithDelayEst, ISBEst, TimeTag, ...
     SatEleWeighting )


% ------------------------------------------------------------------ %
% MAP3_2
% ------------------------------------------------------------------ %
% Estimation of receiver position and clock offset from smoothed
%      pseudodistances by using a complete weight matrix
%
% ------------------------------------------------------------------ %
%
% input:
% ---------------
%   SatList             = list of satellites
%   sp3i
%       .(satid).X      = (n,3) interpolated sat coordinates      [m]
%       .(satid).V      = (n,3) interpolated sat velocities     [m/s]
%       .(satid).Clk    = (n,1) interpolated sat clock offsets    [s]
%       .(satid).elev   = (n,1) sat elevation angle             [rad]
%                          n: num. of epochs
%   pseud
%       .(satid).ro     = (n,2) smoothed pseudodistances and std  [m]
%       .(satid).Sroro  = (1,2) a and d values for the weight
%                                  matrix
%       .(satid).sig2pseu=(n,1) a posteriori variances obtained
%                             in multif_algo_1
%   apriori
%       .X0             = (1,3) apriori position from rinex       [m]
%       .dtr            = (n,1) a priori station clk offset       [s]
%       .Tropo          = (1,1) initial value for ZWD             [m]
%
%   Tgps                = (n,1) GPS time                          [s]
%   TropoZenithDelayEst = %b   true for ZWD estimation
%   ISBEst              = %b   true for GPS-Giove ISB estimation
%   TimeTag             = (1,1) Time Tag between observations
%                               for processing              [epochs]
%   SatEleWeighting     = %b if elevation weighting
%                               is to be applied
%
% output:
% ---------------
%   EstPos              = (n,5) [x y z t Tzd ISB]
%                           estimated position, clock offset,
%                           Tropo zenit delay, ISB  [m,m,m,ns,m,ns]
```

```
%   StdPos              = (n,5) [sdx sdy sdz sdt sTzd sISB]
%                               std of the estimated parameters    [m]
%
%   res_sat.(satid)     = (n,1) satellite residuals                [m]
%
%
%   programmed by: bmorenom@mat.ucm.es
% ------------------------------------------------------------------ %


%% 1. INITIALIZE
constants

% useful constants
NObsT   = length(Tgps);                  % total number of epochs
NObs1   = floor((NObsT-1)/ TimeTag) +1; % # observations to be used
SamRate = Tgps(2) - Tgps(1);             % [s] receiver sampling rate
Nobs2h  = floor(7200/(SamRate*TimeTag));% # observations in 2 hours
N2hint  = floor((NObs1-1)/Nobs2h) + 1;  % # 2-hour intervals
NSat    = length(SatList);               % # satellites
Tgps    = Tgps(1:TimeTag:end);

% look for satellites without observations
ignore = zeros(1,NSat);
for n_sat = 1: NSat
    satid  = SatList { n_sat };
    if all(isnan(pseud.(satid).ro(1:TimeTag:end,1)))
       fprintf('\n ** Satellite %s ignored.' );...
       fprintf('No observations have been found **\n \n',satid);
       ignore(n_sat) = 1;
    else
        nobs.(satid) = sum(~isnan(pseud.(satid).ro(1:TimeTag:end,1)));
    end
end
SatList = SatList(~ignore);
NSat    = length(SatList) ;

% look for empty epochs and reshape
obsepo = zeros(NObs1,1);
for n_sat = 1: NSat
    satid  = SatList { n_sat };
    obsepo = obsepo + ~isnan( pseud.(satid).ro(1:TimeTag:end,1) );
end
noobs = obsepo==0;

if ~isempty( find(noobs == 1,1) )
```

```
    NObs = NObs1 - length(find(noobs == 1));
    Tgps = Tgps(~noobs);
else
    NObs = NObs1;
end

% compute # unknowns
Nunk  = 3;                                          % (X,Y,Z)
if TropoZenithDelayEst,                  % 1 ZWD every 2 hours
    Nunk = Nunk + N2hint;
end
for kint = 1: N2hint
    interval = ((kint-1)*Nobs2h+1 : min([ kint*Nobs2h, NObs1 ]) );
    interval = interval(~noobs(interval));
    if isempty(interval), Nunk = Nunk - 1; end
end

if ~isempty(strfind(strcat(SatList{:}),'G')) && ... % ISB
        ~isempty(strfind(strcat(SatList{:}),'E')) && ISBEst
    Nunk = Nunk + 1;
    gps_giove_ISB = 1;
else
    gps_giove_ISB = 0;
end

% a priori values
Xaux= apriori.X0;                   % Station coordinates
dtr = apriori.dtr(1:TimeTag:end); % [s] (Num_Obs, 1) Clock offset
dtr = dtr(~noobs);
ZWD = apriori.Tropo; % initial value for zenith wet component
if length( ZWD ) == 1, ZWD = ZWD*ones(NObs,1); end

% station geographic coordinates
[B0,L0,h0] = car2geo( Xaux(1),Xaux(2),Xaux(3) );

% output initialization
EstPos (1:NObsT,4) = nan;
StdPos = [];
for i = 1 : NSat,
    res_sat.(SatList{i}) = NaN*zeros(NObsT,1);
end


%% 2. CREATE MODELS
%% 2.1 Stochastic model: Cyyi.(INT).(satid)
for j = 1: NSat
```

```
    satid = SatList{j};
    ele   = sp3i.(satid).elev(1:TimeTag:end,:);
    pseu  = pseud.(satid).ro(1:TimeTag:end,1);
    ele   = ele (~noobs,:);
    pseu  = pseu(~noobs,:);

    a_ = pseud.(satid).Sroro(1); % depend on num of freq
    d_ = pseud.(satid).Sroro(2);

    sig2pseu = pseud.(satid).sig2pos(1:TimeTag:end,1);
    sig2pseu = sig2pseu(~noobs,:);

    % create block matrix in continuous arcs
    pos_isnan.(satid) = isnan(pseu); clear pseu
    int_edges = diff([1, pos_isnan.(satid)', 1]);
    ini_edge  = find(int_edges == -1) ;
    end_edge  = find(int_edges ==  1)- 1;

    sig2 = sig2pseu(ini_edge);

    Cyy_1.(satid) = sparse(NObs,NObs);
    for kint = 1: length(ini_edge)
    int = (ini_edge(kint):  end_edge(kint));

    if SatEleWeighting
        sumKei   = sum( cos(pi/2-ele(int)).^2 )^-1;

        a = a_ * sumKei;
        d = d_ ./cos(pi/2-ele(int)).^2;

        Cyy = sig2(kint) * ( a*ones(length(int),length(int)) + ...
            diag(d) );
        % Invert: inv() is faster than Cholesky decomp. with small ...
            matrices
        Cyy_1.(satid)(int,int) = inv( Cyy ) ;
        clear Cyy d int
    else
        a = a_/length(int);
        Cyy_1.(satid)(int,int) =  1/sig2(kint) * 1/d_ * ...
            (eye(length(int)) - a/(d_+length(int)*a) * ...
            ones(length(int),length(int)));
    end
    end
end
```

```
%% Estimate parameters and iterate until convergence
iterdX = 1;
while iterdX

    %% Estimate ZWD and iterate for short observation periods
    iterZWD = 1;
    while iterZWD

    %% 2.2. Mathematical model
    for j = 1: NSat
        satid = SatList{j};
        Xs    = sp3i.(satid).X(1:TimeTag:end,:);
        ele   = sp3i.(satid).elev(1:TimeTag:end,:);
        pseu  = pseud.(satid).ro(1:TimeTag:end,1);

        Xs   = Xs(~noobs,:);
        ele  = ele(~noobs,:);
        pseu = pseu(~noobs,:);

        %% A. Design matrix
        Dir  = sqrt(( Xs(:,1)-Xaux(1)).^2 + ...
            ( Xs(:,2)-Xaux(2)).^2 +( Xs(:,3)-Xaux(3)).^2);

        Gi.(satid)  = -[(Xs(:,1)-Xaux(1))./ Dir, ...
            (Xs(:,2)-Xaux(2))./ Dir, (Xs(:,3)-Xaux(3))./ Dir] ;

         % Add ZWD coeficients to design matrix
        [gmfh,gmfw] = gmf_f_hu (Tgps,B0,L0,h0,pi/2-ele);
        if TropoZenithDelayEst,
            lst_epo=0;
        for kint = 1: N2hint
            interval = ((kint-1)*Nobs2h+1 : min([ kint*Nobs2h, ...
               NObs1 ]) );
            interval = interval(~noobs(interval));
            if ~isempty(interval)
               l_new   = length(interval) + lst_epo;
               Gi.(satid)(lst_epo+1:l_new, 3+kint) = ...
                  gmfh(lst_epo+1:l_new);
               lst_epo = l_new;
            end
        end
        end
          % Add ISB coeficient in case gps + giove obs used
        if gps_giove_ISB, % 1 if giove, 0 if gps
            Gi.(satid)(:,end+1) = strcmp(satid(1),'E')*ones(NObs,1);
        end
```

```
    %% B. Observation vector yk.(satid)
    yi.(satid) = pseu - Dir - c*dtr - ZWD.*gmfw ;
    clear gmfw gmfh pseu Dir

    %% remove epochs without data in Gi
    pos_isnan.(satid) = isnan(yi.(satid));
    Gi.(satid)(pos_isnan.(satid),:) = 0;
    yi.(satid)(pos_isnan.(satid))   = 0;

end % for j = 1: NSat

%% 3. COMPUTE BLOCK MATRICES
Ntilde = zeros(NObs,NObs);
F = zeros(Nunk,Nunk);
E = zeros(NObs,Nunk);
d1 = zeros(NObs,1);
d2 = zeros(Nunk,1);

for j = 1: NSat
    satid = SatList{j};

    % N matrix
    Ntilde = Ntilde + Cyy_1.(satid);

    Cyy_1_Gi = Cyy_1.(satid)*Gi.(satid); % to fasten the process
    E  = E + Cyy_1_Gi;
    F  = F + Gi.(satid)'*Cyy_1_Gi;

    % d vector
    Cyy_1_yi = Cyy_1.(satid) * yi.(satid);% to fasten process
    d1 = d1  + Cyy_1_yi;
    d2 = d2+ Gi.(satid)' * Cyy_1_yi;

end
clear Cyy_1_yi Cyy_1_Gi

%% 4. INVERT
CholeskyN = inv( chol(Ntilde) ); % Cholesky decomposition
Ntilde_1  = CholeskyN*CholeskyN'; % Here Cholesky is faster ...
   than inv()

clear CholeskyN

gamma = inv( F - E' * Ntilde_1 * E );
Delta = -Ntilde_1 * E * gamma;
```

```
Gamma = Ntilde_1 * (eye(NObs) - E*Delta');


%% 5.  ESTIMATE PARAMETERS
cdtr =  Gamma * d1 + Delta* d2;
dX   =  Delta'* d1 + gamma* d2;

clear E Ntilde F Delta d2 Ntilde_1 d1

%% 6. RESIDUALS AND A POSTERIORI VARIANCE
VTPV = 0; NObsEq =0;
for k = 1:NSat
    satid = SatList{k};
    I = eye(NObs);
    I(pos_isnan.(satid),:) = 0;
    res_sat.(satid) = [Gi.(satid), I ] * [dX; cdtr ] - yi.(satid);
    VTPV   = VTPV + res_sat.(satid)' * Cyy_1.(satid) * ...
       res_sat.(satid);
    NObsEq = NObsEq + nobs.(satid);
end
sigpos2  = VTPV /( NObsEq  - (Nunk+NObs)  );
clear VTPV I


%% 7. UPDATE AND ITERATE WITH LESS UNKNOWNS
if TropoZenithDelayEst && NObs < 4*Nobs2h

    kunk = 0;lst_epo=0;
for kint = 1: N2hint,
    interval = ((kint-1)*Nobs2h+1 : min([ kint*Nobs2h, NObs1 ]) );
    interval = interval(~noobs(interval));
    if ~isempty(interval)
        l_new   = length(interval)+lst_epo;
        kunk    = kunk+1;
        ZWD(lst_epo+1:l_new,1) = ZWD(lst_epo+1:l_new,1) + ...
           dX(3+kunk);
        lst_epo = l_new;
    end
end

TropoZenithDelayEst = 0;
Nunk = Nunk - N2hint;
Xaux = Xaux+ dX(1:3)';
dtr  = dtr + cdtr/c;

clear Gi yi d2 d1 gamma Gamma
```

```
    continue
    else
        iterZWD = 0;
    end

    end % while iterZWD

    %%  8. UPDATE AND ITERATE
    if sum(abs(dX(1:3))) > 1e-3
        Xaux    = Xaux+ dX(1:3)';
        dtr     = dtr + cdtr/c;
    if TropoZenithDelayEst
        kunk = 0;lst_epo=0;
        for kint = 1: N2hint,
            interval = ((kint-1)*Nobs2h+1 : min([ kint*Nobs2h, ...
               NObs1 ]) );
            interval = interval(~noobs(interval));
            if ~isempty(interval)
                l_new   = length(interval) + lst_epo;
                kunk    = kunk+1;
                ZWD(lst_epo+1:l_new,1) = ZWD(lst_epo+1:l_new,1) + ...
                   dX(3+kunk);
                lst_epo = l_new;
            end
        end
    end
        clear Gi yi d2 d1 gamma Gamma
    else
        iterdX = 0;
        clear Gi yi d2 d1
    end

end % while iterdX


%% 9. OUTPUT
% 9.1 Estimations
EstPos(:,1:3)   = repmat(Xaux + dX(1:3)',NObsT,1);
EstPos(~noobs,4)= dtr*1e9 + cdtr/c*1e9 ;

if TropoZenithDelayEst,
    kunk = 0; lst_epo=0;
    for kint = 1: N2hint,
        interval = ((kint-1)*Nobs2h+1 : min([ kint*Nobs2h, NObs1 ]) );
        interval = interval(~noobs(interval));
        interval2= ((kint-1)*Nobs2h+1 : min([ kint*Nobs2h, NObsT ]) );
```

```
        if ~isempty(interval)
            l_new   = length(interval)+lst_epo;
            kunk    = kunk+1;
            EstPos(interval2,5)= ZWD(lst_epo+1,1) + dX(3+kunk);
            lst_epo = l_new;
        end
    end
else
    EstPos(~noobs,5) = ZWD;
end
if gps_giove_ISB,
    EstPos(:,6) = repmat(dX(end)/c*1e9,size(EstPos,1),1);
end

% 9.2 Standard deviation of estimations
StdPos(:,1:3)   = repmat(sqrt(sigpos2 * ...
   diag(gamma(1:3,1:3)))',NObsT,1);
StdPos(~noobs,4)= sqrt(sigpos2 *diag(Gamma));
if gps_giove_ISB,
    StdPos(:,6) = repmat(sqrt(sigpos2 * ...
       diag(gamma(end,end)))',NObsT,1);
end
```

References

M. A. Abdu, I. S. Batista, H. Takahashi, J. MacDougall, J. H. Sobral, A. F. Medeiros, and N. B. Trivedi. Magnetospheric disturbance induced equatorial plasma bubble development and dynamics: A case study in Brazilian sector. *Journal of Geophysical Research*, 108 (A12):1449, 2003.

D. Aloi and F. van Graas. Ground-Multipath Mitigation via Polarization Steering of GPS Signal. *IEEE Transactions of Aerospace and Electronic systems*, 40(2):536–552, 2004.

N. Ashby. *Relativity in the Global Positioning System*. Living Reviews in Relativity, 6, 2003.

W. Baarda. A testing procedure for use in geodetic networks. *NGC-publications on geodesy*, 2(5), 1968.

S. Banville, R. B. Langley, and M. C. Santos. The Precise Point Positioning Software Centre: An Insight Into Online PPP Services. Poster presented at the IAG Meeting, 2009.

Y. E. Bar-Sever. A new model for GPS yaw attitude. *Journal of Geodesy*, 70(11): 714–723, 1996.

Y. E. Bar-Sever. New and Improved Solar Radiation Models for GPS Satellites Based on Flight Data. Technical report, Jet Propulsion Laboratory, 1997.

Y. E. Bar-Sever, P. M. Kroger, and J. A. Borjesson. Estimating horizontal gradients of tropospheric path delay with a single GPS receiver. *Journal of Geophysical Research*, 103(B3):5019–5035, 1998.

R. C. Barbosa. China launches another navigation satellite - End 2010 with record 15 launches. *NASA spaceflight com*, 2010a.

R. C. Barbosa. Long March launches fifth GPS satellite for China. *NASA spaceflight com*, 2010b.

S. Bassiri and G. A. Hajj. Higher-order ionospheric effect on the Global Positioning System and means of modelling them. *Manuscripta Geodaetica*, 18(6): 280–289, 1993.

L. Bastos and H. Landau. Fixing cycle slips in dual-frequency kinematic GPS-applications using Kalman filtering. *Manuscripta Geodaetica*, 13(4):249–256, 1988.

S. Basu, S. Basu, J. LaBelle, E. Kudeki, B. G. Fejer, M. C. Kelley, H. E. Whitney, and A. Bushby. Gigahertz Scintillations and Spaced Receiver Drift Measurements During Project Condor Equatorial F Region Rocket Campaign in Peru. *Journal of Geophysical Research*, 91(A5):5526–5538, 1986.

J. Beckheinrich. Status and Impact of Stochastic models in GNSS Evaluation. In *Proceedings of NAVITEC, Noordwijk, The Netherlands*, 2008.

J. Benedicto and D. Ludwig. Galileo System Architecture and Services. In *Seventh International Workshop on Digital Signal Processing Techniques for Space Communications, Sesimbra, Portugal*, 2001.

N. Bergeot, C. Bruyninx, P. Defraigne, S. Pireaux, J. Legrand, E. Pottiaux, and Q. Baire. Impact of the Halloween 2003 ionospheric storm on kinematic GPS positioning in Europe. *GPS Solutions*, 15(2):171–180, 2010.

M. Bevis, S. Businger, T. A. Herring, C. Rocken, R. A. Anthes, and R. H. Ware. GPS Meteorology: Remote Sensing of Atmospheric Water Vapor Using the Global Positioning System. *Journal of Geophysical Research*, 97(D14):15787–15801, 1992.

G. Beyerle. Carrier phase wind-up in GPS reflectometry. *GPS Solutions*, 13(3): 191–198, 2009.

S. Bisnath and Y. Gao. Current state of precise point positioning and future prospects and limitations. In *Proceedings of IUGG 24th General Assembly*, 2007.

S. Bisnath and Y. Gao. Innovation: Precise Point Positioning. A powerful technique with a promising future. *GPS World*, April:43–50, 2009.

P. Bona. Precision, Cross Correlation, and Time Correlation of GPS Phase and Code Observations. *GPS Solutions*, 4(2):3–13, 2000.

C. Boucher and Z. Altamimi. International Terrestrial Reference Frame. *GPS World*, September, 1996.

F. K. Brunner and M. Gu. An improved model for the dual frequency ionospheric correction of GPS observation. *Manuscripta Geodaetica*, 16:205–214, 1991.

G. Buble, R. Benet, and S. Hreinsdóttir. Tide gauge and GPS measurements of crustal motion and sea level rise along the eastern margin of Adria. *Journal of Geophysical Research*, 115:02404, 2010.

F. Butsch. Galileo signals, frequencies, performance, current activities, project status. In *ICAO Aeronautical Spectrum Management Seminar, Nairobi, Kenia*, 2007.

C. Cai and Y. Gao. Positioning model and accuracy analysis of Precise Point Positioning with GPS and GLONASS. Poster paper, Geoide Annual Meeting, 2007.

P. Charlot. TN19. Earth orientation, reference frames and atmospheric excitation functions submitted for the 1994 IERS Annual report, 1995.

G. Chen and T. A. Herring. Effects of atmospheric azimuthal asymmetry on the analysis of space geodetic data. *Journal of Geophysical Research*, 102(B9):20489–20502, 1997.

C. Chong. Status of COMPASS/BeiDou Development. In *Stanford's PNT Challenges and Opportunities Symposium*, 2009.

P. Collins, F. Lahaye, P. Héroux, and S. Bisnath. precise point positioning with ambiguity resolution using a decoupled clock model. In *Proceedings of the 21st ION International technical meeting of the satellite division*, 2008.

C. J. Comp and P. Axelrad. Adaptive SNR-based carrier phase multipath mitigation technique. *IEEE Transactions on Aerospace and Electronic Systems*, 34(1): 264–276, 2002.

M. Crisci, M. Hollreiser, M. Falcone, M. Colina, and J. Giraud. GIOVE mission sensor station performance characterization: overview of the results. In *ION GNSS*, 2007.

U. Dach, U. Hugentobler, R. Fridez, and P. Meindl. *Bernese GPS Software Version 5.0*, 2007.

Z. Dai, S. Knedlik, and O. Loffeld. Instantaneous Triple-Frequency GPS Cycle-Slip Detection and Repair. *International Journal of Navigation and Observation*, 2009. doi: 10.1155/2009/407231.

P. F. de Bakker, C. C. J. M. Tiberius, H. van der Marel, and R. J. P. van Bree. Short and zero baseline analysis of GPS L1 C/A, L5Q, GIOVE E1B, and E5aQ signals. *GPS Solutions*, 2011. doi: 10.1007/s10291-011-0202-3.

M. C. de Lacy, A. J. Gil, G. Rodriguez-Caderot, and B. Moreno. A method to estimate the ionospheric bias by using the new GNSS frequencies: an analysis of its theoretical accuracy in a PPP context. *Fisica de la Tierra*, 20:133–150, 2008a.

M. C. de Lacy, M. Reguzzoni, F. Sansó, and G. Venuti. The Bayesian detection of discontinuities in a polynomial regression and its application to the cycle-slip problem. *Journal of Geodesy*, 82(9):527–542, 2008b.

S. D. Desai. Observing the pole tide with satellite altimetry. *Journal of Geophysical Research*, 107(C11):3186–3199, 2002.

A. J. V. Dierendonck. Eye on the Ionosphere: Measuring Ionospheric Scintillation effects from GPS signals. *GPS Solutions*, 2(4):60–63, 1999.

A. J. V. Dierendonck and M. S. Braasch. Evaluation of GNSS receiver correlation processing techniques for multipath and noise mitigation. In *Proceedings of the ION National Technical Meeting*, 1997.

J. M. Dow, R. E. Neilan, and C. Rizos. The International GNSS Service in a changing landscape of Global Navigation Satellite Systems. *Journal of Geodesy*, 83: 191–198, 2009.

S. Dubey, R. Wahi, and A. K. Gwal. Effect of ionospheric scintillation on GPS receiver at equatorial anomaly region Bhopal. In *Proceedings of the XXVIIth General Assembly of the Union Radio-Scientifique Internationale*, 2005.

R. Ebner and W. E. Featherstone. How well can online GPS PPP post-processing services be used to establish geodetic survey control networks? *Journal of Applied Geodesy*, 2:149–157, 2008.

A. El-Rabbany. *The Effect of Physical Correlations on the Ambiguity Resolution and Accuracy Estimation in GPS Differential Positioning*. PhD thesis, University of New Brunswick, 1994.

A. El-Rabbany. *GPS: The Global Positioning System*. Artech House, 2002.

G. Elgered. Exploitation of ground-based GPS for climate and numerical weather prediction applications. Technical report, COST Action 716 223/98, 1998.

H. J. Euler and C. C. Goad. On optimal filtering of GPS dual frequency observations without using orbit information. *Bulletin Geodesique*, 65:130–143, 1991.

European Commission, 2003. *The Galilei Project. Galileo Design Consolidation*. ESYS plc, Guildford, UK, 2003.

M. Fritsche, R. Dietrich, C. Knofel, A. Rulke, S. Vey, M. Rothacher, and P. Steigenberger. Impact of higher-order ionospheric terms on GPS estimates. *Geophysical Research Letters*, 32:23311, 2005.

G. X. Gao, L. Heng, D. de Lorenzo, S. Lo, D. Akos, A. Chen, T. Walter, P. Enge, and B. Parkinson. Modernization Milestone Observing the first GPS satellite with an L5 payload. *InsideGNSS*, may/june:30–36, 2009.

Y. Gao and X. Shen. Improving convergence speed of carrier phase based Precise Point Positioning. In *Proceedings of ION GPS*, 2001.

Y. Gao, Z. Liu, and Z. Z. Liu. Internet-Based Real-Time Kinematic Positioning. *GPS Solutions*, 5(3):61–69, 2002.

Y. Gao, Y. Zhang, and K. Chen. Development of a real-time single-frequency precise point positioning system and test results. In *Prodeedings of the ION GNSS*, 2006.

C. S. Gardner. Correction of laser tracking data for the effects of horizontal refractivity gradients. *Applied Optics*, 16(9):2427–2432, 1977.

M. Ge, G. Gendt, and M. Rothacher. Integer ambiguity resolution for precise point positioning. In *Proceedings of VI Hotine-Marussi Symposium of Theoretical and computational Geodesy*, 2006.

M. Ge, G. Gendt, M. Rothacher, C. Shi, and J. Liu. Resolution of GPS carrier-phase ambiguities in Precise Point Positioning (PPP) with daily observations. *Journal of Geodesy*, 82:389–399, 2008.

G. Gendt. IGS switch to absolute antenna model and ITRF2005. *IGS Mail No. 5438, IGS Central Bureau Information System*, 2006.

G. Gendt, Z. Altamimi, R. Dach, W. Sohne, T. Springer, and T. G. prototype Team. GGSP: realisation and maintenance of the Galileo Terrestrial Reference Frame. *Advances in Space Research*, 47(2):174–185, 2011.

J. Geng, F. N. Teferle, C. Shi, X. Meng, A. H. Dodson, and J. Liu. Ambiguity resolution in precise point positioning with hourly data. *GPS Solutions*, 13(4): 263–270, 2009.

J. Geng, F. N. Teferle, X. Meng, and A. H. Dodson. Towards PPP-RTK: Ambiguity resolution in real-time precise point positioning. *Advances in Space Research*, 47(10):1664–1673, 2010.

Giove SIS ICD. GIOVE A + B Navigation Signal-in-Space. Interface Control Document, 2008.

GLONASS SIS ICD. Global Navigation Satellite System. Interface Control Document, 2008.

W. Gurtner and L. Estey. RINEX The Receiver Independent Exchange format Version 3.00, 2007.

J. K. Hargreaves. *The solar-terrestrial environment*. Cambridge University Press, 1992.

A. Hauschild. New GPS + GIOVE Real-Time Clock Product. *IGS Mail No. 6133, IGS Central Bureau Information System*, 2010.

G. Hein, J. Godet, J. L. Issier, J. C. Martin, P. Erhard, R. Lucas, and T. Pratt. Status of Galileo frequency and Signal Design. In *ION GNSS*, 2002.

M. Hernandez-Pajares, J. M. Juan, J. Sanz, and R. Orus. Second-order ionospheric term in GPS: Implementation and impact on geodetic estimates. *Journal of Geophysical research*, 112:8417–8433, 2007.

P. Héroux, Y. Gao, J. Kouba, F. Lahaye, Y. Mireault, P. Collins, K. Macleod, P. Tetreault, and K. Chen. Products and applications for precise point positioning - moving towards real-time. In *Proceedings of ION GNSS*, 2004.

B. Hofmann-Wellenhof, H. Lichtenegger, and E. Wasle. *GNSS Global Navigation Satellite Systems*. SpringerWienNewYork, 2008.

D. B. Holdridge. An alternate expression for light time using general relativity. Technical report, Jet Propulsion Laboratory, 1967.

H. S. Hopfield. Two-Quartic Tropospheric Refractivity Profile for Correcting Satellite Data. *Journal of Geophysical Research*, 74(18):4487–4499, 1969.

H. S. Hopfield. *Tropospheric range error parameters: further studies*. The Johns Hopkins University - Applied Physics Laboratory, 1972.

M. M. Hoque and N. Jakowski. Higher order ionospheric effects in precise GNSS positioning. *Journal of Geodesy*, 81(4):259–268, 2007.

C. Y. Huang, W. J. Burke, J. S. Machuzak, L. C. Gentile, and P. J. Sultan. DMSP observations of equatorial plasma bubbles in the topside ionosphere near solar maximum. *Journal of Geophysical Research*, 106(A5):8131–8142, 2001.

IS-GPS-200E. Global positioning system wing (GPSW) systems engineering and integrations, 2010.

IS-GPS-705A. Global positioning system wing (GPSW) systems engineering and integrations, 2010.

IS-GPS-800A. Global positioning system wing (GPSW) systems engineering and integrations, 2010.

P. K. Jain. Indian Satellite Navigation Programme: an update. In *45th Session of S&T Subcommittee of UN-COPUOS, Vienna, Feb 11-22*, 2008.

N. Jakowski, R. Leitinger, and M. Angling. Radio occultation techniques for probing the ionosphere. *Annals of geophysics, supplement*, 47(2-3):1049–1066, 2004.

N. Jakowski, C. Mayer, V. Wilken, and M. M. Hoque. Ionospheric Impact on GNSS Signal. *Física de la Tierra*, 20:11–25, 2008.

S. Kedar, G. A. Hajj, B. D. Wilson, and M. B. Heflin. The Effect of the Second Order GPS Ionospheric Correction on Receiver Positions. *Geophysical Research Letters*, 30(16):1829–1833, 2003.

W. Kertz. Einführung in die Geophysik II. *B. I. Wissenschaftsverlag*, 218, 1971.

M. O. Keshin, A. Q. Le, and H. van der Marel. Single and dual-frequency precise point positioning: approaches and performances. In *Proceedings of NAVITEC, Noordwijk, The Netherlands*, 2006.

B. C. Kim and M. V. Tinin. Effect of Ionospheric Irregularities on Accuracy of Dual-frequency GPS systems. *Geomagnetism and Aeronomy*, 47(2):238–243, 2007.

J. Y. Kim. Commercial Opportunities to Use GPS for Sustainable Development. In *Global Space Technology Forum Abu Dhabi, United Arab Emirates*, 2009.

J. A. Klobuchar. Ionospheric time-delay algorithm for single-frequency GPS users. *IEEE Trans. Aerospace Electron. Syst.*, 23(3):325–331, 1986.

K.-R. Koch. *Parameter estimation and hypothesis testing in linear models*. Springer Verlag Germany, 1999.

J. Kouba. *A guide to using international GPS service IGS products*, 2009a.

J. Kouba. A simplified yaw-attitude model for eclipsing GPS satellites. *GPS Solutions*, 13(1):1–12, 2009b.

J. Kouba and P. Héroux. Precise point positioning using IGS orbit and clock products. *GPS Solutions*, 5(2):12–28, 2001.

J. Kumar. Control point positioning using GPS. *Geospatialworld*, 2001.

R. Langley. Expert Advice: Cause Identified for Pseudorange Error from New GPS Satellite SVN-49. *GPS World*, August:8–8, 2009.

A. Le and C. Tiberius. Single-frequency precise point positioning with optimal filtering. *GPS Solutions*, 11(1):61–69, 2007.

A. Leick. *GPS Satellite Surveying*. John Wiley & Sons, Inc., 2004.

Z. Liu. A new automated cycle slip detection and repair method for a single dual-frequency GPS receiver. *Journal of Geodesy*, 85(3):171–183, 2011.

G. Mader. GPS antenna calibration at the National Geodetic Survey. *GPS Solutions*, 3(1):50–58, 1999.

J. W. Marini. Correction of satellite tracking data for an arbitrary tropospheric profile. *Radio Science*, 7(2):223–231, 1972.

M. Martín-Neira, M. Caparrini, J. Font-Rossello, S. Lannelongue, and C. S. Vallmitjana. The PARIS Concept: An Experimental Demonstration of Sea Surface Altimetry Using GPS Reflected Signals. *IEEE Transactions of Geoscience and Remote Sensing*, 39(1):142–150, 2001.

D. D. McCarthy. TN3. IERS Standards, 1989.

L. F. McNamara. *The Ionosphere: Communications, Surveillance and Direction finding*. Krieger publishing company, Malabar, Florida, 1991.

M. Miranian and W. Klepczynski. Time Transfer via GPS at USNO. In *Proceedings of ION GPS*, 1991.

Y. Mireault, P. Tétrault, F. Lahaye, P. Héroux, and J. Kouba. Innovation: Online Precise Point Positioning. *GPS World*, 19:59–64, 2008.

P. Misra and P. Enge. *Global Positioning System*. Ganga-Jamuna Press, 2006.

D. Moelker. Multiple Antennas for Advanced GNSS Multiple Mitigation and Multipath Direction Finding. In *Proceedings of ION GPS*, 1997.

O. Montenbruck, C. Gunther, S. Graf, M. Garcia-Fernandez, J. Furthner, and H. Kuhlen. GIOVE-A initial signal analysis. *GPS Solutions*, 10(2):146–153, 2006.

O. Montenbruck, A. Hauschild, S. Erker, M. Meurer, R. B. Langley, and P. Steigenberger. System: GPS L5, The Real Stuff. *GPS World*, July:13–14, 2010.

B. Moreno, G. Rodriguez-Caderot, and M. de Lacy. The state of the art of a new approach in precise point positioning. Poster paper, 2nd International Colloquium - scientific and fundamental aspects of the Galileo programme, 2009.

B. Moreno, S. Radicella, M. C. de Lacy, M. Herraiz, and G. Rodriguez-Caderot. On the effects of the ionospheric disturbances on precise point positioning at equatorial latitudes. *GPS Solutions*, 15(4):381–390, 2011.

H. Munekane. A semi-analytical estimation of the effect of second-order ionospheric correction on the GPS positioning. *Geophysical Journal International*, 163(1):10–17, 2005.

T. A. Murphy. Local-area Augmentation System for satellite navigation precision-approach system, 1998.

NATO. STANAG 4294. NAVSTAR Global Positioning System (GPS) System Characteristics. Technical report, NATO, 1993.

R. V. Nee. Multipath Effects on GPS Code Phase Measurement. In *Proceedings of ION GPS*, 1991.

Niell. Global mapping functions for the atmosphere delay at radio wavelengths. *Journal of geophysical research*, 101(B2):3227–3246, 1996.

V. Oehler, J. M. Krueger, T. Beck, M. Kirchner, H. L. Trautenberg, J. Hahn, and D. Blonski. Galileo System Performance Status Report. In *ION GNSS, Savannah, Georgia*, 2009.

D. Orgiazzi and P. Tavella. Experimental assessment of the time transfer capability of Precise Point Positioning (PPP). In *Proceedings of the IEEE International Frequency Control Symposium and Exposition*, 2005.

OS SIS ICD. European GNSS (Galileo) Open Service. Signal In Space. Interface Control Document, 2010.

L. Panadero, B. Moreno, M. Herraiz, and G. Rodriguez-Caderot. A preliminary analysis of the slant total electron content (sTEC) obtained from GPS observations in Tucuman region and its relationship with the ionospheric scintillation. Poster paper, Beacon Satellite Symposium, 2010.

G. Petit and B. Luzum. TN36. IERS Conventions, 2010.

R. Píriz. Orbit and clock characterization: ODTS methodology and quality control. In *Galileo one year in orbit workshop ESA/ESTEC*, 2007.

R. Píriz, A. M. Garcia, G. Tobias, V. Fernandez, P. Tavella, I. Sesia, G. Cerreto, and J. Hahn. GNSS interoperability: offset between reference time scales and timing biases. *BIPM and IOP Publishing Ltd. Metrologia*, 45:87–102, 2008.

A. J. Pope. *The statistics of residuals and the detection of outliers*. U.S. Dept. of Commerce, National Oceanic and Atmospheric Administration, National Ocean Survey, Geodetic Research and Development Laboratory in Rockville, Md., 1976.

A. Portillo, M. Herraiz, S. Radicella, and L. Ciraolo. Equatorial plasma bubbles studied using African slant total electron content observations. *Journal of atmospheric Solar-Terrestrial physics*, 70(6):907–917, 2008.

R. Prasad and M. Ruggieri. *Applied Satellite Navigation Using GPS, GALILEO, and Augmentation Systems*. Artech House Publishers, 2005.

S. M. Radicella and R. Leitinger. The evolution of the DGR approach to model electron density profiles. *Advances in Space Research*, 27(1):35–40, 2001.

R. D. Ray and R. M. Ponte. Barometric tides from ECMWF operational analyses. *Annales Geophysicae*, 21(8):1897–1910, 2003.

S. G. Revnivykh. GLONASS Status and Progress. In *47th CGSIC Meeting, Texas*, 2007.

H. Rishbeth. The equatorial F-layer: progress and puzzles. *Annales Geophysic*, 18: 730–739, 2000.

M. Rothacher. Comparison of Absolute and Relative Antenna Phase Center Variations. *GPS Solutions*, 4(4):55–60, 2001.

M. Rothacher and G. Beutler. Estimation of Nutation terms using GPS. In *Proceedings of the IGS AC Workshop, Darmstadt, Germany*, 1998.

J. Saastamoinen. Contribution to the theory of atmospheric refraction. *Bulletin Geodesique*, 105(1):279–298, 1973.

F. Sansó. *La verifica di ipotesi*. CittáStudi Edizioni, 1996.

F. Sansó. Il posizionamento da satellite (GNSS). `geomatica.como.polimi.it`, 2006.

C. Satirapod and J. Wang. Comparing the quality indicators of GPS carrier phase observations. *Geomatics research australasia*, 73:75–92, 2000.

S. Schaer. How to use CODE's Global Ionosphere Maps, 1997.

S. Schaer. Monitoring P1C1 code biases. *IGS Mail No. 2827, IGS Central Bureau Information System*, 2000.

S. Schaer. New PRN01/SVN63 active. *IGS Mail No. 6437, IGS Central Bureau Information System*, 2011.

S. Schaer and R. Dach. Biases in GNSS Analysis. In *IGS Workshop, Newcastle, England*, 2010.

R. Schmid. Upcoming switch to IGS08/igs08.atx - Details on igs08.atx. *IGS Mail No. 6355, IGS Central Bureau Information System*, 2011.

R. Schmid and M. Rothacher. Estimation of elevation-dependent satellite antenna phase center variations of GPS satellites. *Journal of Geodesy*, 77(7-8):440–446, 2003.

S. Schön and F. K. Brunner. Modelling physical correlation of GPS phase observations: first results. In *Proceedings of 3rd Symp. Geodesy for Geotechnical and Structural Engineering*, 2006.

G. Seeber. *Satellite Geodesy*. Walter de Gruyter - Berlin - New York, 2003.

M. J. Sevilla. Colocación mínimos cuadrados. *Publicaciones del Instituto de Astronomía y Geodesia. UCM - CSIC. Madrid*, 1987.

M. Shaw, K. Sandhoo, and D. Turner. Modernization of the Global Positioning System. *GPS World*, 11(9), 2000.

X. Shen and Y. Gao. Analysing the impacts of Galileo and modernized GPS on precise point positioning. In *Proceedings of ION NTM*, 2006.

A. Simsky, J. M. Sleewaegen, W. D. Wilde, and F. Wilms. Galileo receiver development at Septentrio. In *ENC GNSS, Munich*, 2005.

A. Simsky, D. Mertens, J. M. Sleewaegen, M. Hollreiser, and M. Crisci. Experimental Results for theMultipath Performance of Galileo Signals Transmitted by GIOVE-A Satellite. *International Journal of Navigation and Observation*, Article ID 416380, 2008a. doi: 10.1155/2008/41638.

A. Simsky, D. Mertens, J.-M. Sleewaegen, W. D. Wilde, M. Hollreiser, and M. Crisci. Multipath and Tracking Performance of Galileo Ranging Signals Transmitted by GIOVE-B. In *Proceedings of ION GNSS*, 2008b.

J. H. Sobral, M. Abdu, H. Takahashi, M. J. Taylor, E. R. de Paula, M. G. de Aquino, and G. L. Borba. Ionospheric plasma bubble climatology over Brazil based on 22 years (1977:1998) of 630 nm airglow observations. *Journal of Atmospheric and Solar-Terrestrial Physics*, 64(12-14):1517–1524, 2002.

T. Springer and F. Dilssner. Saving SVN49 A Detailed look at a GPS signal anomaly. *InsideGNSS*, july/august:32–36, 2009.

C.-C. Su. Reinterpretation of the Michelson-Morley experiment based on the GPS Sagnac correction. *Europhysics Letters*, 56(2):170–174, 2001.

P. J. G. Teunissen. The GPS phase-adjusted pseudorange. In *Proceedings of 2nd Workshop on high precision navigation, Stuttgart, Germany*, 1991.

S. Thoelert, S. Erker, J. Furthner, and M. Meurer. Latest Signal in Space Analysis of GPS IIF, COMPASS and GLONASS. Poster paper Navitec, Noordwijk, The Netherlands, 2010.

R. Tiwari, S. Bhattacharya, P. K. Purohit, and A. K. Gwal. Effect of TEC Variation on GPS Precise Point at Low Latitude. *The Open Atmospheric Science Journal*, 3(1):1–12, 2009.

G. Tobías, I. Hidalgo, A. Mozo, D. Rodríguez, S. Binda, F. González, A. Mudrak, P. Tavella, I. Sesia, and G. Cerretto. Building Galileo Navigation System: Two Years of GIOVE-M Experimentation. In *Proceedings of ION GNSS*, 2009.

R. T. Tsunoda. Control of the seasonal and longitudinal ocurrence of equatorial scintillations by the longitudinal gradient in integrated E region Pedersen conductivity. *Journal of Geophysical Research*, 90(A1):447–456, 1985.

J. van Haaften. Five Satellites in Geostationary Orbit China's Beidou Navigation Project. *GEOInformatics*, January/February, 2007.

J. Ventura-Traveset and D. Flament. *EGNOS: The European Geostationary Navigation Overlay System - A cornerstone of Galileo*. ESA Publications Division, 2006.

J. M. Wahr. Body tides on an elliptical, rotating, elastic and oceanless Earth. *Geophys. J. Roy. Astr. Soc.*, 64(3):677–703, 1981.

J. Wang, M. P. Stewart, and M. Tsakiri. Stochastic modelling for static GPS baseline data processing. *Journal of surveying engineering*, 124(4):171–181, 1998.

J. Wang, C. Satirapod, and C. Rizos. Stochastic assessment of GPS carrier phase measurements for precise static relative positioning. *Journal of Geodesy*, 76(2): 95–104, 2002.

R. Weber, C. Bruyninx, H. Scherneck, M. Rothacher, P. Andersen, T. Baker, and T. van Dam. GPS / GLONASS and Tidal Effects. Final Report for 1997-2000. Technical report, IAG/ETC Working Group 6 Solid Earth tides in space geodetic techniques, 2003.

J. Wu, C. Wu, G. Hajj, W. Bertiger, and S. Lichtenr. Effects of antenna orientation on GPS carrier phase. *Manuscripta Geodaetica*, 18:1647–1660, 1993.

G. Wübbena, M. Schmitz, F. Menge, V. Boder, and G. Seeber. Automated Absolute Field Calibration of GPS Antennas. In *Prodeedings of the ION GPS-00, Salt Lake City, Utah.*, 2000.

G. Wübbena, M. Schmitz, and A. Bagg. PPP-RTK: precise point positioning using state-space representation in RTK networks. In *Prodeedings of the ION GNSS*, 2005.

S. Zaidman. Global Positioning System Wide Area Augmentation System (WAAS) Performance Standard, 2008.

R. Zandbergen and D. Navarro. Specification of Galileo and GIOVE space segment properties relevant for satellite laser ranging. Technical report, European Space Agency, 2006.

S. Y. Zhu and E. Groten. Relativistic effects in GPS. *Lecture notes in Earth Sciences*, 19:41–46, 1988.

J. Zumberge. Automated GPS data analysis service. *GPS Solutions*, 2(3):76–78, 1999.

J. Zumberge, M. Heflin, D. Jefferson, M. Watkins, and F. Webb. Precise point positioning for the efficient and robust analysis of GPS data from large networks. *Journal of Geophysical research*, 102(B3):5005–5017, 1997.